

Cover Page



Universiteit Leiden



The handle <http://hdl.handle.net/1887/66824> holds various files of this Leiden University dissertation.

Author: Barber, C.R.

Title: Monsters in the deep: using simulations to understand the excess baryonic mass in the centres of high-mass, early-type galaxies

Issue Date: 2018-11-20

Monsters in the Deep

Using simulations to understand the excess baryonic mass
in the centres of high-mass, early-type galaxies

Proefschrift

ter verkrijging van
de graad van Doctor aan de Universiteit Leiden,
op gezag van Rector Magnificus prof. mr. C.J.J.M. Stolker,
volgens besluit van het College voor Promoties
te verdedigen op dinsdag 20 November 2018
klokke 10.00 uur

door

Christopher Ryan Barber

geboren te Ottawa, Ontario, Canada
in 1989

Promotor: Prof. dr. Joop Schaye
Co-promotor: Dr. Robert A. Crain (Liverpool John Moores University, UK)

Promotiecommissie: Prof. dr. Huub Röttgering
Prof. dr. Marijn Franx
Prof. dr. Charlie Conroy (Harvard University, USA)
Dr. Madusha Gunawardhana
Dr. Russell Smith (Durham University, UK)

An electronic version of this thesis can be found at openaccess.leidenuniv.nl

Cover designed and created by Kyle Barber

ISBN: 978-94-028-1252-7

For Zoë

*“If you wish to make an apple pie from scratch,
you must first invent the Universe.”*
– Carl Sagan¹

¹Cosmos (1980)

Contents

1	Introduction	1
1.1	Galaxy formation and evolution	2
1.2	Black hole monsters	3
1.3	Stellar population monsters	6
1.4	Simulations of galaxy formation and evolution	9
1.5	This thesis	11
1.6	Outlook	13
2	The origin of compact galaxies with anomalously high black hole masses	15
2.1	Introduction	16
2.2	The EAGLE Simulations	18
2.2.1	Subgrid physics	18
2.2.2	Subhalo identification and corrections	20
2.3	Outliers in the $M_{\text{BH}} - M_{\star}$ relation	21
2.4	The origin of outliers from the $M_{\text{BH}} - M_{\star}$ relation	25
2.4.1	Environment at $z = 0$	27
2.4.2	Evolution	28
2.4.3	Tidal stripping as the primary cause of anomalously high $M_{\text{BH}}(M_{\star})$	29
2.4.4	Early formation time as a secondary cause of anomalously high $M_{\text{BH}}(M_{\star})$	32
2.4.5	The relative importance of tidal stripping and early formation	35
2.4.6	Galaxies with “monstrous” black holes in galaxy cluster environments	38
2.5	Relation to compact galaxies	42
2.6	Summary and Conclusions	46
3	Calibrated, cosmological, hydrodynamical simulations with variable IMFs	
	I:	
	Method and effect on global galaxy scaling relations	49
3.1	Introduction	50
3.2	Methods	53
3.2.1	The EAGLE simulations	54
3.2.2	IMF calibration	55
3.2.3	Preparations for self-consistent simulations with a variable IMF	63
3.3	Self-consistent simulations with a variable IMF	65

3.3.1	IMF vs stellar velocity dispersion	65
3.3.2	Subgrid calibration diagnostics	71
3.4	Effect of variable IMFs on galaxy properties	76
3.4.1	Alpha enhancement	76
3.4.2	Metallicities	77
3.4.3	Star formation	81
3.4.4	ETG galaxy sizes	84
3.5	Summary and Conclusions	86
3.A	Aperture effects and IMF calibration details	89
3.B	Self-consistency tests	91
3.C	The dwarf-to-giant ratio	94
4	Calibrated, cosmological, hydrodynamical simulations with variable IMFs	
	II:	
	Correlations between the IMF and global galaxy properties	99
4.1	Introduction	100
4.2	Simulations	101
4.3	Is the (M/L)-excess a good tracer of the IMF?	105
4.4	Trends between the (M/L)-excess and global galactic properties	107
4.4.1	MLE vs age	107
4.4.2	MLE vs metallicity	111
4.4.3	MLE vs $[Mg/Fe]$	112
4.4.4	MLE vs Chabrier-inferred galaxy mass, luminosity, and size	113
4.4.5	MLE vs M_{BH}/M_*	116
4.4.6	Which observables correlate most strongly with the MLE?	118
4.5	MLE of satellite galaxies	120
4.6	Summary and Conclusions	121
5	Calibrated, cosmological, hydrodynamical simulations with variable IMFs	
	III:	
	Spatially-resolved properties and evolution	125
5.1	Introduction	126
5.2	Simulations	128
5.3	IMF trends within galaxies	131
5.3.1	Sample selection	131
5.3.2	Radial IMF gradients	134
5.3.3	Radial gradients in stellar population properties	143
5.3.4	IMF vs local quantities	145
5.4	Redshift dependence of galaxy properties	148
5.4.1	Redshift dependence of the IMF	148
5.4.2	Redshift-dependent cosmic properties	155
5.5	Discussion	157
5.6	Summary and Conclusions	159
	Bibliography	163

Contents	vii
Nederlandse Samenvatting	171
Publications	175
Curriculum Vitae	177
Acknowledgements	179



Introduction

Astronomy is one of the most popular sciences for a reason – it’s beautiful. Images of astronomical objects ranging from the rocky surfaces of solar system bodies, to planets orbiting distant stars, to the great spiral arms of discy galaxies, have inspired people of all ages to think critically about our place in the Universe, both spatially and metaphysically. Doing so has allowed us to learn in a scientific way about where we, and the world in which we live, actually come from.

Our continued understanding of the cosmos is in no small part due to the study of galaxies. While the exact definition of a galaxy may be slightly nebulous, it is generally described as a self-bound system of stars, which typically also contains appreciable amounts of gas and dark matter. Not only are they often visually stunning, but they are physically extremely interesting due to the complex interplay of physical processes necessary for their construction.

For most of human existence, galaxies were simply known as fuzzy blobs in the sky, which eventually earned the name “nebulae”. It was only in 1920, less than 100 years ago as of this writing, when astronomers began to seriously question whether these nebulae either belonged to the Milky Way (MW), or were extragalactic in nature (called the “Great Debate” between Harlow Shapley and Heber Curtis). Only a few years later, Edwin Hubble discovered¹ that some of these nebulae were, in fact, distant galaxies of their own, completely unassociated with the MW. This discovery opened up the Universe considerably, shifting our paradigm of our place in it and inspiring future generations of astronomers to understand the origin and physical nature of these systems.

Since then, great strides have been made in our understanding of the Universe through the study of galaxies. This thesis aims to enhance this understanding by testing theoretical models of galaxy formation against observations of real galaxies, particularly in the cases of extreme systems which have been found to have an excess of baryonic mass in their central regions, in the form of either supermassive black holes

¹Georges Lemaître actually discovered “Hubble’s law” two years before Hubble, but is historically not given the credit since his paper was originally written in French (Lemaître 1927), and wasn’t translated into English until after Hubble’s publication.

(BHs) or stellar populations, thus harbouring “monsters” in the deep.

1.1 Galaxy formation and evolution

Thus follows a simplified overview of galaxy formation and evolution. It is by no means exhaustive, but is meant to give a first order intuition of the most important physical processes involved.

After the Big Bang, the matter in the Universe consisted of dark matter and gas, distributed almost completely uniformly. The “almost” here is important, since it was small density perturbations that grew under their own self-gravity to become the large scale structure that we see today. These fluctuations can be thought of as a superposition of plane waves, where they first collapse into vast sheets, and where these sheets intersect they form filaments, and at the intersection of these filaments are formed great knots of matter, called “haloes”. These haloes can be continually fed more gas and dark matter through smooth accretion along the filaments (Kereš et al. 2005; Dekel et al. 2009; Brooks et al. 2009) and mergers with other haloes (e.g. Robertson et al. 2006; Naab et al. 2006; Lagos et al. 2018). Thus forms the great cosmic web, and it is in its densest regions where the majority of galaxies form.

Consider an individual halo that initially consists of dark matter and gas. The dark matter virializes into a halo supported by random motions, while the gas can collapse further due to its ability to radiatively cool away its energy. Due to conservation of the angular momentum given to the halo via primordial gravitational torques, the gas does not collapse to a point, but forms a rotationally-supported disc (e.g. Fall & Efstathiou 1980; Mo et al. 1998).

Once this disc of gas forms, the gas can fragment into dense clouds that are cool enough to form molecules, which help it cool even further, eventually becoming dense enough to form stars, often with many stars forming per birth cloud. These stars burn hydrogen into heavier elements like helium and metals², where the most massive stars are able to generate the heaviest metals up to iron. The most massive stars are very short lived and end their lives with a core collapse supernova (SN) explosion, redistributing the star’s gas into the interstellar medium, enriching it with the metals produced during its lifetime as well as those produced by the explosion itself. The supernova adds energy and momentum to the gas, which can generate turbulence in the interstellar medium and potentially eject gas out of the galaxy as well as preventing further accretion of primordial gas from the cosmic web. Since it is this gas that is needed for further star formation, these supernovae act as a negative feedback effect, regulating the formation of future generations of stars. It is this stellar feedback that prevents galaxies from collapsing into very dense clumps of stars by ejecting low angular momentum gas from the galaxy, something that galaxy formation models had struggled to understand for many years (e.g. White & Rees 1978; Katz 1992; Navarro et al. 1995; Benson et al. 2003).

²Since hydrogen and helium together make up about 98 per cent of the baryonic mass in the Universe, astronomers refer to all other elements collectively as “metals”.

If a galaxy becomes massive enough (with a stellar mass $M_* \gtrsim 10^{10.5} M_\odot$)³, stellar feedback is no longer sufficient to keep the gas from accreting onto the galaxy. This is because, to first order, the binding energy of a galaxy per unit mass scales as $M^{2/3}$ under the virial theorem (assuming that size scales as $M^{1/3}$), which means that as the mass of a galaxy increases, it becomes increasingly difficult to expel its gas. And since the number of supernovae per unit stellar mass formed is on average 1 per cent (for a standard distribution of stellar masses at birth), there is a critical mass above which stellar feedback can no longer prevent gas from accreting onto the galaxy.⁴ In this case, gas can funnel into the central regions of the galaxy, accreting onto a supermassive BH. As the BH grows in mass, it produces its own feedback due to the intense heat caused by the friction in its gaseous accretion disc. The energy that it outputs is proportional to the accretion rate, which in turn increases with its mass (Bondi & Hoyle 1944; Rosas-Guevara et al. 2015), so it grows until the energy that is output is high enough to once again keep the gas at bay and prevent further BH growth, which is roughly when the output energy is comparable to the binding energy of the halo (e.g. Booth & Schaye 2010). This BH feedback (often called active galactic nucleus or AGN feedback), is potentially powerful enough to halt star formation throughout the entire galaxy, thus “quenching” star formation.

Once a galaxy’s star formation is quenched, the high-mass, bluer stars die off, leaving only the redder, lower-mass dwarf stars with mass $m \lesssim 1 M_\odot$. The galaxy can then continue to grow via mergers with other galaxies, which can disrupt the disc out of which its stars formed as well as adding stars formed in external galaxies on orbits misaligned with the disc, resulting in a more ellipsoidal shape (e.g. Toomre & Toomre 1972; Barnes & Hernquist 1992; Clauwens et al. 2018). Such systems are known as “red and dead” or “early-type” galaxies (ETGs). One such example, M60, which is on the verge of interacting with its neighbouring star-forming companion galaxy NGC 5647, is shown in Fig. 1.1. While actively star-forming (late-type) galaxies tend to exhibit discs of young, blue stars, early-type galaxies are much redder with a more diffuse stellar structure.

1.2 Black hole monsters

A linear correlation exists between the stellar mass of an early-type galaxy and its central BH mass, with a mean ratio $M_{\text{BH}}/M_* \approx 3 \times 10^{-3}$ (e.g. McConnell & Ma 2013; Kormendy & Ho 2013). The physical origin of this relationship is, however, currently unclear. It may be due to a causal effect, where the BH feedback helps to regulate the stellar mass (e.g. Silk & Rees 1998; Fabian 1999; King 2003), or the fact that more stellar mass means higher binding energy so that the BH must grow to higher mass in order to self-regulate (Booth & Schaye 2010; Bower et al. 2017). It may also be that they both grow due to gas-free mergers with other galaxies, increasing the BH and stellar mass in lock-step (Peng 2007; Jahnke & Macciò 2011). Whatever the reason,

³The mass of the Sun, a “Solar mass”, where $1 M_\odot \approx 2 \times 10^{30}$ kg.

⁴Note that this is only true for haloes if the stellar-to-halo mass ratio is roughly constant.

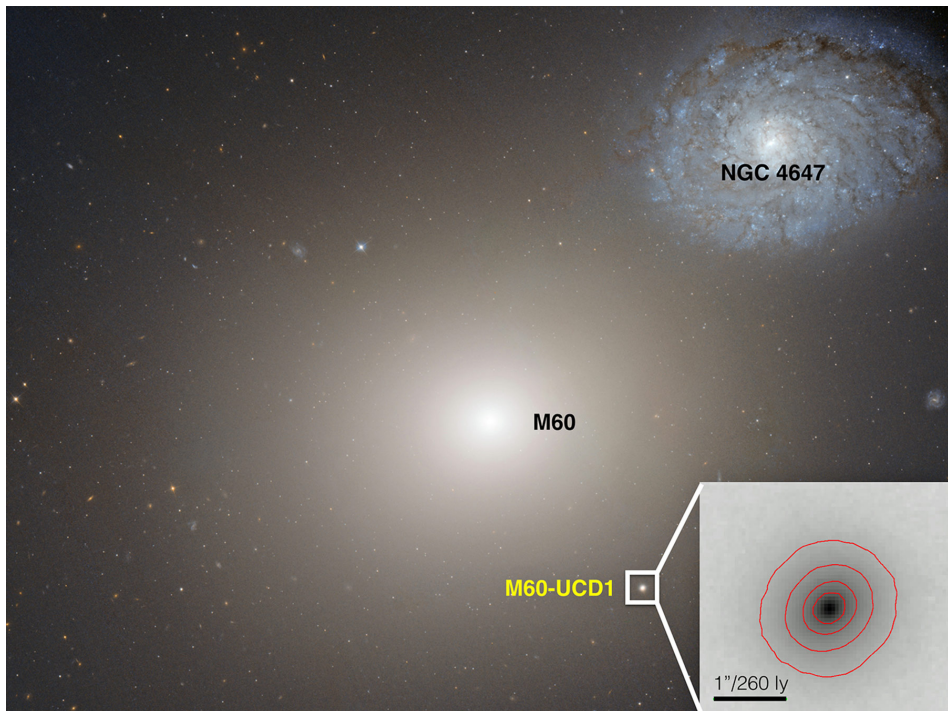


Figure 1.1: The M60 – NGC 4647 system, as seen by the Hubble Space Telescope. M60-UCD1, a black hole monster galaxy, lies to the lower right of M60. The inset in the lower right shows a zoomed surface brightness image of M60-UCD1 in the *g*-band, where red lines show contours of surface brightness in intervals of 1 magnitude per arcsecond. M60-UCD1 may have been a much more massive galaxy in the past, and is estimated to have lost ≈ 99 per cent of its stellar mass through tidal interactions with M60. Credit: NASA / ESA / Seth et al. (2014).



Figure 1.2: NGC 1277, a black hole monster galaxy, as seen by the Hubble Space Telescope. The old stellar populations of NGC 1277 imply that it may be a relic of the high-redshift Universe, when the $M_{\text{BH}} - M_{\star}$ relation may have had a higher normalization. Credit: NASA / ESA / Andrew C. Fabian / Remco C. E. van den Bosch (MPIA).

understanding the physical origin of this relation can aid in the understanding of how galaxies form and evolve.

A great way of understanding any correlation is to investigate its outliers. Studying the extreme cases can amplify the otherwise subtle physical effects governing the correlation for the general population. Indeed, some outliers of the $M_{\text{BH}} - M_{\star}$ relation have been discovered observationally. One notable example is NGC 1277 (Fig. 1.2) which may have a BH with mass as high as $(4.9 \pm 1.6) \times 10^9 M_{\odot}$ in its centre, an order of magnitude more massive than expected given the empirical $M_{\text{BH}} - M_{\star}$ relation (Walsh et al. 2016; but see Graham et al. 2016). Given its old stellar populations, it is thought that NGC 1277 may be a relic of the early Universe. At higher redshift⁵, the higher mean density of the Universe implies that the binding energy of a given halo was typically higher at fixed stellar mass, causing supermassive BHs in such haloes to grow to higher mass to begin self-regulating. Thus, if a galaxy forms at high redshift and remains undisturbed until the present day, it may today lie preferentially above the present-day $M_{\text{BH}} - M_{\star}$ relation (e.g. Booth & Schaye 2011; Ferré-Mateu et al. 2015).

Another prominent example of a BH monster galaxy is M60-UCD1, an ultracompact dwarf galaxy orbiting the massive elliptical galaxy M60 (Fig. 1.1). This galaxy has a BH mass of about 20 per cent of its stellar mass, much larger than the expected 0.3 per cent (Seth et al. 2014). The fact that it is a satellite implies that its extreme BH mass may have to do with its interaction with its host galaxy. During a merger between two galaxies, depending on the geometry and their mass difference, the two systems may temporarily form a host-satellite pair, where the satellite (the lower-mass galaxy) gradually loses stellar mass due to the tidal forces of the more massive companion. The

⁵Redshift is a measure of distance from Earth, and refers to the fact that galaxies that are further away appear redder due to a Doppler shift of the light resulting from the expansion of the Universe. Due to the finite speed of light, when we look at galaxies that are further away, we see them further back in time. Thus, redshift is generally used as a measure of time, where $z = 0$ is today, $z = 1$ is when the Universe was roughly half its current age, and $z \approx 2 - 3$ is when the cosmic star formation rate density peaked.

stripped galaxy will lose stellar mass beginning with the outermost, most loosely bound stars. If the satellite hosts a supermassive BH in its centre, stripping will thus increase its M_{BH}/M_* ratio, causing it to become an outlier of the $M_{\text{BH}} - M_*$ relation before it finally merges with the host galaxy, being completely disrupted and adding its M_* and M_{BH} to the host. This mechanism may be how many ultracompact dwarf galaxies are actually formed (e.g. Mieske et al. 2013). However, an alternative explanation for the excess mass in the centres of these systems may be not monstrous BHs, but instead monstrous stellar populations, a topic which we visit in the next section.

1.3 Stellar population monsters

The probability distribution of masses of stars at their time of formation is incredibly important for astronomy due to the fact that the evolution of a star, and thus the evolution of an entire galaxy of stars, depends sensitively on the star’s mass. Low-mass stars, with mass $m \lesssim 1 M_\odot$, tend to live for a very long time, with the lowest-mass stars living longer than the current age of the Universe. These “dwarf” stars are dim, but plentiful, and thus contribute significantly to the mass, but not to the light, of a galaxy. Higher-mass stars, with $m > 8 M_\odot$, tend to live much shorter, but exciting lives. Because they are so massive, they burn hot, bright, and fast, living for less than a few 10’s of millions of years (Myr), a blink of an eye compared to the 13.8 billion year (Gyr) age of the Universe. Thus, they are only around while a galaxy is actively forming stars, and are most often seen in the discs of galaxies where stars are typically born. They are the reason that spiral arms seen in galaxy images (like NGC 4648 in Fig. 1.1) are blue. However, there are relatively so few of them (about 1 per $100 M_\odot$ of stars formed) that they do not actually contribute much toward the mass of a galaxy, but they do contribute much of the light when a galaxy is actively forming stars. When they die, they leave behind BHs or neutron stars, depending on their mass. As the galaxy grows older, the growing number of such remnants can also contribute significantly to the mass of a galaxy.

Due to the primarily observational nature of astronomy, nearly all of what we know about the Universe is based on converting the light that is observed from the cosmos into physical quantities. For instance, if one intends to infer the mass of a galaxy from its total luminosity, one needs to make an assumption about the ratio of mass to light (M/L) in the galaxy. To estimate this quantity, one must make an assumption about the distribution of stellar masses in the galaxy, particularly because most of the mass is in low-mass stars that contribute very little light, whereas most of the light only comes from the highest-mass stars.

The translation between light and mass inherently depends on the assumed distribution of stellar masses in a given simple stellar population at birth, called the stellar initial mass function (IMF). It was first determined for our MW galaxy by Salpeter (1955) by directly counting the numbers of stars of different masses, finding that it takes the form of a power law, shown as the red solid line in Fig. 1.3. It was later updated by Kroupa (2001) and Chabrier (2003) to become slightly shallower for masses $\lesssim 0.5 M_\odot$. Indeed, the IMF in the MW appears to be universal, meaning

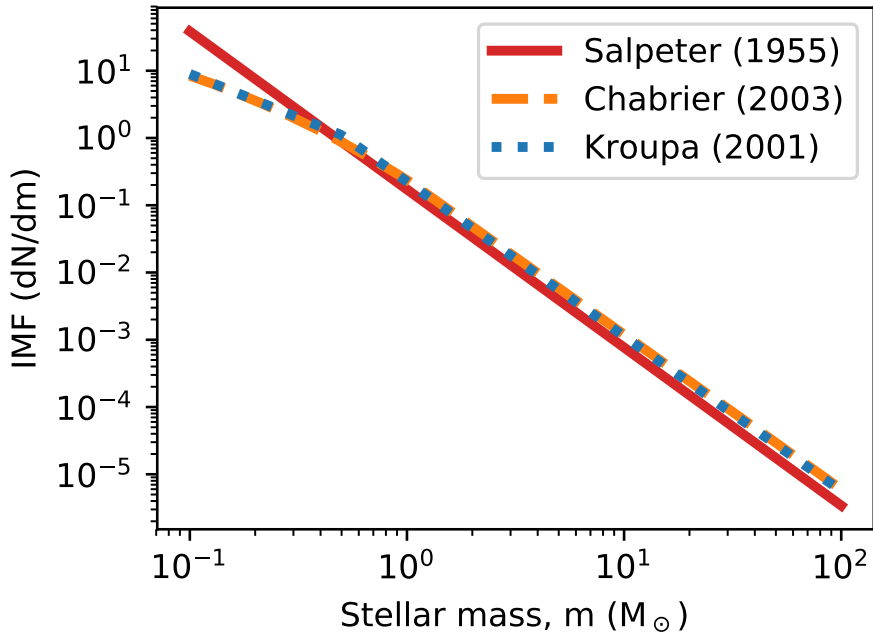


Figure 1.3: The stellar initial mass function (IMF), defined as the distribution of masses of stars in a simple stellar population at birth, for the Milky Way galaxy. The Salpeter (1955) functional form is plotted as a red solid line. The more recent forms determined by Chabrier (2003) and Kroupa (2001) are plotted as orange-dashed and blue-dotted lines, respectively.

that it has the same form no matter where one looks in the Galaxy (see Bastian et al. 2010 for a review). For stellar systems beyond the MW, it is much trickier to measure the IMF since individual stars cannot be resolved due to their distance. However, the universality of the IMF within the MW has led the vast majority of astronomers, both observers and theorists, to assume that a universal IMF may be applied to all galaxies in any environment.

Recently, some studies have had success at measuring the IMF in external galaxies, particularly in the central regions of high-mass early-type galaxies (ETGs). One method of doing so is to measure the stellar M/L ratio dynamically, by modelling the motions of the stars under the assumption that the system is dynamically relaxed, and making some assumption of the contribution to the gravitational potential of dark matter and a supermassive BH. Such studies have found that the stellar mass-to-light ratio, measured dynamically, is larger than would be expected given a standard MW-like IMF (e.g. Thomas et al. 2011b; Dutton et al. 2012; Tortora et al. 2013; Cappellari et al. 2013b; Li et al. 2017). This excess mass-to-light ratio (hereafter referred to as the MLE) appears to increase with the stellar velocity dispersion of the galaxy, which is closely related to its mass. From these observations alone, it is difficult to determine how the IMF is actually varying, as the extra “invisible” stellar mass may be due to an excess of very faint low-mass stars (a “bottom-heavy” IMF), or to high-mass stars, which have died long ago and left behind BHs and neutron stars (a “top-heavy” IMF).

A method of solving this degeneracy is by constraining the IMF through spectroscopy. Stellar spectra contain absorption lines that are sensitive to the surface gravity (and hence the mass) of a star, where, at fixed metallicity and age, some lines are stronger in dwarfs than in giant stars, and vice versa (e.g. Conroy & van Dokkum 2012a; La Barbera et al. 2013). It is thus possible to constrain the ratio of dwarf-to-giant stars in a given stellar population by fitting stellar population synthesis models to the spectra with the IMF as a free parameter. It is, however, unclear how the shape of the IMF should vary, since the dwarf-to-giant ratio can be increased by steepening the IMF slope at all masses (e.g. Spiniello et al. 2014), only at low masses (e.g. Conroy & van Dokkum 2012b; Conroy et al. 2017), or only at high masses (e.g. La Barbera et al. 2013). However, the choice of IMF parametrization can be critical for models of galaxy formation, since the high-mass end of the IMF governs stellar feedback and metal enrichment (e.g. Martín-Navarro 2016). Another issue is that the strengths of these IMF-sensitive absorption features often also depend on metallicity, so determination of the IMF may depend on one’s ability to separate these potentially degenerate variables (e.g. Vaughan et al. 2018a). Nevertheless, the majority of studies which constrain the IMF spectroscopically conclude that the dwarf-to-giant ratio, and thus the MLE, increases with stellar velocity dispersion in the centres of ETGs, in agreement with IMF constraints based on kinematics (Cenarro et al. 2003; Van Dokkum & Conroy 2010; Conroy & van Dokkum 2012b; Spiniello et al. 2012; Ferreras et al. 2013; La Barbera et al. 2013, 2015; Spiniello et al. 2014; Rosani et al. 2018).

On the other hand, these spectroscopic results for high-mass ETGs appear to be at odds with IMF constraints for actively star-forming galaxies. In such systems, the bright, short-lived, high-mass stars are still present, allowing their numbers to

be constrained (Baugh et al. 2005; Meurer et al. 2009; Haberman et al. 2010; Gunawardhana et al. 2011; Narayanan & Davé 2013; Nanayakkara et al. 2017; Zhang et al. 2018). However, due to their short lifetimes, the very highest-mass stars are still embedded in their birth clouds and are not directly observable. On the other hand, since they produce so much ionizing radiation, they ionize parts of their birth clouds, which re-emit the light as an H α emission line. By comparing the H α luminosity with the luminosity of the rest of the stellar population for which the birth clouds have dispersed, some of these studies have been able to place constraints on the high-mass end of the IMF. These studies tend to find that the fraction of high-mass stars increases with the star formation rate, implying that regions of high pressure could have top-heavy IMFs (Meurer et al. 2009; Gunawardhana et al. 2011; Zhang et al. 2018). However, since ETGs form their central stellar populations in high-pressure, high SFR episodes, it is unclear how to reconcile the observations of top-heavy IMF in star-forming regions with the bottom-heavy IMF in ETGs.

1.4 Simulations of galaxy formation and evolution

The picture of galaxy formation put forward in Section 1.1 is extremely simplified, and may be accurate only to first order for much of the galaxy population. In order to rigorously test theories of galaxy formation and evolution, one must be able to generate predictions of galaxy properties in a statistical sense and in a way that can be directly compared with observations. It is incredibly difficult to do so analytically, since in reality galaxy formation is a messy process, with a complex interplay between, for example, gas inflows and feedback-driven outflows, the distribution of metals within and outside of galaxies, and interactions between galaxies.

To test galaxy formation models, one must capture as closely as possible the complex interactions between the different relevant physical mechanisms, for which numerical simulations are required. One of the major difficulties in performing simulations of galaxy formation is the vast range of physical scales that are important. These range from the subatomic, where the atomic composition of the gas determines its ability to cool and condense, to parsec (pc) scales relevant for star formation, to Mpc scales to capture the interaction of galaxies with their environment, to 100's of Mpc in order to obtain a statistically representative sample of galaxies. Since it is computationally infeasible to simulate every atom in the Universe, the matter distribution in simulations is generally sampled either in Eulerian methods within fixed or adaptively-sized grid cells (e.g. Teyssier 2002; Quilis 2004) or in Lagrangian methods with discrete particles (smoothed particle hydrodynamics, or SPH; e.g. Springel 2005), or a combination thereof (e.g. Springel 2010). For physical processes that are expected to occur below the resolution limit of the simulation, (semi-)analytical prescriptions are generally employed.

The simulations used in this thesis are based on the EAGLE project (Schaye et al. 2015; Crain et al. 2015), which is a suite of cosmological, hydrodynamical simulations of galaxy formation and evolution. These simulations sample the spatial distribution of gas and dark matter via SPH, with a fiducial particle mass of $m_{\text{gas}} = 1.8 \times 10^6 M_{\odot}$ and

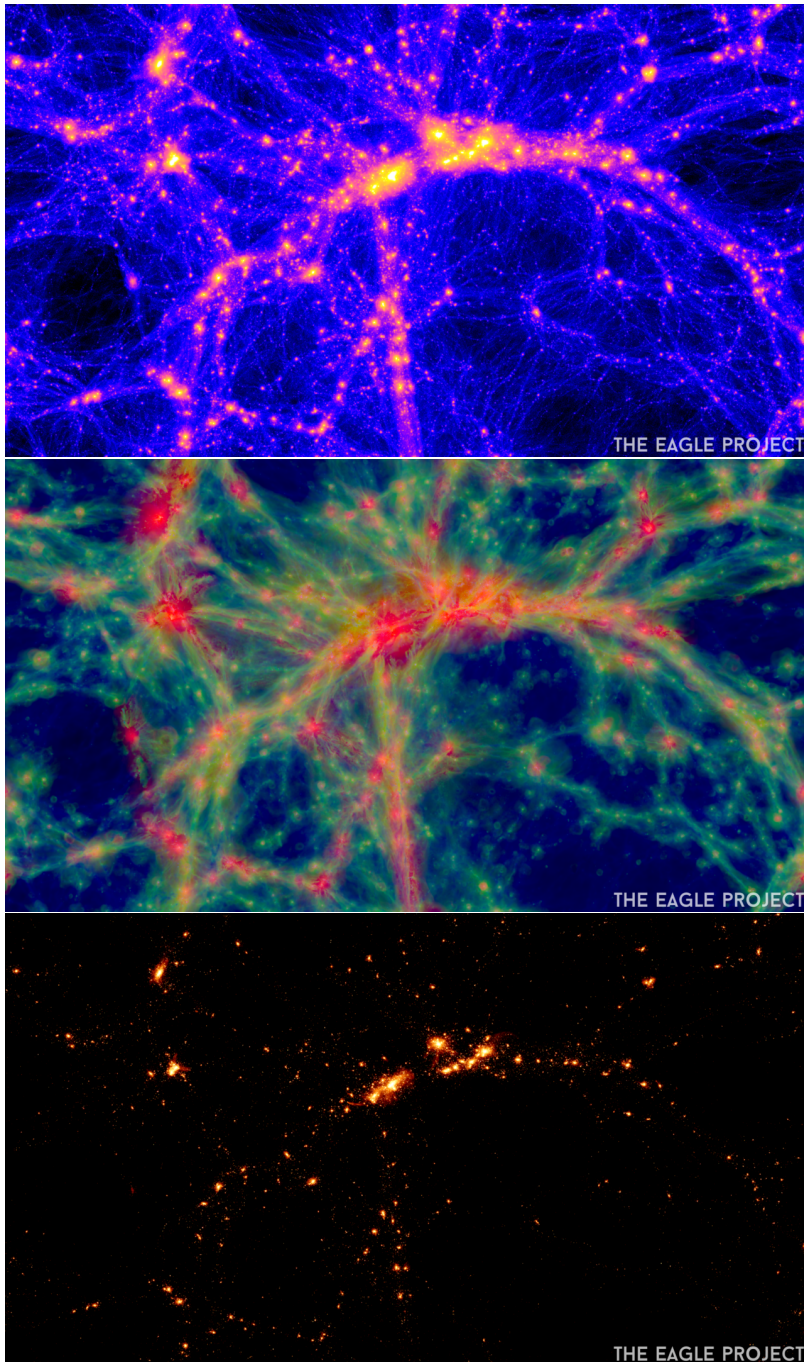


Figure 1.4: The EAGLE simulation. Each panel shows a 20 Mpc-thick slice through the reference (100 Mpc)³ volume EAGLE simulation at $z = 0$ for a different matter component. The width of each panel is 100 Mpc. The upper panel shows the dark matter distribution, where lighter colours encode denser regions. The middle panel shows the gas distribution, where the intensity shows the density of the gas while colour denotes the temperature: $T < 10^{4.5}$ K in blue, $10^{4.5} < T < 10^{5.5}$ K in green, and $T > 10^{5.5}$ K in red. The lower panel shows the stellar density distribution. Image credit: The EAGLE project, <http://icc.dur.ac.uk/Eagle/downloads.php>

$m_{\text{DM}} = 9.7 \times 10^6 M_{\odot}$, respectively. The simulations begin soon after the Big Bang, at $z = 127$, with an initially nearly-uniform density distribution, but with small density fluctuations consistent with observations of the cosmic microwave background (Planck Collaboration 2014). Both gas and dark matter particles then evolve under their own self-gravity, with the gas additionally constrained by hydrodynamical equations, until the present day ($z = 0$). The simulations contain sub-grid prescriptions for gas cooling, conversion of gas particles into star particles (each of which represents an entire simple stellar population), the enrichment of the interstellar medium with mass, metals, and energy due to stellar feedback, and the seeding and growth of supermassive BHs via gas accretion and mergers with other BHs. Gas accretion onto supermassive BHs leads to AGN feedback, which is able to quench star formation in high-mass galaxies. Due to uncertainties in how strongly the stellar feedback energy should couple with the gas, the strength of stellar feedback was calibrated such that the simulations match the galaxy stellar mass function and that galaxies have reasonable sizes.

With 13,300 well-resolved galaxies (with stellar mass $M_{\star} > 10^9 M_{\odot}$) in the largest simulation volume (a cube of 100 Mpc per side), EAGLE is well suited to test our current understanding of galaxy formation physics in a statistical sense over a large population of galaxies. A slice through this simulation is shown in Fig. 1.4, where we show the large-scale structure of the cosmic web composed of dark matter and gas, traced by the stars of galaxies like beads on a string.

1.5 This thesis

In this thesis, we use cosmological, hydrodynamical simulations to investigate the origin and consequences of “monsters” in the centres of galaxies in the context of current galaxy formation models. Chapter 2 investigates the origin of BH monster galaxies in EAGLE, while in Chapters 3, 4, and 5 we study the consequences of modifying the EAGLE model to include variations in the IMF that have been calibrated to match observations. Here follows a brief overview of the results of each chapter.

In **Chapter 2** we use the $(100 \text{ Mpc})^3$ volume reference EAGLE simulation to test if BH monster galaxies are predicted to exist in the model, and if so, to provide an explanation of what physically happened to these galaxies during their evolution that separates them from the rest of the galaxy population. We find that galaxies with overmassive BHs as extreme as observed outlier galaxies exist in EAGLE, and they get that way via a combination of two physical mechanisms. The first is tidal stripping, where the M_{BH}/M_{\star} ratio is increased due to the loss of stellar material. The other is a early assembly time, where galaxies that formed earlier, and are thus relics of the high- z universe, tend to have high M_{BH}/M_{\star} due to the higher normalization of the M_{BH}/M_{\star} relation at high redshift. These same mechanisms lead to these galaxies becoming more compact, in agreement with observed high- z relics and in support of a tidal stripping origin of ultracompact dwarf galaxies. This work is based on Barber et al. (2016). A summary of an extension of this work by Lieke van Son, Christopher Barber, et al. (2018, submitted to MNRAS) has been inserted into Chapter 2 as Section 4.6, where we perform a similar analysis on galaxies in the Hydrangea simulations.

These simulations are based on the EAGLE model, but model galaxy clusters and their surrounding regions, a mass regime missing from the reference EAGLE simulations. We find higher-mass BH monster galaxies in these simulations, with similar stellar and BH masses to NGC 1277 and NGC 1271.

In **Chapter 3** we present two new (50 Mpc)³ simulations based on the EAGLE model that include prescriptions for varying the IMF on a per-particle basis. By varying the IMF with the pressure of the interstellar medium (ISM) out of which individual star particles are born, we have calibrated these prescriptions such that the observed relation between the MLE and stellar velocity dispersion is roughly reproduced. These simulations are fully self-consistent, such that the stellar feedback, star formation law, and metal enrichment are modified to account for the locally-varying IMF. The first simulation, LoM-50, varies the low-mass slope of the IMF to obtain a higher fraction of dwarf stars (and thus a higher MLE) with increasing central stellar velocity dispersion, σ_e , in high-mass ETGs. The second simulation, HiM-50, instead varies the high-mass slope to increase the fraction of high-mass stars (and thus stellar remnants) in high-pressure environments, which also results in an increasing MLE with increasing σ_e . We discuss the implications of these different IMF variation prescriptions on physical as well as observational galaxy properties including stellar mass, luminosity, metal enrichment, star formation rate, and sizes.

Although the majority of IMF studies agree that the MLE becomes heavier with increasing σ_e in high-mass ETGs, there is little agreement on how it varies with other galaxy properties (Conroy & van Dokkum 2012b; Smith et al. 2012; McDermid et al. 2014; La Barbera et al. 2015). In **Chapter 4**, we investigate the trends between the MLE and various global galaxy properties that are predicted by our variable IMF models. In particular, we find trends between the MLE and galaxy age, metallicity, and [Mg/Fe] that agree qualitatively with observations. Interestingly, we find that the MLE correlates more strongly with age than with birth ISM pressure for high-mass IMF slope variations, despite birth ISM pressure being the property that actually governs the IMF. This result is due to the age dependence of the MLE at fixed IMF when the high-mass IMF slope is shallow. We also find that galaxies with overmassive BHs tend to also have heavier MLE, meaning stellar monster galaxies are also BH monster galaxies. We also show that satellite galaxies tend to scatter toward high MLE, likely due to tidal stripping removing the outskirts of galaxies first, which tend to have lower MLE.

Recent observational studies have found that the IMF may vary radially within high-mass ETGs galaxies, becoming heavier toward the central regions (Martín-Navarro et al. 2015b; La Barbera et al. 2016; van Dokkum et al. 2017; Oldham & Auger 2018a; Sarzi et al. 2018). In **Chapter 5**, we investigate the trends between the MLE and local galaxy properties predicted by our variable IMF simulations. We find that the MLE increases toward the centres of high-mass ETGs, in agreement with observations. We also find strong positive trends between the local MLE and local metallicity, in qualitative agreement with recent spatially-resolved spectroscopic observations. The local correlation between MLE and [Mg/Fe] is significantly negative and positive for LoM-50 and HiM-50, respectively, and thus serves as a useful diagnostic in discriminating between high-mass and low-mass IMF slope variation scenarios (which

is currently prohibited by the lack of such a correlation for observed ETGs). We also investigate the redshift evolution of IMF-related observables in each simulation. At $z \approx 2$, the MLE– σ_e relation had a higher and lower normalization than today in LoM-50 and HiM-50, respectively. The former trend is the result of the higher birth ISM pressures at high redshift, while the latter is due to the age dependence of the MLE for a shallow IMF slope, where younger stars have lower MLE despite having even shallower high-mass IMF slopes than at low redshift.

1.6 Outlook

One of the most important lessons that we have learned from our variable IMF studies is that an IMF that becomes either top- or bottom-heavy in high-pressure environments is insufficient to simultaneously explain the observed enhanced dwarf-to-giant ratios seen in massive ETGs as well as the top-heavy IMF inferred for actively star-forming galaxies – the progenitors of present-day ETGs. In the future, it would be interesting to explore more complex forms of IMF variations in our simulations in order to try to reconcile these observations.

For instance, in order to have the IMF become top- and bottom-heavy simultaneously, one could imagine a “butterfly” IMF, that becomes “middle-light” at high pressure, where the low-mass slope (for $m < 1 M_\odot$) steepens while the high-mass slope (for $m \gtrsim 10 M_\odot$) becomes shallower in such environments. Such an IMF prescription would increase the dwarf-to-giant ratio as well as the M/L ratio through the addition of dwarf stars *and* stellar remnants, and yield shallower high-mass slopes in star-forming galaxies at low and high redshift. Such an IMF may be able to reconcile the apparent discrepancies between IMF-sensitive observations. Indeed, some studies are already exploring similar IMF parametrizations using semi-analytic methods (Fontanot et al. 2018a).

A similar idea was explored by Weidner et al. (2013), who attempted to reconcile different types of observations with a model in which the IMF in the progenitors of present-day ETGs begins top-heavy during a short starburst which enriches the ISM with metals, followed by a prolonged top-light mode in which most of the stellar mass forms, producing high-metallicity stellar populations with enhanced dwarf-to-giant ratios. While a transition to a bottom-heavy (i.e. steeper low-mass slope) rather than a top-light (steeper high-mass slope) phase would be preferred given its expected weaker effect on metal enrichment and stellar feedback (Clauwens et al. 2016), such a scenario may be possible to implement in our simulations with an additional metallicity dependence on the IMF, where the IMF transitions to the bottom-heavy mode once the gas becomes metal-rich. A metallicity dependence could be physically motivated given that metallicity has a strong effect on the ability of gas to cool and form stars. A local metallicity dependence (Martín-Navarro et al. 2015c) was implemented in simulations of Milky Way-like galaxies by Gutcke & Springel (2017), who found a similar transition. It is, however, not clear that such a scenario would still be compatible with the shallow high-mass slopes observed in low-redshift star-forming galaxies, which have already had time to enrich their ISM with metals. Additionally, given the degeneracy between

the time-scale for switching between these IMFs and the IMF slopes (Weidner et al. 2013), calibration of such a prescription may be difficult. Regardless, such models should be tested with cosmological simulations in order to assess their validity.



The origin of compact galaxies with anomalously high black hole masses

Observations of local galaxies harbouring supermassive black holes (BHs) of anomalously high mass, M_{BH} , relative to their stellar mass, M_* , appear to be at odds with simple models of the co-evolution between galaxies and their central BHs. We study the origin of such outliers in a Λ cold dark matter context using the EAGLE cosmological, hydrodynamical simulation. We find 15 ‘ $M_{\text{BH}}(M_*)$ -outlier’ galaxies, defined as having M_{BH} more than 1.5 dex above the median $M_{\text{BH}}(M_*)$ relation in the simulation, $M_{\text{BH,med}}(M_*)$. All $M_{\text{BH}}(M_*)$ -outliers are satellite galaxies, typically with $M_* \sim 10^{10} M_\odot$ and $M_{\text{BH}} \sim 10^8 M_\odot$. They have all become outliers due to a combination of tidal stripping of their outer stellar component acting over several Gyr and early formation times leading to rapid BH growth at high redshift, with the former mechanism being most important for 67 per cent of these outliers. The same mechanisms also cause the $M_{\text{BH}}(M_*)$ -outlier satellites to be amongst the most compact galaxies in the simulation, making them ideal candidates for ultracompact dwarf galaxy progenitors. The 10 most extreme central galaxies found at $z = 0$ (with $\log_{10}(M_{\text{BH}}/M_{\text{BH,med}}(M_*)) \in [1.2, 1.5]$) grow rapidly in M_{BH} to lie well above the present-day $M_{\text{BH}} - M_*$ relation at early times ($z \gtrsim 2$), and either continue to evolve parallel to the $z = 0$ relation or remain unchanged until the present day, making them ‘relics’ of the high-redshift universe. This high- z formation mechanism may help to explain the origin of observed $M_{\text{BH}}(M_*)$ -outliers with extended dark matter haloes and undisturbed morphologies.

Christopher Barber, Joop Schaye, Richard G. Bower,
Robert A. Crain, Matthieu Schaller and Tom Theuns
MNRAS, 460, 1147 (2016).

Section 2.4.6 based on the work of
Lieke van Son, Christopher Barber, et al., *submitted to MNRAS*.

2.1 Introduction

A growing body of evidence correlating the properties of local ($z \approx 0$) galaxies with their central supermassive black holes (BHs) has been accumulating over the past two decades. Such correlations include relations between the BH mass, M_{BH} , and the host galaxy’s bulge luminosity, bulge stellar mass, and stellar velocity dispersion (e.g., Kormendy & Richstone 1995; Ferrarese & Merritt 2000; Gebhardt et al. 2000; Kormendy & Ho 2013; McConnell & Ma 2013, and references therein). These correlations are suggestive of co-evolution between the BH and its host galaxy. It is, however, unclear whether there is a direct causal link between them, as in the case of active galactic nucleus (AGN) feedback from the BH acting on the galaxy (e.g. Silk & Rees 1998; Fabian 1999; King 2003), or if they both result from a common physical mechanism such as galaxy-galaxy merging (e.g. Peng 2007; Jahnke & Macciò 2011).

However, every rule has its exceptions. Of the ~ 80 galaxies with dynamical M_{BH} estimates (McConnell & Ma 2013), several have been found to host BHs that are approximately an order of magnitude more massive than their bulge luminosities or masses would imply, given the above-mentioned relations. Such BHs have been termed ‘monsters’ (Kormendy & Ho 2013), ‘übermassive’ (Lasker et al. 2013; Ferré-Mateu et al. 2015), ‘ultramassive’ (Fabian et al. 2013), and even ‘obese’ (Agarwal et al. 2013); we refer to galaxies hosting overmassive BHs as $M_{\text{BH}}(M_*)$ -outliers. Most notable are the massive elliptical NGC 1277 (van den Bosch et al. 2012; Emsellem 2013; Fabian et al. 2013; Yıldırım et al. 2015; Scharwächter et al. 2016; Walsh et al. 2016; Graham et al. 2016), NGC 4486B (Magorrian et al. 1998; Gültekin et al. 2009; Saglia et al. 2016), and the compact galaxy M60-UCD1 (Seth et al. 2014). All of these observed $M_{\text{BH}}(M_*)$ -outlier galaxies have been found to lie well above the scatter in the $M_{\text{BH}} - \text{bulge mass } (M_{\text{bulge}})$ relation, with $M_{\text{BH}}/M_{\text{bulge}} > 5$ per cent, as opposed to the expected ratio of ~ 0.3 per cent (Kormendy & Ho 2013; McConnell & Ma 2013). Other notable, recent examples of $M_{\text{BH}}(M_*)$ -outliers are NGC 1332 (Humphrey et al. 2009; Rusli et al. 2011; Barth et al. 2016), NGC 4342 and 4291 (Bogdán et al. 2012), SAGE1C J053634.78-722658.5 (hereafter referred to as S536; van Loon & Sansom 2015), MRK 1216 (Yıldırım et al. 2015), and NGC 1271 (Walsh et al. 2015), and possibly SDSS J151741.75-004217.6 (hereafter referred to as b19; Lasker et al. 2013).

The presence of such outliers appears to challenge theories of co-evolution between galaxies and their central BHs, and a physical explanation for how they became $M_{\text{BH}}(M_*)$ -outliers is needed. Two such explanations have been put forward: (1) they formed on the local $M_{\text{BH}} - M_{\text{bulge}}$ relation, but the galaxies have since been tidally stripped of stars, leaving behind only the galactic core of stars containing a now overmassive BH (e.g. Volonteri et al. 2008; Mieske et al. 2013; Seth et al. 2014); and (2) they are relics of the early ($z \gtrsim 2$) Universe when the $M_{\text{BH}} - M_{\text{bulge}}$ relation may have had a higher normalization (e.g., Jahnke et al. 2009; Caplar et al. 2015; Ferré-Mateu et al. 2015). In this latter case the $M_{\text{BH}}(M_*)$ -outlier galaxies would have formed their stars and BH rapidly at very early times ($z \gtrsim 2$) and have remained mostly undisturbed until the present day. In this scenario they are expected to have old stellar populations ($\gtrsim 10$ Gyr old) and to be compact (effective radius less than 2 kpc).

Indeed, both mechanisms may be possible. For example, NGC 1277 has extremely regular isophotes and a flat rotation curve out to 5 times the half light radius, each implying that it is very unlikely to have been tidally stripped (van den Bosch et al. 2012). Ferré-Mateu et al. (2015) also find that NGC 1277, along with six other $M_{\text{BH}}(M_*)$ -outlier candidates, is compact given its stellar mass and has stellar populations older than 10 Gyr, confirming the likelihood of the ‘relic’ scenario. Indeed, there is some observational evidence that the $M_{\text{BH}} - M_{\text{bulge}}$ relation was higher at high- z , mainly based on the modelling of quasar luminosities and emission lines to measure M_{BH} . However, observational biases and modelling uncertainties make this result highly uncertain (e.g., Greene et al. 2010, and references therein).

On the other hand, the less-massive galaxies NGC 4486B and M60-UCD1 are much more likely to have been tidally stripped of stars, being located a mere 34 and 6.6 projected kpc from much more massive nearby galaxies, M87 and M60, respectively. A stream of globular clusters has been found extending between NGC 4342 and the massive elliptical galaxy NGC 4365, suggestive of severe tidal interactions (Blom et al. 2014). Indeed, one of the favoured theories for the formation of ultracompact dwarf (UCD) galaxies is the tidal stripping of massive progenitors, leaving behind galaxy cores that may contain supermassive BHs (e.g. Bekki et al. 2003; Pfeffer et al. 2014, 2016). Recently, Mieske et al. (2013) computed stellar masses and dynamical mass-to-light (M/L) ratios for 53 UCDs, finding that their high dynamical M/L ratios (relative to their inferred stellar M/L ratios) can be explained by hypothetical central BHs. Thus the tidal stripping of the stellar component of progenitor galaxies is another promising mechanism for creating perhaps lower mass $M_{\text{BH}}(M_*)$ -outlier galaxies.

It is also possible that the offsets in the M_{BH} estimates for some of these galaxies are due to modelling uncertainties (e.g. the assumed stellar mass-to-light (M/L) ratio, initial mass function (IMF), or spatial geometry). For example, using new kinematical maps from the Keck I Telescope combined with Jeans Anisotropic Modelling, Graham et al. (2016) recently computed $M_{\text{BH}} = (1.2 \pm 0.3) \times 10^9 M_{\odot}$ for NGC 1277, an order of magnitude lower than originally estimated by van den Bosch et al. (2012) using Schwarzschild modelling of *HST* data. Further examples include the fact that the high dynamical (M/L) ratios of UCDs can also be explained by a variable IMF rather than an overmassive BH (Mieske et al. 2013) and that the double nucleus of NGC 4486B has put to question the validity of the spherical isotropic dynamical models used to calculate its M_{BH} (Gültekin et al. 2009). If analyses of other galaxies also suffer from such uncertainties, the very existence of such $M_{\text{BH}}(M_*)$ -outlier galaxies seems unclear and thus should be compared with theoretical predictions.

A powerful method of testing scenarios for the formation of atypical galaxies is to look in cosmological simulations of galaxy formation and evolution. In recent years, such simulations have provided both the statistics and the resolution required to study populations of galaxies, within which analogues of these atypical galaxies can be sought. In this paper we use the EAGLE hydrodynamical simulations (Schaye et al. 2015; Crain et al. 2015, hereafter S15 and C15, respectively) to investigate first whether such $M_{\text{BH}}(M_*)$ -outliers are predicted to exist in a Λ cold dark matter (Λ CDM) framework, and if so, to evaluate which physical mechanism, or mechanisms, leads to

their existence.

We proceed as follows. In Section 2.2 we outline the EAGLE simulations used in this paper. Section 2.3 describes $M_{\text{BH}}(M_*)$ -outliers found in EAGLE while Section 2.4 investigates their physical origins. We relate our results to compact galaxies in Section 2.5 and conclude in Section 2.6.

2.2 The EAGLE Simulations

The EAGLE project is a suite of state-of-the-art cosmological hydrodynamical simulations with the goal of studying galaxy formation and evolution from shortly after the big bang to the present day. We refer the reader to S15 and C15 for a full description of the simulations, and here provide only a brief overview for completeness.

The EAGLE simulations were run using a modified version of the Tree-Particle-Mesh smoothed-particle hydrodynamics (SPH) code GADGET-3, last described in Springel (2005), using periodic boxes with varying sizes and resolutions. The modifications to the SPH implementation are collectively known as ‘Anarchy’ (Dalla Vecchia, in prep; see also Hopkins 2013; Schaller et al. 2015b, appendix A of S15) which alleviates issues with unphysical surface tension at contact discontinuities, includes an improved treatment of artificial viscosity, and a time-step limiter to conserve energy during sudden feedback events. In this paper we focus on the largest EAGLE simulation: the reference $(100 \text{ Mpc})^3$ model, simulated with 1504^3 particles each of dark matter and gas, with particle masses $(9.7 \text{ and } 1.8) \times 10^6 M_\odot$, respectively (referred to as Ref-L0100N1504 by S15). A Λ CDM cosmogony consistent with the *Planck* 2013 satellite data release was used ($\Omega_b = 0.04825$, $\Omega_m = 0.307$, $\Omega_\Lambda = 0.693$, $h = 0.6777$; Planck Collaboration 2014). The gravitational softening was kept fixed at 2.66 comoving kpc for $z > 2.8$ and at 0.70 proper kpc thereafter.

The subgrid parameters were calibrated to match the observed $z \approx 0$ galaxy stellar mass function (GSMF), galaxy sizes, and the normalization of the median $M_{\text{BH}} - M_*$ relation. In doing so, it has been used to make predictions that match other observables remarkably well, including the Tully Fisher relation and specific star formation rates (S15), the evolution of the GSMF and galaxy sizes (Furlong et al. 2015, 2017), H_2 and HI properties of galaxies (Lagos et al. 2015; Bahé et al. 2016), the column density distribution of intergalactic metals (S15; Rahmati et al. 2016) and of HI (Rahmati et al. 2015), galaxy rotation curves (Schaller et al. 2015a), and galaxy luminosities and colours (Trayford et al. 2015). A public data base of the properties of EAGLE galaxies is available at <http://icc.dur.ac.uk/Eagle/database.php> (McAlpine et al. 2016).

In Sections 2.2.1 and 2.2.2 we describe the subgrid physics and the method of tracking galaxies in the simulations, respectively.

2.2.1 Subgrid physics

Due to the finite resolution of the simulations, many physical processes that operate on scales smaller than can be simulated accurately (termed ‘subgrid’ physics) are modelled using (analytic) prescriptions. In EAGLE, radiative cooling and photoheating

are implemented as per the scheme described by Wiersma et al. (2009a), where the 11 elements that dominate radiative cooling are followed individually in the presence of the cosmic microwave background and a Haardt & Madau (2001) evolving, homogeneous, ionizing UV/X-ray background switched on at $z = 11.5$.

Star formation is implemented with the pressure-dependent star formation law of Schaye & Dalla Vecchia (2008) which reproduces by construction the observed Kennicutt-Schmidt relation. Gas particles are stochastically converted to star particles when their densities are above the metallicity-dependent star formation threshold of Schaye (2004) which accounts for the metallicity dependence of the density and pressure at which the ISM transitions from a warm, neutral to a cold, molecular phase. A density-dependent temperature floor corresponding to an equation of state, $P_{\text{eos}} \propto \rho_{\text{g}}^{4/3}$, with P_{eos} and ρ_{g} the gas pressure and density respectively, is also implemented to guarantee that the Jeans mass of the warm interstellar medium (ISM) is resolved (albeit marginally), thus preventing artificial fragmentation in cold, dense gas (Schaye & Dalla Vecchia 2008).

Each newly formed star particle represents a simple stellar population with a Chabrier (2003) IMF. Stellar particles lose mass over time according to the metallicity-dependent lifetimes of Portinari et al. (1997). During the life cycle of a stellar particle, elements are individually injected into the ISM to account for mass loss from core collapse supernovae, winds from AGB stars, and winds from massive stars following the scheme described by Wiersma et al. (2009b); the mass and energy lost via SNIa are also taken into account. Stellar feedback is implemented by stochastically injecting thermal energy into the gas as described by Dalla Vecchia & Schaye (2012). For each feedback event, the amount of energy injected into each gas particle is kept fixed, but the number of gas particles heated depends on the local gas metallicity and density. The former dependency accounts for the unresolved transition from cooling losses via H and He to the more efficient metal-line cooling at higher metallicity, while the latter prevents excessive artificial thermal losses in high density environments which would otherwise have resulted in the formation of overly compact galaxies (C15, S15). These dependencies were calibrated to match the $z \approx 0$ GSMF and galaxy sizes.

Perhaps most relevant for this paper is the treatment of BHs in the simulation. Once a halo that does not already harbour a BH¹ has reached a total mass greater than $10^{10} h^{-1} M_{\odot}$, it is seeded with a BH by converting the bound gas particle with the highest density into a collisionless BH particle. This particle begins with a (subgrid) BH seed mass of $10^5 h^{-1} M_{\odot}$ and grows through mergers with other BHs and accretion of low angular momentum gas, a prescription first introduced by Springel et al. (2005) and later modified by Booth & Schaye (2009) and Rosas-Guevara et al. (2015). The gas accretion rate is the minimum of the Eddington rate and the Bondi & Hoyle (1944) rate for spherically symmetric accretion, modified to account for the angular momentum of infalling gas (Rosas-Guevara et al. 2015). The BH mass growth rate is then 0.9 times the mass accretion rate, accounting for the assumed radiative efficiency of the accretion disc. BHs are merged when their separation is comparable to the gravitational softening length and their relative velocity smaller than the circular velocity at the

¹This criterion is necessary since halo mass can fluctuate due to interactions with other haloes.

smoothing length of the more massive BH. This choice of BH merging model does not affect our results since the galaxies hosting two BHs would be completely merged before the BHs merge and we use the mass of all bound BHs in a halo to define M_{BH} .

Finally, AGN feedback is performed similarly as done by Booth & Schaye (2009). At each time step AGN feedback energy is injected into a subgrid reservoir of feedback energy, which is allowed to heat stochastically the gas neighbouring the BH only after the total energy in the reservoir has reached a high enough value to heat some number of its nearest neighbours by a temperature ΔT_{AGN} , a value that affects the simulated properties of the intracluster medium but is less important for the GSMF (S15). The rate at which the reservoir is filled with energy is proportional to the accretion rate of the BH, with a proportionality constant $\epsilon_r \epsilon_f$, where $\epsilon_r = 0.1$ is the radiative efficiency of the accretion disc and $\epsilon_f = 0.15$ accounts for the fraction of the radiated energy that couples to the gas. As outlined by Booth & Schaye (2009, 2010), averaged over sufficiently long time-scales, BHs regulate their growth by generating large-scale gas outflows that balance inflows. Since this balance takes place on mass scales much larger than M_{BH} , the energy deposition by the BH required for this balance is not directly dependent on M_{BH} ; thus the BH will grow until reaching a critical mass for which the energy output required for self-regulation is reached. Because this critical mass is inversely proportional to ϵ_f for Eddington-limited accretion, this constant was calibrated such that BH masses lie on the $M_{\text{BH}} - M_*$ and $M_{\text{BH}} - \sigma$ relations at $z = 0$. This point is important, as it implies that the normalization of the $M_{\text{BH}} - M_*$ relation in EAGLE is not a prediction, but can be calibrated up or down without affecting the rest of the simulation.

2.2.2 Subhalo identification and corrections

Dark matter haloes are identified in EAGLE using a Friends-of-Friends (FoF) algorithm with linking length 0.2 times the mean interparticle spacing (Davis et al. 1985). The `SUBFIND` algorithm (Springel et al. 2001; Dolag et al. 2009) is then used to identify self-bound substructures within haloes, termed ‘subhaloes’, using all particle types (i.e., dark matter, stars, gas, and BHs), subject to the requirement that a subhalo must contain at least 20 particles in total. Within an FoF group the central subhalo is defined as the one that contains the particle with the minimum gravitational potential, the others are labelled as satellites. We define a ‘galaxy’ as a subhalo with more than one bound stellar particle. The stellar (BH) mass, M_* (M_{BH}), of a galaxy is defined as the total mass of all bound stellar (BH) particles. Note that this definition of M_* differs from the mass within a 30 kpc aperture used by S15; however, this choice only makes a significant difference for galaxies with $M_* > 10^{11} M_\odot$ in the simulation, a mass greater than any galaxies important in this work (S15). Using the mass of only the most massive bound BH for M_{BH} also does not affect our results.

Since `SUBFIND` looks for bound structures, occasionally galaxies can spuriously pop in and out of existence when supermassive BHs in the centres of massive galaxies temporarily become their own bound system, stealing a handful of stars or even the entire galaxy nucleus from the true surrounding galaxy. As mentioned in S15, such

artefacts can be prevented by merging subhaloes when one is within both 3 proper kpc and the 3D stellar half-mass radius, $R_{1/2,*}$, of the other. This procedure is crucial to this paper, as here we look specifically for objects that have unusually high M_{BH} , and thus the BH may dominate the total mass of the galaxies in which we are interested. Hence, all $M_{\text{BH}}(M_*)$ -outlier galaxies presented in this paper were followed through time (in “snipshots” with time resolution of ≈ 60 Myr) to ensure they are not spurious. Indeed, without this step, we find ≈ 30 subhaloes with $M_{\text{BH}} \sim 10^9 M_\odot$ and $M_* \sim 10^{7-8} M_\odot$, all but one of which were found to be SUBFIND artefacts.

Another important issue is that occasionally SUBFIND incorrectly assigns the BH of a satellite galaxy to its host galaxy, temporarily setting M_{BH} of the satellite to zero. To avoid such incorrect assignments, we reassigned BHs via the following procedure. For each BH, we search for subhaloes for which the BH is within both $R_{1/2,*}$ and 3 pkpc. If such subhaloes exist and the BH’s host is not one of these subhaloes, we reassign the BH to the most massive one. This procedure is vital for properly tracking satellite galaxies through the $M_{\text{BH}} - M_*$ plane over time (as in Section 2.4.2), and applies to ≈ 1500 BHs at the $z = 0$ snapshot. Note, however, that none of our $M_{\text{BH}}(M_*)$ -outlier galaxies (defined in Section 2.3) are affected by this correction at $z = 0$.

To track the evolution of individual galaxies through cosmic time, we make use of the merger trees discussed briefly by McAlpine et al. (2016). The trees were constructed using the algorithm described by Jiang et al. (2014). In short, a merger tree is constructed by first identifying each subhalo’s descendant between consecutive snapshots by tracing N_{link} of its most bound particles (with $N_{\text{link}} \in [10, 100]$, depending on the number of particles in the subhalo). Descendant-progenitor links are then transformed into a merger tree. Main progenitors are defined as those with the highest branch mass, which is the total mass of all progenitors sitting on a branch beyond some redshift. A full description of the merger trees will be presented by Qu et al. (2016).

2.3 Outliers in the $M_{\text{BH}} - M_*$ relation

Since $M_{\text{BH}}(M_*)$ -outliers are observed, we first ask whether similar outliers exist in EAGLE *at all* (and indeed whether we even expect to find them given our resolution and limited volume). Fig. 2.1 shows the relation between M_{BH} and M_* for galaxies in the Ref-L0100N1504 EAGLE simulation, separated into satellite (left-hand panel) and central (right-hand panel) galaxies. The median relation for all galaxies in the simulation is shown as a red solid line. As discussed by S15, the flattening of the simulated data at $M_* \ll 10^{10} M_\odot$ is due to the BH seed mass of $2 \times 10^5 M_\odot$. For $M_* \gtrsim 10^{10} M_\odot$ the relation steepens due to rapid BH growth, and it flattens slightly above $10^{11} M_\odot$.

The observational trend between M_{BH} and M_{bulge} from McConnell & Ma (2013) for elliptical galaxies is shown as a cyan solid line. Note that for $M_* > 10^{11} M_\odot$ most galaxies are elliptical, so here the bulge mass closely approximates M_* . In this regime, the simulations agree well with the observations considering the ~ 0.35 dex intrinsic scatter in the observed trend, shown as a cyan band in Fig. 2.1.

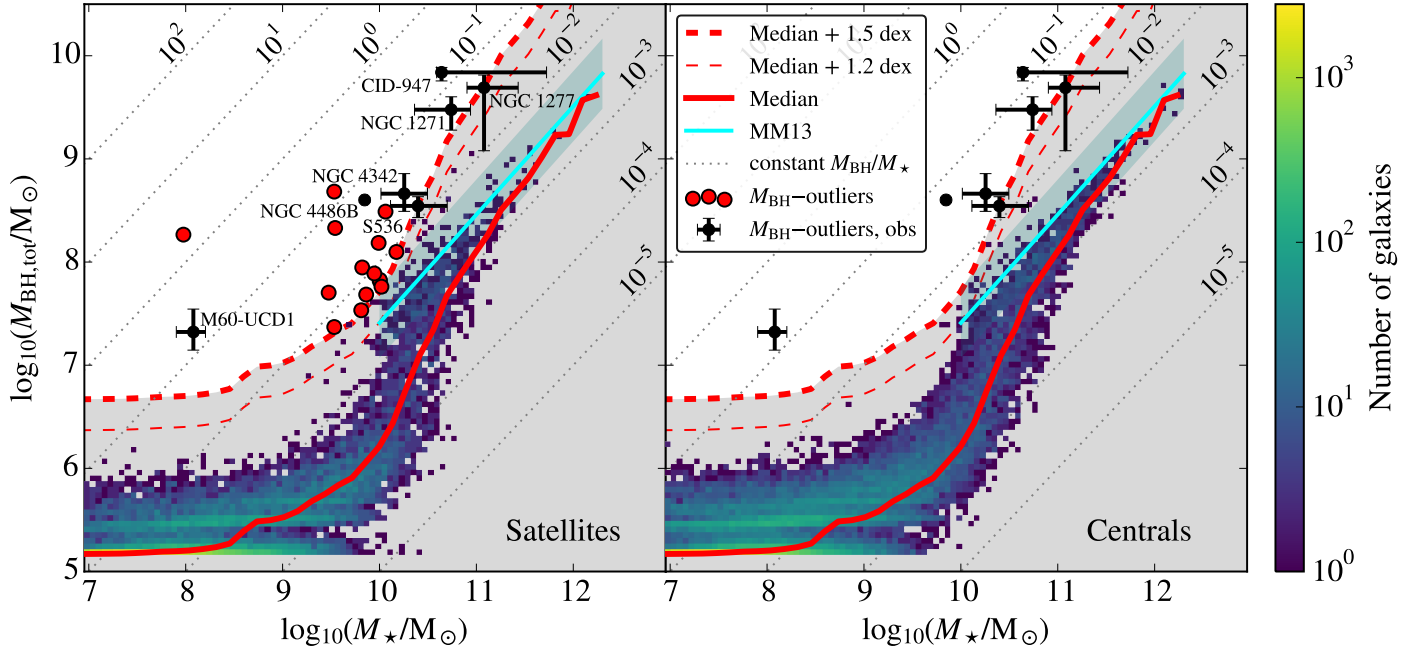


Figure 2.1: Two-dimensional histogram of BH mass, M_{BH} , as a function of stellar mass, M_* , in Ref-L0100N1504 for satellite (left) and central (right) galaxies at $z = 0$. The median M_{BH} in bins of M_* for all galaxies is drawn as a red solid line in both panels. For reference, the median is redrawn 1.5 and 1.2 dex (see Section 2.4.4) higher in dashed red thick and thin lines, respectively. Lines of constant M_{BH}/M_* are shown as thin grey dotted lines, with corresponding M_{BH}/M_* ratios labelled. We define the 15 galaxies that are at least 1.5 dex above the median to be ‘ $M_{\text{BH}}(M_*)$ -outlier’ galaxies (solid red circles), all of which are satellites, most with $M_* \sim 10^{10} M_\odot$ and $M_{\text{BH}} \sim 10^8 M_\odot$. The observational $M_{\text{BH}} - M_{\text{bulge}}$ relation of McConnell & Ma (2013) is shown as a cyan line with the intrinsic scatter indicated with a cyan band. Various observed $M_{\text{BH}}(M_*)$ -outlier galaxies are indicated in black (N.B. for some observed galaxies only M_{bulge} data are available; see text for details and references).

Table 2.1: Properties of $z = 0$ $M_{\text{BH}}(M_*)$ -outlier galaxies discovered in EAGLE, all of which are satellites. From left-to-right the columns show: OutlierID used in this paper, GalaxyID in the public EAGLE data base, M_* , M_{BH} , initial stellar mass, peak initial stellar mass, latest redshift at which the galaxy would not be considered a $M_{\text{BH}}(M_*)$ -outlier, earliest redshift at which $M_*(z) > 0.5M_{*,i,\text{peak}}$, the stellar mass of its host galaxy, the virial mass of its host galaxy, and its separation from the host.

OutlierID	GalaxyID	M_* [$10^9 M_\odot$]	M_{BH} [$10^7 M_\odot$]	$M_{*,i}$ [$10^9 M_\odot$]	$M_{*,i,\text{peak}}$ [$10^9 M_\odot$]	z_{outlier}	$z_{\text{assemble},*}$	$M_{*,\text{host}}$ [$10^9 M_\odot$]	$M_{200,\text{host}}$ [$10^{12} M_\odot$]	D_{host} [kpc]
1	989925	8.85	7.75	16.13	29.12	0.3	2.0	167.89	16.1	125
2	2506301	6.48	3.41	11.63	23.61	0.1	2.0	33.96	3.2	22
3	5307530	10.05	6.56	18.36	22.23	0.9	3.0	703.05	93.9	187
4	5356576	7.29	4.84	13.38	20.25	0.9	5.0	697.19	85.6	187
5	5374884	9.80	15.34	18.06	46.24	0.1	2.5	665.39	72.7	24
6	6043240	14.94	12.53	27.44	67.81	0.3	2.2	639.12	65.5	238
7	6656922	10.09	6.72	18.25	20.50	1.3	4.0	414.12	43.6	176
8	6659446	11.54	30.82	20.81	242.76	0.1	0.4	414.12	43.6	34
9	7694028	10.48	5.77	19.15	52.76	0.1	1.5	185.33	17.5	17
10	22092348	0.09	18.44	0.17	54.88	0.6	3.5	641.28	72.3	43
11	52605772	6.64	8.86	12.02	127.74	0.1	0.6	268.16	21.0	26
12	55576881	3.41	2.35	6.23	20.03	0.1	1.5	136.74	9.2	31
13	58905530	2.99	5.05	5.48	34.31	0.3	2.2	16.42	1.6	38
14	63905307	3.49	21.39	6.40	68.46	0.1	3.5	639.12	65.5	15
15	63927059	3.41	48.19	6.25	266.94	0.1	1.3	480.14	53.4	16

We define $M_{\text{BH}}(M_*)$ -outliers as those with M_{BH} at least 1.5 dex above the median $M_{\text{BH}}(M_*)$ relation in the simulation [i.e. $\log_{10}(M_{\text{BH}}/M_{\text{BH,med}}(M_*)) > 1.5$; thick red dashed line in Fig. 2.1]. This criterion was chosen in order to exclude any outliers in the scatter of the low- M_* (BH seed mass resolution-dominated) regime, and to select only the most extreme outliers in the simulation². This very simple (and mostly arbitrary) cut leaves us with 15 $M_{\text{BH}}(M_*)$ -outliers, all of which are satellite galaxies (solid red circles). They have values of $M_{\text{BH}} = 10^{7-9} M_{\odot}$ and $M_* \sim 10^{10} M_{\odot}$, with one interesting case of $M_{\text{BH}} \simeq 2 \times 10^8 M_{\odot}$ and $M_* \simeq 10^8 M_{\odot}$ which we hereafter refer to as our ‘most extreme’ $M_{\text{BH}}(M_*)$ -outlier (OutlierID = 10 in Table 2.1). Note that a slightly lower choice of $M_{\text{BH}}/M_{\text{BH,med}}(M_*)$ threshold would add central galaxies to our $M_{\text{BH}}(M_*)$ -outlier sample; such galaxies are discussed in Section 2.4.4. We reiterate here that the absolute value of M_{BH} is not a prediction of EAGLE – the AGN feedback efficiency was calibrated such that the normalization of the $M_{\text{BH}} - M_*$ relation would broadly match observations. This is why we define $M_{\text{BH}}(M_*)$ -outliers with respect to the simulation only, not to the observations.

M_{BH} and M_* estimates for various observed galaxies with overmassive BHs are also shown for reference. Values were taken from Seth et al. (2014); Saglia et al. (2016); McConnell & Ma (2013); van Loon & Sansom (2015); Trakhtenbrot et al. (2015); Walsh et al. (2015, 2016) for M60-UCD1, NGC 4486B, NGC 4342, S536, CID-947, NGC 1271, and NGC 1277, respectively. Note that for NGC 4486B, 4342, 1271, and CID-947, we plot M_{bulge} since total M_* is not available, thus M_* may be underestimated for these galaxies. For CID-947 (observed at $z \approx 3.3$), we plot the expected $z = 0$ M_* as estimated by Trakhtenbrot et al. (2015) as its upper M_* limit. For NGC 1277, we use recent values from Walsh et al. (2016), but extend the error bars to encompass the new results from Graham et al. (2016). Overall we see that outliers similar in M_{BH} and M_* to S536, NGC 4486B, and 4342 exist in EAGLE, but we find none similar to those with the largest BH masses: NGC 1277, NGC 1271 or CID-947. Interestingly, our most extreme $M_{\text{BH}}(M_*)$ -outlier has similar M_* to M60-UCD1, but with an order of magnitude larger M_{BH} .

Given our box size and resolution, it is not surprising that most of our $M_{\text{BH}}(M_*)$ -outliers have $M_* \sim 10^{10} M_{\odot}$ and $M_{\text{BH}} \sim 10^8 M_{\odot}$. To be an outlier, i.e. to be above the thick red dashed line in Fig. 2.1, the deficit of M_* at fixed M_{BH} increases sharply for $M_* < 10^{10} M_{\odot}$ due to the BH seed mass. Thus, in terms of M_* deficit, we cannot reliably predict the number of $M_{\text{BH}}(M_*)$ -outliers for these lower masses. However, in terms of M_{BH} excess, the lack of $M_{\text{BH}}(M_*)$ -outliers at $M_* < 10^{9.5} M_{\odot}$ is significant, since it implies that BHs simply do not grow quickly in such low-mass galaxies without stellar mass increasing even faster.

At the high-mass end, the number of outliers is affected by the limited box size of the simulation. For $M_{\text{BH}} \in [10^{7.5}, 10^{8.5}] M_{\odot}$, we find 13 $M_{\text{BH}}(M_*)$ -outliers out of 389 satellite galaxies. Assuming that the fraction of outliers is the same for all M_{BH} (~ 3 per cent), for $M_{\text{BH}} \in [10^{8.5}, 10^{9.5}] M_{\odot}$ we only expect to find one $M_{\text{BH}}(M_*)$ -outlier

²The scatter around the median $M_{\text{BH}}(M_*)$ relation in the simulation peaks at $M_* \sim 10^{10} M_{\odot}$, with 68- and 95-percentiles 0.3 and 0.95 dex above the median, respectively. We thus consider our $M_{\text{BH}}(M_*)$ -outlier definition to be conservative.

since we have only 33 satellite galaxies in our box with M_{BH} in this mass range (and indeed, we do find one). Additionally, in our limited volume we have only a handful of objects with M_{BH} as high as those found in NGC 1271, CID-947, and NGC 1277, so we cannot accurately determine the expected frequency of such objects with this simulation. Indeed, Saulder et al. (2015) found that the frequency of massive, compact, high velocity-dispersion analogues of high- z galaxies (e.g. NGC 1277 and b19) in the local Universe is $\sim 10^{-7}$ galaxies Mpc^{-3} which corresponds to 0.1 galaxies given our simulation volume. Thus, a larger simulation volume would be required to predict the frequency of such galaxies.

Additionally, with higher resolution we may expect to find more $M_{\text{BH}}(M_*)$ -outliers with $M_* \lesssim 10^{10} M_\odot$ because satellites that lose stellar mass due to tidal stripping by a more massive host are eventually lost by our subhalo finder, perhaps earlier than they would be at a higher resolution. The only EAGLE simulation that has a higher resolution has a particle mass that is 8 times lower than for Ref-L0100N1504 but has a volume of only $(25 \text{ Mpc})^3$ (the L0025N0752 simulation in S15) and has only one $M_{\text{BH}}(M_*)$ -outlier under the above definition, while the $(25 \text{ Mpc})^3$ simulation with the same resolution as Ref-L0100N1504 (L0025N0376 in S15) has none. Thus, a robust resolution test is unfortunately not possible. However, once all of the stars have been stripped from a galaxy in the simulation, its BH may still exist as a lone particle, unassociated with any subhalo, prior to merging with the host's BH. We have checked for any such lone BHs and found none. Alternatively, one may expect such BHs to belong to the more massive host prior to merging with its BH. We have searched for BHs with $M_{\text{BH}} > 10^7 M_\odot$ at $z = 0$ that are *not* the most massive BH in their assigned subhalo, finding 99 such BHs with M_{BH} up to $2 \times 10^9 M_\odot$. However, due to the rather ad hoc method of merging BHs in the simulation, it is unclear whether these BHs should be expected to have merged earlier or not.

Each of the $M_{\text{BH}}(M_*)$ -outlier galaxies was inspected visually in multiple consecutive snipshots to ensure that they are indeed real galaxies and not spurious `SUBFIND` artefacts missed by the subhalo merging procedure outlined in Section 2.2.2. Their properties from `SUBFIND` and those derived in this work can be found in Table 2.1. In the next section we describe how these satellite galaxies came to be such strong outliers relative to the $M_{\text{BH}} - M_*$ relation.

2.4 The origin of outliers from the $M_{\text{BH}} - M_*$ relation

How did these galaxies become such strong $M_{\text{BH}}(M_*)$ -outliers? Did they simply form a supermassive BH without forming many stars, or are they the tidally stripped remnants of more massive progenitor galaxies? We discuss their environments at $z = 0$ in Section 2.4.1, their evolution through time in Section 2.4.2, and identify their common origins in Sections 2.4.3 and 2.4.4.

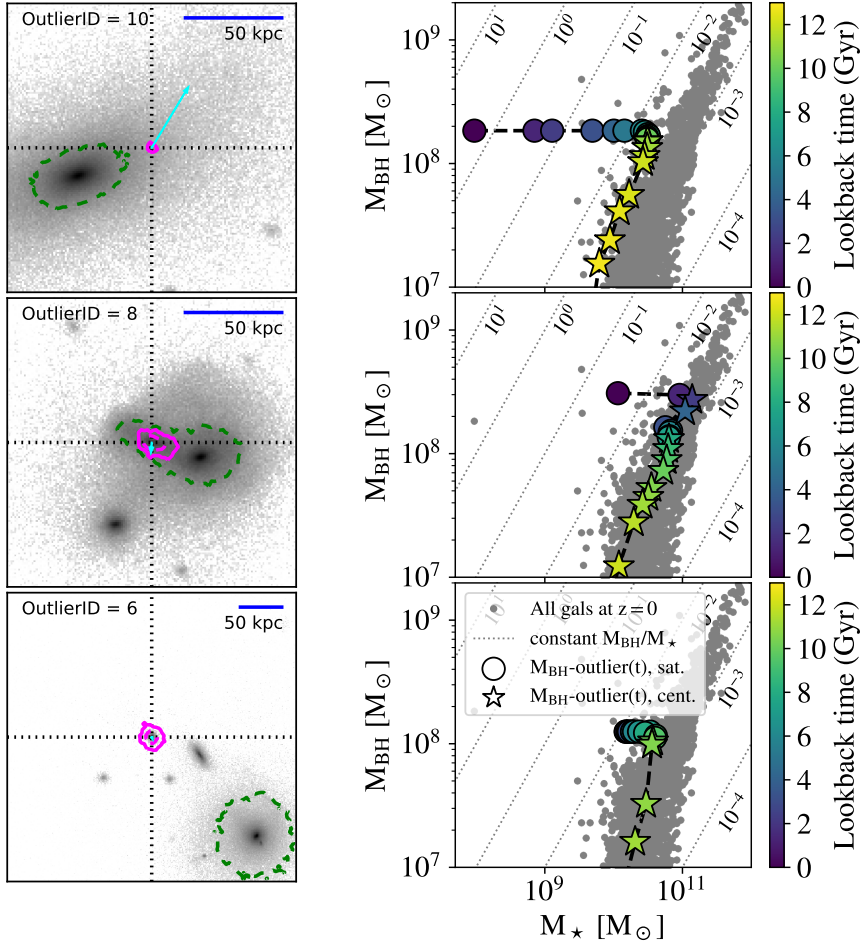


Figure 2.2: Environment and evolution of three example $M_{\text{BH}}(M_*)$ -outlier galaxies (from top-to-bottom: OutlierID 10, 8, and 6 from Table 2.1). *Left panels:* positions of outliers relative to the nearby stellar particle distribution at $z = 0$, centred on their central BHs. The underlying stellar particle distribution is shown as a logarithmic grey-scale surface mass density plot projected ± 75 kpc along the z -direction (± 175 kpc for the bottom panel). In each panel the $M_{\text{BH}}(M_*)$ -outlier galaxy and its host are outlined in magenta and green contours, respectively, with solid and dashed contours enclosing bins of at least 1 and 100 star particles per pixel, respectively (solid green contours are omitted for clarity). Cyan vectors show the instantaneous velocity in the plotted plane, in units of $\text{kpc}(50 \text{ Myr})^{-1}$. *Right panels:* the evolution of the main progenitors of these three galaxies in the $M_{\text{BH}} - M_*$ plane. Symbols are colour-coded by lookback time, t_{LB} , ranging from 12 to 0 Gyr from light yellow to dark blue. Stars and circles show when each $M_{\text{BH}}(M_*)$ -outlier was a central or satellite, respectively. The underlying distribution for all galaxies at $z = 0$ is shown in grey for reference. *Top row:* the $M_{\text{BH}}(M_*)$ -outlier with lowest stellar mass, stripped slowly but substantially over the past ~ 8 Gyr. *Middle row:* an outlier that has lost ≈ 90 per cent of its stellar mass within the past 1 Gyr. *Bottom row:* an outlier that looks seemingly undisturbed at $z = 0$, but was stripped of stars at $t_{\text{LB}} \sim 6 - 8$ Gyr.

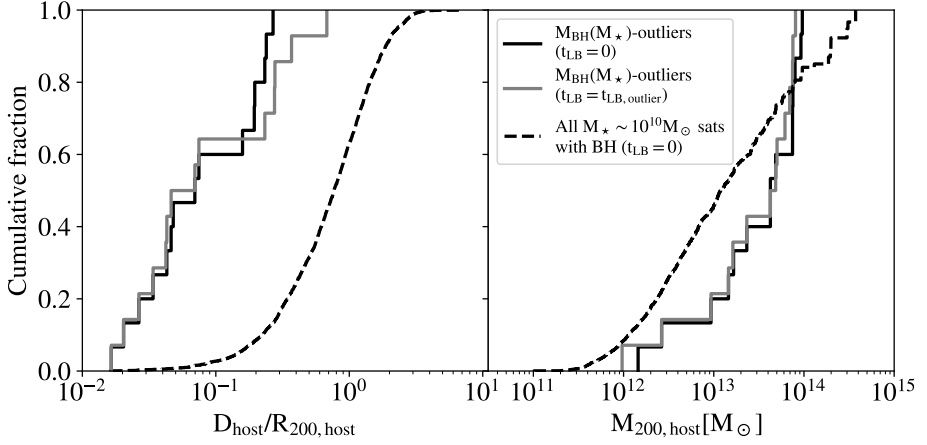


Figure 2.3: Cumulative distribution functions of the separation between satellite galaxies and their host galaxies normalized to R_{200} of the host (*left panel*) and of M_{200} of each satellite’s host galaxy (*right panel*). Distributions are shown for $M_{\text{BH}}(M_*)$ -outlier galaxies at $t_{\text{LB}} = 0$ (solid black lines) and when they became outliers in the instantaneous $M_{\text{BH}} - M_*$ relation ($t_{\text{LB, outlier}}$; solid grey lines). Distributions at $t_{\text{LB}} = 0$ for all satellites with BHs and $\log_{10}(M_*/M_{\odot}) \in [9.5, 10.5]$ are shown as dashed lines. From the time at which they became $M_{\text{BH}}(M_*)$ -outliers to $z = 0$, $M_{\text{BH}}(M_*)$ -outlier galaxies reside significantly closer to their host galaxies (all are within $0.5R_{200}$) than do typical satellite galaxies of similar stellar mass.

2.4.1 Environment at $z = 0$

The left column of Fig. 2.2 shows the distribution of stars around three example $M_{\text{BH}}(M_*)$ -outlier galaxies that represent the range of environments in which our sample of 15 $M_{\text{BH}}(M_*)$ -outliers reside at $z = 0$ (from top-to-bottom, OutlierIDs 10, 8, and 6 in Table 2.1). The top-left panel shows our most extreme (and lowest M_*) $M_{\text{BH}}(M_*)$ -outlier with $M_{\text{BH}} \simeq 2 \times 10^8 M_{\odot}$ and $M_* \simeq 10^8 M_{\odot}$, comprised of 85 stellar particles and one BH particle. This satellite is a mere 43 kpc from its much more massive ($M_* \simeq 6 \times 10^{11} M_{\odot}$) host galaxy, but from the image there does not appear to be any sign of ongoing stellar stripping.³ On the other hand, the middle-left panel shows another $M_{\text{BH}}(M_*)$ -outlier that is clearly undergoing extensive stellar stripping due to tidal interactions. Finally, the $M_{\text{BH}}(M_*)$ -outlier in the bottom-left panel is currently quite far (240 kpc) from its host and does not show any clear sign of ongoing tidal disturbances. Thus, these $M_{\text{BH}}(M_*)$ -outliers can be found in many different dynamical states at $z = 0$ (even though they are all indeed satellites).

In order to quantify their environments further, it is useful to determine the host of a given satellite galaxy. To this end, it is insufficient to simply select the central galaxy in its FoF group as the host. This is because in many cases a satellite may join the FoF group as a subhalo of a more massive satellite, and thus its dynamical history may be more closely linked to the more massive satellite than to the FoF central. To account

³We have confirmed that there is indeed a stellar overdensity here – the stellar mass density within 2 kpc is 10 times that between 2 and 10 kpc of this $M_{\text{BH}}(M_*)$ -outlier.

for this situation, we compute for each satellite the tidal radius due to all of the more massive subhaloes in its FoF group using equation 7-84 of Binney & Tremaine (1987) – whichever subhalo yields the minimum tidal radius is then defined as the ‘host’ galaxy. While this calculation is approximate (it assumes the haloes are point masses and the satellites are on circular orbits), it is sufficient to identify the true tidal perturber of a subhalo even though the computed tidal radius may be inaccurate.

In Fig. 2.3 we show the distance of all 15 $M_{\text{BH}}(M_*)$ -outliers to their respective host galaxies relative to the host virial radius ($D_{\text{host}}/R_{200,\text{host}}$), along with the host virial mass, $M_{200,\text{host}}$, at $z = 0$ (black solid lines).⁴ Relative to the other satellites in the simulation that host BHs and have similar stellar mass ($\log_{10}(M_*/M_\odot) \in [9.5, 10.5]$; black dashed lines in Fig. 2.3), the $M_{\text{BH}}(M_*)$ -outliers tend to be closer to their hosts (all within $0.5R_{200,\text{host}}$; Kolmogorov-Smirnov (KS) test p -value, p_{KS} , much less than 1 per cent between these two distributions) and to have hosts slightly (but not significantly; $p_{\text{KS}} \approx 10$ per cent) more massive than average, indicating that $M_{\text{BH}}(M_*)$ -outliers are typically subject to much stronger tidal forces than the majority of similar satellite galaxies.

2.4.2 Evolution

The right column of Fig. 2.2 shows the evolutionary tracks of these three example $M_{\text{BH}}(M_*)$ -outliers in the $M_{\text{BH}} - M_*$ plane obtained using the merger trees, with time running from light-yellow to dark-blue as indicated by the colour bar. For reference, the distribution for all galaxies at $z = 0$ is shown underneath in grey (note that in the simulation this relation evolves towards higher M_* from high redshift down to a lookback time $t_{\text{LB}} \sim 9$ Gyr ($z \sim 1.5$), after which it remains constant in time; see Section 2.4.4). The subhalo is represented by a star or circle when it is a central or satellite, respectively.

Our most extreme $M_{\text{BH}}(M_*)$ -outlier (top-right panel of Fig. 2.2; OutlierID = 10) was indeed a much more massive galaxy in the past. Its stellar mass peaked at $3 \times 10^{10} M_\odot$ at $z = 2$ ($t_{\text{LB}} \simeq 10$ Gyr) before it became a satellite and gradually lost stellar mass until $z = 0$. Indeed, since its M_* at $z = 0$ is very close to the resolution limit of the simulation, it is likely to be completely disrupted and lost within a Gyr after $z = 0$. In the middle-right panel, we see that the $M_{\text{BH}}(M_*)$ -outlier with obvious ongoing stellar stripping (OutlierID = 8) only became a satellite at $t_{\text{LB}} \approx 1$ Gyr before quickly becoming an outlier at $z \approx 0$ while it rapidly merges with its host galaxy (likely to be completely disrupted within the next several 100 Myr). Finally, the bottom-right panel shows that even the $M_{\text{BH}}(M_*)$ -outlier satellite that looks relatively undisturbed at $z = 0$ (OutlierID = 6) actually has lost most (≈ 60 per cent) of its stellar mass over the past 8 Gyr, but only after it became a satellite. For all three cases we have verified that this mass loss is due to the loss of stellar particles rather than stellar evolution. This

⁴We define the virial radius, R_{200} , as the radius within which the enclosed average density is 200 times the critical density of the universe at a given time; M_{200} is the mass within R_{200} . Note that for subhaloes that are not the central of their FoF group, we approximate M_{200} via the mean relation between M_{200} and total (SUBFIND) mass relation for centrals in the simulation.

evidence supports the idea that tidal stripping of more massive progenitor satellites may be the main cause of galaxies with overmassive BHs.

In Fig. 2.3 we show the distance of all 15 $M_{\text{BH}}(M_*)$ -outliers from their host galaxy relative to the virial radius of the host, as well as the host virial mass, measured at the time that each $M_{\text{BH}}(M_*)$ -outlier became an outlier (i.e., when its M_{BH} last rose higher than 1.5 dex above the (evolving) median $M_{\text{BH}}(M_*, z)$ relation; hereafter referred to as $t_{\text{LB, outlier}}$; grey solid line). The distribution of separation from the host looks very similar to the $z = 0$ case, albeit slightly more extended given some $M_{\text{BH}}(M_*)$ -outliers may have only recently accreted on to the host at that time. However, all are within R_{200} of the host, suggesting that tidal forces are likely to be responsible for the decrease in stellar mass since $t_{\text{LB, outlier}}$. The M_{200} distribution does not change significantly from $t_{\text{LB, outlier}}$ to $z = 0$.

Note that there is one fewer $M_{\text{BH}}(M_*)$ -outlier at $t_{\text{LB, outlier}}$ than at $z = 0$ in Fig. 2.3. This missing galaxy had $\log_{10}(M_{\text{BH}}/M_{\text{BH, med}}(M_*)) > 1.5$ before it became a satellite, having gained in M_{BH} and lost M_* through stellar evolution at early times ($z = 1 - 2$) and, as we shall see in the next section, has also not been stripped significantly of stars. With $M_* = 10^{10} M_{\odot}$ and $M_{\text{BH}} \sim 6 \times 10^7 M_{\odot}$, it is just at the edge of the general scatter in the $M_{\text{BH}} - M_*$ relation and thus may represent the high-mass tail end of ‘normal’ M_{BH} growth. Indeed, at $z = 0$ it only just satisfies our $M_{\text{BH}}(M_*)$ -outlier definition, lying ≈ 1.6 dex above the median.

2.4.3 Tidal stripping as the primary cause of anomalously high $M_{\text{BH}}(M_*)$

If tidal stripping is responsible for creating $M_{\text{BH}}(M_*)$ -outliers, then we can expect most of them to have become outliers recently, as those that begin to strip at earlier times are more likely to have been completely tidally disrupted by $z = 0$. Fig. 2.4 shows the stellar mass loss (defined at the stellar mass at $z = 0$ divided by the maximum stellar mass that it ever had, $M_{*, i}/M_{*, i, \text{peak}}$) as a function of the time since the $M_{\text{BH}}(M_*)$ -outliers were last not outliers (i.e. the snapshot before $t_{\text{LB, outlier}}$; see Section 2.4.2). Note that here we use the sum of the *initial* stellar mass of each star particle, $M_{*, i}$, to ensure that the analysis is insensitive to any mass loss due to stellar evolution.

Most of the EAGLE $M_{\text{BH}}(M_*)$ -outliers became outliers in the past few Gyr and have been severely stripped by $z = 0$, most having lost over 50 per cent of their maximum stellar mass. We do, however, find three galaxies that have been $M_{\text{BH}}(M_*)$ -outliers for the past 7 to 9 Gyr, and have lost relatively little stellar mass. One of them was a $M_{\text{BH}}(M_*)$ -outlier before becoming a satellite (as discussed in Section 2.4.2), while the other two were already > 1.3 dex above the median before becoming satellites, with a small amount of subsequent stellar mass loss pushing them just over the 1.5 dex cut soon thereafter. Indeed, the value of $t_{\text{LB, outlier}}$ for these three galaxies is very sensitive to the definition of $M_{\text{BH}}(M_*)$ -outliers as they are all only just above the 1.5 dex cut for most of their duration as satellites, rising only to ~ 1.6 dex at $z \sim 0$.

Near the bottom of Fig. 2.4 another $M_{\text{BH}}(M_*)$ -outlier has lost nearly all of its $M_{*, i}$ by $z = 0$ – this is the most extreme $M_{\text{BH}}(M_*)$ -outlier shown in the top row of Fig. 2.2

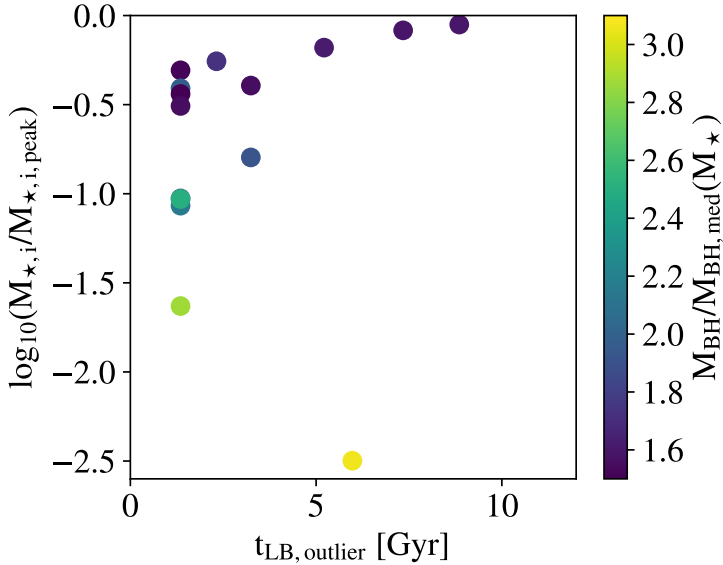


Figure 2.4: Ratio of stellar mass over maximum stellar mass that a galaxy ever had as a function of elapsed time since it first became an outlier in the $M_{\text{BH}} - M_*$ relation, for all 15 $M_{\text{BH}}(M_*)$ -outlier galaxies in EAGLE (see Table 2.1). Points are coloured by $M_{\text{BH}}/M_{\text{BH,med}}(M_*)$ at $z = 0$. To remove the effect of mass loss due to stellar evolution, we use the sum of the *initial* masses of each galaxy’s stellar particles, $M_{*,i}$. The most extreme $M_{\text{BH}}(M_*)$ -outliers have been severely stripped, and became outliers within the past few Gyr.

(OutlierID = 10 in Table 2.1). In Fig. 2.4 we see it has indeed lost 99.7 per cent of its peak (initial) stellar mass since it became a $M_{\text{BH}}(M_*)$ -outlier 6 Gyr ago.

Another expectation of the tidal stripping hypothesis is that we should find a correlation between $M_{\text{BH}}/M_{\text{BH,med}}(M_*)$ and stellar stripping. This test is especially important since it is insensitive to the $M_{\text{BH}}(M_*)$ -outlier cut of $\log_{10}(M_{\text{BH}}/M_{\text{BH,med}}(M_*)) > 1.5$. In Fig. 2.5 we plot this relation for all galaxies with $M_{\text{BH}} > 10^7 M_{\odot}$, thus avoiding galaxies strongly affected by the finite BH seed mass (see Fig. 2.1).

The left-hand panel of Fig. 2.5 shows $M_{\text{BH}}/M_{\text{BH,med}}(M_*)$ as a function of the ratio between the maximum circular velocity, V_{max} , at $z = 0$ and the highest value that it ever had, $V_{\text{max,peak}}$, found by tracking its most massive progenitor back in time through the merger trees. There is a significant trend of stronger $M_{\text{BH}}(M_*)$ -outliers with decreasing $V_{\text{max}}/V_{\text{max,peak}}$ for $\log_{10}(V_{\text{max}}/V_{\text{max,peak}}) < -0.2$ (Spearman rank-order correlation coefficient of -0.6 with p -value $\ll 1$ per cent), which is the regime where galaxies tend to begin losing stellar mass due to tidal stripping.

In the right-hand panel of Fig. 2.5 we repeat the above analysis but use the ratio of the $z = 0$ and peak initial stellar mass directly as a proxy for stellar stripping. Of the ≈ 2000 galaxies with $M_{\text{BH}} > 10^7 M_{\odot}$, 24 per cent have $\log_{10}(M_{*,i}/M_{*,i,\text{peak}}) < 0$, the vast majority of which are satellites. All of our $M_{\text{BH}}(M_*)$ -outlier galaxies have been

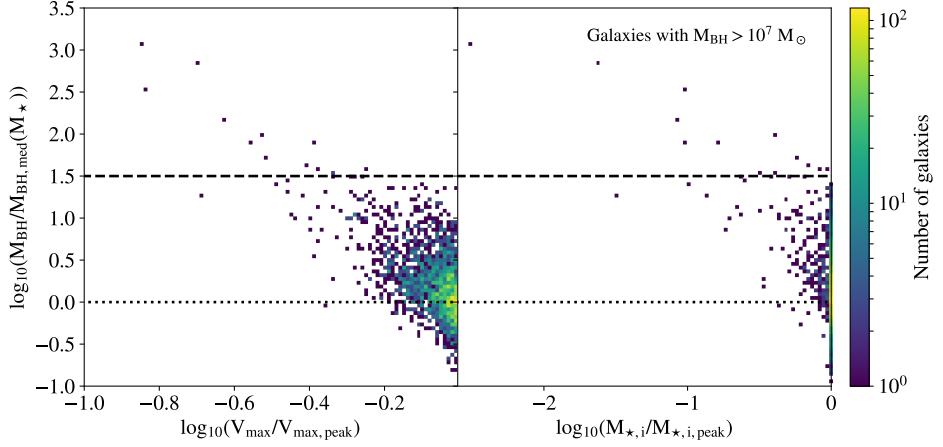


Figure 2.5: Ratio of M_{BH} over the median M_{BH} for each galaxy's M_* as a function of mass stripping proxy $V_{\text{max}}/V_{\text{max,peak}}$ (left-hand panel) and $M_{*,i}/M_{*,i,\text{peak}}$ (right-hand panel). Only galaxies with $M_{\text{BH}} > 10^7 M_{\odot}$ at $z = 0$ are shown in order to avoid BH seed mass resolution effects. Our 1.5 dex cut (definition of $M_{\text{BH}}(M_*)$ -outliers) and the median M_{BH} are shown as horizontal dashed and dotted lines, respectively. Galaxies that have significantly been stripped of stars tend to have M_{BH} above the median value for their M_* , and indeed all $M_{\text{BH}}(M_*)$ -outlier galaxies have lost some amount of stellar mass through tidal interactions.

stripped of stars, with the strongest outliers having lost the highest fraction of their maximum initial stellar mass. For galaxies with $\log_{10}(M_{*,i}/M_{*,i,\text{peak}}) < 0$, we obtain a Spearman rank-order correlation coefficient of -0.3 with $p \ll 1$ per cent, indicating a significant correlation between $M_{\text{BH}}/M_{\text{BH,med}}(M_*)$ and stellar stripping.

The scatter in $M_{\text{BH}}/M_{\text{BH,med}}(M_*)$ as a function of $V_{\text{max}}/V_{\text{max,peak}}$ is tighter than when plotted as a function of $M_{*,i}/M_{*,i,\text{peak}}$, which is surprising if stellar stripping is the direct cause of outliers in the $M_{\text{BH}} - M_*$ relation. This result is a consequence of the facts that M_{BH} correlates more strongly with $V_{\text{max,peak}}$ than with $M_{*,i,\text{peak}}$ due to the strong dependence of M_{BH} on halo binding energy (Booth & Schaye 2010), and that tidal stripping reduces M_* and V_{max} by roughly the same fraction for $\log_{10}(V_{\text{max}}/V_{\text{max,peak}}) < 0.8$ and $M_* > 10^8 M_{\odot}$.

It is worth noting as well that these $M_{\text{BH}}(M_*)$ -outlier (satellite) galaxies are also significant outliers in the relation between M_{BH} and stellar velocity dispersion, σ , in the simulation. This is further evidence that they are inconsistent with being undisturbed relics of the high- z universe, as such relic galaxies are expected to be outliers in $M_{\text{BH}}(M_*)$ but not in $M_{\text{BH}}(\sigma)$ (Ferré-Mateu et al. 2015, but see Section 2.4.4).

Galaxies can also lose stellar mass through internal processes that cause the evaporation of stellar particles, such as three-body interactions with other stars or BHs (although the SPH softening prevents this so such processes are not captured in these simulations) or scattering off of large perturbations in the potential such as spiral arms or massive gas clumps. The impact that such processes have on galaxy stellar masses are not trivial to quantify. However, since these processes are internal to galaxies,

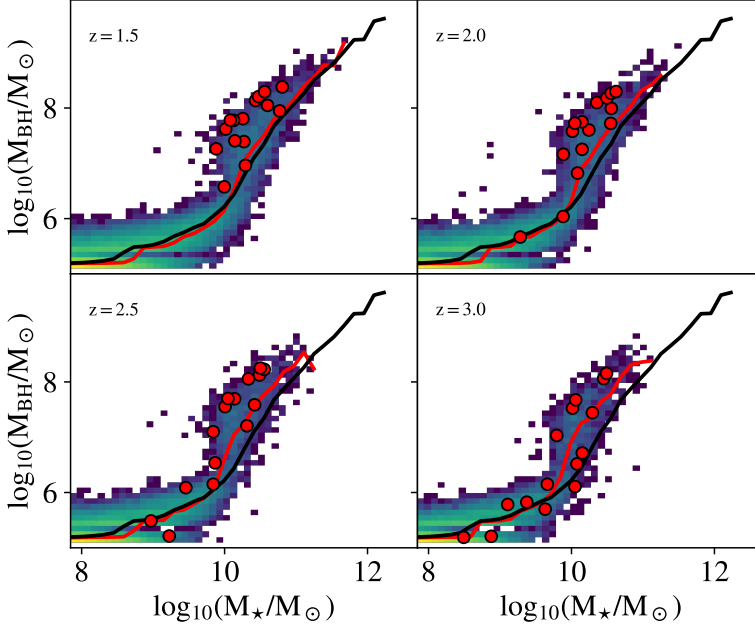


Figure 2.6: Evolution of the $M_{\text{BH}} - M_*$ relation with redshift (different panels). The main progenitors of the $z = 0$ $M_{\text{BH}}(M_*)$ -outliers are shown as red points. The median $M_{\text{BH}}(M_*)$ relation at each redshift is shown as a red curve. For reference, the median relation at $z = 0$ is repeated in each panel as a black curve. The $M_{\text{BH}} - M_*$ relation evolved substantially from $z = 3$ to $z = 1.5$, dropping by nearly an order of magnitude at $M_* \sim 10^{10} M_\odot$. Progenitors of the $z = 0$ $M_{\text{BH}}(M_*)$ -outliers were not outliers from the $M_{\text{BH}} - M_*$ relation at $z = 3$ and formed most of their stars and M_{BH} from $z = 3 - 2$ while the median $M_{\text{BH}}(M_*)$ relation was evolving, leaving them $0.5 - 1$ dex above the median relation by $z = 1.5$, before most of them had become satellites. Galaxies that form most of their stars at high redshift tend to lie above the $M_{\text{BH}} - M_*$ relation at $z = 0$ due to the evolution of the relation.

one would expect both satellites and centrals to be affected equally. Thus, although it cannot be ruled out here, stellar evaporation is not expected to affect the relative offset between galaxies in the $M_{\text{BH}} - M_*$ relation.

We thus conclude that tidal stripping is the dominant formation mechanism of galaxies with anomalously high BH masses in EAGLE.

2.4.4 Early formation time as a secondary cause of anomalously high $M_{\text{BH}}(M_*)$

While all of our $M_{\text{BH}}(M_*)$ -outliers [defined as $\log_{10}(M_{\text{BH}}/M_{\text{BH,med}}(M_*)) > 1.5$] are tidally stripped satellites, tidal stripping may not be the only mechanism causing these galaxies to have unusually high M_{BH} . The left-hand panel of Fig. 2.7 shows the $z = 0$ relation between M_{BH} and $M_{*,i,\text{peak}}$ for satellite galaxies, with the $M_{\text{BH}}(M_*)$ -outlier galaxies highlighted in red. If tidal stripping were the only important mechanism in creating $M_{\text{BH}}(M_*)$ -outliers, they would be expected to fall within the scatter in

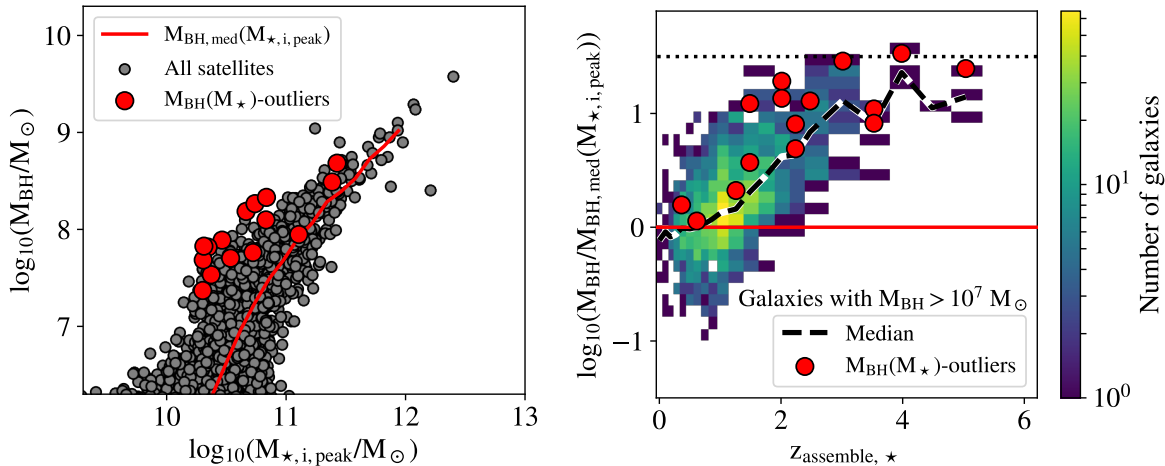


Figure 2.7: *Left-hand panel:* M_{BH} as a function of $M_{*,i,\text{peak}}$ for all satellite galaxies in EAGLE at $z = 0$. The median $M_{\text{BH}}(M_{*,i,\text{peak}})$ is shown as a red solid line while $M_{\text{BH}}(M_*)$ -outlier galaxies are shown as red points. Even though the use of $M_{*,i,\text{peak}}$ removes the effect of stellar stripping, many $M_{\text{BH}}(M_*)$ -outlier galaxies are ≈ 1 dex above the median $M_{\text{BH}}(M_{*,i,\text{peak}})$ relation. *Right-hand panel:* ratio of M_{BH} over the median $M_{\text{BH}}(M_{*,i,\text{peak}})$ at $z = 0$ as a function of stellar assembly redshift, $z_{\text{assemble},*}$, defined as the earliest redshift at which $M_*(z) > 0.5M_{*,i,\text{peak}}$, for galaxies with $M_{\text{BH}} > 10^7 M_{\odot}$. The dotted horizontal line denotes the $M_{\text{BH}}(M_*)$ -outlier cut of 1.5 dex, while the solid red horizontal line denotes the median $M_{\text{BH}}(M_{*,i,\text{peak}})$ relation (at $z = 0$). The black dashed line shows the median deviation above the median $M_{\text{BH}}(M_*)$ -outliers and other galaxies of similar peak stellar mass is mostly due to their typically earlier stellar assembly times, as evidenced by the fact that the red points are close to the black dashed curve.

this relation. However, we find that most of them lie ≈ 1 dex above the median $M_{\text{BH}}(M_{\star,i,\text{peak}})$ relation (red line), implying that, indeed, another physical mechanism must be affecting these galaxies.

An alternate explanation of $M_{\text{BH}}(M_{\star})$ -outliers is that they are relics of the high-redshift Universe, when the $M_{\text{BH}} - M_{\star}$ relation may have had a higher normalization. We test this scenario by measuring their stellar assembly redshifts, $z_{\text{assemble},\star}$, defined as the earliest redshift at which $M_{\star,i}(z) \geq 0.5M_{\star,i,\text{peak}}$.

In the right-hand panel of Fig. 2.7, we plot the ratio between M_{BH} and the median $M_{\text{BH}}(M_{\star,i,\text{peak}})$ relation at $z = 0$ as a function of $z_{\text{assemble},\star}$. To avoid BH seed mass resolution effects we only consider galaxies with $M_{\text{BH}} > 10^7 M_{\odot}$. Here we see a clear trend of increasing $M_{\text{BH}}/M_{\text{BH,med}}(M_{\star,i,\text{peak}})$ with higher $z_{\text{assemble},\star}$, a trend that the $M_{\text{BH}}(M_{\star})$ -outlier galaxies follow. Indeed, the vast majority of galaxies that formed before $z = 1.5$ have $\log_{10}(M_{\text{BH}}/M_{\text{BH,med}}(M_{\star})) > 0$. Of the 15 $M_{\text{BH}}(M_{\star})$ -outlier galaxies, 10 (13) assembled most of their stars by $z = 2$ (1). Such early assembly times are atypical of satellite galaxies of similar stellar mass: the median $z_{\text{assemble},\star}$ of satellites with $M_{\star,i,\text{peak}} = 10^{10-11} M_{\odot}$ is ≈ 0.5 , much later than the $M_{\text{BH}}(M_{\star})$ -outliers stellar assembly redshift of ≈ 2 .

This trend with $z_{\text{assemble},\star}$ can be explained via the evolution of the median $M_{\text{BH}}(M_{\star})$ relation. Fig. 2.6 shows M_{BH} as a function of M_{\star} for all galaxies from $z = 3 - 1.5$, the redshift range where this evolution is strongest. For $z > 1.5$, the median $M_{\text{BH}}(M_{\star})$ was higher than it is at $z = 0$ for $M_{\star} \gtrsim 10^{10} M_{\odot}$, with the largest deviation being approximately an order of magnitude at $z = 3 - 4$ for $M_{\star} \sim 10^{10} M_{\odot}$. The main progenitors of the $M_{\text{BH}}(M_{\star})$ -outliers (red points) are typical in terms of their BH and stellar mass at $z = 3$, falling within the scatter of the relation at that redshift. Between $z = 3$ and $z = 2$, many of them grow rapidly in M_{BH} while the median relation drops to lower BH masses, and already by $z = 2$ most lie $\approx 0.5 - 1$ dex above the median relation. It was only after these processes occurred that these galaxies became satellites and began losing stellar mass, causing them to become the ‘extreme’ $M_{\text{BH}}(M_{\star})$ -outliers we find at $z = 0$. For a more detailed discussion of the evolution of M_{BH} in EAGLE, see Rosas-Guevara et al. (2016).

It is interesting that we do not find more $M_{\text{BH}}(M_{\star})$ -outliers with $z_{\text{assemble},\star}$ close to the more typical value of 0.5. One possibility is that the $M_{\text{BH}}(M_{\star})$ -outliers that we *do* find are more resistant to complete tidal disruption than typical satellite galaxies. This would be the case if they are unusually compact, a hypothesis that is consistent with their early formation times (Furlong et al. 2017), and one we explore in Section 2.5.

This early formation process occurred for central galaxies as well. While all of our $M_{\text{BH}}(M_{\star})$ -outliers [defined as $\log_{10}(M_{\text{BH}}/M_{\text{BH,med}}(M_{\star})) > 1.5$] are tidally stripped satellites, a slightly lower choice of $M_{\text{BH}}/M_{\text{BH,med}}(M_{\star})$ threshold would have added central galaxies into our $M_{\text{BH}}(M_{\star})$ -outlier sample, most of which have never been stripped. Indeed, a cut of 1.2 dex (thin dashed red line in Fig. 2.1) yields 47 $M_{\text{BH}}(M_{\star})$ -outlier galaxies, 10 of which are centrals (we will hereafter refer to these centrals as ‘marginal $M_{\text{BH}}(M_{\star})$ -outlier’ galaxies). The evolution of these marginal $M_{\text{BH}}(M_{\star})$ -outliers in the $M_{\text{BH}} - M_{\star}$ plane has been tracked in the same manner as the $M_{\text{BH}}(M_{\star})$ -outliers in Section 2.4.2. We find that none of them have been significantly stripped

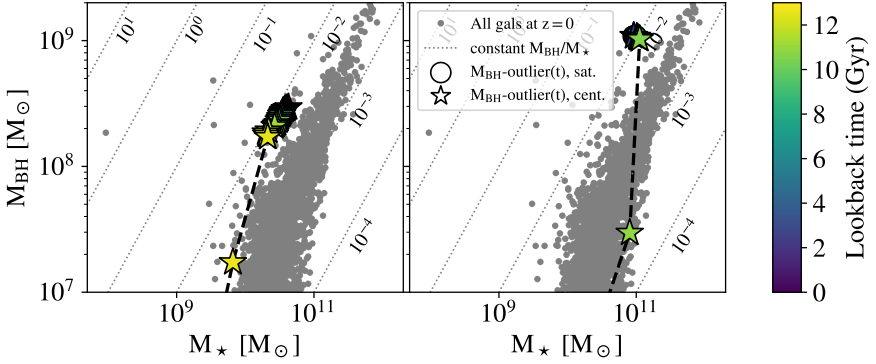


Figure 2.8: As in the right column of Fig. 2.3 but showing less extreme $M_{\text{BH}}(M_*)$ -outliers that have not been stripped of stars. These are examples of high- z ‘relic’ galaxies.

of stars – most had a brief period of rapid BH growth at early times ($t_{\text{LB}} \gtrsim 12$ Gyr or $z \gtrsim 3$), and subsequently either grew following the same slope as the $z = 0$ $M_{\text{BH}} - M_*$ relation, or simply stopped evolving.

Two illustrative examples are shown in Fig. 2.8. In the left-hand panel, we see one galaxy that already had a M_{BH}/M_* ratio of 1 per cent by $t_{\text{LB}} = 12$ Gyr and thereafter evolved slowly with the same slope as the $z = 0$ $M_{\text{BH}} - M_*$ relation. In the right-hand panel, we show a galaxy that grew very quickly in M_{BH} up to a M_{BH}/M_* ratio of 1 per cent at $t_{\text{LB}} = 11$ Gyr and remained stationary in the $M_{\text{BH}} - M_*$ plane thereafter. This result is consistent with the ‘high- z relic’ mechanism of $M_{\text{BH}}(M_*)$ -outlier formation (Ferré-Mateu et al. 2015).

Indeed, the $z_{\text{assemble},*}$ values of these 10 marginal $M_{\text{BH}}(M_*)$ -outlier central galaxies are all higher than $z \simeq 2.5$ (see Fig. 2.7), making them bona fide relics of the early EAGLE universe. We note as well that these galaxies are not significant outliers from the median $M_{\text{BH}}(\sigma)$ relation (less than 0.5 dex above the median), consistent with the expected weak evolution of σ since $z \approx 2$ for individual galaxies (e.g. Javier Cenarro & Trujillo 2009; Hilz et al. 2012; Oser et al. 2012). Thus, these relic galaxies were not strong outliers when they formed, but became (marginal) outliers from the $z = 0$ $M_{\text{BH}} - M_*$ relation primarily due to the evolution of the $M_{\text{BH}} - M_*$ relation in time.

2.4.5 The relative importance of tidal stripping and early formation

We now quantify the individual contributions of stellar stripping and early formation times to the M_{BH} offsets of $M_{\text{BH}}(M_*)$ -outlier galaxies. We define the tidal stripping contribution by the difference between $\log_{10}(M_{\text{BH,med}}(M_*))$ and $\log_{10}(M_{\text{BH,med}}(M_{*,i,\text{peak}}))$ measured at the M_* and $M_{*,i,\text{peak}}$ of each galaxy respectively. The contribution from early formation is defined as the median $M_{\text{BH}}/M_{\text{BH,med}}(M_{*,i,\text{peak}})$

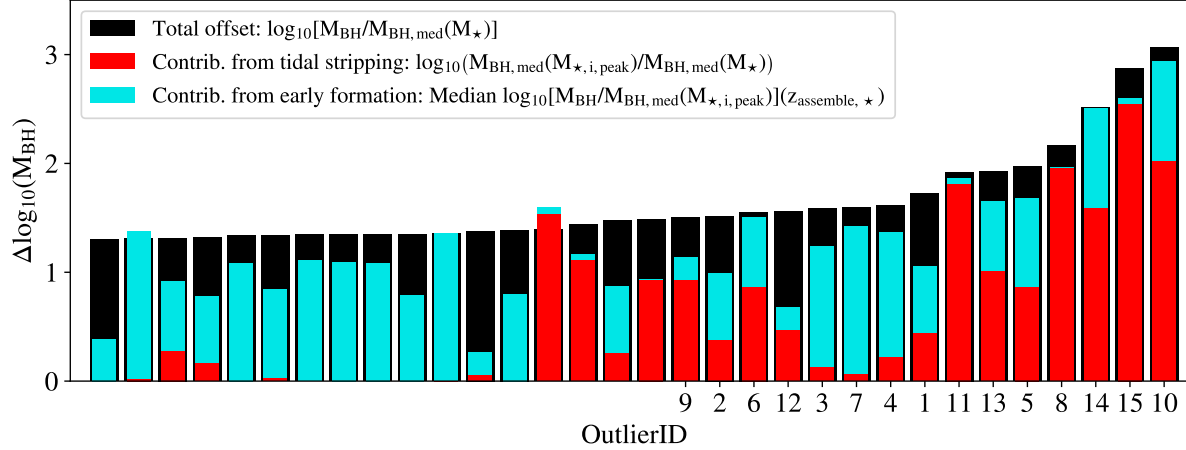


Figure 2.9: Individual contributions of tidal stripping (red bars) and early formation time (cyan bars, stacked) to the offset between M_{BH} and $M_{\text{BH,med}}(M_{\star})$ at $z = 0$ (black bars) for galaxies with $\log_{10}(M_{\text{BH}}/M_{\text{BH,med}}(M_{\star})) > 1.3$. The 15 most extreme $M_{\text{BH}}(M_{\star})$ -outliers (with $\log_{10}(M_{\text{BH}}/M_{\text{BH,med}}(M_{\star})) > 1.5$) are labelled with their OutlierIDs from Table 2.1. Tidal stripping dominates over early formation for 10 of the 15 most extreme $M_{\text{BH}}(M_{\star})$ -outliers, while stellar assembly time dominates for 80 per cent of galaxies with $\log_{10}(M_{\text{BH}}/M_{\text{BH,med}}(M_{\star})) \in [1.3, 1.5]$. Summed together, these two mechanisms account for on average 86 per cent of the offset for the most extreme outliers.

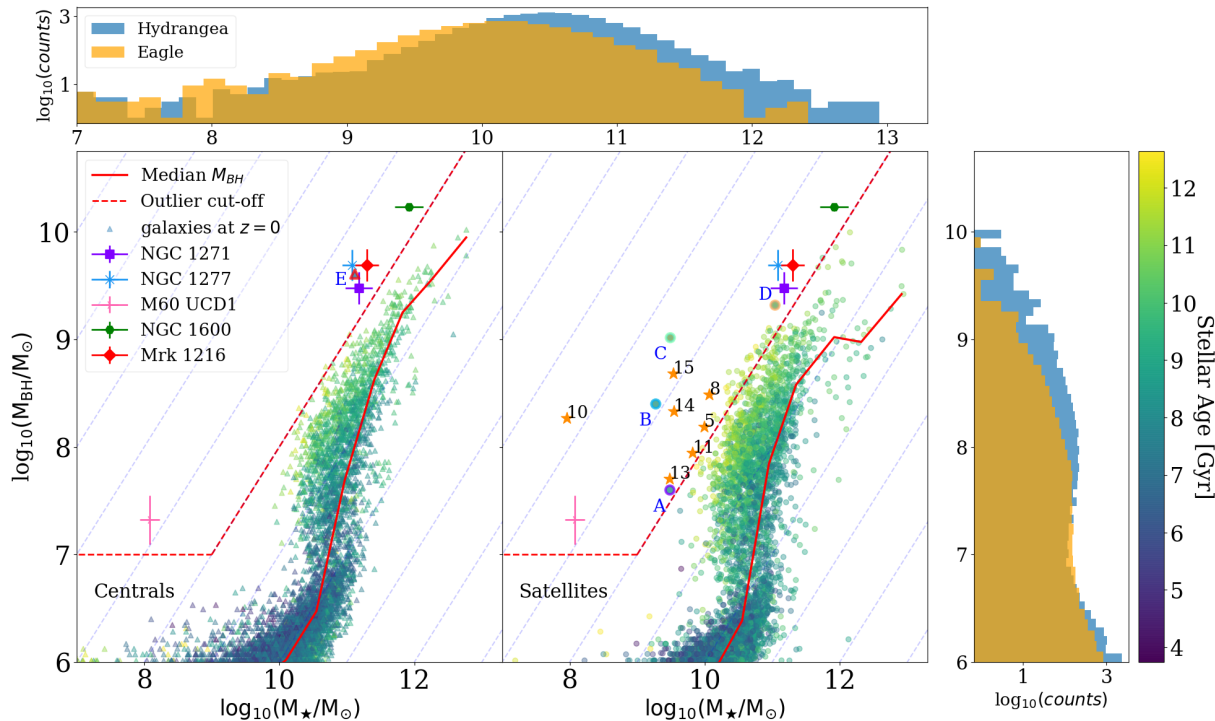


Figure 2.10: M_{BH} as a function of M_* for central (lower left panel) and satellite (lower middle panel) galaxies in the Hydrangea simulations of galaxy clusters at $z = 0$. Galaxies are coloured by their mean mass-weighted stellar age (see colour bar). Solid red lines indicate running medians. M_{BH} outliers are defined as those with $M_{\text{BH}} > 10^7 M_{\odot}$ and $M_*/M_{\text{BH}} > 0.01$, indicated by the dashed red line. Black hole “monster” galaxies (BMGs) are indicated with letters, while numbered star symbols indicate the M_{BH} -outlier galaxies from the reference EAGLE (100 Mpc)³ simulation (Ref-100) that would be considered outliers under this definition, with numbers corresponding to their outlier ID in Barber et al. (2016, i.e. this chapter excluding Section 2.4.6). Several observed high-mass M_{BH} outliers are shown with error bars (see legend). The top and right panels show histograms of M_{BH} and M_* , respectively, in Ref-100 and Hydrangea. We predict the existence of M_{BH} -outliers with M_{BH} up to $4 \times 10^9 M_{\odot}$ in these cluster environments, comparable to some of the most massive M_{BH} -outliers observed. Figure taken from van Son et al. (2018).

at $z = 0$ as a function of $z_{\text{assemble},*}$ (the dashed line in the right-hand panel of Fig. 2.7), evaluated at the $z_{\text{assemble},*}$ of each galaxy. These contributions are plotted in Fig. 2.9 for galaxies with $\log_{10}(M_{\text{BH}}/M_{\text{BH,med}}(M_*)) > 1.3$, sorted by their M_{BH} offset. Immediately we see that the contributions can vary wildly between galaxies, ranging from stripped late-assemblers to unstripped early-assemblers. Tidal stripping dominates for 10 of the 15 $M_{\text{BH}}(M_*)$ -outlier galaxies (including the four most extreme outliers; $\log_{10}[M_{\text{BH}}/M_{\text{BH,med}}(M_*)] > 2$), while early formation is more important for ≈ 80 per cent of the 18 less extreme $M_{\text{BH}}(M_*)$ -outliers (with $\log_{10}(M_{\text{BH}}/M_{\text{BH,med}}(M_*)) \in [1.3, 1.5]$)⁵. The contribution from stripped galaxies found here may even be an underestimate, since with increased mass resolution it would be possible to track satellites down to smaller masses and thus for longer times during the stripping process before being lost by the subhalo finder, increasing the number of stripped galaxies at any given time.

Summed together, the contributions from tidal stripping and early stellar assembly times account for on average 86 per cent of the offset in $M_{\text{BH}}(M_*)$ at $z = 0$ for the extreme $M_{\text{BH}}(M_*)$ -outliers, leaving them on average 0.3 ± 0.2 dex above the median $M_{\text{BH}}(M_{*,i,\text{peak}})$ relation after these two effects have been taken into account, well within the 95 percentile scatter of ≈ 0.6 dex around the median at $M_{*,i,\text{peak}} \sim 10^{10.5} M_{\odot}$. We attribute this additional offset of 0.3 ± 0.2 dex above the median to a selection bias. At fixed $M_{*,i,\text{peak}}$, the deficit in M_* at $z = 0$ required to be a $M_{\text{BH}}(M_*)$ -outlier by our definition increases strongly with decreasing M_{BH} . Thus, we expect the $M_{\text{BH}}(M_*)$ -outliers to be biased to high M_{BH} even with the effects of tidal stripping and early formation taken into account.

These results are qualitatively consistent with the properties of galaxies with overmassive BHs in the (142 Mpc)³ cosmological simulation HorizonAGN, where the most extreme outliers in the simulated $M_{\text{BH}} - M_*$ relation are stripped satellites of more massive host galaxies while relic galaxies have the highest BH masses of the central galaxies but do not have as extreme BH masses as stripped satellites (Volonteri et al. 2016).

We conclude that, while the extreme $M_{\text{BH}}(M_*)$ -outliers result primarily from tidally-induced stellar stripping, it is certainly possible for galaxies to simply form a high-mass BH at very early times and then stop evolving, becoming ‘relics’ of the early Universe by $z = 0$. Indeed, the most extreme outliers formed relatively early and already had relatively massive BHs prior to losing stars due to stellar stripping.

2.4.6 Galaxies with “monstrous” black holes in galaxy cluster environments

This section provides a short summary of work done by Master’s student Lieke van Son, whom Christopher Baber supervised for her minor Master’s project. This summary did not appear in the published version of this Chapter (i.e. Barber et al. 2016), but is based on Lieke’s paper which has recently been submitted for publication in MNRAS

⁵The same result is found for the 32 galaxies with $\log_{10}(M_{\text{BH}}/M_{\text{BH,med}}(M_*)) \in [1.2, 1.5]$.

(van Son et al. 2018; hereafter vS18). The rest of this Chapter is unchanged relative to Barber et al. (2016).

One of the major limitations of using the EAGLE simulations to search for M_{BH} -outlier galaxies is the limited simulation volume. The largest EAGLE run has a volume of only $(100 \text{ Mpc})^3$ (Ref-100). While this is great for studying large populations of field galaxies, it has limited statistics at the high-mass end of the galaxy stellar mass function. Indeed, in the Ref-100 volume, we expect to find $\sim 10^{-1}$ massive, compact, high velocity-dispersion analogues of high- z galaxies (Saulder et al. 2015). The limited volume is thus likely the primary reason that M_{BH} -outliers with M_{BH} as high as that found in, e.g., NGC 1277 or NGC 1271 were not found in Ref-100 by Barber et al. (2016, i.e. this Chapter excluding Section 2.4.6).

In vS18, we extend the work of Barber et al. (2016) to cluster environments in an effort to enhance the statistics at the high-mass end. In doing so we can place stronger constraints on the existence of M_{BH} -outliers with M_{BH} as high as those observed. To this end we employed the Hydrangea project, a suite of cosmological, hydrodynamical zoom-in simulations of galaxy clusters (Bahé et al. 2017; Barnes et al. 2017). These simulations use the same model of galaxy formation as in EAGLE but with a larger AGN heating temperature which produces more realistic hot gas haloes of galaxy groups (model AGNdT9 from Schaye et al. 2015). Thirty clusters are simulated, ranging in mass from $M_{200} \approx 10^{14}$ to $2 \times 10^{15} M_{\odot}$. Each cluster is simulated at the same resolution as the reference EAGLE model, with gas and dark matter particle masses of $1.8 \times 10^6 M_{\odot}$ and $9.7 \times 10^6 M_{\odot}$, respectively. These high-resolution regions extend out to $10 r_{200}$, allowing for a detailed investigation of galaxies embedded in these cluster environments.

We performed the same analysis as in Barber et al. (2016) on these cluster simulations to further investigate the predicted existence and origin of high-mass M_{BH} outlier galaxies. In vS18 these galaxies are referred to as black hole “monster” galaxies (BMGs). Histograms shown in the upper and right-hand panels of Fig. 2.10 compare the distributions of M_{BH} and M_* in Ref-100 and Hydrangea at $z = 0$. Already we see that Hydrangea contains more galaxies with $M_{\text{BH}} > 10^8 M_{\odot}$ and $M_* > 10^{10} M_{\odot}$ than in Ref-100, making it better-equipped for searching for high-mass M_{BH} -outliers.

The lower-left and -middle panels of Fig. 2.10 show M_{BH} as a function of M_* for central and satellite galaxies, respectively, in the Hydrangea simulations at $z = 0$. We define M_{BH} -outliers as those with $M_{\text{BH}} > 10^7 M_{\odot}$ and $M_*/M_{\text{BH}} > 0.01$. This definition differs from that of Barber et al. (2016) due to the large number of galaxies that would be selected in Hydrangea using that definition (10 per cent of those with $M_{\text{BH}} > 10^7 M_{\odot}$). The majority of M_{BH} -outliers are satellite galaxies, implying that environment may play a role in their enhanced M_{BH}/M_* ratios. We also colour the galaxies by mean mass-weighted age, where we can see clearly that the galaxies with the largest M_{BH} at fixed M_* are much older than the general population. Five of the qualitatively most interesting outliers (termed black hole “monsters” or BMGs) were selected for further study, and are labeled with letters A-E. The two highest-mass BMGs (D and E) have M_{BH} and M_* very similar to observed BMGs NGC 1271, NGC 1277, and Mrk 1216. We thus confirm for the first time that such galaxies are expected to exist

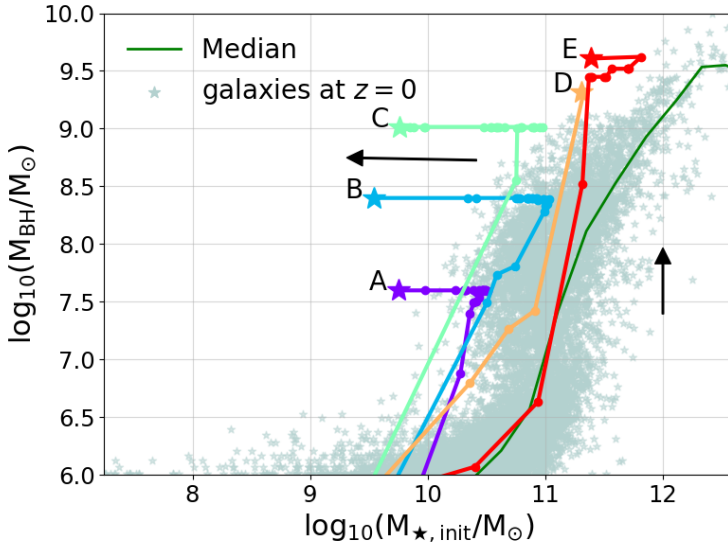


Figure 2.11: Evolution of the 5 BMGs from the Hydrangea simulations through the $M_{\text{BH}} - M_{\star, \text{init}}$ plane. Arrows indicate the general direction in which these galaxies move over time. Their positions at $z = 0$ are indicated with star symbols, while dots along the tracks are separated by 500 Myr intervals. The general distribution of Hydrangea galaxies at $z = 0$ is shown in light gray symbols, with the median M_{BH} in bins of $M_{\star, \text{init}}$ indicated with a green solid line. Stellar stripping is an important contributor to the enhanced $M_{\text{BH}}/M_{\star, \text{init}}$ ratios of most of these BMGs. Figure taken from van Son et al. (2018).

(within the EAGLE model).

2.4.6.1 The origin of BH monster galaxies

As in Barber et al. (2016), we find that tidal stripping as well as early formation time are significant contributors to the enhanced M_{BH} in these BMGs.

Fig. 2.11 shows the evolution of these 5 BMGs through the $M_{\text{BH}} - M_{\star, \text{init}}$ plane, where $M_{\star, \text{init}}$ is the stellar mass computed using the initial mass of each star particle, thus removing the effect of mass loss due to stellar evolution⁶. All of these galaxies initially grew to large M_{BH}/M_{\star} , with most lying above the typical scatter in the $M_{\text{BH}} - M_{\star, \text{init}}$ relation. The three with lowest M_{BH} (A, B, and C) subsequently began to lose the majority of their stellar mass over time, likely as a result of tidal stripping by a more massive host galaxy. The two BMGs with largest M_{BH} ($\approx 10^{9.5} M_{\odot}$) initially grew to lie well above the median $M_{\text{BH}}(M_{\star, \text{init}})$ relation without stellar mass loss (although the most massive one, BMG E, has begun losing stellar mass in the final 500 Myr). Thus, stellar stripping appears to be an important contributor to enhancing M_{BH}/M_{\star} ratios, but may not be as important for the highest-mass systems.

⁶Note that $M_{\star, \text{init}}$ is called $M_{\star, i}$ in the rest of this Chapter. We use the former nomenclature in Section 2.4.6 for consistency with the figures from vS18.

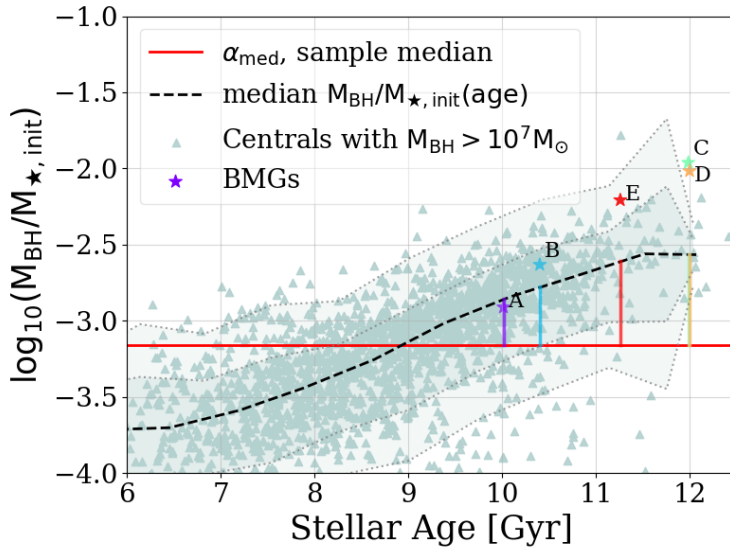


Figure 2.12: $M_{\text{BH}}/M_{\star, \text{init}}$ as a function of mass-weighted stellar age at $z = 0$ for central galaxies from the Hydrangea simulations with $M_{\text{BH}} > 10^7 M_{\odot}$ (grey triangles). The running median is indicated with a dashed black line, while the median value for the whole sample is shown as a red dashed horizontal line. Our 5 BMGs are plotted using the maximum $M_{\star, \text{init}}$ they ever reached in order to remove the effect of stellar stripping. The contributions of old age to the enhanced M_{BH}/M_{\star} ratios of these BMGs are indicated with solid coloured vertical lines. Galaxies with older stellar populations tend to have larger $M_{\text{BH}}/M_{\star, \text{init}}$ ratios. Old age is an important contributor to the enhanced M_{BH}/M_{\star} in these BMGs. Figure taken from van Son et al. (2018).

In Fig. 2.12 we show the $M_{\text{BH}}/M_{\star, \text{init}}$ ratio as a function of mean mass-weighted stellar age for central galaxies with $M_{\text{BH}} > 10^7 M_{\odot}$ at $z = 0$. Here we see a strong positive correlation, where the oldest galaxies tend to have the largest $M_{\text{BH}}/M_{\star, \text{init}}$, in agreement with the results of Barber et al. (2016). We quantify the contribution of stellar age to the enhanced M_{BH}/M_{\star} ratios in our galaxies as the difference between the running median (black solid line) and the median computed for the entire sample (red dashed line). We plot our 5 BMGs using the maximum $M_{\star, \text{init}}$ that the galaxies have ever had to eliminate the effect of stellar stripping. We find that all of our BMGs are old, with ages > 10 Gyr, indicating that stellar age has indeed contributed to their large $M_{\text{BH}}/M_{\star, \text{init}}$ ratios, indicated with solid vertical lines.

However, the oldest BMGs (C, D, and E) actually lie more than 1σ above the $M_{\text{BH}}/M_{\star, \text{init}} - \text{age}$ relation, indicating that another mechanism may be at play here. We have investigated the formation of these galaxies in detail, finding that they have experienced multiple major mergers just before the rapid BH growth phase, which, depending on the nature of the (stochastic) geometry and timing of the mergers, may have led to a “perfect storm” of conditions that allowed the BHs to grow to such high masses. However, since major mergers are quite common at high redshift, and major mergers in general do not seem to be important for triggering the rapid BH growth phase in EAGLE at high redshift (McAlpine et al. 2018), it is not clear how important these mergers were for the formation of their overmassive BHs.

2.5 Relation to compact galaxies

The formation of UCDs has recently received much attention. The general picture that is emerging posits that the highest mass UCDs ($M_{\star} \simeq 10^8 M_{\odot}$) may be the surviving nuclei of dwarf elliptical galaxies whose outer parts have been tidally ‘threshed’ by more massive host galaxies (e.g., Bekki et al. 2003; Brodie et al. 2011; Chilingarian et al. 2011; Da Rocha et al. 2011; Pfeffer et al. 2014; Norris et al. 2014, 2015). Recently, Mieske et al. (2013) found that massive UCDs ($M_{\star} > 10^7 M_{\odot}$) have excess dark mass which can be explained by massive BHs (or a bottom-heavy IMF), which would offset them by up to 2 dex above the $M_{\text{BH}} - \sigma$ and $M_{\text{BH}} - L_{\text{bulge}}$ relations. Thus, if the existence of their central BHs is confirmed, they would be strong $M_{\text{BH}}(M_{\star})$ -outliers. Indeed, the confirmation of a central BH in M60-UCD1 (Seth et al. 2014, see also Fig. 2.1) suggests that the tidal formation mechanism may dominate UCD formation, at least for the most massive UCDs.

As our $M_{\text{BH}}(M_{\star})$ -outliers are the tidally threshed nuclei of more massive progenitors, it is thus natural to ask if there is some connection between the $M_{\text{BH}}(M_{\star})$ -outliers and compact galaxies in the simulation, and whether this can be used to shed some light on the formation mechanism of UCDs. Note that at our resolution we cannot resolve galaxies as low in mass (M_{\star} typically between 2×10^6 and $10^8 M_{\odot}$) or as small (effective radii $\lesssim 100$ pc) as UCDs. Indeed, we find only one $M_{\text{BH}}(M_{\star})$ -outlier with $M_{\star} \sim 10^8 M_{\odot}$, and even this one has M_{BH} an order of magnitude higher than what would be consistent with UCDs (OutlierID=10 in Table 2.1). However, if UCDs are the tidally threshed nuclei of more massive progenitors, then we can likely catch these

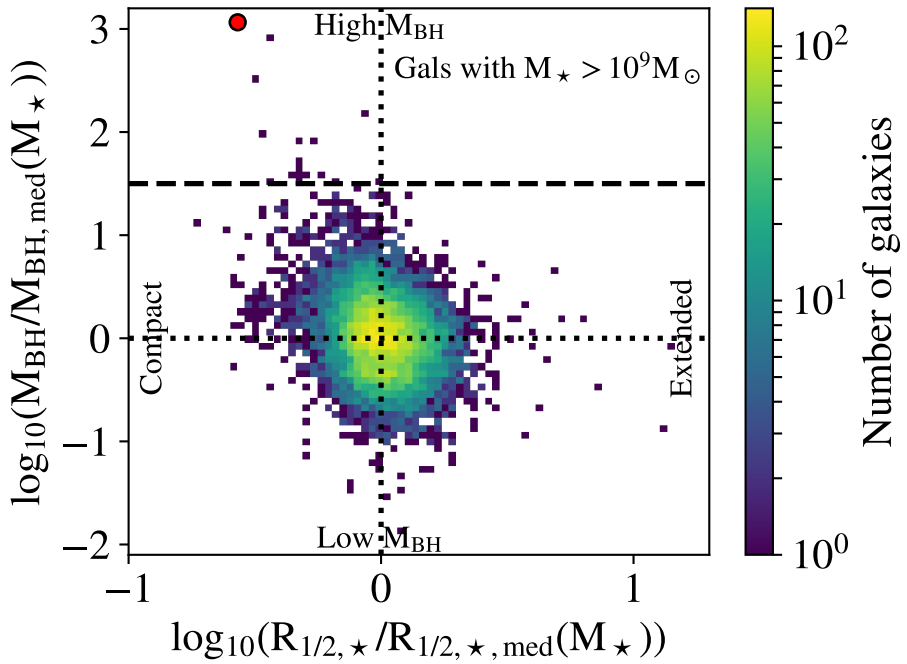


Figure 2.13: 2D histogram of the number of dex above the median $M_{\text{BH}}(M_{\star})$ relation as a function of compactness for galaxies with $M_{\star} > 10^9 M_{\odot}$. Our $\log_{10}(M_{\text{BH}}/M_{\text{BH,med}}(M_{\star})) > 1.5$ cut defining $M_{\text{BH}}(M_{\star})$ -outliers is shown as a dashed horizontal line, while the median M_{BH} and $R_{1/2,\star}$ are shown as horizontal and vertical dotted lines, respectively. For completeness we include the most extreme $M_{\text{BH}}(M_{\star})$ -outlier (OutlierID = 10) as a red circle. More compact galaxies tend to have higher-than-average M_{BH} , especially those with half-mass radii more than 0.3 dex below the median value for their stellar mass.

progenitors after they have started to lose mass, but before they are stripped to masses below our resolution limit. Indeed, if the $M_{\text{BH}}(M_*)$ -outliers tend to be more compact than average, then they could very well be on their way to becoming compact galaxies similar to UCDs.

To this end, we now investigate whether the $M_{\text{BH}}(M_*)$ -outlier galaxies are unusually compact given their M_* , and if so, whether compact galaxies at $z = 0$ generally have been stripped of stars. The evolution of galaxy sizes in EAGLE, including high- z compact galaxies, has already been discussed by Furlong et al. (2017); thus in this section we perform a qualitative treatment of compact galaxies, looking only for general trends.

We define ‘compactness’ as the ratio between the 3D stellar half-mass radius of a galaxy, $R_{1/2,*}$, and the median value for galaxies with the same M_* , $R_{1/2,*,\text{med}}(M_*)$; galaxies with lower ratios are more compact. Only galaxies with $M_* > 10^9 M_\odot$ are considered here since below this limit the measured size is unconverged in the Ref-L0100N1504 simulation for typical galaxies (S15). For completeness we also include the most extreme $M_{\text{BH}}(M_*)$ -outlier (OutlierID = 10, $M_* \simeq 10^8 M_\odot$); its inclusion does not affect our results. Our $M_{\text{BH}}(M_*)$ -outlier galaxies have $R_{1/2,*} \sim 1 - 3$ kpc, which approaches the softening length of 0.7 proper kpc. Thus, their sizes may still be affected by resolution and should be taken as upper limits.

Fig. 2.13 shows the relation between $M_{\text{BH}}/M_{\text{BH,med}}(M_*)$ and $R_{1/2,*}/R_{1/2,*,\text{med}}(M_*)$. We find that the $M_{\text{BH}}(M_*)$ -outlier galaxies are significantly more compact than the median size given their stellar masses, with most of them $\sim 0.2 - 0.5$ dex below the median. In general, we see that galaxies more compact than $\log_{10}(R_{1/2,*}/R_{1/2,*,\text{med}}(M_*)) = -0.3$ tend to have higher M_{BH} than expected given their M_* (with a median $\log_{10}(M_{\text{BH}}/M_{\text{BH,med}}(M_*)) \approx 0.35$). On the other hand, galaxies with $\log_{10}(M_{\text{BH}}/M_{\text{BH,med}}(M_*)) > 1$ tend to be more compact than the median (with median $\log_{10}(R_{1/2,*}/R_{1/2,*,\text{med}}(M_*)) \approx -0.18$). Thus, there does seem to be a strong connection between overmassive BHs and compactness. This result supports the hypothesis that UCDs are the tidally threshed nuclei of more massive progenitor galaxies. Note, however, that this result does not imply that all compact galaxies have overmassive BHs. To answer this question one would need to resolve $R_{1/2,*} \lesssim 1$ kpc (corresponding to $\log_{10}(R_{1/2,*}/R_{1/2,*,\text{med}}(M_*)) < -0.6$ at $M_* \sim 10^{10} M_\odot$), which is not possible at this resolution.

Since the combination of a high stellar assembly redshift and, most importantly, tidal stripping are responsible for creating $M_{\text{BH}}(M_*)$ -outlier galaxies, we now investigate if the same mechanisms cause galaxies to be more compact in general. Fig. 2.14 shows $R_{1/2,*}/R_{1/2,*,\text{med}}(M_*)$ as a function of $M_{*,i}/M_{*,i,\text{peak}}$ and $z_{\text{assemble},*}$, for all galaxies with $M_* > 10^9 M_\odot$, regardless of whether or not they harbour a BH. We see that, indeed, galaxies that have lost more than 40 per cent of their stellar mass and/or have assembled more than half of their stellar mass before $z = 2.5$ tend to be more compact than expected given their (current) mass, with median $R_{1/2,*}/R_{1/2,*,\text{med}}(M_*) \approx -0.2$. For reference, we overplot the $M_{\text{BH}}(M_*)$ -outlier galaxies, finding that 13 of 15 lie in at least one of these two regimes. Thus, the compactness of the $M_{\text{BH}}(M_*)$ -outlier galaxies, as is the case for their high BH masses, is caused by a

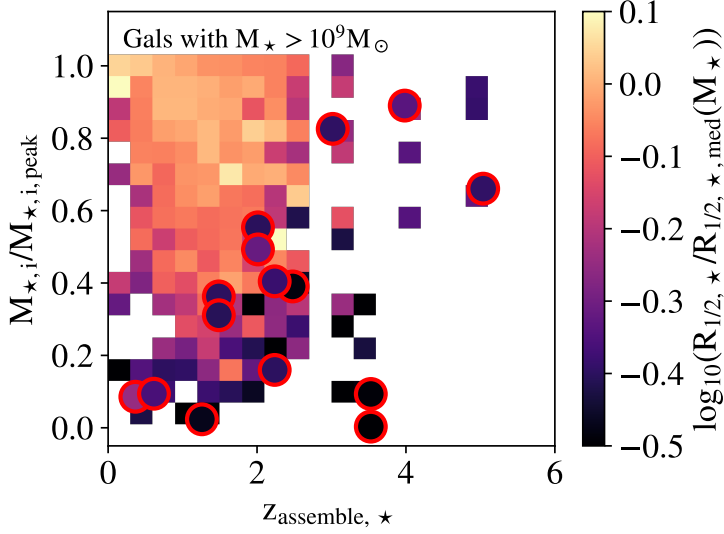


Figure 2.14: Median compactness in bins of $M_{*,i}/M_{*,i,\text{peak}}$ and $z_{\text{assemble},*}$ for all galaxies with $M_* > 10^9 M_\odot$. The $M_{\text{BH}}(M_*)$ -outlier galaxies are shown as red circles. Galaxy compactness increases with a higher degree of stellar stripping and with an earlier assembly redshift. The $M_{\text{BH}}(M_*)$ -outlier galaxies are compact because they assembled their stars at high- z and/or were tidally stripped of stars after becoming satellite galaxies.

combination of their early assembly times and stellar stripping.

The fact that all of our (stripped) $M_{\text{BH}}(M_*)$ -outlier satellites are compact has at least two possible explanations: (1) a physical explanation where more extended satellite galaxies are not able to withstand significant tidal stripping before being completely disrupted, or (2) a numerical explanation where more extended $M_{\text{BH}}(M_*)$ -outliers *do* exist at $z = 0$, but are undetectable by our halo finder (and in observations) because they represent much weaker overdensities relative to the host galaxy. More sophisticated subhalo finding techniques would be required to detect such extended satellite galaxies, a task beyond the scope of this work.

We conclude that galaxies with overly massive BHs tend to be more compact than typical galaxies of the same stellar mass, as expected for the tidal threshing hypothesis of UCD formation as well as in the early formation scenario. $M_{\text{BH}}(M_*)$ -outlier galaxies are compact due to a combination of their high degree of stellar stripping and their early formation times. While this tidal threshing mechanism clearly occurs within the framework of EAGLE, higher-resolution simulations would be needed to follow UCD formation in detail.

2.6 Summary and Conclusions

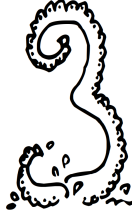
We have investigated the existence and evolution of galaxies that are positive outliers relative to the $z = 0$ $M_{\text{BH}} - M_*$ relation using the (100 Mpc)³ EAGLE cosmological hydrodynamical simulation. Our main conclusions are as follows.

- Positive outliers from the $M_{\text{BH}} - M_*$ relation (referred to as $M_{\text{BH}}(M_*)$ -outliers) similar to those presented in the recent observational literature exist in EAGLE. Most $M_{\text{BH}}(M_*)$ -outliers have stellar masses $M_* \sim 10^{10} M_\odot$ and black hole masses $M_{\text{BH}} \sim 10^8 M_\odot$. These mass ranges are similar to observed $M_{\text{BH}}(M_*)$ -outliers NGC 4486B, NGC 4342 and S536. However, we cannot make predictions for the existence of $M_{\text{BH}}(M_*)$ -outliers as massive as, e.g., NGC 1277 due to the limited box size, or as low in mass as ultracompact dwarf (UCD) galaxies due to the finite resolution of EAGLE (Fig. 2.1).
- The 15 most extreme $M_{\text{BH}}(M_*)$ -outlier galaxies (defined as those with $\log_{10}[M_{\text{BH}}/M_{\text{BH,med}}(M_*)] > 1.5$) are satellites of larger host galaxies, each residing within half the virial radius of its host halo (Fig. 2.3).
- These extreme $M_{\text{BH}}(M_*)$ -outliers became outliers through a combination of early stellar assembly times (Figs. 2.7 and 2.6) and subsequent extensive stellar stripping due to tidal forces from their host haloes (Figs. 2.2 and 2.5). Tidal stripping is the dominant mechanism responsible for the overmassive BHs in 67 per cent of the extreme outliers (Fig. 2.9), a fraction that may increase for higher-resolution simulations. Some $M_{\text{BH}}(M_*)$ -outliers have only recently begun to undergo stripping while others are survivors of slow tidal stripping occurring over several Gyr (Figs. 2.2 and 2.4). The most extreme $M_{\text{BH}}(M_*)$ -outliers are currently undergoing severe stellar disruption.
- Early formation is more important than tidal stripping for causing the M_{BH} offsets in 80 per cent of the 32 less extreme $M_{\text{BH}}(M_*)$ -outliers ($1.2 < M_{\text{BH}}/M_{\text{BH,med}}(M_*) < 1.5$; Fig. 2.9). Such galaxies formed with overmassive BHs at high redshift ($z > 2$) when the normalization of the $M_{\text{BH}} - M_*$ relation was higher (Figs. 2.7 and 2.6). Of these early-forming galaxies, 10 are centrals that subsequently either evolved parallel to the $z = 0$ $M_{\text{BH}} - M_*$ relation or remained unchanged until $z = 0$, becoming ‘relics’ of the high- z EAGLE universe (Fig 2.8).
- Together, the combination of tidal stripping and early stellar assembly times accounts for an average of 86 per cent of the offset above the median $M_{\text{BH}}(M_*)$ for the extreme $M_{\text{BH}}(M_*)$ -outliers (Fig. 2.9).
- The extreme $M_{\text{BH}}(M_*)$ -outliers are amongst the most compact galaxies in the simulation, with stellar half-mass radii, $R_{1/2,*}$, typically 0.2 – 0.5 dex smaller than the median value for other galaxies of similar stellar mass, $R_{1/2,*,\text{med}}(M_*)$, making them ideal candidates for UCD progenitors. Similarly, galaxies with $M_* > 10^9 M_\odot$ that are more than 0.3 dex below $R_{1/2,*,\text{med}}(M_*)$ tend to host

overmassive BHs. These $M_{\text{BH}}(M_*)$ -outliers, and galaxies with $M_* > 10^9 M_\odot$ in general, become compact via a combination of early formation and/or tidal stripping (Figs. 2.13 and 2.14).

Acknowledgements

The authors are grateful to the anonymous referee for a very constructive report that improved the quality of the paper. CB thanks Remco van den Bosch, Tiago Costa, and Joseph Silk for helpful comments and suggestions, and Stuart McAlpine for many useful discussions regarding spurious galaxies in EAGLE. This work used the DiRAC Data Centric system at Durham University, operated by the Institute for Computational Cosmology on behalf of the STFC DiRAC HPC Facility (www.dirac.ac.uk). This equipment was funded by BIS National E-infrastructure capital grant ST/K00042X/1, STFC capital grants ST/H008519/1 and ST/K00087X/1, STFC DiRAC Operations grant ST/K003267/1 and Durham University. DiRAC is part of the National E-Infrastructure. RAC is a Royal Society University Research Fellowship. We also gratefully acknowledge PRACE for awarding us access to the resource Curie based in France at Très Grand Centre de Calcul. This work was sponsored by the Dutch National Computing Facilities Foundation (NCF) for the use of supercomputer facilities, with financial support from the Netherlands Organization for Scientific Research (NWO). The research was supported in part by the European Research Council under the European Union's Seventh Framework Programme (FP7/2007-2013)/ERC grant agreement 278594-GasAroundGalaxies and 267291-Cosmiway. This research was funded by the Interuniversity Attraction Poles Programme initiated by the Belgian Science Policy Office (AP P7/08 CHARM). This research made use of `ASTROPY`, a community-developed core `PYTHON` package for Astronomy (Astropy Collaboration 2013).



*Calibrated, cosmological,
hydrodynamical simulations with
variable IMFs I:
Method and effect on global galaxy
scaling relations*

The recently inferred variations in the stellar initial mass function (IMF) among local high-mass early-type galaxies may require a reinterpretation of observations of galaxy populations and may have important consequences for the predictions of models of galaxy formation and evolution. We present a new pair of cosmological, hydrodynamical simulations based on the EAGLE model that self-consistently adopt an IMF that respectively becomes bottom- or top-heavy in high-pressure environments for individual star-forming gas particles. In such models, the excess stellar mass-to-light (M/L) ratio with respect to a reference IMF is increased due to an overabundance of low-mass dwarf stars or stellar remnants, respectively. Crucially, both pressure-dependent IMFs have been calibrated to reproduce the observed trends of increasing excess M/L with central stellar velocity dispersion (σ_e) in early-type galaxies, while maintaining agreement with the observables used to calibrate the EAGLE model, namely the galaxy luminosity function, half-light radii of late-type galaxies, and black hole masses. We find that while the M/L excess is a good measure of the IMF for low-mass slope variations, it depends strongly on the age of the stellar population for high-mass slope variations. The normalization of the $[\text{Mg}/\text{Fe}] - \sigma_e$ relation is decreased (increased) for bottom- (top-)heavy IMF variations, while the slope is not strongly affected. Bottom-heavy variations have little impact on galaxy metallicities, half-light radii of early-type galaxies, or star formation rates, while top-heavy variations significantly increase these quantities for high-mass galaxies, leading to tension with observations.

Christopher Barber, Robert A. Crain and Joop Schaye
MNRAS, 479, 5448 (2018).

3.1 Introduction

The stellar initial mass function (IMF) is a crucial ingredient in the interpretation of galaxy observations as well as for predictions of models of galaxy formation. It defines the translation between physical quantities and observables, and is one of the largest sources of uncertainty in model predictions. In the Milky Way (MW), the IMF seems to be insensitive to environment, with a steep high-mass slope that flattens below $\sim 1 M_{\odot}$ (Kroupa 2001; Chabrier 2003; Bastian et al. 2010). Observational and theoretical studies alike nearly always adopt such a universal IMF in stellar evolution models, applying it to all galaxies, regardless of the conditions under which their stars were formed.

In the past decade, evidence for variations in the IMF has been steadily mounting, leading to a near-consensus that the IMF becomes “heavier” in the regions of high global stellar velocity dispersion, σ , found in the centres of high-mass early-type galaxies (ETGs). In unresolved systems, the IMF is often parametrized by the excess stellar mass-to-light ratio (M/L) of the stars relative to the M/L one would derive spectroscopically assuming a standard IMF. The M/L -excess (hereafter MLE; also known as the “IMF mismatch parameter”)¹ is constrained observationally via several independent methods, including gravitational lensing (e.g. Auger et al. 2010; Treu et al. 2010; Spiniello et al. 2011; Barnabè et al. 2013; Sonnenfeld et al. 2015; Posacki et al. 2015; Smith et al. 2015; Collier et al. 2018), stellar population synthesis (SPS) modelling of IMF-sensitive spectral absorption features (e.g. Cenarro et al. 2003; Van Dokkum & Conroy 2010; Conroy & van Dokkum 2012b; Spiniello et al. 2012; Ferreras et al. 2013; La Barbera et al. 2013, 2015; Spiniello et al. 2014; Rosani et al. 2018), or dynamical modelling of the stellar kinematics (e.g. Thomas et al. 2011b; Dutton et al. 2012; Tortora et al. 2013; Cappellari et al. 2013b; Li et al. 2017), with many of these studies employing a combination thereof. All three methods point to a strong trend of increasing MLE, and thus a “heavier” IMF, with σ . Some studies find additional (and sometimes stronger) trends between the IMF and metallicity and/or alpha enhancement, but there is still much debate on this issue (Conroy & van Dokkum 2012b; La Barbera et al. 2013; McDermid et al. 2014; La Barbera et al. 2015; Martín-Navarro et al. 2015c).

Puzzlingly, constraints on the IMF seem to be inconsistent on a case-by-case basis. Smith (2014) has shown that for a sample of 34 ETGs, while both SPS and dynamical modelling imply heavier IMFs in high-mass ETGs, there seems to be no correlation between the MLE values derived using the two methods. Newman et al. (2017) compared the MLE derived using lensing, stellar dynamics, and SPS modelling for 3 SNELLS lenses (Smith et al. 2015), also finding inconsistent results between the methods. Conversely, Lyubenova et al. (2016) finds consistent MLE values for SPS and dynamical modelling for a sample of 27 ETGs, arguing that inconsistencies found in other studies may be due to differences in aperture sizes, SPS models employed, or non-optimal dark matter halo corrections. These findings imply that the systematic

¹We introduce the notation “MLE” rather than the more-popular “ α ” for the IMF mismatch parameter to avoid confusion in discussions involving abundances of α -elements.

errors involved in some of these analyses may not be well understood. Indeed, Clauwens et al. (2015) have shown that IMF trends inferred from stellar kinematics arise also in models assuming a universal IMF if the measurements and/or modelling errors have been underestimated. Furthermore, they found that the data shows an IMF dependence on distance from the Galaxy, suggesting the presence of systematic errors. These results imply that further study is required.

Although the majority of the evidence points toward a non-universal IMF, it is not clear *how* it varies. Dynamical modelling and gravitational lensing constrain only the dynamical M/L , and indicate that it is higher than expected assuming a stellar population with a fixed IMF. This generally implies that either the IMF is more bottom-heavy, leading to more low-mass dwarf stars that contribute significantly to the mass but not the total luminosity, or that the IMF is top-heavy, implying the extra mass comes from stellar remnants: black holes (BHs), neutron stars, and white dwarfs. Some spectroscopic IMF studies are thought to be able to constrain the shape of the low-mass end of the IMF, as a number of absorption features are sensitive to the surface gravity of stars and thus measure the ratio of dwarf-to-giant stars. The majority of these studies find that this ratio is higher in high- σ galaxies, but the means by which this is achieved is similarly unclear, since the increased ratio of dwarf-to-giant stars can be achieved either through a steepening of the IMF low-mass slope (e.g. Conroy & van Dokkum 2012b; Conroy et al. 2017), or steepening of the high-mass slope (e.g. La Barbera et al. 2013). On the other hand, $H\alpha$ and $g-r$ colours of local star-forming galaxies from the GAMA survey imply that the high-mass end of the IMF becomes shallower in strongly star-bursting environments (Gunawardhana et al. 2011). The large variety of parametrizations of IMF variations makes comparison between different methods difficult, and has dramatic consequences for the uncertainty in the physical properties of galaxies inferred from observational surveys (Clauwens et al. 2016).

The consequences of a variable IMF on the predictions from galaxy formation models are unclear. While the IMF determines the present-day stellar M/L ratios of galaxies, it also governs the strength of stellar feedback and metal yields. For example, a more top-heavy (bottom-heavy) IMF produces more (fewer) high-mass stars that end their lives as supernovae and return mass and energy to the interstellar medium (ISM), affecting the production and distribution of metals throughout the ISM. Metallicity affects the rate at which gas cools and forms future generations of stars, while stellar feedback governs the balance between the flow of gas into, and out of, galaxies, thus regulating star formation. The situation becomes even more complex with the inclusion of supermassive BHs, whose growth depends on the ability of supernova feedback to remove gas from the central regions of galaxies where such BHs reside (Bower et al. 2017). BH gas accretion generates AGN feedback, which is important for quenching star formation in high-mass galaxies. These processes are non-linear and deeply intertwined, rendering the question of how variations in the IMF would impact galaxies in such models non-trivial.

To address this question, recent studies have begun investigating the effect of IMF variations by post-processing cosmological simulations and semi-analytic models, and by conducting self-consistent, small-scale, numerical simulations. In a post-processing

analysis of the Illustris simulations, Blancato et al. (2017) study how variations in the IMF of individual star particles manifests as global IMF trends between galaxies, finding that the IMF of individual particles must vary much more strongly than the global trends imply in order to obtain the observed MLE- σ trends. Sonnenfeld et al. (2017) use an evolutionary model based on dark matter-only numerical simulations to predict the evolution of the IMF in early-type galaxies due to dry mergers from $z = 2$ to 0, finding that dry mergers tend to decrease the MLE of individual galaxies over time, while the correlation between the IMF and σ should remain time-invariant. Much can be learned from post-processing of such large-scale simulations, but such studies by construction neglect the effect that a variable IMF may have on galaxy properties during their formation and evolution due to the change in stellar feedback and metal yields.

IMF variations have also been investigated in semi-analytic models (SAMs) of galaxy formation. Fontanot (2014) find that the variations at the high-mass end of the IMF have a much stronger effect on galaxy properties than variations at the low-mass end. By implementing the “integrated galactic IMF theory” (Kroupa & Weidner 2003), which predicts that the IMF should become top-heavy in galaxies with high SFRs, into SAMs, Fontanot et al. (2017) and Gargiulo et al. (2015) both find that models with a variable IMF are better able to reproduce observed abundance scaling relations than those with a universal IMF. While such SAMs are useful as a computationally inexpensive method of exploring many types of IMF variations, they lack the ability to resolve the internal properties of galaxies, which may be important for IMF studies in light of recent evidence for significant radial gradients in the IMF in individual high-mass ETGs (Martín-Navarro et al. 2015b; La Barbera et al. 2016; van Dokkum et al. 2017; Oldham & Auger 2018a; Sarzi et al. 2018; but see Davis & McDermid 2017; Alton et al. 2017).

Hydrodynamical simulations with the ability to resolve the internal structure of galaxies have been run with self-consistent IMF variations for a limited number of idealized galaxies. Bekki (2013) implement a density and metallicity-dependent IMF prescription to idealized chemodynamical simulations of dwarf-to-MW mass galaxies. They find that a top-heavy IMF in the high-density environments of actively star-forming galaxies suppresses the formation of dense clumps and thus suppresses star formation, as well as increasing the overall metallicities and α -enhancement of such galaxies. Gutcke & Springel (2017) apply the local metallicity-dependent IMF of Martín-Navarro et al. (2015c) to numerical simulations of 6 MW-analogues using AREPO, finding a strong effect on the metallicity evolution in such systems. Guszejnov et al. (2017) apply various prescriptions of IMF variations from giant molecular cloud (GMC) theory in a simulation of an individual MW analogue galaxy, finding that most prescriptions produce variations within the MW that are much stronger than observed. Such simulations are an excellent starting point to study the effect of IMF variations on galaxy formation and evolution, but are currently limited in statistics, especially for high-mass ETGs where the IMF is observed to vary the strongest.

In this paper, we present a pair of fully cosmological, hydrodynamical simulations, based on the EAGLE project (Schaye et al. 2015; Crain et al. 2015, hereafter referred

to as S15 and C15, respectively), each of which includes a prescription for varying the IMF on a per-particle basis to become either bottom-heavy or top-heavy in high-pressure environments, while self-consistently modelling its consequences for feedback and heavy element synthesis. While a pressure-dependent IMF has been studied before using self-consistent, cosmological, hydrodynamical simulations as part of the OWLS project (Schaye et al. 2010; Haas et al. 2013), the adopted IMF was in that case not motivated by the recent observations discussed above, and the OWLS models did not agree well with basic observables such as the galaxy luminosity function. In contrast, our prescription has been calibrated to broadly reproduce the observed relationship between the MLE and the central stellar velocity dispersion, and we verify that the simulations maintain good agreement with the observed luminosity function. It is the goal of this paper to investigate the effect that a variable IMF has on the properties of the galaxy population in the EAGLE model of galaxy formation, such as the galaxy stellar mass function, luminosity function, star formation rates, metallicities, alpha-enhancement, and sizes. In doing so, we may inform how the IMF should correlate with many galaxy observables, both across the galaxy population as well as within individual galaxies.

This paper is organized as follows. In Section 3.2 we describe the EAGLE simulations and the calibration of IMF variation prescriptions to match the local empirical MLE- σ correlations, and discuss how these prescriptions are self-consistently incorporated into the EAGLE model. Section 3.3.1 introduces the variable IMF simulations and details the resulting correlations between the galaxy-averaged IMF and central stellar velocity dispersion. In Section 3.3.2 we show that IMF variations have little effect on galaxy observables used to calibrate the reference EAGLE model, while Section 3.4 investigates the impact on predicted galaxy properties such as metallicity, alpha-enhancement, SFR, and sizes. Our conclusions are summarized in Section 3.5. Appendix 3.A gives extra details regarding aperture effects and the IMF calibration, while Appendix 3.B shows the effect of incrementally making individual physical processes in the simulations consistent with a variable IMF.

Paper II in this series will discuss trends between the MLE and global galaxy observables and determine which correlate most strongly with the MLE. In Paper III we will discuss the spatially-resolved IMF trends within individual high-mass galaxies and the redshift-dependence of the MLE- σ relation. The simulation data is publicly available at <http://icc.dur.ac.uk/Eagle/database.php>.

3.2 Methods

In this section we describe the EAGLE model (Section 3.2.1) and our procedure of calibrating IMF variations in post-processing to match observed trends with galaxy velocity dispersion (Section 3.2.2), followed by a description of the modifications to the EAGLE model necessary to produce simulations that are self-consistent when including a variable IMF (Section 3.2.3).

3.2.1 The EAGLE simulations

In this study we use the EAGLE model (S15, C15) to study the effect of a variable IMF on predictions of galaxy properties. Here we briefly summarize the simulation model, but refer the reader to S15 for a full description.

EAGLE, short for “Evolution and Assembly of GaLaxies and their Environments”, is a suite of hydrodynamical, cosmological simulations aimed at studying the formation and evolution of galaxies from the early Universe to $z = 0$. It was run with a modified version of the Tree-PM Smoothed Particle Hydrodynamics (SPH) code Gadget-3, last described by Springel (2005). The modifications to the SPH implementation, collectively known as Anarchy (Schaller et al. 2015b, appendix A of S15), improve the treatment of artificial viscosity, time-stepping, and alleviate issues stemming from unphysical surface tension at contact discontinuities. Cubic volumes of up to $(100 \text{ comoving Mpc})^3$ were simulated at various resolutions – in this paper we focus only on the “intermediate” resolution simulations, with $m_{\text{gas}} = 1.6 \times 10^6 M_{\odot}$ and $m_{\text{DM}} = 9.7 \times 10^6 M_{\odot}$ for gas and dark matter particles, respectively. The gravitational softening is kept fixed at 2.66 co-moving kpc for $z > 2.8$ and at 0.70 proper kpc at lower redshifts. A Lambda cold dark matter cosmogony is assumed, with cosmological parameters chosen for consistency with Planck 2013: ($\Omega_b = 0.04825$, $\Omega_m = 0.307$, $\Omega_{\Lambda} = 0.693$, $h = 0.6777$; Planck Collaboration 2014).

Physical processes acting on scales below the resolution limit of the simulation (termed “subgrid physics”) are modelled using analytic prescriptions whose inputs are quantities resolved by the simulation. The efficiency of feedback associated with the formation of stars and the growth of BHs was calibrated to match the observed $z = 0.1$ galaxy stellar mass function (GSMF), galaxy sizes, and the $M_{\text{BH}}-M_{\star}$ relation.

Radiative cooling and photo-heating of gas are implemented element-by-element for the 11 elements most important for these processes, computing their heating and cooling rates via Cloudy assuming a Haardt & Madau (2001) UV and X-ray background (Wiersma et al. 2009a).

Star formation is implemented by converting gas particles into star particles stochastically with a probability proportional to their pressure, such that the simulations reproduce by construction the empirical Kennicutt-Schmidt relation (Schaye & Dalla Vecchia 2008), renormalized for a Chabrier (2003, hereafter “Chabrier”) IMF. For a self-gravitating gaseous disk this star formation law is equivalent to the observed Kennicutt, Jr. (1998) surface density law. The density threshold for star formation increases with decreasing metallicity according to the model of Schaye (2004) to account for the metallicity dependence of the transition from the warm (i.e. $T \sim 10^4$ K) atomic to the cold ($T \ll 10^4$ K), molecular interstellar gas phase. Once stars are formed, their subsequent mass loss is computed assuming a Chabrier IMF and the metallicity-dependent stellar lifetimes of Portinari et al. (1997). Heavy element synthesis and mass-loss from stellar evolution are accounted for, including that due to winds from asymptotic giant branch stars and high-mass stars, as well as ejecta from core-collapse and type Ia supernovae (Wiersma et al. 2009b). Stellar feedback is implemented by stochastically injecting a fixed amount of thermal energy into some number of the surrounding gas particles (Dalla Vecchia & Schaye 2012), where the

probability of heating depends on the local density and metallicity (S15).

Supermassive black holes are seeded in haloes that reach a Friends of Friends (FoF) mass of $10^{10} M_{\odot}/h$ by injecting a subgrid seed BH of mass $10^5 M_{\odot}/h$ into the most bound gas particle (Springel et al. 2005). BHs grow at the minimum of the Eddington rate and the Bondi & Hoyle (1944) rate for spherically symmetric accretion, taking into account angular momentum of in-falling gas (Rosas-Guevara et al. 2015). BHs provide AGN feedback by building up an energy reservoir until they can heat at least one of their nearest neighbours by a minimum temperature, at which point they may stochastically heat their SPH neighbours (Booth & Schaye 2009). This procedure prevents gas from cooling too quickly after being heated, preventing over-cooling.

We classify DM haloes using a FoF algorithm with a linking length of 0.2 times the mean inter-particle spacing (Davis et al. 1985). Baryons are assigned to the halo (if any) of their nearest DM particle. Self-bound substructures within haloes, termed “subhaloes”, are then identified using the `SUBFIND` algorithm (Springel et al. 2001; Dolag et al. 2009). The “central” subhalo within a halo is defined as the one containing the gas particle most tightly bound to the group, while all others are classified as “satellites”. We only consider subhaloes containing at least 100 star particles as resolved “galaxies”. For consistency with S15, we define stellar mass, M_* , as the mass of stars within a spherical aperture of radius 30 proper kpc around each galaxy. To compare with observations, we measured all other quantities, such as stellar velocity dispersion (σ_e), M/L , metallicity (Z), and alpha enhancement ($[Mg/Fe]$), within a 2D circular aperture with the SDSS r -band projected half-light radius, r_e , of each galaxy, observed along the z -axis of the simulation.

In the next section we discuss how we can use the Reference EAGLE simulations to calibrate a prescription that varies the IMF to match the observed trend between MLE and σ .

3.2.2 IMF calibration

The first goal of this paper is to implement a variable IMF into the EAGLE simulations that yields the observed trends of IMF with galaxy properties. While it is debated how the IMF varies as a function of metallicity or alpha-abundances, there is mounting evidence that the MLE in the centres of massive elliptical galaxies increases with stellar velocity dispersion (e.g. Treu et al. 2010; La Barbera et al. 2013; Cappellari et al. 2013b; Spiniello et al. 2014; Li et al. 2017). This increase could be either due to a higher number of low-luminosity dwarf stars (“bottom-heavy” IMF) or stellar remnants (“top-heavy” IMF).

We follow Cappellari et al. (2013b, hereafter C13) and define the MLE relative to the (M/L) one would obtain assuming a Salpeter IMF:

$$\text{MLE}_i = \log_{10}(M/L_i) - \log_{10}(M/L_i)_{\text{Salp}}, \quad (3.1)$$

where i denotes the observational filter in which the luminosity is measured. In the upper panel of Fig. 3.1, in green we plot the observed relation between SDSS r -band MLE_r and stellar velocity dispersion, σ_e , both measured within r_e , obtained by C13

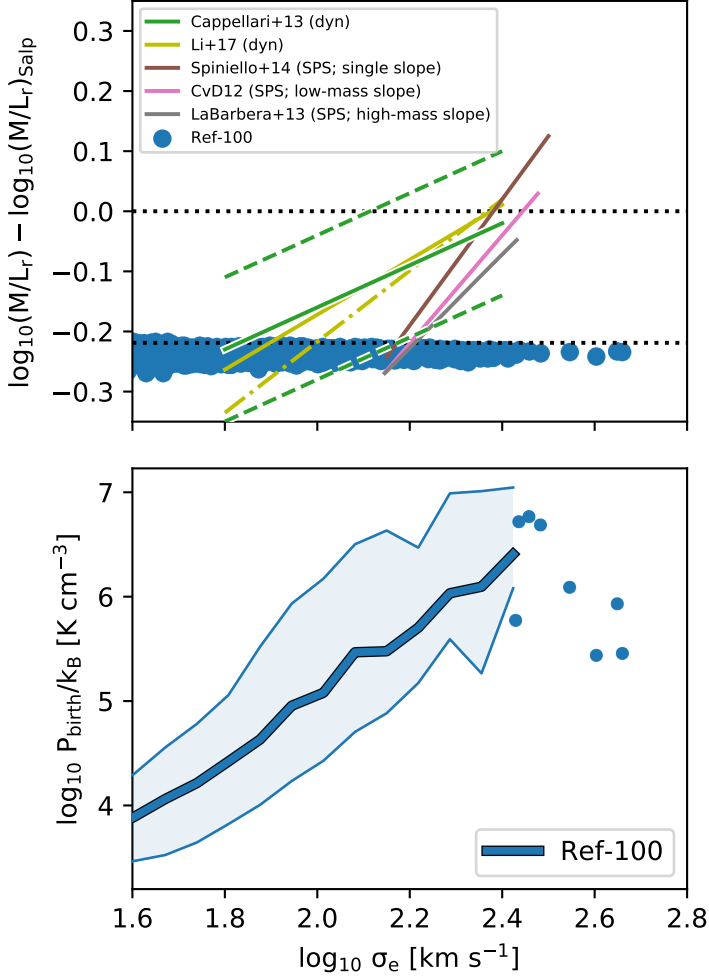


Figure 3.1: IMF-dependent properties of galaxies in the $(100 \text{ Mpc})^3$ EAGLE reference simulation (Ref-100) at $z = 0.1$. All quantities are measured within the half-light radius, r_e . Top panel: Stellar mass-to-light ratio excess (MLE) as a function of stellar velocity dispersion, σ_e . Horizontal dotted lines at $\text{MLE} = 0$ and -0.22 show the expected MLE for a Salpeter and Chabrier IMF, respectively. The observed trend from Cappellari et al. (2013b) is shown as a green solid line, with the intrinsic scatter shown as dashed lines. Also shown are the observed trends from Li et al. (2017) (yellow solid and dash-dotted for two different SPS models, respectively), Spiniello et al. (2014) (brown solid), Conroy & van Dokkum (2012b) (pink solid) and La Barbera et al. (2013) (grey solid). In brackets we indicate the method of IMF determination, either dynamical or spectroscopic, where for the latter case we also indicate the region of the IMF that is varied in the study. The reference model clearly does not reproduce the observed variation. Bottom panel: Stellar birth ISM pressure as a function of σ_e . The thick and thin lines show the median and 10-90th percentiles in σ_e bins. Where a bin has fewer than 10 galaxies, individual galaxies are shown. It is due to this correlation that we are able to vary the IMF for each individual star-forming gas particle as a function of its pressure in order to achieve a trend in integrated galactic IMF with σ_e , as observed.

for high-mass elliptical galaxies in the ATLAS^{3D} survey. Also included are observed trends from Conroy & van Dokkum (2012b), La Barbera et al. (2013), Spiniello et al. (2014), and Li et al. (2017). Note that for Li et al. (2017) we show the fits for elliptical and lenticular galaxies using two different SPS models to derive $(M/L)_{\text{Salp}}$. For comparison, we also show the same relation for galaxies in the (100 Mpc)³ reference EAGLE simulation (hereafter Ref-100). As expected, the EAGLE galaxies lie along a line of constant $\text{MLE}_r \approx -0.22$, corresponding to the asymptotic value reached by a stellar population with constant star formation rate and a Chabrier IMF, and are clearly inconsistent with the observational trends. The goal of this paper is to implement a prescription for an IMF variation that reproduces the observed C13 relation, and to investigate the effect it has on galaxy properties and observables.

In principle, in order to achieve this correlation, one could simply vary the IMF with the velocity dispersion of the galaxy in which it is born. However, this prescription lacks a physical basis, as there should not be any reason why a star born in a low-mass halo at high redshift should have direct “knowledge” of the stellar velocity dispersion of its host galaxy. Indeed, it would have to know the future velocity dispersion of its host galaxy at $z \approx 0$ at the time it was born, which is infeasible to simulate. A more physical approach is to vary the IMF with respect to some gas property local to a star-forming gas particle at the time it is formed. This affords us the ability to seek connections between physical conditions and $z = 0$ observables, and to perform controlled experiments whereby the various consequences of a variable IMF are selectively enabled/disabled. Moreover, it is a philosophical choice of the EAGLE project to only allow subgrid routines to be ‘driven’ by physically meaningful properties, such as gas density, metallicity, or temperature.

Many physical models of the formation of the IMF on the scales of giant molecular clouds (GMCs) predict the IMF to depend on the temperature, density, and/or pressure of the GMC from which the stars form (e.g. Bate & Bonnell 2005; Jappsen et al. 2005; Bate 2009; Krumholz 2011; Hopkins 2012; Hennebelle & Chabrier 2013). One could in principle simply apply these models to star-forming gas particles in the EAGLE simulation using their individual densities and temperatures (as is done in Guszejnov et al. 2017), but it is not clear that such an approach is appropriate here given the much coarser resolution of EAGLE compared to current GMC-scale IMF simulations. Indeed, EAGLE does not resolve the cold phase of the ISM. An alternate approach is to vary the IMF with some parameter of the star-forming gas that is found to vary with stellar velocity dispersion, and attempt to calibrate this local dependence to obtain the observed global IMF-velocity dispersion relationship. One enticing possibility is to vary the IMF with the pressure at which gas particles are converted to star particles in the simulation (Schaye et al. 2010; Haas et al. 2013). Although the cold interstellar gas phase, which EAGLE does not attempt to model, will have very different densities and temperatures than the gas in EAGLE, pressure equilibrium implies that its pressure may be much more similar. However, note that the pressure in the simulation is smoothed on scales of $\sim 10^2 - 10^3$ pc, corresponding to L_{Jeans} of the warm ISM. Note as well that since the local star formation rate (SFR) in EAGLE galaxies depends only on pressure, varying the IMF with pressure is equivalent to varying it with local SFR density.

In the lower panel of Fig. 3.1 we plot the mean r -band light-weighted ISM pressure

at which stellar particles within (2D projected) r_e were formed, as a function of σ_e for galaxies in Ref-100 at $z = 0.1$. We see a strong correlation, where stars in galaxies with larger σ_e formed at higher pressures. Thus, by invoking an IMF that varies with birth ISM pressure, we can potentially match the observed $\text{MLE}_r - \sigma_e$ correlation.

To calibrate the IMF pressure-dependence to match the C13 trend, we post-processed the Ref-100 simulation using the Flexible Stellar Population Synthesis (FSPS) software package (Conroy et al. 2009; Conroy & Gunn 2010). With FSPS, it is possible to generate tables of masses and luminosities in many common observational filters for simple stellar populations (SSPs) as a function of their age, metallicity, and IMF. Here we used the Basel spectral library (Lejeune et al. 1997, 1998; Westera et al. 2002) with Padova isochrones (Marigo & Girardi 2007; Marigo et al. 2008), but note that using the different available libraries would not affect our conclusions. Using FSPS in post-processing on Ref-100, star particles were reassigned masses and luminosities via interpolation of these tables, given their age, metallicity, initial mass, and birth ISM pressure. As a check, we verified that, for a Chabrier IMF, the SSP masses derived in post-processing using FSPS match the output masses of EAGLE stellar particles computed using the Wiersma et al. (2009b) models built into the simulation to within 2 per cent. However, the agreement between the models is not as good for IMFs with shallow high-mass slopes. Differences in how BH remnants from high-mass stars are treated between the two models result in small differences in mass for a Chabrier-like IMF, but when the high-mass IMF slope is shallow, BH masses begin to become important and these differences are amplified, resulting in ≈ 0.1 dex lower M_* from the Wiersma et al. (2009b) models than with FSPS for high-mass ($M_* > 10^{11} M_\odot$) galaxies with shallow high-mass IMF slopes (applicable to the HiM prescription, below). For consistency, we use stellar masses computed via FSPS for stellar M/L ratios as well as M_* throughout this paper. Note as well that we do not perform radiative transfer to estimate dust extinction. We do not expect dust to be very important here since we investigate mostly old, gas-poor galaxies and measure luminosities in the K or r -band, which are not as strongly affected by dust extinction as bluer wavelengths. However, we do neglect the luminosities of stellar particles with ages younger than 10 Myr, as such stars should still be embedded in their birth clouds, and thus are not expected to be observable (Charlot & Fall 2000).

We define the IMF piecewise as $dn/dM \propto M^x$, such that a Salpeter (1955) IMF has $x = -2.35$ for all M , and a Kroupa (2001, hereafter ‘‘Kroupa’’) IMF has a slope of $x = -1.3$ and -2.3 for stellar masses below and above $0.5 M_\odot$, respectively. Consistent with the EAGLE reference model, we integrate the IMF from 0.1 to $100 M_\odot$.

We began the calibration with a Kroupa IMF which is practically indistinguishable from the Chabrier IMF over this mass range, but is easier to work with due to its simpler double power-law shape. We tried different methods of varying the IMF, including varying the low-mass slope, high-mass slope, and the stellar mass at which the IMF transitions between these slopes. Varying only the transition mass to make the IMF more bottom-heavy in high-pressure environments (without changing the low-mass cut-off of $0.1 M_\odot$) did not yield a strong enough variation in the IMF to reproduce the

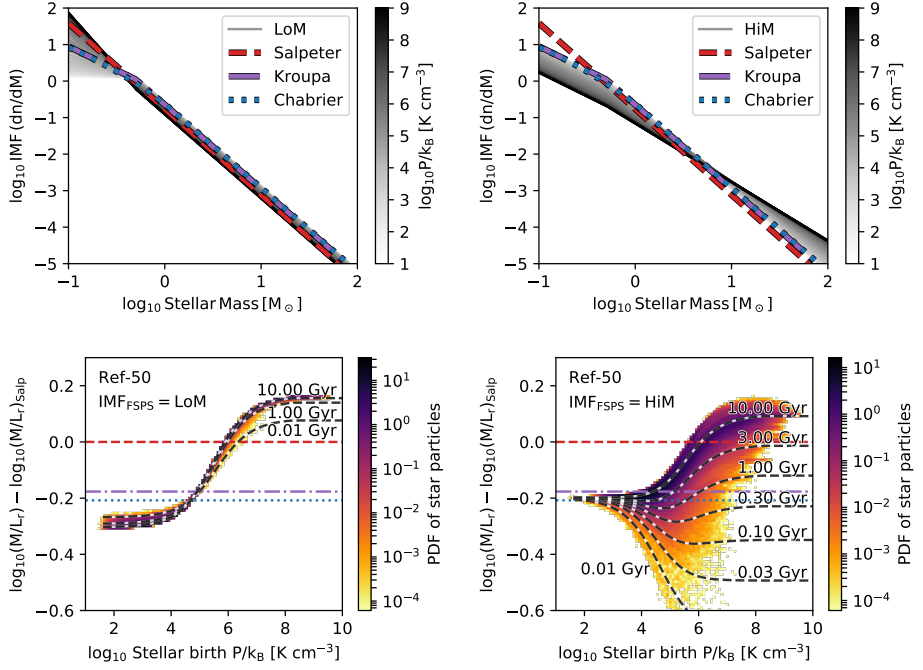


Figure 3.2: Top row: The two variable IMF prescriptions used in this study shown for a range in stellar birth ISM pressures (see greyscale bar). Top Left: Variable IMF in which the slope below $0.5 M_{\odot}$ is varied (hereafter called LoM) such that the IMF transitions from bottom-light at low P to bottom-heavy at high P . Top Right: As in top-left but instead varying the IMF slope *above* $0.5 M_{\odot}$ (hereafter HiM) such that it becomes top-heavy at high P . For all IMFs the integrated mass is normalized to $1 M_{\odot}$, causing the low-mass end of the HiM IMF to greatly decrease in normalization at high pressures. Bottom panels: 2D probability distribution functions of the r -band mass-to-light ratio excess (MLE_r) of individual star particles as a function of the pressure of the ISM out of which the star particles formed, for the Ref-50 simulation post-processed assuming LoM and HiM in the bottom-left and -right panels, respectively. Black dashed lines show the $\text{MLE}-P$ relation for SSPs at the indicated fixed ages. For reference, in all panels Salpeter, Kroupa, and Chabrier IMFs are shown in red dashed, purple dash-dotted, and blue dotted lines, respectively. Note the small scatter at fixed birth P for LoM, despite the wide range in the ages and metallicities of the stars. This shows that the MLE is a good proxy for the IMF when the high-mass slope is close to Salpeter. However, HiM yields a larger scatter in the MLE because in this case the MLE increases strongly with age at fixed P .

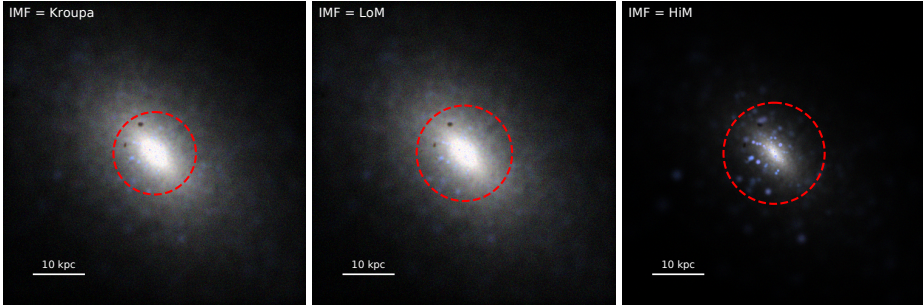


Figure 3.3: Images of a massive elliptical galaxy in the Ref-50 simulation, post-processed using SKIRT assuming 3 different variable IMF prescriptions. The images are 60 proper kpc per side and 60 proper kpc deep, centred on the galaxy. From left to right: Kroupa (universal), LoM, and HiM IMF prescriptions are implemented. The 2D projected r -band half-light radius is indicated in each panel as a dashed red circle. RGB colour channels correspond to SDSS g , r , and i peak wavelengths, respectively, normalized using the Lupton et al. (2004) scaling procedure. Assuming the LoM prescription, we produce a nearly identical image to that assuming a Chabrier IMF, while assuming the HiM prescription significantly reduces the luminosity of the diffuse stellar light due to a reduced fraction of low- and intermediate-mass stars, while increasing the fraction of very young stars.

observed trends. We briefly experimented with instead increasing the transition mass to make the IMF top-heavy in high-pressure environments (e.g. Fontanot et al. 2018b), and found similar results to our “HiM” prescription, outlined below.

We chose to vary the IMF with pressure according to two different prescriptions: one in which the low-mass slope is varied while the high-mass slope is kept fixed (hereafter referred to as LoM) and another where the high-mass slope is varied, keeping the low-mass slope fixed (HiM). These IMF prescriptions are depicted in the top row of Fig. 3.2. In both prescriptions, we vary the IMF slope between two fixed values x_{lowP} and x_{highP} that are asymptotically reached at low and high pressure, respectively, transitioning between them smoothly via a sigmoid function,

$$x = \frac{x_{\text{lowP}} - x_{\text{highP}}}{1 + \exp(2[\log_{10}(P/P_{\text{trans}})])} + x_{\text{highP}}. \quad (3.2)$$

Here P_{trans} defines the pressure (and thus the typical σ) at which the IMF transitions from light to heavy. We find that in both cases a value $\log_{10}(P_{\text{trans}}/k_B/[K \text{ cm}^{-3}]) = 5$ (corresponding to $\sigma_e \approx 80 \text{ km s}^{-1}$ works well for reproducing the C13 trend.

In the LoM case (top left panel of Fig. 3.2), the slope from 0.5 to 100 M_{\odot} is kept fixed at $x = -2.3$ (as for a Kroupa IMF) but the low-mass slope (0.1 to 0.5 M_{\odot}) is varied from $x_{\text{LoM,lowP}} = 0$ at low pressure to $x_{\text{LoM,highP}} = -3$ at high pressure. Note that this is by no means the only IMF variation prescription that reproduces the C13 trend, especially given the degeneracies between the slopes and the parameters of the sigmoid function, but we find that it is simple, intuitive, and works quite well at producing a clean trend between MLE_r and σ_e .

In the lower left panel of Fig. 3.2 we plot the resulting MLE_r as a function of birth ISM pressure for individual star particles in Ref-50, post-processed with the LoM IMF prescription. With this IMF, stars born with $P/k_B \lesssim 10^4 \text{ K cm}^{-3}$ are bottom-light, while

those with $P/k_B \gtrsim 10^6 \text{ K cm}^{-3}$ are bottom-heavy, with a smooth transition between these values. Such a prescription increases the fraction of dwarf stars in the stellar population at high pressure. This increases the mass and decreases the luminosity of ageing star particles, both leading to an increased MLE. Note the small amount of scatter at fixed birth P , despite the fact that stars of all ages and metallicities are plotted here. Thus, for low-mass slope variations, the MLE-parameter seems to be a good proxy for the IMF.

For our second variable IMF prescription, HiM (shown in the top right panel of Fig. 3.2), we instead keep the IMF slope below $0.5 M_\odot$ fixed at $x = -1.3$ (the Kroupa value), while making the slope above this mass shallower at high pressures, again varying according to the sigmoid function of Equation (3.2). Specifically, we have $x_{\text{HiM,lowP}} = -2.3$ and $x_{\text{HiM,highP}} = -1.6$, again with $\log_{10}(P_{\text{trans}}/k_B/[\text{K cm}^{-3}]) = 5$. Similar “top-heavy” forms of IMF variations have been proposed in the literature to explain the observed properties of strongly star-forming galaxies at both high and low redshifts (e.g. Baugh et al. 2005; Meurer et al. 2009; Haberman et al. 2010; Gunawardhana et al. 2011; Narayanan & Davé 2012, 2013; Zhang et al. 2018).

The lower right panel of Fig. 3.2 shows MLE_r as a function of birth ISM pressure for individual star particles in Ref-50, this time post-processed assuming the HiM variable IMF. This prescription allows us to increase the MLE at high pressure by adding more stellar remnants such as black holes and neutron stars, while at the same time reducing the total luminosity of old stellar populations. Note that here the mass of ageing star particles is overall lower due to the increased stellar mass loss associated with the increased fraction of high-mass stars, but the stronger decrease in luminosity results in a net increase in the M/L ratio. Here we see much larger scatter than for LoM due to the fact that the MLE_r for a given star particle is no longer independent of age. The age-independence of the MLE for LoM was solely due to the fact that the high-mass slope is approximately the same as the reference (Salpeter) IMF. In that case, ageing the population removes roughly an equal fraction of mass and luminosity from the LoM IMF as it does from an SSP with a Salpeter IMF. For stars with a shallower high-mass IMF slope, the MLE_r is initially small, owing to the high luminosity, but increases over time as the luminosity decreases faster with age than for a Salpeter IMF. The resulting global correlations between the MLE_r and birth ISM pressure for individual galaxies in self-consistent simulations that include these IMF variations are shown in Appendix 3.A.

These two IMF variation prescriptions were carefully calibrated by post-processing the Ref-100 simulation to reproduce the C13 trend between MLE_r and σ_e . Further details of this calibration procedure can be found in Appendix 3.A. In the next sections we will confirm that this trend is still reproduced when the variable IMF is implemented self-consistently into a full cosmological hydrodynamical simulation.

As an aside, we also experimented with making the IMF become “top-light”, meaning that the high-mass slope becomes steeper, rather than shallower, at high pressure. This prescription was inspired by observational studies that infer IMF variations spectroscopically using the MILES SPS models (Vazdekis et al. 2010, 2012), which allow users to vary only the high-mass slope of the IMF, using the (perhaps

confusingly nicknamed) “bimodal” IMF of Vazdekis et al. (1996). Such studies find that the fraction of dwarf to giant stars increases with increasing σ in high-mass ETGs, which for this parameterization results in a steeper high-mass slope (or a top-light IMF) (e.g. La Barbera et al. 2013, 2015). While we were able to obtain a match to the C13 trend with this bimodal parameterization in post-processing of the reference EAGLE simulations, we opted to use the LoM prescription instead due to the fact that the latter already increases the fraction of dwarf stars with less of an effect on feedback or metal production, making it more likely that the variable IMF model would match the galaxy observables used to originally calibrate the EAGLE reference model. Indeed, it has been shown by Martín-Navarro (2016) that the bimodal IMF prescription can have significant effects on the [Mg/Fe] abundances in massive ETGs. Confirmation of the validity of such a top-light IMF prescription would require a fully self-consistent simulation, which we have not performed for this prescription. It would be interesting for future work to test how well these SPS models can fit IMF-sensitive absorption features using a “LoM” IMF variation parameterization instead.

We also attempted to implement the local metallicity-dependent IMF prescription from Martín-Navarro et al. (2015c), where the high-mass slope of this bimodal IMF is shallower (steeper) than a Kroupa IMF at low (high) metallicities. This prescription was recently used by Clauwens et al. (2016) to reinterpret observational galaxy surveys and was implemented into hydrodynamical simulations of MW-analogues by Gutcke & Springel (2017). In post-processing of Ref-100, we found no clear trend between the MLE and σ_e when implementing this IMF variation prescription. We suspect that this may be partially due to the relatively flat mass-metallicity relation in high-mass galaxies in intermediate-resolution EAGLE (S15).

To provide an idea of the effect of these variable IMF prescriptions on the light output of galaxies, we generate images of galaxies using a modified version of the SKIRT radiative transfer code (Camps & Baes 2015). These modifications allow the user to generate images using SED templates from FSPS, for different variable IMF prescriptions. This new functionality in SKIRT is publicly available in a very general form at <http://www.skirt.ugent.be/>. In particular, it allows the user to specify for each star particle either the low-mass or high-mass slope of the IMF while keeping the other end fixed at the Kroupa value. In this way, one may vary the IMF according to many desired prescriptions, not only those presented in this paper.

We show in Fig. 3.3 RGB images of the SDSS gri central wavelengths of a massive elliptical galaxy from Ref-50, assuming a Kroupa (left panel), LoM (middle) and HiM (right) IMF. For a Kroupa IMF we see clumps of blue, young star particles embedded in a white, diffuse, intragalactic stellar background. For LoM, the image looks almost identical to the Kroupa image since this IMF mostly adds very dim, low-mass stars to the stellar population, which do not strongly affect the light. On the other hand, in the HiM case the diffuse starlight is much dimmer than the young stars. This is to be expected because for the HiM IMF, older populations should be overall dimmer because a much higher proportion of their mass is invested into the high-mass stars that have since died off. Note, however, that since a top-heavy IMF produces in general more metals per stellar mass formed, the impact of dust on the HiM image is likely

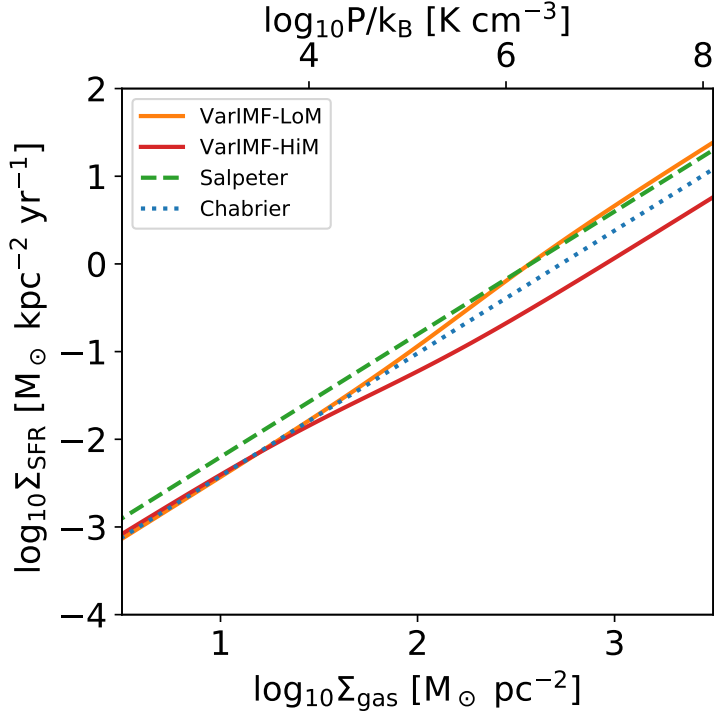


Figure 3.4: Star-formation law recalibration applied to gas particles in our simulations with a variable IMF. For reference, the laws calibrated for a Chabrier (used in Ref-50) and Salpeter IMF are shown in blue-dotted and green-dashed lines, respectively. The recalibrations that are used in our simulations with LoM and HiM are shown as orange and red solid lines, respectively. The pressure corresponding to the gas surface densities on the lower axis is shown along the top axis. To remain consistent with the observed KS law, at high pressure, SFRs are increased (decreased) by ≈ 0.3 dex relative to the reference simulations for simulations using the LoM (HiM) variable IMF prescription.

underestimated.

3.2.3 Preparations for self-consistent simulations with a variable IMF

The best way to test the full effect of a variable IMF on simulated galaxies is to run a new simulation that explicitly includes this IMF. This is because, for example, the IMF affects the metals released into the ISM by stars, which then affect cooling rates, which further affect future star formation, and so on. Additionally, the IMF affects the available energy from supernovae to provide feedback and regulate star formation. Such effects cannot be accounted for in post-processing. In this section we describe modifications to the EAGLE code that were implemented to maintain self-consistency when adopting a variable IMF.

In EAGLE, the star formation law reproduces the empirical Kennicutt-Schmidt (KS) law (Kennicutt, Jr. 1998). This relation was originally derived by converting $H\alpha$ fluxes to SFRs assuming a Salpeter IMF. In the reference EAGLE model, S15 accounted for the lower (M/L) obtained from the assumed Chabrier IMF by dividing the normalization of the KS law by a factor 1.65. This factor is the asymptotic ratio between the number of ionizing photons per solar mass formed after 100 Myr of evolution with a constant SFR as predicted by the Bruzual & Charlot (2003) model for a Chabrier and a Salpeter IMF. Because our IMF is not fixed, but varies with pressure, if we wish to maintain the same relationship between $H\alpha$ surface brightness and Σ_{gas} , we need to instead divide by a factor that is not constant but varies with pressure.

We recalibrate the star formation law by using the FSPS software to compute, for a given pressure, the ratio of the luminosity in the GALEX FUV-band for a stellar population with a constant star formation rate, between the variable IMF and a population with a Salpeter IMF, i.e.,

$$f_{\text{KS,mod}}(P) = \frac{L_{\text{FUV}}(\text{VarIMF}(P))}{L_{\text{FUV}}(\text{Salpeter})}. \quad (3.3)$$

In Fig. 3.4 we plot the recalibrated star formation law as orange and red solid lines for LoM and HiM, respectively, and compare them to the original (Salpeter-derived) relation and EAGLE’s Chabrier IMF-corrected version. We used Equation 8 of Schaye & Dalla Vecchia (2008) to convert gas pressure to gas surface density, assuming a gas mass fraction of unity and ratio of specific heats of 5/3. In the low- P regime, the normalization remains close to the reference EAGLE value, but at high pressures we multiply (divide) the normalization relative to reference EAGLE by a factor of ≈ 2 for LoM (HiM). Note that for a Chabrier IMF, by the above method we obtain $f_{\text{KS,mod}}(P) \simeq 1.57$, not far from the factor 1.65 assumed in EAGLE. The difference here comes from the differences in the FSPS and BC03 models, and has no noticeable effect on our results.

We also make self-consistent the mass evolution of the stellar populations as well as the heavy element synthesis and mass ejected into the ISM from stellar winds and supernovae. This modification is straightforward since these processes already include an integration over the IMF in the EAGLE code.

Another consideration is that the IMF has a direct impact on the number of massive stars and thus the amount of stellar feedback energy that is returned to the ISM per unit stellar mass formed. We also make this self-consistent, which effectively results in a factor ≈ 2 less (more) feedback energy produced per stellar mass formed at high pressures for LoM (HiM). In the reference model, such a large change in the feedback efficiency can have significant effects on many galaxy properties (C15). However, in the case of our variable IMF simulations, the modified star formation law counteracts this effect, making the time-averaged feedback energy consistent with the reference model at fixed gas surface density. We refer the reader to Appendix 3.B for further details regarding the individual impact of each of these effects on galaxy properties. As we will show in Section 3.3.2, performing variable-IMF simulations with these modifications yields excellent agreement with the observational diagnostics that were originally used to calibrate the subgrid feedback physics in the reference EAGLE model.

The SNIa rate per star particle in EAGLE depends only on the particle’s initial mass and an empirical delay time distribution function, calibrated to match the observed (IMF-independent) evolution of the SNIa rate density (S15). Because of the strong dependency of alpha-enhancement on SNIa rates, having these rates match observations directly is important. While an IMF-dependent SNIa rate model would be ideal from a theoretical point of view, it is precluded by the large uncertainties in parameters that would factor into such a model, such as white dwarf binary fractions, binary separations, and merger rates. While the SNIa rates therefore do not depend directly on the IMF, they do depend on the star formation history of the simulation which can be affected by the IMF. We will show in Section 3.3.2.2 that the SNIa rates are not strongly affected in our variable IMF simulations.

In the next section we will present our simulations and discuss the resulting trend between the galaxy-averaged IMF and central stellar velocity dispersion. We discuss the impact of these variable IMF prescriptions on galaxy properties such as metal abundances and SFR in Section 3.4.

3.3 Self-consistent simulations with a variable IMF

We ran two new (50 Mpc)³ simulations with the same physics and resolution as the reference EAGLE model, except that we imposed two different IMF variation prescriptions. The IMF becomes either bottom-heavy (LoM) or top-heavy (HiM) when the pressure of the ISM out of which star particles are born is high. In Section 3.2.2 we described how in post-processing we calibrated the pressure dependencies to match the observed trend of excess M/L -ratio with stellar velocity dispersion of Cappellari et al. (2013b). Including the IMF variation prescriptions explicitly in these simulations allows the IMF variations to affect self-consistently the mass evolution, metal yields, and the stellar energetic feedback during the simulations. The simulations also include a recalibrated KS law normalization to account for the change in UV luminosity per stellar mass formed due to the variable IMF prescriptions (see Section 3.2.3 for details). Throughout we will refer to these simulations with bottom-heavy and top-heavy IMF prescriptions as LoM-50 and HiM-50, respectively, and the reference (50 Mpc)³ box (with a universal Chabrier IMF) as Ref-50. In Section 3.3.1 we present the resulting trends between the IMF, MLE_r and σ_e in high-mass galaxies, while in Section 3.3.2 we show that both simulations agree well with the observational diagnostics used to calibrate the subgrid physics in the reference EAGLE model. Unless otherwise specified, all quantities are measured within a 2D aperture of radius r_e , the projected half-light radius in the r -band. This choice is motivated by the fact that many IMF studies (e.g. Cappellari et al. 2013b) measure the IMF within such an aperture.

3.3.1 IMF vs stellar velocity dispersion

The trend between the IMF and central stellar velocity dispersion, σ_e , is the most prevalent correlation between the IMF and galaxy properties in the observational literature. In Fig. 3.5 we plot r -band light-weighted diagnostics related to the IMF as

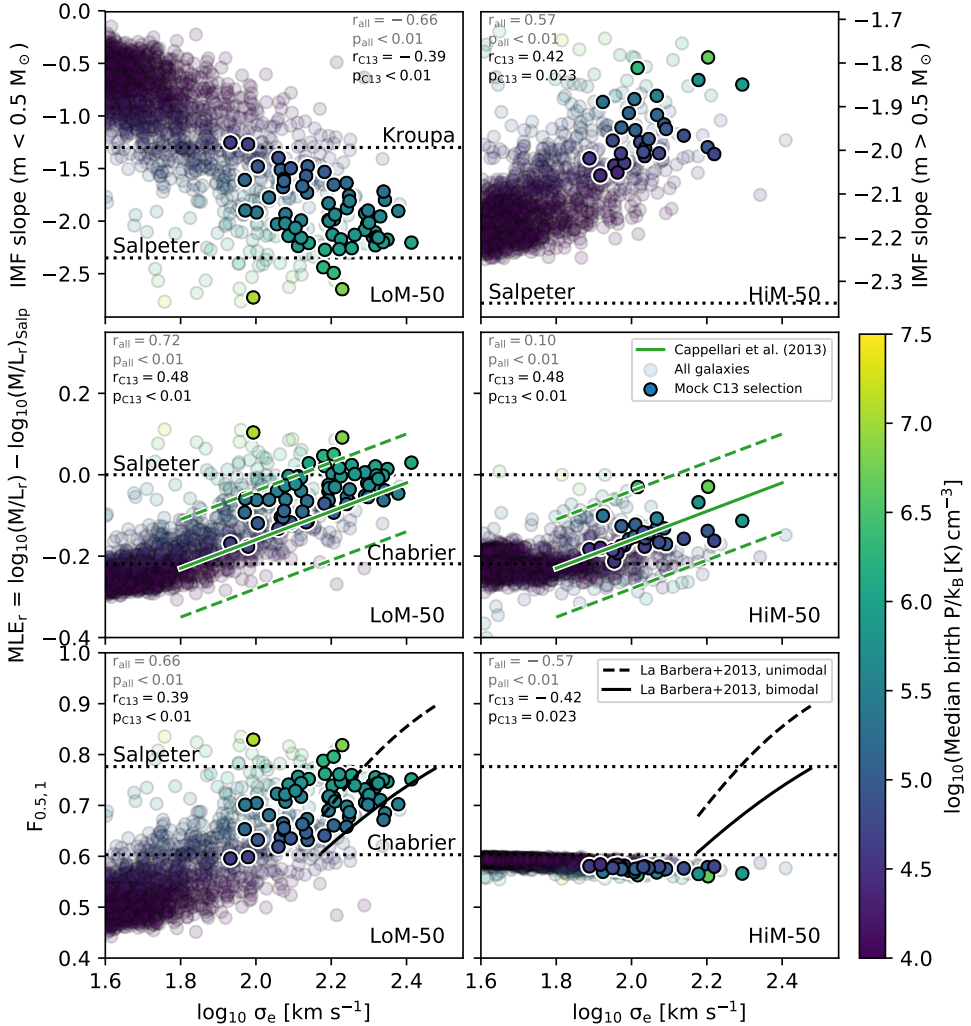


Figure 3.5: IMF diagnostics as a function of light-weighted stellar velocity dispersion, σ_e , all measured within the 2D, projected, r -band half-light radius, r_e , for all galaxies with $\sigma_e > 10^{1.6} \text{ km s}^{-1}$ in our LoM-50 (left column) and HiM-50 (right column) simulations at $z = 0.1$. Upper row: low-mass ($m < 0.5 M_\odot$) and high-mass ($m > 0.5 M_\odot$) r -band light weighted mean IMF slope for LoM-50 and HiM-50, respectively. Middle row: (M/L_r) -excess with respect to a Salpeter IMF. Lower row: Mass fraction of stars in the IMF with $m < 0.5 M_\odot$ relative to that for stars with $m < 1 M_\odot$, $F_{0.5,1}$ (Equation 3.4). Expected values for fixed IMFs are indicated as dotted horizontal lines. To facilitate comparison with Cappellari et al. (2013b, C13), we make a “mock C13” selection of early-type galaxies with $M_K < -21.5$ mag and intrinsic $u^* - r^* > 2$ (C13 cut; see text for details), indicated with opaque filled circles coloured by the light-weighted mean birth ISM pressure; points for galaxies outside this sample are translucent. The observed $\text{MLE}-\sigma_e$ trend from C13 is shown as a green solid line, with the intrinsic scatter shown as dashed lines. Dwarf-to-giant mass fractions derived from the correlations between IMF slope and σ by La Barbera et al. (2013) are shown as black-solid and -dashed lines for bimodal and unimodal IMF parameterizations, respectively. The Pearson correlation coefficient, r , and its p -value are indicated in each panel for the full sample with $\sigma > 10^{1.6} \text{ km s}^{-1}$ and the C13 cut in grey and black, respectively.

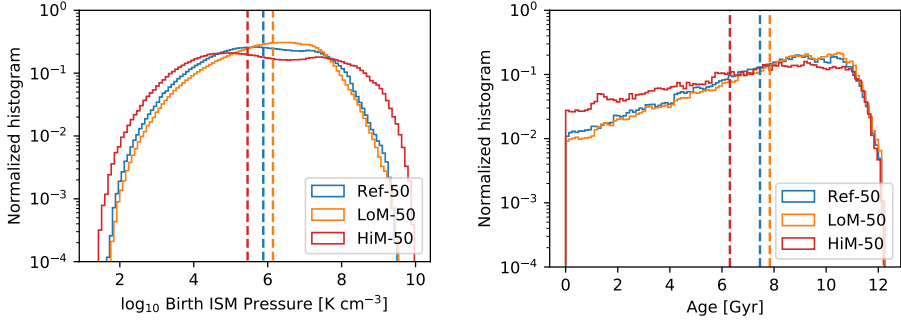


Figure 3.6: Properties of stars within the half-light radii of galaxies with $\sigma_e > 100 \text{ km s}^{-1}$ in our LoM-50 (orange) and HiM-50 (red) simulations compared with Ref-50 (blue). The left and right panels show birth ISM pressures and stellar ages, respectively. Vertical dashed lines denote medians. While LoM-50 matches Ref-50 reasonably well, HiM-50 produces stars with lower median birth ISM pressures and younger ages.

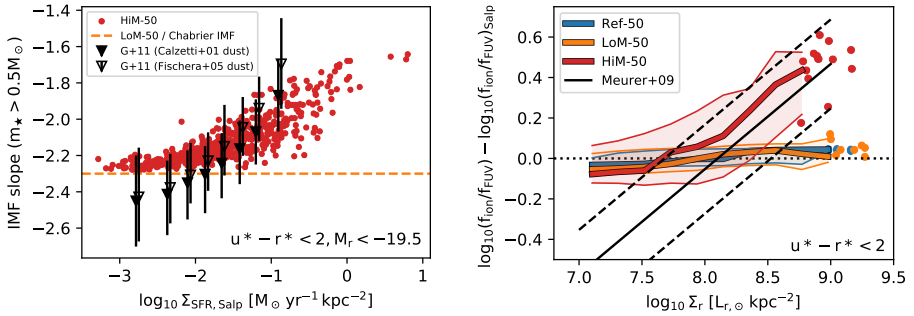


Figure 3.7: **Upper panel:** FUV-weighted high-mass ($m > 0.5 M_\odot$) IMF slope as a function of the Salpeter-reinterpreted star formation rate surface density, $\Sigma_{\text{SFR, Salp}}$, of star-forming (intrinsic $u^* - r^* < 2$) galaxies at $z = 0.1$. To compare with Gunawardhana et al. (2011), we only include galaxies also with $M_r < -19.5$. The horizontal orange dashed line shows the high-mass slope for all galaxies in LoM-50, corresponding to the Kroupa/Chabrier value. Open and filled triangles show results from the GAMA survey by Gunawardhana et al. (2011) assuming Calzetti (2001)/Cardelli et al. (1989) and Fischera & Dopita (2005) dust corrections, respectively. **Lower panel:** Ratio of flux in ionizing photons to that in the GALEX FUV band, normalized to the value expected for a Salpeter IMF, as a function of r -band luminosity surface density for star-forming galaxies in Ref-50 (blue), LoM-50 (orange), and HiM-50 (red). Solid thick lines indicate medians, while filled regions denote 10-90th percentiles. The black solid line shows results from Meurer et al. (2009) for the flux in H α relative to FUV, normalized to the expected Salpeter value, for star-forming galaxies. Dashed black lines indicate rms residuals. The positive trends seen in observations are qualitatively reproduced for HiM-50 star-forming galaxies, while an IMF prescription that varies only the low-mass slope of the IMF by construction does not.

a function of σ_e for galaxies in the LoM-50 (left column) and HiM-50 (right column) simulations. As translucent coloured circles we show all galaxies with $\sigma_e > 10^{1.6}$ (≈ 40) km s^{-1} , coloured by the light-weighted mean pressure at which the stars within each galaxy's r_e were formed.

The upper row shows the r -band light-weighted mean IMF slope for individual galaxies, where in the upper-left and -right panels we plot the low-mass ($m < 0.5 M_\odot$) and high-mass ($m > 0.5 M_\odot$) slopes, respectively. As expected, for LoM-50 the IMF slope transitions from shallower than Kroupa to a steeper Salpeter-like slope with increasing σ_e , while for HiM-50, the high-mass slope becomes shallower than Salpeter with increasing σ_e , reaching values up to ≈ -1.8 , comparable to the shallowest slopes inferred in local highly star-forming galaxies (Gunawardhana et al. 2011).

In the middle row we plot the resulting relation between MLE_r and σ_e for our variable IMF simulations. For both simulations, galaxies with $\sigma_e < 10^{1.8}$ (≈ 60) km s^{-1} lie close to the Chabrier MLE_r value of -0.22 , with MLE_r increasing for higher-mass galaxies. To compare with C13, we select galaxies in a similar way to that study. The C13 sample consists of 260 early-type elliptical and lenticular galaxies selected morphologically based on whether they contain dust lanes or spiral arms, and is complete down to an absolute magnitude of $M_K = -21.5$ mag. We mimic their selection by first taking only galaxies with $M_K < -21.5$ mag (without any dust correction). This cut roughly corresponds to a stellar mass $\gtrsim 10^{10.5} M_\odot$ for all models (although the exact correspondence depends on the IMF assumed). Then, to select only early-type galaxies, we make a cut in intrinsic $u^* - r^* > 2.0$, which roughly separates the blue cloud from the red sequence in EAGLE (Correa et al. 2017) and is similar to removing galaxies with specific star formation rate (sSFR) $\gtrsim 10^{-1.8}$ and $10^{-1.7} \text{ Gyr}^{-1}$ for LoM-50 and HiM-50, respectively. C13 additionally remove galaxies with very young stellar populations by excluding those with an $\text{H}\beta$ stellar absorption line with equivalent width greater than 2.3 \AA . McDermid et al. (2015) show that this cut corresponds roughly to an SSP age of 3.1 Gyr, which is already younger than any of our galaxies with $u^* - r^* > 2.0$. We refer to this selection as the ‘‘mock C13’’ sample.

The mock C13 galaxies are highlighted as the opaque coloured circles in Fig. 3.5. When selecting galaxies in this manner, both simulations produce galaxies reasonably consistent with the C13 $\text{MLE}_r - \sigma_e$ trend, with the majority of galaxies lying within the intrinsic scatter.

For LoM-50, a least absolute deviation (LAD) fit to the $\text{MLE}_r - \sigma_e$ relation for these mock C13 galaxies yields a slope of 0.23 ± 0.07 , which agrees with the slope of 0.35 ± 0.06 reported by C13. However, our galaxies are offset by ≈ 0.05 dex above the C13 trend. This small discrepancy is partly due to the fact that the LoM prescription was initially calibrated using stars within an aperture larger than r_e , which we show in Appendix 3.A can make a significant difference to the normalization of the $\text{MLE}_r - \sigma_e$ relation. Indeed, with a slightly larger choice of aperture, one can decrease the normalization of the LoM-50 $\text{MLE}_r - \sigma_e$ trend to match or even lie below the C13 trend. We caution that care with regards to aperture choices should be taken when comparing variable IMF claims between observational studies. Aperture choices vary between observational IMF studies (e.g. McDermid et al. 2014 and Conroy & van

Dokkum 2012b measure M/L within r_e and $r_e/8$, respectively) and even within them (McDermid et al. 2014 measure other properties like age and metallicity within $r_e/8$). Consistent apertures are crucial for making fair comparisons between such studies.

This positive offset is further increased (slightly) due to the fact that stars in LoM-50 tend to form from gas at slightly higher pressures than in Ref-50, which was used for the IMF calibrations. This can be seen in Fig. 3.6, where we show the distribution of gas birth ISM pressures and ages for stars within r_e of galaxies with $\sigma_e > 100 \text{ km s}^{-1}$ for the two variable IMF simulations and Ref-50. This result is likely due to the weaker stellar feedback resulting from the more bottom-heavy IMF.

For HiM-50, while nearly all of the mock C13 galaxies lie within one standard deviation of the C13 $\text{MLE}_r - \sigma_e$ relation, an LAD fit is slightly shallower for the simulation, with a slope of 0.16 ± 0.09 (compared to the C13 slope of 0.35 ± 0.06). This shallower trend is the result of several factors. Firstly, we are no longer sampling as many galaxies at high- σ_e ; Ref-50 had poor sampling to begin with for $\sigma_e > 10^{2.3} \text{ km s}^{-1}$ due to the limited simulation volume, which is now compounded by the fact that galaxies at fixed M_{DM} tend to have lower σ_e in HiM-50 than in Ref-50 due to the more efficient feedback.

A second factor is the impact that the stronger stellar feedback from HiM has on the times and gas pressures at which stars form in the simulation. In Fig. 3.6, we see that for HiM-50, stars in the centres of $\sigma_e > 100 \text{ km s}^{-1}$ galaxies typically form at lower pressures and later times than they did in Ref-50. This behaviour is due to the stronger stellar feedback delaying star formation to later times (and thus lower pressures). Consequently, galaxies in the simulation obtained IMFs with steeper high-mass slopes than expected, as well as less time to evolve, both of which lower the MLE relative to the post-processing analysis of Ref-50 (although this is not a strong effect for mock C13 galaxies; see Appendix 3.A).

Despite the trend between MLE_r and σ_e being less clear for HiM-50 than LoM-50, the high- σ_e galaxies in HiM-50 are certainly not inconsistent with the C13 trend, and thus represent a conservative approach to studying top-heavy IMF variations in high-mass galaxies. Indeed, we will show in Paper II that this HiM IMF prescription causes the MLE to vary much more strongly with age than with σ_e .

We note that while the $\text{MLE}_r - \sigma_e$ trends for both simulations are consistent with dynamical IMF measurements, HiM-50 may not be consistent with spectroscopic IMF studies that are sensitive to the present-day fraction of dwarf to giant stars, which tend to find an increasing dwarf-to-giant ratio with increasing σ_e (e.g. La Barbera et al. 2013). To show this explicitly, following Clauwens et al. (2016), we compute for each galaxy the fraction of the mass in stars with $m < 0.5 M_\odot$ relative to the mass of stars with $m < 1 M_\odot$ given its IMF. Specifically, we compute

$$F_{0.5,1} = \frac{\int_{0.1}^{0.5} M \Phi(M) dM}{\int_{0.1}^1 M \Phi(M) dM}. \quad (3.4)$$

where $\Phi(M)$ is the IMF. This upper limit of $m < 1 M_\odot$ in the denominator roughly corresponds to the highest stellar mass expected in the old stellar populations of ETGs.

These results are plotted in the lower row of Fig. 3.5, where, while $f_{0.5,1}$ increases strongly with σ_e for LoM-50 galaxies, it is relatively constant for HiM-50, remaining close to the value expected for a Chabrier IMF. This demonstrates that the increase in MLE_r for high- σ_e galaxies in HiM-50 is the result of excess mass in stellar remnants, rather than dwarf stars.

We compare with the results of La Barbera et al. (2013) by converting their IMF slopes for their 2SSP models with bimodal and unimodal IMF parameterizations to $F_{0.5,1}$. Note that we do not use their definition of $F_{0.5}$ which integrates the denominator in Equation (3.4) to $100 M_\odot$, since $F_{0.5}$ is sensitive to the choice of IMF parameterization at fixed (present-day) $F_{0.5,1}$, which we show explicitly in Appendix 3.C. In the LoM-50 case, $F_{0.5,1}$ agrees very well with the La Barbera et al. (2013) results of increasing mass fraction of dwarf stars in high- σ_e galaxies. HiM-50, as expected, does not agree.

On the other hand, recall that the HiM prescription was motivated by the fact that highly star-forming galaxies have recently been found to have top-heavy IMFs. For example, Gunawardhana et al. (2011) have found that for local, bright ($M_r < -19.5$) star-forming galaxies, those with larger H α -inferred star formation rate surface density are redder than expected given their SFR and a standard IMF, implying that the high-mass IMF slope may be shallower in such systems. In Fig. 3.7, we compare with the results of Gunawardhana et al. (2011) by plotting the Galex FUV-weighted high-mass slope of the IMF for star-forming (intrinsic $u^* - r^* < 2$) galaxies with $M_r < -19.5$ at $z = 0.1$ in HiM-50 as a function of the star formation rate surface density, defined as $\Sigma_{\text{SFR,Salp}} = \text{SFR}_{\text{Salp}} / (2\pi r_{e,\text{FUV}}^2)$, where SFR_{Salp} is the Salpeter-reinterpreted total star formation rate within a 3D aperture of radius 30 pkpc and $r_{e,\text{FUV}}$ is the half-light radius in the FUV band. The Salpeter reinterpretation is performed by multiplying the true SFR by the ratio of the FUV flux relative to that expected for a Salpeter IMF, similar to that done by Clauwens et al. (2016). The result from Gunawardhana et al. (2011) is shown for two assumptions for the dust corrections. The positive trend for HiM-50 is qualitatively consistent with the observations, albeit slightly shallower. For reference, we include as a horizontal line the high-mass slope in all LoM-50 (as well as Ref-50) galaxies, corresponding to the Kroupa/Chabrier high-mass value. LoM-50 is, as expected, inconsistent with the observations since the high-mass slope is not varied in that model.

Another example comes from Meurer et al. (2009), who conclude that the increasing ratio of H α to FUV flux toward higher-pressure environments implies that the high-mass slope of the IMF may be becoming shallower in such environments. To compare with their data, we compute the flux of ionizing radiation, f_{ion} , by integrating the spectra output by FSPS up to 912 Å (as in Clauwens et al. 2016) and dividing by the flux in the FUV band, f_{FUV} . Since the ionizing flux is not identical to the H α flux, we normalize by the value of the ratio expected for a Salpeter IMF. In the lower panel of Fig. 3.7, we plot this ratio for our star-forming galaxies in Ref-50, LoM-50, and HiM-50 as a function of r -band luminosity surface density, Σ_r . We compare with the corresponding relation from Meurer et al. (2009) shown as a solid black line. Ref-50 and LoM-50 show a constant ‘‘Salpeter’’-like $f_{\text{ion}}/f_{\text{FUV}}$ at all Σ_r .

For $\Sigma_r > 8L_{r,\odot} \text{ kpc}^{-2}$, HiM-50 galaxies increase in $f_{\text{ion}}/f_{\text{FUV}}$ with increasing Σ_r , in agreement with the observations. At lower Σ_r , the relation flattens to the Salpeter value since in HiM we do not vary the IMF high-mass slope to values steeper than Salpeter. This result implies that the IMF high-mass slope may need to become steeper than Salpeter at low pressures to conform with these observations. However, it is not clear that the MLE- σ_e correlation would then still match the observed C13 trend, as this would increase the MLE at low pressure (or low σ_e), weakening the otherwise positive MLE- σ_e correlation.

Since strongly star-forming galaxies are the progenitors of present-day high-mass ETGs, it is not clear how to reconcile the observed top-heavy IMF in strongly star-forming galaxies with the observed bottom-heavy IMF seen in present-day ETGs as constrained by the dwarf-to-giant ratio (lower row of Fig. 3.5). These variable IMF simulations will thus be extremely useful in testing these different, possibly conflicting, IMF variation scenarios with galaxy formation models.

3.3.2 Subgrid calibration diagnostics

The success of the EAGLE model stems in part from calibrating the subgrid feedback parameters to match key observables (the GSMF, sizes, and BH masses) that are difficult to predict from first principles in cosmological simulations. Thus, a first check to see if the variable IMF simulations are reasonable is to verify that they also reproduce these calibration diagnostics.

3.3.2.1 Observable diagnostics

Since physical quantities like the GSMF and galaxy half-mass radii can only be derived from observables once an IMF is assumed, we must compare the “observable” versions of the calibration diagnostics with the reference model and observations. The left column of Fig. 3.8 shows the galaxy K -band luminosity function, 2D projected r -band half-light radii for late-type galaxies, and BH masses as a function of luminosity for Ref-50 (blue), LoM-50 (orange) and HiM-50 (red).

We show the $z = 0.1$ K -band luminosity functions of our simulations in the top-left panel of Fig. 3.8, and compare them to observational data from the GAMA survey (Driver et al. 2012) down to $M_K - 5 \log_{10} h = -16$, corresponding to galaxies with ≈ 100 stellar particles, the resolution limit of the GSMF (S15). Both variable IMF runs agree well with Ref-50, with HiM-50 slightly under-predicting the luminosity function relative to Ref-50 by $\lesssim 0.1$ dex at all luminosities. This under-prediction is likely caused by the stronger stellar feedback in HiM-50.

In the reference model, the density-dependence of the stellar feedback strength was calibrated to broadly match the observed sizes of late-type galaxies. This calibration was necessary to prevent the formation of overly compact galaxies due to artificial thermal losses in high-density environments due to the limited resolution of the simulation. It is thus important to verify that our variable IMF simulations also reproduce the sizes of such galaxies. In the middle-left panel of Fig. 3.8, we plot the r -band 2D projected half-light radii as a function of M_r for all star-forming galaxies

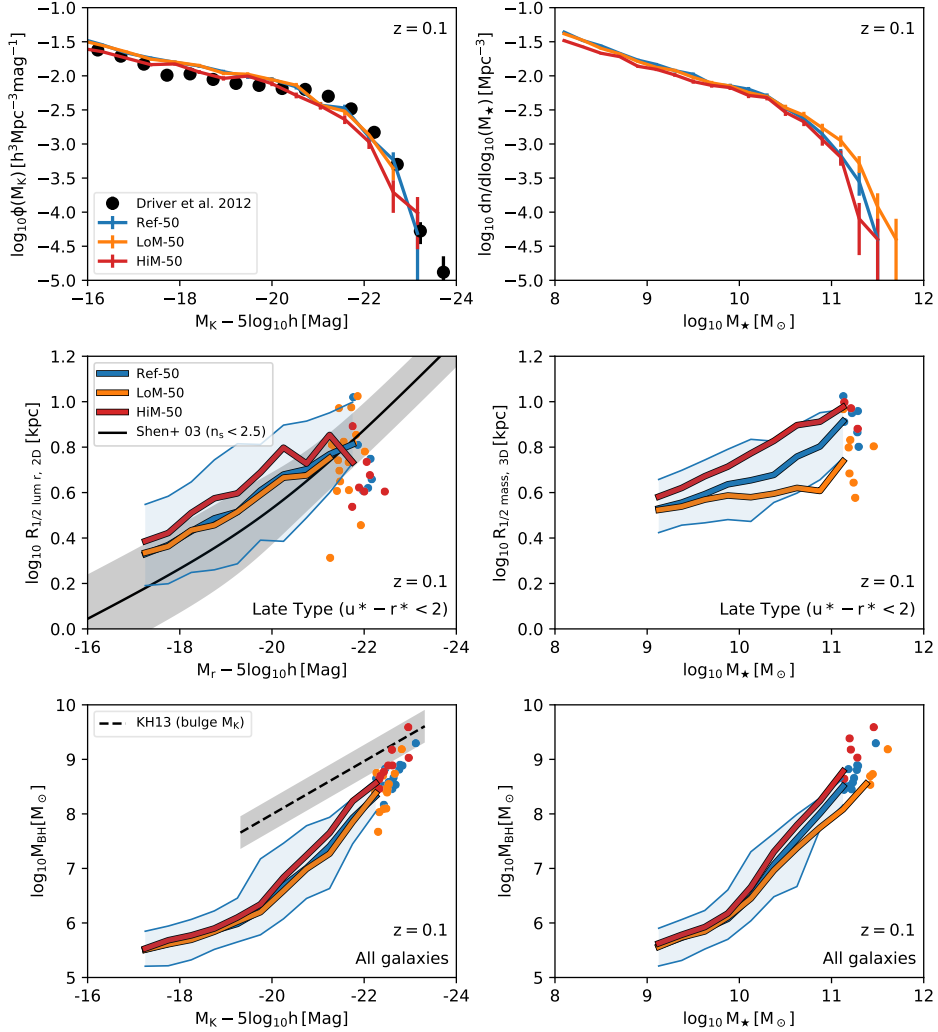


Figure 3.8: **Left column:** Subgrid calibration diagnostics for the LoM-50 (orange), HiM-50 (red) simulations, compared to the reference model (Ref-50; blue) and observations for galaxies at $z = 0.1$. To remain consistent with S15, masses and luminosities (sizes) are measured within a 30 kpc 3D (2D) aperture. Top-left panel: K-band galaxy luminosity (M_K) function. Observational data from the GAMA survey are shown as black points with 1σ error bars (Driver et al. 2012). Middle-left panel: Projected K-band stellar half-light radius as a function of M_K for star-forming galaxies (intrinsic $u^* - r^* < 2.0$) with more than 600 star particles. Filled regions show the 10 to 90th percentile range for Ref-50; the other curves have similar scatter. Individual points are shown for bins containing fewer than 10 galaxies. Sersic r -band half-light radii from SDSS are shown for galaxies with Sersic indices $n_s < 2.5$ as a black solid line (Shen et al. 2003, the grey shaded region indicates 1σ scatter). Lower-left panel: As in the middle-left panel but showing the black hole mass—galaxy M_K relation. For reference we show the observed relation with bulge luminosity (converted to AB magnitudes) from Kormendy & Ho (2013) as a dashed black line with intrinsic scatter indicated with the grey filled region. **Right column:** Physical quantities corresponding to the subgrid calibration diagnostics shown in the left column. Top-right panel: Galaxy stellar mass function. Middle-right and bottom-right panels: 3D half-mass radius and M_{BH} , respectively, as a function of M_* . Galaxies in LoM-50 with $M_* > 10^{10.5} M_\odot$ have higher masses at fixed number density and smaller physical sizes at fixed mass than in Ref-50 due to an excess (dark) mass of dwarf stars in the central regions. Both LoM-50 and HiM-50 produce galaxies with reasonably realistic luminosities, half-light radii, and BH masses.

at $z = 0.1$ with at least 600 bound stellar particles, corresponding to $M_* \approx 10^9 M_\odot$ or $M_r - 5 \log_{10} h < -17$. It was shown in S15 that galaxy sizes are converged down to this limit. To compare with observed sizes of late-type galaxies, we plot only star-forming galaxies defined as those with intrinsic (dust-free) $u^* - r^* < 2$. The variable IMF simulations match Ref-50 well, with HiM-50 producing larger galaxies by ≈ 0.1 dex, which is less than the typical discrepancies between observational studies of galaxy sizes (e.g. Shen et al. 2003; Baldry et al. 2012). These slightly larger sizes may be caused by the fact that galaxies in HiM-50 typically form at later times, from higher angular momentum gas, giving them larger sizes for the same amount of stellar mass formed. This effect is compounded by the fact that stars in the central regions of these galaxies typically formed at higher pressures than those in the outskirts, and thus with more top-heavy IMFs, yielding dimmer present-day stellar populations and boosting the half-light radii to larger values.

For reference, we include the observed relation between Petrosian r -band half-light radius and r -band absolute magnitude for SDSS galaxies with Sersic indices $n < 2.5$ (Shen et al. 2003). Such indices correspond to surface density profiles typical of discy, star-forming galaxies. Note that a fairer comparison would be to also select simulated galaxies with $n < 2.5$. However, Shen et al. (2003) showed that the size-luminosity relation is not significantly affected for different reasonable choices of morphological discriminator. Indeed, S15 found that such an $n < 2.5$ cut selects 94 per cent of EAGLE galaxies with more than 600 star particles. We have checked that selecting all galaxies instead of only those with $u^* - r^* < 2$ makes little difference to this plot, so we expect that an $n < 2.5$ cut for the simulated galaxies would not change our result. While LoM-50 and Ref-50 agree relatively well with the data, HiM-50 systematically over-predicts galaxy sizes relative to SDSS by ≈ 0.2 dex, which differs from the observations at the 1σ level. Despite this good agreement for late type galaxies, we will show in Section 3.4.4 that the same is not true for ETGs in HiM-50.

The efficiency of AGN feedback was calibrated to match the normalization of the observed $M_{\text{BH}} - M_*$ relation by Booth & Schaye (2009) as part of the OWLS project (Schaye et al. 2010). Since it also gave good results for the much higher-resolution EAGLE simulations, this efficiency was adopted for the reference model. The lower-left panel of Fig. 3.8 shows M_{BH} as a function of M_K . Note that we use the actual M_{BH} values from the simulation rather than attempting to reinterpret them observationally. Both of the variable IMF simulations agree with Ref-50 extremely well for $M_K > -20$, while for more luminous objects there are slight variations of up to ≈ 0.1 and 0.3 dex above the Ref-50 relation for LoM-50 and HiM-50, respectively. These variations are much smaller than the scatter in the observed $M_{\text{BH}} - M_*$ relation and are an acceptable match to Ref-50. Note that the BH masses agree much more poorly if the KS law is recalibrated but feedback is not made self-consistent (see discussion in Section 3.2.3 and Appendix 3.B).

The observed relation between M_{BH} and bulge K -band luminosity from Kormendy & Ho (2013) for classical bulges and elliptical galaxies is also shown in the lower left panel of Fig. 3.8. Since we plot total rather than bulge K -band luminosity, we expect our results to fall to the right of the observed relation, which is indeed the case. At the

brightest end, where most galaxies are elliptical, all of our simulations converge to the normalization of the observed relation.

We conclude that the luminosities, sizes, and BH masses of galaxies in the variable IMF simulations are reasonable, and match the Ref-50 run quite well. This is encouraging, since it means that we do not need to recalibrate the simulations to obtain an acceptable match to the observed luminosity function, galaxy sizes and BH masses, even when including self-consistent feedback.

3.3.2.2 Physical diagnostics

While the observable calibration diagnostics are consistent with Ref-50, the same is not necessarily true for the associated physical quantities. In the right-hand column of Fig. 3.8, we plot the physical quantities corresponding to the diagnostics in the left-hand column, namely: the GSMF, 3D half-mass radii, and M_{BH} as a function of M_* for galaxies in our variable IMF simulations and Ref-50. We cannot compare with observations here, as these typically assume a universal IMF when deriving physical quantities. While it is possible in principle to reinterpret these physical quantities assuming a Chabrier IMF, thus allowing a comparison with observations, we choose to show the true physical quantities here to highlight the importance of IMF assumptions in the translation between observables and true physical quantities.

The GSMF is shown in the top-right panel. At low masses ($\lesssim 10^{10} M_{\odot}$), the variable IMF runs and Ref-50 match very well, owing to the fact that since these galaxies tend to have lower stellar birth ISM pressures, they form stars with an IMF similar to the Chabrier IMF used in the reference model. At higher masses ($M_* \gtrsim 10^{11} M_{\odot}$), HiM-50 is consistent with Ref-50 but LoM-50 predicts larger masses at fixed number density by ≈ 0.12 dex. Since the luminosity function in LoM-50 traces Ref-50 nearly perfectly, this difference in their GSMFs is purely due to the increased stellar mass required to produce a fixed luminosity for a bottom-heavy IMF, due to an excess mass of (dim) dwarf stars. Thus, this difference represents the error one incurs when converting K-band luminosity to stellar mass assuming a Chabrier IMF for a galaxy with an intrinsically bottom-heavy IMF. These results are consistent with the recent work of Clauwens et al. (2016) and Bernardi et al. (2018a), who investigated the effect that bottom-heavy IMF variations in high-mass ETGs would have on the GSMF derived from SDSS galaxies.

Intrinsic sizes are also significantly affected by a variable IMF. In the middle-right panel of Fig. 3.8 we show the 3D half-mass radii of our galaxies as a function of M_* . As in the middle-left panel of Fig. 3.8, we show only late-type galaxies. At fixed M_* , galaxies in LoM-50 and HiM-50 are smaller and larger, respectively, than Ref-50 by ≈ 0.2 dex at the highest masses. For LoM-50, the smaller physical sizes are due to the excess mass in dwarf stars in the central regions, while high-mass galaxies in HiM-50 are larger due to a deficit of low- and intermediate-mass stars in these regions which is not quite balanced by the excess mass in stellar remnants, as well as the stronger stellar feedback that tends to yield larger galaxies (e.g. Sales et al. 2010; Crain et al. 2015).

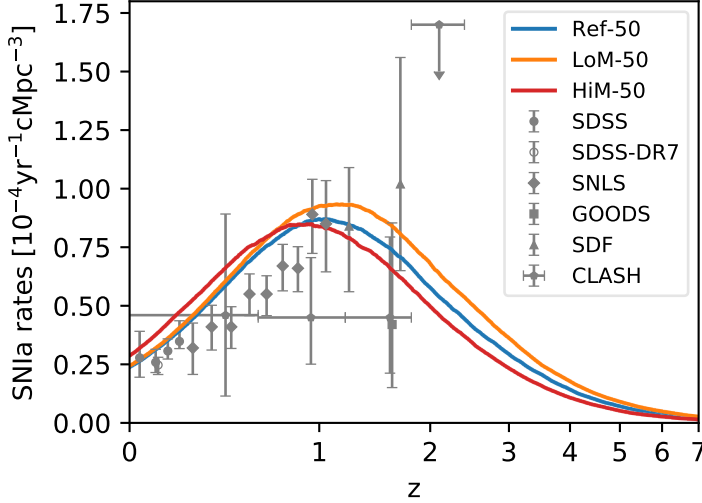


Figure 3.9: Cosmic supernova Ia rate density as a function of redshift in the LoM-50 (orange), HiM-50 (red) and Ref-50 (blue) simulations. Grey data points show observations compiled by and classified as the “most accurate and precise measurements” by Graur et al. (2014): SDSS Stripe 82 (Dilday et al. 2010), SDSS-DR7 (Graur & Maoz 2013), SNLS (Perrett et al. 2012), GOODS (Dahlen & al. 2008), SDF (Graur et al. 2014), and CLASH (Graur et al. 2014). The 1σ systematic and statistical uncertainties are indicated with error bars. The SNIa rates are not strongly affected in the variable IMF simulations and match observations about as well as the reference model.

The $M_{\text{BH}} - M_*$ relation is plotted in the bottom-right panel of Fig. 3.8. The relation for LoM-50 is shallower than for Ref-50 owing to the increased M_* of the most-massive galaxies. The discrepancy for HiM-50 is similar to that for the $M_{\text{BH}} - M_K$ relation, and is reasonably consistent with Ref-50.

As a check, we reinterpreted M_* and the half-mass radii of these galaxies assuming a Chabrier IMF by multiplying their K-band luminosities by the M/L ratio they would have had if they had evolved with a Chabrier IMF. We refer to this reinterpreted mass as $M_{*,\text{Chab}}$. Doing so puts the masses, sizes, and BH masses of the LoM-50 galaxies into excellent agreement with Ref-50 by decreasing the inferred masses of high-mass galaxies by a factor ≈ 2 , but has little effect for HiM-50 (not shown).

Finally, we investigate the SNIa rate evolution in the simulations. As mentioned in Section 3.2.3, the predicted rates do not explicitly depend on the IMF, but they are affected by the star formation history of the simulations. Fig. 3.9 compares the evolution of the SNIa rate density with observations compiled by Graur et al. (2014). The rates are not strongly affected in either variable IMF simulation, where the agreement with observations is about as good as it is for Ref-50. This is encouraging, since a strong deviation from the observed rates would require a recalibration of the empirical time-delay function. All differences here are due to the effect that the IMF has on the star formation history, which is slightly delayed in HiM-50 relative to Ref-50.

3.4 Effect of variable IMFs on galaxy properties

In this section we investigate the effect that our variable IMF prescriptions have on the predicted properties of galaxies in the $(50 \text{ Mpc})^3$ self-consistent variable IMF simulations relative to Ref-50 and observations. Specifically, Sections 3.4.1, 3.4.2, 3.4.3, and 3.4.4 discuss the effect on alpha enhancement, metal abundances, star formation rates, and ETG sizes, respectively. All results are shown for galaxies at $z = 0.1$; properties at higher redshift will be discussed in a future work.

3.4.1 Alpha enhancement

One of the strongest effects that the variable IMF has in the simulations is on the abundances of α -elements in high- σ_e galaxies. In the upper panel of Fig. 3.10 we show $[\text{Mg}/\text{Fe}]$ as a function of σ_e for early-type galaxies (defined as those with $u^* - r^* > 2.0$) in our variable IMF simulations.

Segers et al. (2016) have already shown that the trend of α -enhancement with stellar velocity dispersion in the reference simulations agrees well with observations of quiescent ETGs although the normalization of the relation is too low by about a factor of 2. We note that nucleosynthetic yields are uncertain at the factor of 2 level (e.g. Wiersma et al. 2009b), while uncertainties in stellar population modelling lead to systematic errors in the observed values of $[\alpha/\text{Fe}]$ of ~ 0.1 dex. Thus, the normalization of the trend is not nearly as constraining as the slope. Least absolute deviation fits to these galaxies above $\sigma_e > 10^{1.8} \text{ km s}^{-1}$ yield slopes of 0.33 ± 0.07 , 0.26 ± 0.04 , and 0.40 ± 0.12 for Ref-50, LoM-50, and HiM-50, respectively. While the slopes for Ref-50 and HiM-50 agree with the observed values of 0.33 ± 0.01 (Thomas et al. 2010) and 0.33 ± 0.03 (Conroy et al. 2014), that for LoM-50 is somewhat shallower.

We have investigated the cause of the difference in the normalization and slopes of these trends, and find that the culprit is the difference in the metal yields in the different simulations. In high-mass galaxies, LoM-50 produces fewer massive stars per unit stellar mass formed and thus less Mg is synthesized for future generations of stars, leading to reduced $[\text{Mg}/\text{Fe}]$. On the other hand, HiM-50 produces many more massive stars per unit stellar mass formed, increasing the Mg yields. By independently switching on the different effects of the variable IMF in smaller $(25 \text{ Mpc})^3$ boxes, we confirmed that indeed the yields, rather than the feedback or the KS law re-normalization, drive these differences. While the differences in the normalization are not large, it is concerning that the $[\text{Mg}/\text{Fe}]$ values in LoM-50 fall so far below those from observations, especially since, following Portinari et al. (1997), the Mg yields have already been doubled in the reference model with respect to the standard yields.

It is interesting that our IMF variations have such little effect on the slope of the $[\text{Mg}/\text{Fe}] - \sigma_e$ relation. Recent studies of IMF variations in SAMs have concluded that a top-heavy IMF in rapidly star-forming environments (which occurs in the high-redshift progenitors of present-day high-mass ETGs) may be necessary to produce a positive correlation in this relation, a result of higher Mg abundances due to a larger number

of SNII (Gargiulo et al. 2015). In the EAGLE model, a variable IMF is not necessary to reproduce this slope, as the positive trend comes from the quenching of star formation via AGN feedback, preventing much of the Fe from type Ia SNe from being incorporated into future stellar populations (Segers et al. 2016). It is thus encouraging that the slope does not become even steeper with a top-heavy IMF in EAGLE. Although the difference in Mg abundance between HiM-50 and Ref-50 increases with σ_e , the same is true for the Fe abundances, maintaining the slope of the $[\text{Mg}/\text{Fe}] - \sigma_e$ relation.

To help support this quenching scenario, in the lower panel of Fig. 3.10 we plot the median formation time, $t_{1/2}$, of stars within the 2d projected half-light radius, r_e , of the same early-type galaxies shown in the upper panel. Here we see a trend of decreasing $t_{1/2}$ with increasing σ_e for all three simulations, in qualitative agreement with recent results from the ATLAS^{3D} survey (McDermid et al. 2015). These results support the idea that short star formation histories leads to higher $[\text{Mg}/\text{Fe}]$ ratios in early-type galaxies.

This quenching scenario is also supported by semi-analytic modelling performed by De Lucia et al. (2017), although they find that abrupt quenching of high-mass galaxies prevents them from reaching high enough metallicities at $z = 0$, requiring a variable IMF to match both the mass-metallicity relation and the alpha-enhancement of high-mass galaxies simultaneously (see also Arrigoni et al. 2010). We will show in the next section that our HiM-50 simulation does indeed match the slope of the observed mass-metallicity relation better than the reference model.

3.4.2 Metallicities

We also investigate the effect of the variable IMFs on the stellar mass-metallicity relation where, in the top panel of Fig. 3.11, we plot the stellar metallicity, Z , measured within r_e , as a function of Chabrier-reinterpreted stellar mass, $M_{*,\text{Chab}}$, for all galaxies with $M_{*,\text{Chab}} > 10^8 M_\odot$. Interestingly, the total metallicities are largely unchanged in the LoM-50 run relative to Ref-50, with only a slight (< 0.1 dex) decrease in Z for $M_{*,\text{Chab}} > 10^{11} M_\odot$. However, for HiM-50, the mass-metallicity relation is much steeper, with $Z/Z_\odot \approx 0.4$ dex higher in high-mass ($M_{*,\text{Chab}} \sim 10^{11} M_\odot$) galaxies. This difference comes from the much higher production of metals per unit stellar mass formed from an IMF with a shallow high-mass slope.

We compare the simulated trends with the observed relation for SDSS galaxies from Gallazzi et al. (2005). For $M_{*,\text{Chab}} > 10^{10.5} M_\odot$, the mass-metallicity relation is observed to flatten off, as is also seen in Ref-50 and LoM-50, albeit at lower mass than observed. HiM-50, on the other hand, shows no sign of a saturating metallicity at high mass, which may be in tension with observations. Zahid et al. (2014) argue that this saturation occurs when the gas-phase abundances are high enough that, during star-formation, the metal mass that is removed from the ISM and locked up into low-mass stars is comparable to that produced and released back into the ISM by high-mass stars. HiM-50 keeps increasing in metallicity because for a top-heavy IMF, many more supernovae are produced per dwarf star formed, producing more metals than are being locked up, delaying saturation to higher metallicities. Note, however, that

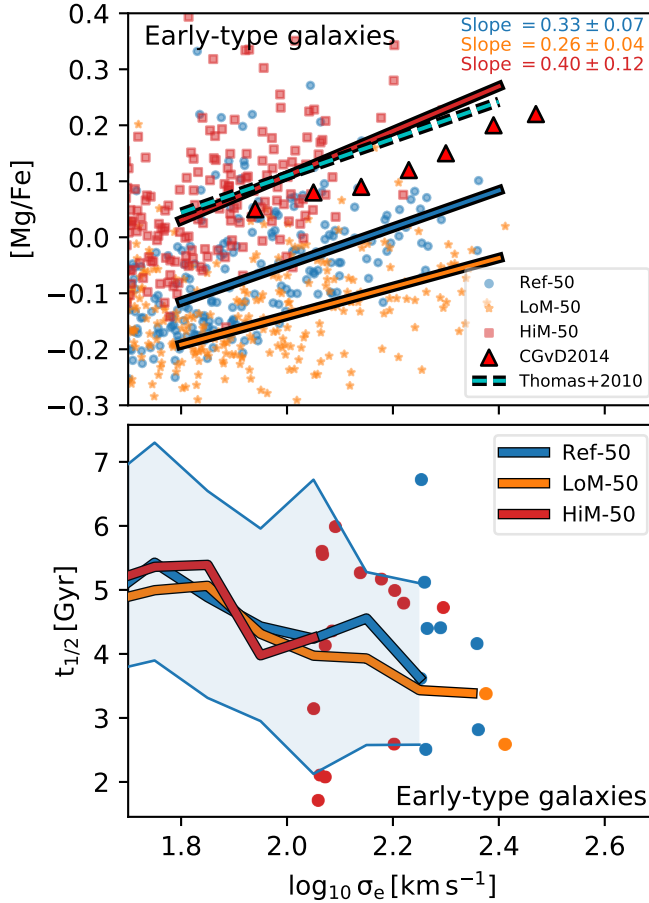


Figure 3.10: Top panel: Stellar $[\text{Mg}/\text{Fe}]$ as a function of stellar velocity dispersion for galaxies at $z = 0.1$ in LoM-50 (orange stars) and HiM-50 (red squares) compared to Ref-50 (blue circles). All quantities are SDSS r -band light-weighted and measured within the projected half-light radius, r_e . To facilitate a fairer comparison with observations, included are only early-type galaxies ($u^* - r^* > 2.0$). The observed trend for ETGs from Thomas et al. (2010) is shown as a dashed cyan line, while the observed trend for quiescent galaxies from Conroy et al. (2014) is shown as red triangles. Least absolute deviation fits for early-type galaxies with $\sigma_e > 10^{1.8} \text{ km s}^{-1}$ in each simulation are shown as solid coloured lines, with slopes labeled. The $[\text{Mg}/\text{Fe}]$ abundances in LoM-50 (HiM-50) are normalized lower (higher) relative to Ref-50 for high-mass galaxies. While the slopes of the $[\text{Mg}/\text{Fe}]$ - σ relation for both Ref-50 and HiM-50 are consistent with observations, that for LoM-50 is somewhat shallower. **Bottom panel:** Median formation time of stars within r_e for the same galaxy samples as the upper panel. The positive $[\text{Mg}/\text{Fe}]$ - σ_e correlation reflects the star formation histories of early-type galaxies.

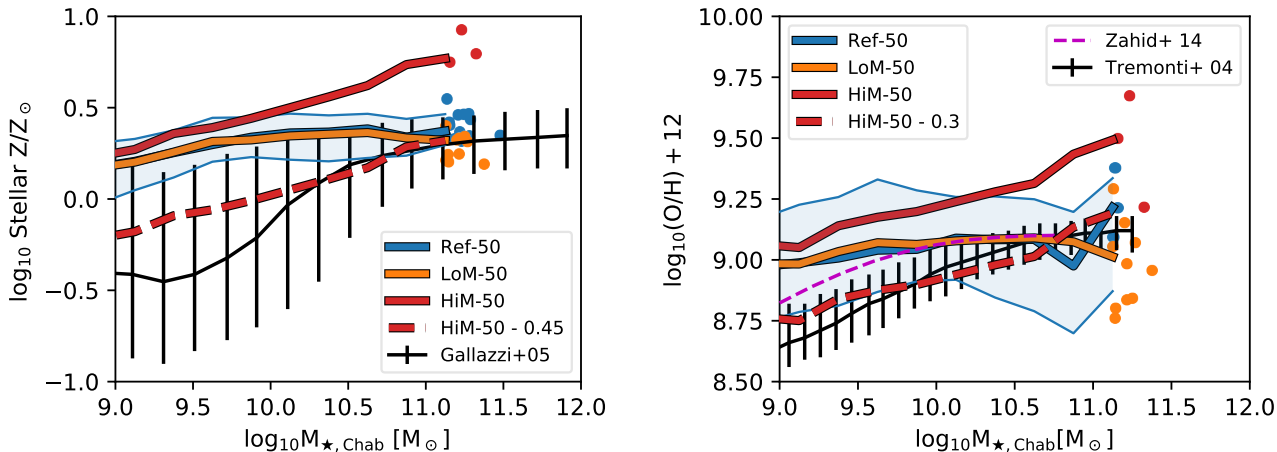


Figure 3.11: Metal abundances in LoM-50 (orange) and HiM-50 (red) compared to Ref-50 (blue) as a function of $M_{\star, \text{Chab}}$ for all galaxies at $z = 0.1$. Medians are indicated by solid lines and filled regions show the 10th to 90th percentile ranges. Abundances are measured in projection within one effective radius, r_e , while $M_{\star, \text{Chab}}$ is measured within a 30 kpc 3D aperture. Top: Stellar metallicity. Observations reported by Gallazzi et al. (2005) are shown as the black solid line with error bars indicating the scatter. Bottom: Gas-phase oxygen abundance for star-forming gas. For each galaxy, abundances are measured for all bound star-forming gas particles. The fit to observations from Zahid et al. (2014) is plotted as a magenta dashed line. Observations from Tremonti et al. (2004) are shown as black error bars. To ease comparison of the slopes with observations, the thick, red dashed curve lowers the trend for HiM-50 in both panels to match the normalization of the observations at $M_{\star, \text{Chab}} \approx 10^{11} M_{\odot}$. Stellar and gas-phase metallicities in high-mass galaxies in LoM-50 are consistent with Ref-50 but rise ≈ 0.4 dex higher for HiM-50 at the highest masses, in tension with the flattening in the observed relation above $10^{10} M_{\odot}$.

De Rossi et al. (2017) have shown that the mass-metallicity relation in EAGLE saturates in part due to AGN feedback quenching star formation and ejecting metal-rich gas out of high-mass galaxies. This implies that the Zahid et al. (2014) explanation is at least incomplete. Indeed, we will show in Section 3.4.3 that galaxies with $M_* \gtrsim 10^{11} M_\odot$ have typically higher SFRs in HiM-50 than in Ref-50, possibly contributing to their higher metallicities.

Given the large uncertainties in the simulated nucleosynthetic yields (Wiersma et al. 2009b) and the calibration of the metallicity indicators applied to observations (e.g. Kewley & Ellison 2008), the slope of the mass-metallicity relation is more constraining than its normalization. Because our (50 Mpc)³ simulations only contain galaxies up to $M_{*,\text{Chab}} \sim 10^{11} M_\odot$, it is not clear if the lack of flattening at the high-mass end is actually inconsistent with the observations. To facilitate visual comparison of the slopes, we lower the normalization of the HiM-50 relation until the high-mass median value matches the value from Gallazzi et al. (2005), which we show as a dashed-red line in Fig. 3.11. Indeed, the reduced HiM-50 trend agrees with Gallazzi et al. (2005) better than is the case for Ref-50 or LoM-50, which begin to flatten at lower stellar masses than observed galaxies. This result is also in qualitative agreement with some SAMs that find that the slope of the mass-metallicity relation and the alpha-enhancement can be simultaneously reproduced with similar top-heavy IMF variations (De Lucia et al. 2017). The better agreement may also be related to the stellar feedback, as S15 found that the higher efficiency of star formation required to match the GSMF in the high-resolution simulation Recal-L025N0752 resulted in stronger outflows that decreased the metallicity of the ISM enough to better match the the observed mass-metallicity relations. Nevertheless, this rescaling is inconsistent with the radiative cooling rates in the simulation, so yields in HiM-50 would need to be rescaled in the simulation input parameters to verify that the better agreement of HiM-50 persists.

It is unclear how stellar metallicities derived from spectroscopic observations depend on the assumed IMF. Because the observationally-inferred gas-phase metallicity may be less sensitive to the assumed IMF, we plot in the lower panel of Fig. 3.11 the mass-weighted gas-phase oxygen abundances for star-forming gas in our variable IMF simulations as a function of $M_{*,\text{Chab}}$ (although gas-phase abundances may still be affected by IMF assumptions in observational studies, see e.g. Paalvast & Brinchmann 2017). We compare our simulations with the observations of Tremonti et al. (2004) and the fit to observations of Zahid et al. (2014) for $z = 0.1$. Note that we again only focus on the slope, rather than the absolute values, as a function of mass. Our trends here are qualitatively similar to those found for the stellar metallicities in the top panel of Fig. 3.11, with perhaps more scatter. HiM-50 continues increasing toward high masses while metallicities in Ref-50 and LoM-50 tend to flatten off above $10^{10} M_\odot$. Lowering the HiM-50 trend by 0.3 dex brings it into reasonable agreement with Tremonti et al. (2004), and yields a better match than Ref-50 or LoM-50. Again, self-consistent rescaling of the yields would be required to confirm this better agreement. We conclude that none of the models are ruled out by the observed trends between α -enhancement or metallicity and mass. For HiM-50 the absence of

any flattening in the mass-metallicity relation is in tension with observations but larger volume simulations are required to judge the severity of the problem.

3.4.3 Star formation

As mentioned in earlier sections, star formation rates can be strongly affected by the IMF, both the SFRs inferred from (virtual) observations as well as the true SFRs in the simulations due to the IMF's effect on metallicity and stellar feedback. Fig. 3.12 details the effect of these variable IMF prescriptions on star formation in the simulations as a function of stellar mass. We show both the true quantities (dashed lines) and the corresponding values after interpreting the M_* and SFR from the K-band and FUV light, respectively, under the assumption of a Chabrier IMF (solid lines). The reinterpreted SFR, SFR_{Chab} , is computed by multiplying the actual SFR by the ratio between the Galex FUV-band luminosity of the stars and that they would have had if evolved with a Chabrier IMF, as also done by Clauwens et al. (2016). We note that this modifies the SFR by only ~ 10 per cent for most galaxies, leading to nearly identical trends of true and Chabrier-reinterpreted SFR with M_* . Note as well that only the Chabrier-interpreted values (solid lines) should be compared with the observations.

The top-left panel of Fig. 3.12 shows the “galaxy formation efficiency” of galaxies for our variable IMF simulations, defined as the ratio $M_{*,\text{Chab}}/M_{\text{DM}}$ normalized to the cosmic baryon fraction. Both variable IMF simulations agree with Ref-50 (solid thick lines), as well as with abundance matching results from Behroozi et al. (2013) and Moster et al. (2013) shown as thin solid lines. For LoM-50, the true efficiency is shifted toward higher values for $M_{*,\text{Chab}} > 10^{11} M_{\odot}$ (dashed orange line), where the excess stellar mass originates from dwarf stars. Interestingly, the true efficiencies for HiM-50 galaxies are quite close to their Chabrier-interpreted values. This implies that any correction to the observed galaxy formation efficiencies to account for IMF variations depends sensitively on how such variations are parameterized.

The specific star formation rates (sSFR), measured within 3D spherical apertures of radius 30 kpc, are shown in the upper right panel of Fig. 3.12 for star-forming galaxies, defined as those with $u^* - r^* < 2$. In all simulations, the sSFRs are consistent for $M_{*,\text{Chab}} < 10^{10.5} M_{\odot}$. At higher masses, sSFRs turn upwards for HiM-50, while they decrease for LoM-50 and Ref-50. The decrease in sSFR is consistent with the observed relations for local star-forming galaxies from the GAMA survey (Davies et al. 2016) and SDSS+WISE (Chang et al. 2015)², while the upturn at high mass in HiM-50 is in tension with the observations. This upturn is not as strong for the true sSFR (red-dashed line), implying that the discrepancy for HiM-50 is partially due to reinterpreting the SFRs assuming a Chabrier IMF.

These higher sSFRs in HiM-50 are due to a lack of quenching at high masses. This can be seen in the middle left panel of Fig. 3.12, where we show total SFR_{Chab} as a function of $M_{*,\text{Chab}}$ for all galaxies at $z = 0.1$. Here it can be seen that in both Ref-50 and LoM-50, the positive trend between SFR_{Chab} and $M_{*,\text{Chab}}$ flattens at

²We show results for galaxies from their online catalogue with FLAG=1, $\text{sSFR} > 10^{-2} \text{Gyr}^{-1}$, and M_* above their mass completeness limit.

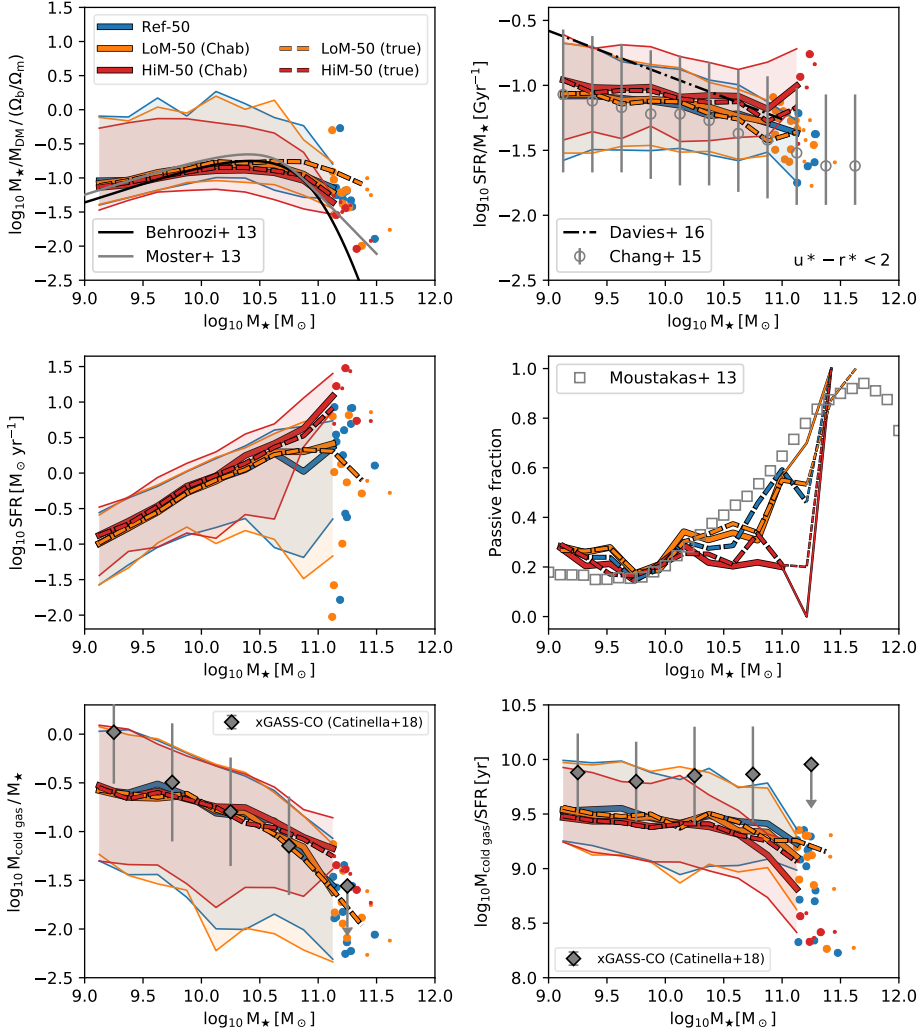


Figure 3.12: Star formation properties of all galaxies with $M_{\star, \text{Chab}} > 10^9 M_{\odot}$ at $z = 0.1$ as a function of stellar mass in our LoM-50 (orange) and HiM-50 (red) simulations, compared with Ref-50 (blue). Solid lines show results when reinterpreting the M_{\star} and SFR assuming a Chabrier IMF, while dashed lines show true values. In reading order from top-left to bottom-right: Galaxy formation efficiency, specific star formation rate (sSFR) for star-forming galaxies, SFR for all galaxies, passive fractions, neutral hydrogen fractions, and gas consumption timescale. Star-forming galaxies are defined as those with intrinsic $u^* - r^* < 2$. Medians are indicated as thick lines and shaded regions mark the 10-90th percentiles for the Chabrier-inferred lines. For bins with fewer than 10 galaxies, we show individual galaxies, where large and small dots refer to Chabrier-inferred and true values, respectively; for passive fractions these bins are indicated with thinner lines. Thin solid black and grey lines show abundance matching results from Behroozi et al. (2013) and Moster et al. (2013), respectively. (continued on following page)

Figure 3.12: (Continued from previous page) Grey circles show the median sSFR for SDSS+WISE galaxies from $z = 0$ to 0.2 with $\text{sSFR} > 10^{-2} \text{ Gyr}^{-1}$, with error bars showing the 10-90th percentiles (Chang et al. 2015). The black dash-dotted line in the upper right panel shows a fit to the observed sSFRs for star-forming galaxies from $z = 0$ to 0.1 from the GAMA survey (Davies et al. 2016). Passive fractions for SDSS galaxies are shown as grey squares (Moustakas et al. 2013). Median neutral hydrogen fractions and gas consumption timescales from the xGASS and xCOLDGASS surveys are shown as grey diamonds (Catinella et al. 2018); error bars denote 1σ scatter while arrows indicate upper limits on the median. The results for LoM-50 are consistent with Ref-50, but for HiM-50 the SFRs are too high for $M_{\star, \text{Chab}} > 10^{11} M_{\odot}$, resulting in lower passive fractions at high mass. These higher SFRs in HiM-50 are due to a higher gas fraction in high-mass galaxies.

$M_{\star, \text{Chab}} > 10^{10.5} M_{\odot}$ with a large amount of scatter toward low SFR_{Chab} as galaxies are quenched. However, in HiM-50, the trend becomes even steeper with less scatter at high mass. This behaviour leads to a lower passive fraction at high mass for HiM-50 galaxies, as shown in the middle right panel of Fig. 3.12, where we define the passive fraction as the fraction of galaxies with intrinsic $u^* - r^* > 2$ in bins of M_{\star} . These low passive fractions in HiM-50 contrast with the increasing passive fraction with increasing M_{\star} seen in observations of SDSS galaxies (Moustakas et al. 2013), as well as Ref-50 and LoM-50.

In the lower-left panel of Fig. 3.12, we show that these higher SFRs in HiM-50 galaxies are a consequence of a larger cold gas fraction. We compute cold gas masses within apertures of 70 pkpc following Crain et al. (2017), where for each gas particle, we compute the mass of neutral hydrogen following the prescription of Rahmati et al. (2013), accounting for self-shielding and assuming a Haardt & Madau (2001) ionizing UV background.³ While the ratio between star-forming gas mass and $M_{\star, \text{Chab}}$ decreases steeply with increasing $M_{\star, \text{Chab}}$ in Ref-50 and LoM-50, this fraction drops less steeply in HiM-50, lying ≈ 0.5 dex above Ref-50 at $M_{\star, \text{Chab}} \gtrsim 10^{11} M_{\odot}$. The higher cold gas fractions in HiM-50 galaxies at $z = 0.1$ are likely due to burstier stellar feedback ejecting more gas out of galaxies at high- z . This effect causes a delay in the peak of star formation – we will investigate the time-dependent properties of galaxies in these variable IMF simulations in a future paper.

We compare our results in the lower-left panel of Fig. 3.12 with the median cold gas fractions of galaxies from the mass-selected xGASS and xCOLD GASS surveys (Catinella et al. 2018). These observations match all of our simulations well for $M_{\star, \text{Chab}} > 10^{9.5} M_{\odot}$ but are too high in the lowest-mass bin. This low-mass tension is likely due to the fact that atomic hydrogen masses are not converged in the “intermediate” resolution EAGLE model, especially in the range $M_{\star, \text{Chab}} \sim 10^{9-10} M_{\odot}$ where they are lower by nearly an order of magnitude relative to higher-resolution models (see Crain et al. 2017). Thus, the use of higher-resolution simulations may resolve this tension with observations for low-mass galaxies.

The SFR change is not due to the re-normalization of the star formation law (see Section 3.2.3). To show this, we plot the gas consumption timescale, parametrized by the cold gas mass divided by the SFR, in the lower-right panel of Fig. 3.12 for all

³As in Catinella et al. (2018), to account for helium we multiply the neutral hydrogen mass by 1.3 to obtain total cold gas mass.

galaxies in each of our simulations. In all of our simulations the true value of this timescale (dashed lines) is quite constant and is barely affected by the variable IMF (by at most 0.1 dex). We thus conclude that a higher cold gas mass fraction, rather than the renormalization of the star formation law, is responsible for the higher SFRs in high-mass HiM-50 galaxies. We also compare these results with the observed xGASS-CO sample, who also find a nearly constant relation. There is, however, a systematic ≈ 0.4 dex offset toward lower gas consumption timescales relative to the observations. The reason for this offset is unclear, but is consistent with the expected systematic uncertainties associated with different SFR calibrators (compare results from Davies et al. 2016 and Chang et al. 2015 in the upper right panel of Fig. 3.12).

3.4.4 ETG galaxy sizes

We showed in Section 3.3.2.1 that the observed sizes of late-type galaxies are reproduced in our variable IMF simulations. We now investigate if this agreement persists for early-type galaxies as well. In the left panel of Fig. 3.13, we plot the half-light radius, r_e , as a function of $M_{\star, \text{Chab}}$ for non-star-forming galaxies, defined as those with $u^* - r^* > 2$. While the relation for LoM-50 agrees well with Ref-50, HiM-50 ETGs are strongly offset to larger sizes at fixed $M_{\star, \text{Chab}}$.

The reasons for this offset in HiM-50 are the same as those responsible for the smaller ≈ 0.1 dex offset seen for late-type galaxies in Section 3.3.2.1. Stronger stellar feedback, later formation times, and the fact that the luminosities of the central, top-heavy regions of the galaxies are dimmer relative to a Chabrier IMF than the less top-heavy outskirts, all inflate the sizes at fixed $M_{\star, \text{Chab}}$ relative to Ref-50. These effects are exacerbated in ETGs due to the fact that they are older, since old, top-heavy stellar populations are much dimmer than those with a Chabrier IMF, causing ETGs to shift toward lower $M_{\star, \text{Chab}}$ at fixed r_e .

For comparison, we plot the observed relations from SDSS (Shen et al. 2003) and the GAMA survey (Lange et al. 2015) for $z < 0.1$ galaxies with Sersic index $n_s > 2.5$. We multiply the Shen et al. (2003) sizes by a factor 1.075 to convert from z - to r -band half-light radii (see Kelvin et al. 2012; Lange et al. 2015). Both LoM-50 and Ref-50 match the observed relations well for $M_{\star, \text{Chab}} > 10^{10} M_{\odot}$, but HiM-50 ETGs are too large by $\approx 0.2 - 0.3$ dex, in tension with the observations.

In the right panel of Fig. 3.13 we plot the true 3D half mass radius as a function of true M_{\star} for the same galaxies. As was the case for star-forming galaxies in Fig. 3.8, the physical sizes of high-mass ETGs in LoM-50 are smaller than in Ref-50 by $\approx 0.2 - 0.3$ dex at fixed M_{\star} due to higher mass fractions of dwarf stars in their central regions. The positive offset in HiM-50 galaxies seen in the observable diagnostics is also present in the physical ones since, as with the light, the masses of the central, old stellar populations with top-heavy IMFs are lower than those with a Chabrier IMF, pushing these galaxies to lower M_{\star} and larger half-mass radii.

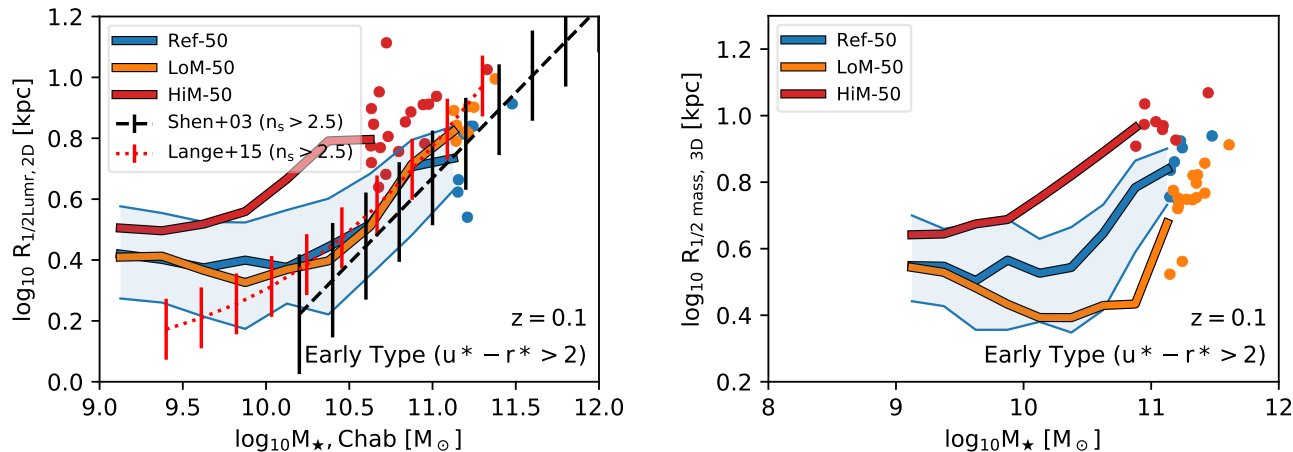


Figure 3.13: Size- M_* relation for early-type galaxies, defined as those with intrinsic $u^* - r^* > 2$, in Ref-50 (blue), LoM-50 (orange), and HiM-50 (red) at $z = 0.1$. Left panel: 2D projected r -band half-light radius as a function of Chabrier-reinterpreted stellar mass, $M_{*,\text{Chab}}$. The black-dashed and red-dotted lines with error bars show the observed trend from SDSS and GAMA, respectively, for galaxies with Sersic index $n_s > 2.5$ (Shen et al. 2003; Lange et al. 2015). For the GAMA data we assume errors of 0.1 dex based on visual inspection of their 25-75th percentiles, while for the SDSS data we assume the errors are the same as those for their same relation for late-type galaxies. Right panel: Physical 3D half-mass radius as a function of M_* . While the half-light radii of ETGs in Ref-50 and LoM-50 are consistent with observations, ETGs in HiM-50 are larger at fixed $M_{*,\text{Chab}}$ by $\approx 0.2 - 0.4$ dex. As is the case for late-type galaxies (see middle row of Fig. 3.8), LoM-50 ETGs are physically smaller by $\approx 0.2 - 0.3$ dex at fixed M_* relative to Ref-50.

3.5 Summary and Conclusions

We have modified the reference EAGLE cosmological, hydrodynamical simulations to self-consistently include a prescription for a stellar initial mass function (IMF) that varies per-star particle as a function of the ISM pressure at which it was formed. Two prescriptions are explored: in both cases we begin with the Kroupa double-power law IMF and vary the slope either below or above $0.5 M_{\odot}$ (hereafter referred to as LoM and HiM, respectively; see Fig. 3.2). For each prescription the dependence of the slope on birth ISM pressure was calibrated such that the observed Cappellari et al. (2013b, hereafter C13) trend of increasing excess stellar mass-to-light (M/L) ratio with central stellar velocity dispersion, σ_e , is roughly recovered. For LoM this recovery is accomplished by an increase in the fraction of low-mass stars, while for HiM the increasing mass fraction in stellar remnants and decreased luminosity are responsible.

The calibration of the pressure-dependence of the IMF was performed by post-processing the $(100 \text{ Mpc})^3$ reference EAGLE simulation. From this post-processing procedure, we have found that:

- In order to reproduce the observed trends between the stellar M/L ratio excess (MLE) relative to that expected for a Salpeter IMF (eq. 3.1), and central stellar velocity dispersion (σ_e), LoM and HiM must respectively become more bottom- and top-heavy in higher-pressure environments (although this may also be possible with a “top-light” HiM prescription, see Section 3.2.2). Since ISM pressures typically decrease with the age of the universe (e.g. Crain et al. 2015), these IMF prescriptions are implicitly time-dependent.
- The MLE is only an excellent proxy for the IMF (i.e. independent of age and metallicity) when the high-mass slope is close to the “reference” IMF (which here is Salpeter). For IMFs with shallower high-mass slopes, the MLE becomes strongly age-dependent for stars less than a few Gyr old (Fig. 3.2).

We ran two new $(50 \text{ Mpc})^3$ simulations with the same physics and resolution as the reference EAGLE model, but now each including one of our variable IMF prescriptions, which we refer to as LoM-50 and HiM-50, respectively. These simulations use variable nucleosynthetic yields, a star formation law, and stellar feedback consistent with their locally varying IMFs. Our conclusions are as follows:

- Both variable IMF simulations are broadly consistent with the observed trend between MLE and σ_e of C13 (Fig. 3.5). However, the trend in HiM-50 is less clear than for LoM-50 due to a lack of high- σ_e galaxies in the former, likely caused by burstier stellar feedback.
- Galaxies in LoM-50 are consistent with the increasing fraction of dwarf stars toward higher σ_e in early-type galaxies inferred by spectroscopic IMF studies, while those in HiM-50 do not show such a trend (Fig. 3.5). On the other hand, star-forming galaxies in HiM-50 show increasing ratios of ionizing flux

to FUV flux with increasing r -band surface brightness, in agreement with recent observations, while LoM-50 galaxies show no trend (Fig. 3.7). It is unclear how to reconcile these apparently conflicting observations.

- Relative to Ref-50, stellar ages and birth ISM pressures are largely unchanged in LoM-50, while HiM-50 produces younger stars at lower birth ISM pressures on average. This change may be due to the stronger stellar feedback from a top-heavy IMF (Fig. 3.6).
- Observational proxies for the EAGLE subgrid calibration diagnostics (galaxy K -band luminosity function, r -band half-light radii (r_e) of late-type galaxies (LTGs), and black hole masses) are consistent with the reference model for LoM-50. The same is true for HiM-50, except that the r_e of LTGs in HiM-50 are larger, but only by ≈ 0.1 dex, at fixed r -band luminosity (left column of Fig. 3.8).
- Stellar masses and LTG half-mass radii are larger and smaller, respectively, by $\approx 0.1 - 0.2$ dex in LoM-50 relative to Ref-50 (right column of Fig. 3.8). This difference is due to an excess of (dim) dwarf stars that increase the mass (but not the light) in the central regions of these galaxies as a result of the bottom-heavy IMF.

We also investigated the effect that the IMF has on predicted global galaxy scaling relations. Our results are as follows:

- While the slopes of the $[\text{Mg}/\text{Fe}] - \sigma_e$ relation in the Ref-50 and HiM-50 simulations for high-mass ($\sigma_e > 60 \text{ km s}^{-1}$), early-type ($u - r > 2$) galaxies (0.33 ± 0.07 and 0.40 ± 0.12 , respectively) are consistent with the observed relation, LoM-50 produces a relation with slightly (but significantly) shallower slope of 0.26 ± 0.04 , compared to observed values 0.33 ± 0.01 (Thomas et al. 2010) and 0.33 ± 0.03 (Conroy et al. 2014) (Fig. 3.10). The normalization of the $[\text{Mg}/\text{Fe}] - \sigma_e$ relation in HiM-50 is ≈ 0.15 dex higher than in Ref-50, bringing it into agreement with observations, while it is $\approx 0.05 - 0.1$ dex lower in LoM-50, ≈ 0.2 dex below the observed relation. However, given the large systematic uncertainties in the normalization for both observations and simulations, these differences in normalization are not significant.
- Stellar and gas-phase metallicities in LoM-50 are consistent with Ref-50, but in HiM-50 both quantities increase steeply with $M_{*,\text{Chab}}$, the stellar mass inferred under the assumption of a Chabrier IMF, above $10^{10} M_\odot$ with no sign of flattening at higher mass. This is contrary to the flattening seen in Ref-50 and LoM-50, and is possibly inconsistent with similar flattening seen in observations.
- The relations between $M_{*,\text{Chab}}/M_{\text{DM}}$ and $M_{*,\text{Chab}}$ for galaxies in LoM-50 and HiM-50 are consistent with Ref-50. Adopting true M_* in place of $M_{*,\text{Chab}}$ increases $M_{*,\text{Chab}}/M_{\text{DM}}$ by ≈ 0.3 dex for LoM-50 galaxies with $M_* > 10^{10.5} M_\odot$, but has little effect for HiM-50 galaxies. Specific SFRs of galaxies with $M_{*,\text{Chab}} \gtrsim$

$10^{10.5} M_{\odot}$ are higher in HiM-50 than in Ref-50, resulting in a lower passive fraction that does not rise with stellar mass up to at least $M_{*,\text{Chab}} = 10^{11} M_{\odot}$, in tension with observations (Fig. 3.12). This higher SFR is a result of a higher star-forming gas fraction in high-mass galaxies, likely due to the burstier feedback being more efficient at ejecting gas from galaxies at early times, delaying star-formation to lower z .

- While the half-light radii of early-type galaxies in LoM-50 are consistent with Ref-50 and observations, those in HiM-50 with $M_{*,\text{Chab}} > 10^{10} M_{\odot}$ are about a factor of 2 larger at fixed $M_{*,\text{Chab}}$, inconsistent with observations. The larger half-light radii are likely due to stronger stellar feedback and the stronger dimming of old stellar populations with a top-heavy IMF relative to a Chabrier IMF, increasing r_e and decreasing $M_{*,\text{Chab}}$, respectively.

The results of this project are intended to aid in the interpretation of evidence for IMF variations in real galaxies, especially in terms of *how* the IMF varies, either at the high-mass or the low-mass end. While a high-mass slope variation cannot be definitively ruled out by the present analysis, the model in which the IMF varies at the low-mass end (as well as the reference model with a Chabrier IMF) produces galaxies that match observations much more closely than one in which the high-mass slope is varied.

It is intriguing that observations that are sensitive to the low-mass and high-mass slopes of the IMF prefer LoM and HiM, respectively, with neither model matching all observations simultaneously (Figs. 3.5 and 3.7). This result could indicate that IMF variations are more complex than those explored in this paper, or that systematic uncertainties in models used to constrain the IMF observationally are underestimated.

This paper lays the groundwork for further analysis of the predicted trends between the IMF (parameterized by the MLE) and galaxy properties, which will be explored in a series of upcoming papers (Papers II and III). Paper II will investigate the trends between the MLE and global properties across the galaxy population, uncovering the observable properties that are predicted to correlate with the MLE most strongly. In Paper III we delve into spatially-resolved properties of individual galaxies, exploring how IMF variations affect radial gradients in M/L , metal abundances, and MLE to further expose the differences in the predictions due to the non-universality of the IMF. Paper III will also investigate the time dependence of the IMF and its effect on the evolution of galaxies in our simulations.

Acknowledgements

We are grateful to the anonymous referee for constructive feedback which increased the overall quality of the paper. We thank Fabio Fontanot for useful comments. C.B. thanks Bart Clauwens, Madusha Gunawardhana, Pdraig Alton, Richard Bower, Tom Theuns, Marijn Franx, and Matthieu Schaller for insightful discussions regarding this project. This work used the DiRAC Data Centric system at Durham University,

operated by the Institute for Computational Cosmology on behalf of the STFC DiRAC HPC Facility (www.dirac.ac.uk). This equipment was funded by BIS National E-infrastructure capital grant ST/K00042X/1, STFC capital grants ST/H008519/1 and ST/K00087X/1, STFC DiRAC Operations grant ST/K003267/1 and Durham University. DiRAC is part of the National E-Infrastructure. RAC is a Royal Society University Research Fellows. We also gratefully acknowledge PRACE for awarding us access to the resource Curie based in France at Très Grand Centre de Calcul. This work was sponsored by the Dutch National Computing Facilities Foundation (NCF) for the use of supercomputer facilities, with financial support from the Netherlands Organization for Scientific Research (NWO). This research made use of `ASTROPY`, a community-developed `CORE PYTHON` package for Astronomy (Astropy Collaboration 2013).

3.A Aperture effects and IMF calibration details

In Fig. 3.14, we show the effect of aperture choice on the $\text{MLE}-\sigma_e$ relation for mock C13 galaxies in LoM-50 and HiM-50. Comparing the left and right columns, we see that the global IMF, measured over all stellar particles in each galaxy, underestimates the MLE values when measured within r_e , by ≈ 0.1 dex. Choosing an even smaller aperture of $r_e/2$ increases the difference further to ≈ 0.1 dex. We did not measure the IMF within $r_e/8$, as for many galaxies this is below the resolution limit of the simulations.

Fig. 3.15 outlines the process of calibrating the variable IMF prescriptions LoM and HiM for mock C13 galaxies in the left and right columns, respectively, by showing the $\text{MLE}-\sigma_e$ relation for different steps in the process. The top row shows the Ref-100 simulation (with the same resolution as Ref-50 but with a volume $(100 \text{ Mpc})^3$), where the $z = 0.1$ masses and luminosities of the stars were recomputed in post-processing assuming they evolved according to either the LoM or HiM variable IMF prescription (upper-left and -right panels, respectively). The positive trend up to high σ_e is clear in both cases. While the best-fit relation in LoM-50 is offset from the C13 relation, the slopes are consistent. As mentioned in Section 3.3.1, this offset is due to the fact that this IMF variation prescription was originally calibrated using apertures larger than r_e . The smaller aperture size in this plot excludes stars with Chabrier-like IMFs, increasing the MLE for the entire relation. For HiM-50, the normalization of the $\text{MLE}_r - \sigma_e$ relation is much closer to the C13 relation, but the slope is slightly shallower. Since these calibrations were done by eye, a perfect match to the C13 slope is not expected. Indeed, the agreement with C13 is still very good, since most of our points lie within the 1σ scatter of their relation.

The middle row shows the same IMF prescriptions applied to the Ref-50 simulation. Here we are missing the high- σ_e galaxies due to the smaller box size, but the positive trend is still significant in both cases. Finally, the bottom row shows the results for LoM-50 and HiM-50, which were run with the LoM and HiM IMF prescriptions self-consistently included. The trend for LoM is preserved in LoM-50, with a slightly higher normalization. As mentioned in Section 3.3.1, this is due to the typically larger birth ISM densities at which stars are born in LoM-50 relative to Ref-50. On the other hand, the trend in HiM-50 is slightly weaker due to smaller values of σ_e as well as younger

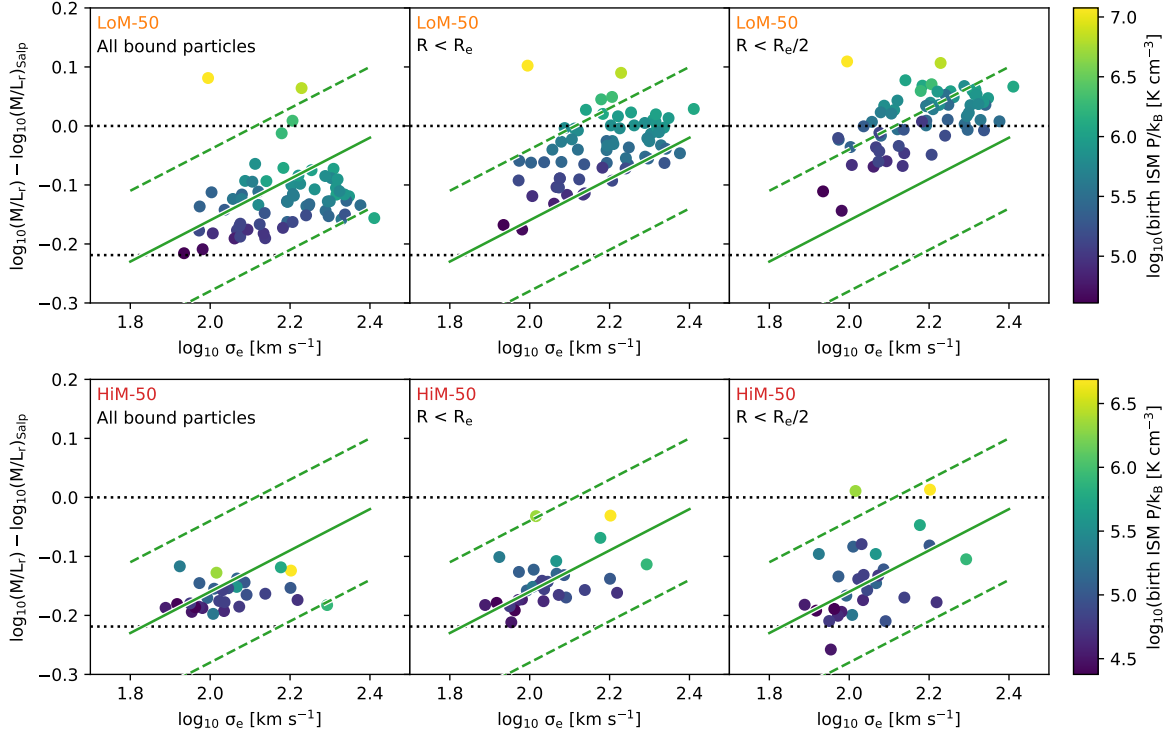


Figure 3.14: Effect of aperture choice on IMF measurement. Mass-to-light excess (MLE) over Salpeter as a function of stellar velocity dispersion for mock C13 galaxies in our LoM-50 (top row) and HiM-50 (bottom row) simulations at $z = 0.1$. From left to right, the MLE is measured for all bound stars, stars within $1 r_e$, and stars within $0.5 r_e$, respectively. For reference, in all panels we plot the $\text{MLE}_r - \sigma_e$ relation of Cappellari et al. (2013b) with 1σ scatter as green-solid and -dashed lines, respectively. Horizontal dashed lines indicate MLE_r for Salpeter and Chabrier IMFs from top to bottom, respectively. The value of MLE is sensitive to the precise choice of aperture.

ages. Better statistics at high- σ_e may be required to determine if galaxies in HiM-50 are inconsistent with the C13 trend.

Fig. 3.16 shows the MLE as a function of the median birth pressure of stars within r_e of galaxies at $z = 0.1$ in LoM-50 (left) and HiM-50 (right). MLE correlates extremely well with pressure in LoM-50, but more weakly in HiM-50. The larger scatter in HiM-50 is due to the age-dependence of MLE for a shallow high-mass IMF slope.

3.B Self-consistency tests

Making the simulations completely self-consistent with the variable IMF while simultaneously ensuring that the subgrid calibration diagnostics remained consistent with the reference model was a challenging and painstaking process. Due to the non-linear process of galaxy formation and its connection with the IMF, it can be unclear which effect of the variable IMF is responsible for changes in the galaxy properties. Thus, we investigated the effect of a variable IMF in smaller, $(25 \text{ Mpc})^3$ boxes, adding new effects of the variable IMFs one at a time until they became self-consistent. Fig. 3.17 shows this process for LoM-50, and its effects on the subgrid physics calibration diagnostics: the K-band luminosity (M_K) function, the $r_e - M_K$ relation, and the $M_{\text{BH}} - M_K$ relation. To emphasize discrepancies in M_{BH} , we plot medians relative to the Ref-25 simulation in the right panel.

First we allowed the IMF to affect only the yields in the simulation, while keeping the feedback and star formation law consistent with that used for the reference (Chabrier IMF) model. This model we refer to as “LoM-25 yields”, represented by the orange curves in Fig. 3.17. For all calibration diagnostics, this model agrees very well with Ref-25, which is not surprising since metallicities are not strongly affected in the LoM-50 runs.

We next added the effect of modifying the physical star-formation law such that the observed star formation law, i.e., intrinsic UV surface brightness as a function of gas surface density, was preserved, shown as the green curve. In this case the simulation produced a larger number of high-mass galaxies, while reducing M_{BH} by over 0.5 dex for these galaxies, without strongly affecting the sizes. This result can be explained by self-regulation of stellar and BH growth. Since the feedback per stellar mass formed was still set as “Chabrier”, the increased normalization of the SF law (i.e. the smaller gas consumption timescale) would result in stronger stellar feedback at fixed gas surface density. Thus, galaxies naturally decrease the gas density (and thus the SFR) until the feedback returns to the value appropriate for self-regulation (i.e. outflows roughly balance inflows). This lower gas density reduces the ability of gas to accrete onto BHs, reducing their accretion rates and thus their final $z = 0.1$ masses. With lower BH masses, AGN feedback is suppressed, causing stellar feedback to compensate, resulting in higher M_* and thus brighter M_K .

To alleviate this issue, we made the feedback self-consistent, shown by the red curves in Fig. 3.17. With decreased stellar feedback per unit stellar mass, the effect of the modified star-formation law is canceled out such that the amount of feedback at fixed gas surface density is more consistent with the reference model. This model

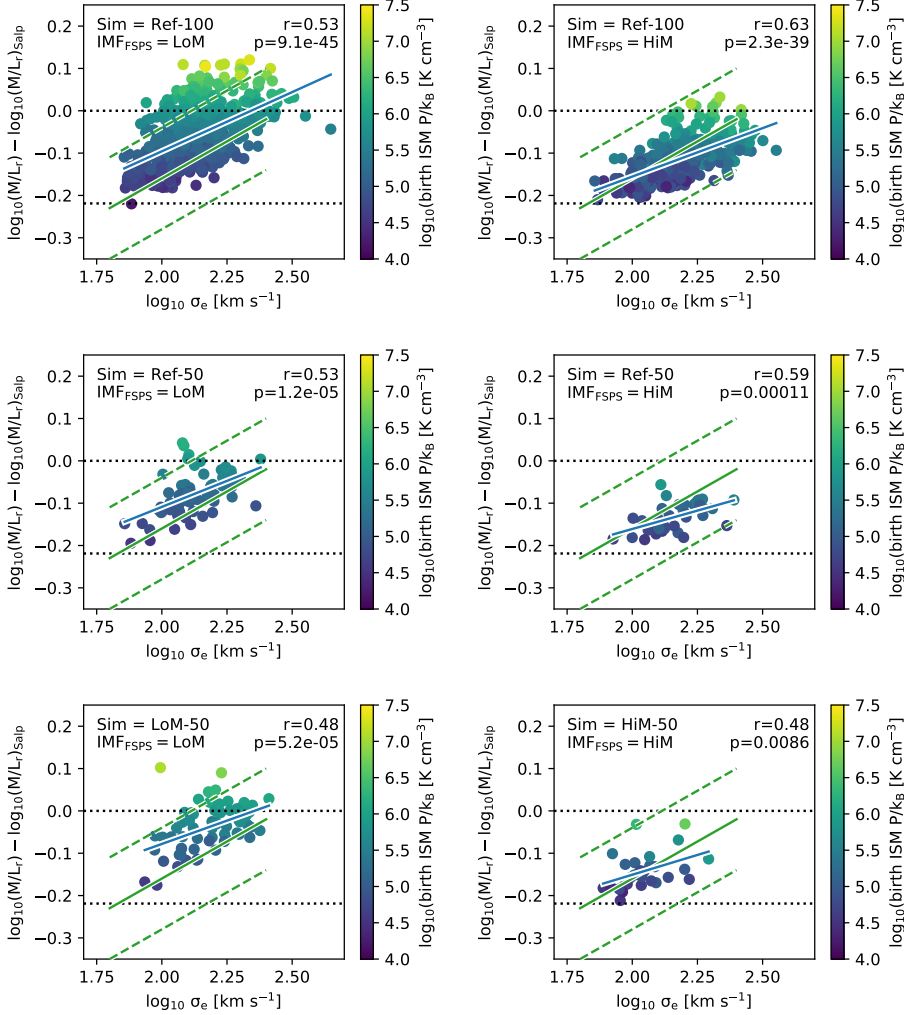


Figure 3.15: Variable IMF prescription calibration. MLE_r as a function of σ_e for galaxies consistent with a C13 selection. All quantities are measured within r_e . Simulations in the left and right columns assume a LoM and HiM IMF variation prescription, respectively. Top row: Post-processed Ref-100 simulation. Middle row: Post-processed Ref-50 simulation. Bottom row: Self-consistent LoM-50 (left) and HiM-50 (right) simulations. Least-absolute deviation fits are shown as blue solid lines, and the Spearman r coefficient and its associated p -value are indicated in the upper right corner of each panel. The calibrated correlation between the MLE_r and σ_e is preserved in the LoM-50 simulation, but is reduced in HiM-50.

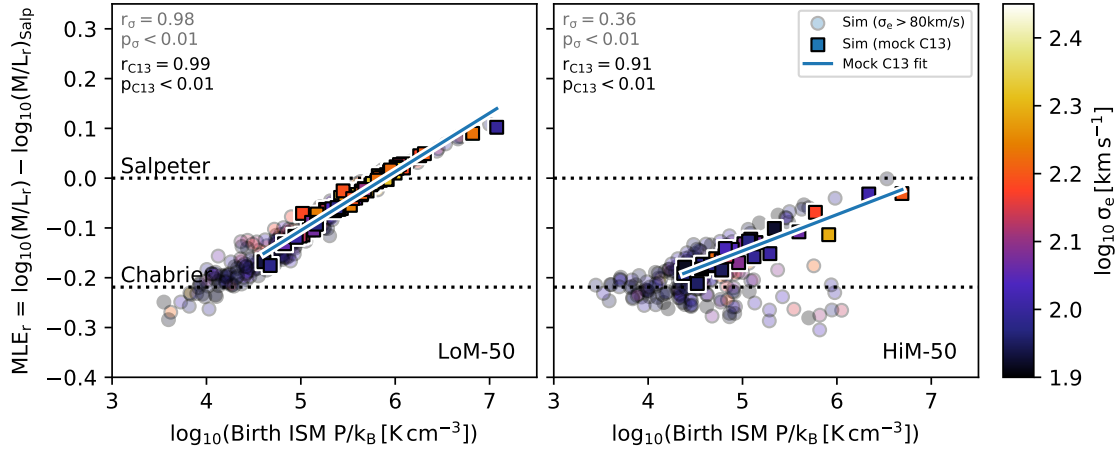


Figure 3.16: MLE_r , as a function of birth ISM pressure for LoM-50 and HiM-50 (left and right panels, respectively), coloured by central stellar velocity dispersion, σ_e . All quantities are r -band light weighted, measured within 2D projected r_e . Galaxies with $\sigma_e > 80 \text{ km s}^{-1}$ are shown as translucent circles, while those that fall under our “mock C13” selection criteria are shown as opaque circles.

is much more consistent with Ref-25 and with the calibration data, and is our fiducial model.

Fig. 3.18 shows the same results but for the HiM IMF and corresponding HiM-25 simulations. Modifying the yields (orange curve) increases the sizes slightly and BH masses more strongly. Since the HiM IMF affects metallicities much more strongly than the LoM IMF, this can be seen as the effect of increasing the cooling rate due to higher metal yields, increasing the ability of gas to accrete onto BH particles and the importance of AGN feedback. Reducing the physical star-formation law at high pressure so as to maintain the same observed law makes the situation worse, further increasing BH masses and sizes, while also strongly suppressing the bright end of the M_K function. The situation is essentially reversed relative to the LoM-25 case: the gas density is increased in order to obtain strong enough stellar feedback for self-regulation, which increases the BH masses and AGN feedback, which lowers stellar masses at the high-mass end of the GSMF. Again, including self-consistent stellar feedback (red curve) removes the need to change the gas densities, correcting the stellar and BH masses. The sizes are still slightly larger, but this is not a large difference from Ref-25.

3.C The dwarf-to-giant ratio

Spectroscopic IMF studies are sensitive to the ratio of dwarf-to-giant stars in the present-day stellar populations of the galaxies for which they constrain the IMF. La Barbera et al. (2013) have concluded that, as long as models that differ only in IMF parameterization fit the IMF-sensitive stellar absorption features equally well, they yield the same dwarf-to-giant ratio. In that study, this ratio is defined as (their eq. 4)

$$F_{0.5} = \frac{\int_{0.1}^{0.5} M \Phi(M) dM}{\int_{0.1}^{100} M \Phi(M) dM} \quad (3.5)$$

where $\Phi(M)$ is the IMF. However, as noted by Clauwens et al. (2016), spectroscopic IMF studies are not able to constrain the denominator since in most ETGs, the stellar populations are so old that the highest stellar mass remaining is $\approx 1 M_\odot$. Thus, while this definition of $F_{0.5}$ is unique for a given IMF, it is not clear that it is unique for a given mass fraction of dwarf stars at the present day. To investigate this, we employ the definition used by Clauwens et al. (2016), where the ratio is instead defined with respect to stars with $m < 1 M_\odot$, $F_{0.5,1}$ (Equation 3.4). $F_{0.5,1}$ is a more accurate representation of the present-day dwarf-to-giant mass ratio, to which spectroscopic IMF studies are sensitive. If it is true that as long as the present-day IMF-sensitive spectral features are well-fit, the choice of IMF parameterization does not affect $F_{0.5}$, it must also be true that it does not affect $F_{0.5,1}$.

In Fig. 3.19, we plot $F_{0.5}$ as a function of $F_{0.5,1}$ for a variety of IMF parameterizations. Note that both of these quantities are unique for a given IMF. As orange and red solid lines we show results for the LoM and HiM IMF parameterizations respectively, where the range of values plotted corresponds to the ranges over which

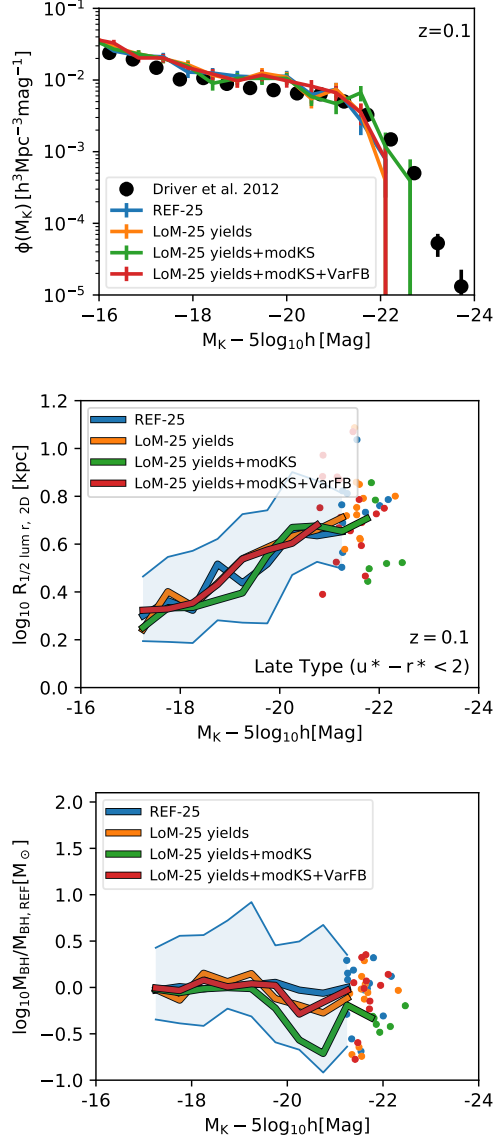


Figure 3.17: As in the left column of Fig. 3.8 but for simulations with the same model as LoM-50 but for a $(25 \text{ Mpc})^3$ volume (rather than $(50 \text{ Mpc})^3$). In blue we show the reference 25 Mpc box (Ref-25), while other colours show simulations with LoM, adding new effects of the variable IMF one at a time. In orange we show the effect of only changing the stellar yields while keeping everything else fixed at the reference (Chabrier) prescription. In green we self-consistently modify the star-formation law. In red we further make the stellar feedback self-consistent with the variable IMF, this being our fiducial LoM model. The left panel shows the K-band luminosity function. The middle panel shows half light radius as a function of K-band absolute magnitude. To clarify the deviations of M_{BH} from the Ref-25 model, the right panel shows the median M_{BH} relative to the median for Ref-25, rather than absolute M_{BH} as in Fig. 3.8. The "yields" model and our fiducial, self-consistent model match the calibrated values of the Ref model very closely, while the model "yields+modKS" deviates with higher luminosities and lower BH masses.

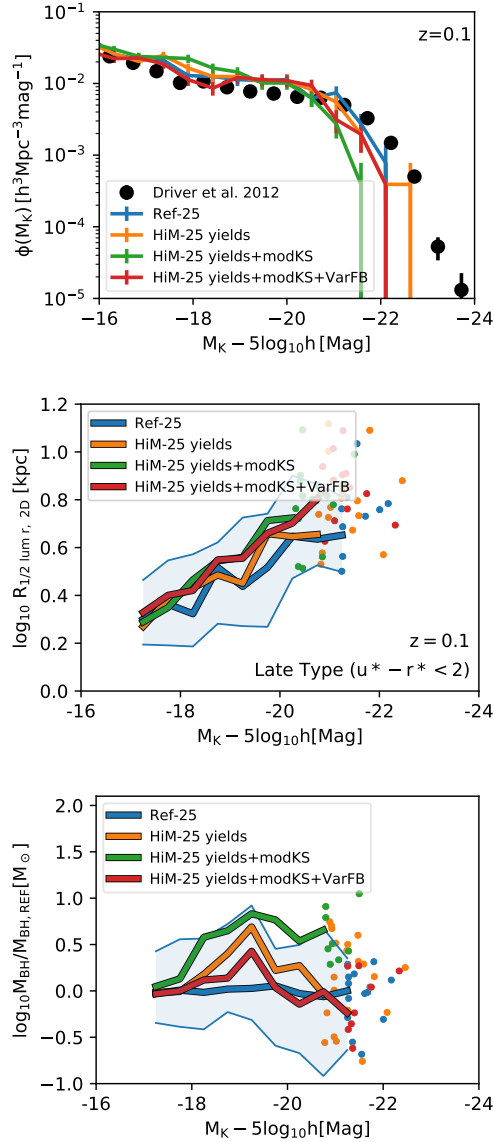


Figure 3.18: As in Fig. 3.17 but for the HiM prescription. Out of these three models, our fiducial, self-consistent model does the best job at matching the reference model and hence the calibration diagnostics, especially for BH masses.

the IMFs are allowed to vary in our model (see Section 3.2.2). As expected, for LoM the dwarf-to-giant ratio spans a wide range under either definition, with both increasing with the steepening of the low-mass slope. HiM also decreases for both dwarf-to-giant ratio definitions as the high-mass slope becomes shallower, but follows a much steeper trend than in the LoM case. This shows that $F_{0.5}$ is much more sensitive to changes in the high-mass slope than is $F_{0.5,1}$. This result indicates that, at a fixed present-day dwarf-to-giant ratio, $F_{0.5}$ is sensitive to the parameterization of the IMF.

To further illustrate this point, we also include in Fig. 3.19 results for the Bimodal IMF parameterization of Vazdekis et al. (1996), where we plot results for the range of high-mass slopes recovered for high-mass early-type galaxies found by La Barbera et al. (2013), corresponding to $\Gamma_b = 1$ to 3 (or $x_{\text{Bimodal}} = -2$ to -4 according to the IMF slope convention used in our paper). Unsurprisingly, the Bimodal IMF line follows the HiM trend and extends it to higher dwarf-to-giant ratios as the high-mass slope steepens. We also include the same trend for a single power-law (or “unimodal”) IMF in brown. Here we also show results for slopes recovered for high-mass early-type galaxies by La Barbera et al. (2013), with $\Gamma = 0.8$ to 2 (or $x = -1.8$ to -3). The trend between $F_{0.5}$ and $F_{0.5,1}$ is also monotonic for this prescription, but again follows a separate track.

It is clear that, for a given IMF parameterization, $F_{0.5}$ is a good tracer of the present-day dwarf-to-giant ratio. However, for a fixed present-day dwarf-to-giant ratio, $F_{0.5,1}$, the corresponding zero-age value, $F_{0.5}$, is extremely sensitive to the choice of IMF parameterization. This is particularly true at $F_{0.5,1} \approx 0.7$, where the range of $F_{0.5}$ values ranges from sub-Chabrier to super-Salpeter, depending on the IMF parameterization employed.

It is thus interesting that La Barbera et al. (2013) find that models with different IMF parameterization are consistent in $F_{0.5}$. However, at fixed $F_{0.5}$, the difference in $F_{0.5,1}$ values between bimodal and unimodal IMFs is not large, and is comparable to the typical differences in $F_{0.5}$ seen between these two IMF parameterizations found by La Barbera et al. (2013). This is because IMF prescriptions that vary the high-mass slope are more sensitive to $F_{0.5}$ than to $F_{0.5,1}$, as can be seen by the steep slopes of the Bimodal and Unimodal lines in Fig. 3.19. It would thus be interesting to see if spectroscopic analyses would still yield consistent $F_{0.5}$ values under the assumption of a LoM-like IMF parameterization, as the differences could be greater.

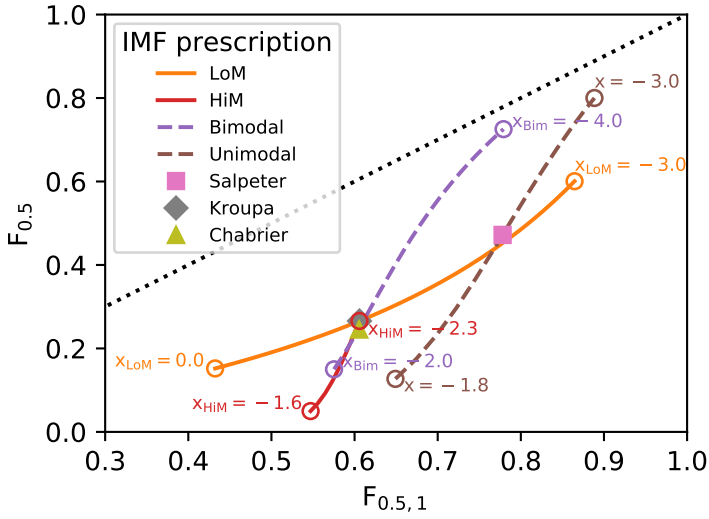
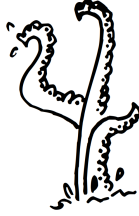


Figure 3.19: Effect of IMF parameterization on the inferred dwarf-to-giant ratio. We show the mass fraction of stars with $m < 0.5 M_{\odot}$ relative to the total mass of the IMF, $F_{0.5}$ (Equation 3.5), as a function of the same fraction but relative to the mass $< 1 M_{\odot}$, $F_{0.5,1}$ (Equation 3.4). The former is the dwarf-to-giant ratio defined by La Barbera et al. (2013, their Equation 4), while the latter is that defined in Clauwens et al. (2016). A dotted black line shows the 1:1 relation. As orange and red solid lines we show the two variable IMF prescriptions used in this work, LoM and HiM, respectively. The dashed purple line shows the bimodal IMF prescription of Vazdekis et al. (1996), while the dashed brown line shows the relation for a single power law IMF slope. The values for Salpeter, Kroupa, and Chabrier IMFs are indicated with filled symbols (see legend). Open circles mark the values of the IMF slope for the range over which the IMF is varied in each parameterization. At fixed $F_{0.5,1}$, the $F_{0.5}$ depends sensitively on the parameterization assumed.



*Calibrated, cosmological,
hydrodynamical simulations with
variable IMFs II:
Correlations between the IMF and
global galaxy properties*

The manner in which the stellar initial mass function (IMF) scales with global galaxy properties is under debate. We use two hydrodynamical, cosmological simulations to predict possible trends for two self-consistent variable IMF prescriptions that respectively become locally bottom-heavy or top-heavy in high-pressure environments. Both simulations have been calibrated to reproduce the observed correlation between central stellar velocity dispersion and the excess mass-to-light ratio (MLE) relative to a Salpeter IMF by increasing the mass fraction of, respectively, dwarf stars or stellar remnants. We find trends of MLE with galaxy age, metallicity and $[\text{Mg}/\text{Fe}]$ that agree qualitatively with observations. Predictions for correlations with luminosity, half-light radius, and black hole mass are presented. The significance of many of these correlations depends sensitively on galaxy selection criteria such as age, luminosity, and morphology. For an IMF with a varying high-mass end, some of these correlations are stronger than the correlation with the birth ISM pressure (the property that governs the form of the IMF), because in this case the MLE has a strong age dependence. Galaxies with large MLE tend to have overmassive central black holes. This indicates that the abnormally high MLE observed in the centres of some high-mass galaxies does not imply that overmassive BHs are merely the result of incorrect IMF assumptions, nor that excess M/L ratios are solely the result of overmassive BHs. Satellite galaxies tend to scatter toward high MLE due to tidal stripping, which may have significant implications for the inferred stellar masses of ultracompact dwarf galaxies.

Christopher Barber, Joop Schaye and Robert A. Crain
Accepted for publication in MNRAS.

4.1 Introduction

The physical interpretation of observational diagnostics of extragalactic stellar populations, as well as predictions for such diagnostics from galaxy formation models, rely on the assumed distribution of masses of stars at birth in a given simple stellar population, the stellar initial mass function (IMF). Such studies often assume a universal functional form, motivated by the apparent universality of the IMF within the Milky Way (MW) galaxy (Kroupa 2001; Chabrier 2003; Bastian et al. 2010).

Recent evidence for IMF variations in the centres of high-mass early-type galaxies challenge this assumption of universality. Some evidence comes from dynamical studies that measure the excess central stellar mass-to-light ratio (MLE) relative to that expected given a fixed IMF. The MLE is typically measured dynamically either via gravitational lensing (e.g. Auger et al. 2010; Treu et al. 2010; Spiniello et al. 2011; Barnabè et al. 2013; Sonnenfeld et al. 2015; Posacki et al. 2015; Smith et al. 2015; Collier et al. 2018) or stellar kinematics (e.g. Thomas et al. 2011b; Dutton et al. 2012; Tortora et al. 2013; Cappellari et al. 2013b; Li et al. 2017), with most studies finding larger values than one would expect for a MW-like IMF. This excess mass may come from excess dim, low-mass, dwarf stars that contribute more to the mass than the light, implying a steeper (bottom-heavy) IMF, or from stellar remnants such as black holes or neutron stars, implying a shallower (top-heavy) form. Some information about the functional form of the IMF can be inferred from spectroscopic studies, which indicate that fits to IMF-sensitive stellar absorption features require a larger ratio of dwarf to giant stars, implying that the IMF has a steeper slope either at all masses (e.g. Cenarro et al. 2003; Van Dokkum & Conroy 2010; Spiniello et al. 2012; Ferreras et al. 2013; Spiniello et al. 2014), or only at the low-mass end (e.g. Conroy & van Dokkum 2012b; Conroy et al. 2017) or only the high-mass end (e.g. Ferreras et al. 2013; La Barbera et al. 2013; Rosani et al. 2018). Interestingly, observations of local vigorously star-forming galaxies instead imply that the IMF becomes more top-heavy with increasing star formation rate (Gunawardhana et al. 2011).

The majority of these studies find that the IMF becomes “heavier” with increasing central stellar velocity dispersion, σ . To understand in more detail what drives IMF variations, it is useful to investigate how the IMF varies as a function of other galaxy properties as well. In the observational literature, there seems to be little consensus regarding the correlation between the IMF and galaxy properties other than central σ , the most notable being $[\text{Mg}/\text{Fe}]$. Some spectroscopic studies report a strong correlation between the MLE and $[\text{Mg}/\text{Fe}]$ for ETGs, even stronger than that with σ (Conroy & van Dokkum 2012b; Smith et al. 2012). On the other hand, the spectroscopic study of La Barbera et al. (2015) concludes that, while the IMF slope correlates with both σ and $[\text{Mg}/\text{Fe}]$ in stacked SDSS spectra of high- σ ETGs, the correlation with $[\text{Mg}/\text{Fe}]$ vanishes at fixed σ . The dynamical study of McDermid et al. (2014) finds a significant (but weak) trend of MLE with $[\text{Mg}/\text{Fe}]$ for ATLAS^{3D} galaxies which however does not appear to be as strong as the correlation with σ (Cappellari et al. 2013b). Smith (2014) shows that studies that employ dynamical methods tend to favour trends between σ with little $[\text{Mg}/\text{Fe}]$ residual dependence, while spectroscopic methods favour a

[Mg/Fe] correlation with no residual σ dependence, even when applied to the same galaxy sample.

The situation is even more uncertain for trends between the IMF and stellar metallicity. Spatially-resolved spectroscopic IMF studies have found that the IMF correlates strongly with local stellar metallicity (Martín-Navarro et al. 2015c; Conroy et al. 2017), while global trends tend to be weaker, with spectroscopic studies finding only weak trends (Conroy & van Dokkum 2012b), and dynamical studies finding no significant correlation at all (McDermid et al. 2014; Li et al. 2017). These discrepancies between the IMF scalings among observational IMF studies are often chalked up to differences in modelling procedures and unknown systematic biases (Clauwens et al. 2015). Clauwens et al. (2016) showed that given the uncertain observational situation, the consequences of the inferred IMF variations for the interpretation of observations of galaxy populations could vary from mild to dramatic.

Recently, Barber et al. (2018a, , hereafter Paper I) presented a suite of cosmological, hydrodynamical simulations that self-consistently vary the IMF on a per-particle basis as a function of the ISM pressure from which star particles are born. These simulations, which adopt respectively a bottom-heavy and a top-heavy IMF, use the EAGLE model for galaxy formation (Schaye et al. 2015). They reproduce the observed $z \approx 0$ galaxy luminosity function, half-light radii and black hole masses, and the IMF dependence on pressure has been calibrated to reproduce the observed MLE– σ relation. The goal of this paper is to determine, for the first time, the relationships between the IMF and global galaxy properties that arise from a self-consistent, hydrodynamical, cosmological model of galaxy formation and evolution with *calibrated* IMF variations. In doing so, we can inform on the differences (and similarities) in such relationships as a result of differences in IMF parametrizations.

This paper is organized as follows. In Section 4.2 we summarize the variable IMF simulations. Section 4.3 shows the circumstances for which the MLE is a reasonable tracer of the IMF. Section 4.4 shows the resulting correlations between the MLE and various galaxy properties, including age, metallicity, [Mg/Fe] stellar mass, luminosity, and size. Section 4.4.5 shows how galaxies with overmassive BHs tend to also have a high MLE. Section 4.4.6 investigates which observables most closely correlate with MLE. Section 4.5 examines the environmental effects on the MLE– σ relation. We summarize in Section 4.6. In a future work (Paper III) we will discuss the spatially-resolved IMF trends within individual galaxies, including the effect of a variable IMF on radial abundance gradients, as well as on the MLE– σ relation at high redshift. These simulations will be publicly available upon publication.

4.2 Simulations

In this paper we investigate IMF scaling relations using cosmological, hydrodynamical simulations that self-consistently vary the IMF on a per-particle basis. These simulations were presented in Paper I, and are based on the EAGLE model (Schaye et al. 2015; Crain et al. 2015; McAlpine et al. 2016). Here we give a brief overview of EAGLE

and the modifications made to self-consistently implement variable IMF prescriptions. We refer the reader to Schaye et al. (2015) and Paper I for further details.

The simulations were run using a heavily modified version of the Tree-PM smooth particle hydrodynamics (SPH) code Gadget-3 (Springel 2005), on a cosmological periodic volume of $(50 \text{ Mpc})^3$ with a fiducial “intermediate” particle mass of $m_g = 1.8 \times 10^6 M_\odot$ and $m_{\text{DM}} = 9.7 \times 10^6 M_\odot$ for gas and dark matter, respectively. The gravitational softening length was kept fixed at 2.66 comoving kpc prior to $z = 2.8$, switching to a fixed 0.7 proper kpc thereafter. Cosmological parameters were chosen for consistency with Planck 2013 in a Lambda cold dark matter cosmogony ($\Omega_b = 0.04825$, $\Omega_m = 0.307$, $\Omega_\Lambda = 0.693$, $h = 0.6777$; Planck Collaboration 2014).

The reference EAGLE model employs analytical prescriptions to model physical processes that occur below the resolution limit of the simulation (referred to as “subgrid” physics). The 11 elements that are most important for radiative cooling and photoheating of gas are tracked individually through the simulation, with cooling and heating rates computed according to Wiersma et al. (2009a) subject to an evolving, homogeneous UV/X-ray background (Haardt & Madau 2001). Once gas particles reach a metallicity-dependent density threshold that corresponds to the transition from the warm, atomic to the cold, molecular gas phase (Schaye 2004), they become eligible for stochastic conversion into star particles at a pressure-dependent star formation rate that reproduces the Kennicutt-Schmidt star formation law (Schaye & Dalla Vecchia 2008). Star particles represent coeval simple stellar populations that, in the reference model, adopt a Chabrier (2003) IMF. They evolve according to the lifetimes of Portinari et al. (1997), accounting for mass loss from winds from massive stars and AGB stars, as well as supernovae (SN) types II and Ia (Wiersma et al. 2009b). Stellar ejecta are followed element-by-element and are returned to the surrounding interstellar medium (ISM), along with thermal energetic stellar feedback (Dalla Vecchia & Schaye 2012) whose efficiency was calibrated to match the $z \approx 0$ galaxy stellar mass function (GSMF) and galaxy sizes. Supermassive black holes (BHs) are seeded in the central regions of high-mass dark matter haloes, and grow via accretion of low angular momentum gas (Springel et al. 2005; Booth & Schaye 2009; Rosas-Guevara et al. 2015) and mergers with other BHs, leading to thermal, stochastic active galactic nucleus (AGN) feedback (Schaye et al. 2015) that acts to quench star formation in high-mass galaxies.

The two simulations used in this study use the same subgrid physics prescriptions as the reference EAGLE model, except that the IMF is varied as a function of the pressure of the ISM from which individual star particles form. To ensure that the simulations remain self-consistent, the stellar mass loss, nucleosynthetic element production, stellar feedback, and star formation law are all modified to be consistent with the IMF variations (see Paper I for details). The variable IMF simulations have the same volume, initial conditions, and resolution as the Ref-L050N0752 (hereafter referred to as Ref-50) simulation of Schaye et al. (2015).

Our two variable IMF simulations differ only in their prescriptions for the IMF. In the first, which we refer to as LoM-50, the low-mass slope of the IMF (from 0.1 to $0.5 M_\odot$) is varied while the slope at higher masses remains fixed at the Kroupa (2001) value of -2.3 . In this prescription the IMF becomes bottom-heavy in high-

pressure environments, with the slope ranging from 0 to -3 in low- and high-pressure environments, respectively, transitioning smoothly between the two regimes via a sigmoid function over the range $P/k_B \approx 10^4 - 10^6 \text{ K cm}^{-3}$. Such a prescription produces stellar populations with larger stellar M/L ratios at high pressures due to an excess mass fraction of low-mass dwarf stars that contribute significantly to the mass but not to the light.

For the second simulation, hereafter HiM-50, we instead keep the low-mass slope fixed at the Kroupa value of -1.3 , and vary the high-mass slope (from 0.5 to $100 M_\odot$) from -2.3 to -1.6 with increasing birth ISM pressure, transitioning smoothly over the same pressure range as in the LoM-50 simulation. This prescription increases the M/L relative to a Kroupa IMF at high pressures by increasing the mass fraction of short-lived high-mass stars, resulting in a larger fraction of stellar remnants such as BHs, neutron stars, and white dwarfs, and lower luminosity once these high-mass stars have died off (after a few 100 Myr). Note that varying the IMF with pressure is essentially equivalent to varying it with star formation rate surface density, since the latter is determined by the former in the EAGLE model.

These IMF parametrizations were individually calibrated to match the observed trend between the excess mass-to-light ratio relative to that expected for a Salpeter IMF (hereafter the MLE) and central stellar velocity dispersion found by Cappellari et al. (2013b) for high-mass elliptical galaxies. This calibration was done in post-processing of the reference $(100 \text{ Mpc})^3$ EAGLE model (Ref-L100N1504) using the Flexible Stellar Population Synthesis (FSPS) software package (Conroy et al. 2009; Conroy & Gunn 2010). Specifically, the allowed range of IMF slopes and the pressure range over which the IMF gradually transitions from one slope to the other were tuned until an acceptable qualitative match to the Cappellari et al. (2013b) trend was obtained. We refer the reader to Paper I for further details on the calibration procedure. In Paper I we verified that the variable IMF runs reproduce the Cappellari et al. (2013b) trend between the MLE and velocity dispersion, but we also demonstrated that calibrating the IMF to reproduce that trend does not guarantee a match to other observational constraints on the IMF, such as the dwarf-to-giant ratio in ETGs or the ratio of ionizing to UV flux in star-forming galaxies.

In Paper I we also showed that our variable IMF simulations maintain agreement with the observables used to calibrate the EAGLE model: the present-day galaxy luminosity function, the relations between galaxy luminosity and half-light radius and black hole mass, and the global rate of type Ia SNe. This result may seem surprising given that the IMF governs the strength of stellar feedback, to which these calibration observables are quite sensitive (Crain et al. 2015). The fact that these galaxy observables are not strongly affected by the modified stellar feedback is likely due to the following (simplified) picture, which we separate into star-forming and quenched regimes:

If galaxy formation is self-regulated and if the outflow rate is large compared with the star formation rate, then the outflow rate will tend to adjust to balance the inflow rate when averaged over sufficiently long timescales. If we neglect preventative feedback and recycling, then the gas inflow rate tracks that of the dark matter and

does not depend on the IMF. If the IMF is modified, then a star-forming galaxy of fixed mass will adjust its star formation rate (SFR) to ensure that the same feedback energy is released in order to generate the same outflow rate that is needed to balance the inflow rate. For a top-heavy IMF, galaxies need to form fewer stars relative to the case of a standard IMF to obtain the same feedback energy. This results in lower SFRs, and thus lower ratios of stellar mass to halo mass, resulting in a lower normalization of the GSMF. However, for star-forming galaxies, M/L is lower due to the top-heavy IMF, so the luminosity at fixed halo mass ends up being similar to the Chabrier case. According to Booth & Schaye (2010) and Bower et al. (2017), BH mass is a function of halo mass (for sufficiently large halo masses) for a fixed AGN feedback efficiency, so the $M_{\text{BH}} - L$ relation is also not strongly affected. For a bottom-heavy IMF, this situation is reversed, where more stars are required to obtain the same feedback energy, increasing the GSMF, but their higher M/L ratios (due to an increased fraction of dwarf stars) makes the luminosity function (and the $M_{\text{BH}} - L$ relation) similar to the Chabrier case.

For low-mass galaxies these effects are small in our simulations, since the IMF only varies away from Chabrier at the high pressures typical of high-mass galaxies. In this regime, AGN feedback quenches galaxies at a particular virial temperature (or rather entropy; Bower et al. 2017), leading to an approximately fixed BH mass – halo mass relation (because M_{BH} must be sufficiently high to drive an outflow and quench star formation). For a top-heavy IMF, the lower $M_{\star}/M_{\text{halo}}$ (assuming the stellar mass formed when star-forming) leads to higher M_{BH}/M_{\star} and a lower GSMF. A quenched galaxy with a top-heavy IMF can have a higher or lower M/L depending on how long it has been quenched – if quenched for more than ≈ 3 Gyr, M/L is higher so the luminosity function cuts off at lower luminosity. However, since high-mass galaxies are not as strongly quenched in HiM-50, this effect is small. For a bottom-heavy IMF, everything is reversed: galaxies are quenched at higher M_{\star} , leading to a higher GSMF, but since M/L is higher, they quench at lower luminosity so the luminosity function remains similar.

In the intermediate mass regime (around the knee of the GSMF), the situation is more complex since both stellar feedback and AGN feedback play an important role in self-regulation and the star formation law becomes important (see Paper I). As noted above, a top-heavy IMF leads to a lower SFR because of the larger amount of feedback energy per unit stellar mass formed. This would imply a lower gas fraction, which would reduce the BH growth. However, this effect is counteracted by the decreased normalization of the observed star formation law at high pressures (relative to that of a standard IMF), which increases the gas surface densities at fixed star formation rate surface density. Thus, AGN feedback and BH growth are not strongly affected at fixed halo mass and galaxy luminosity. Again, the situation is reversed for bottom-heavy IMF variations. These effects, as well as the relatively poor statistics at the high-mass end relative to the $(100 \text{ Mpc})^3$ EAGLE simulation, likely eliminated any need to adjust the feedback parameters originally used to calibrate the EAGLE model.

Structures in the simulation are separated into “haloes” using a friends-of-friends halo finder with a linking length of 0.2 times the mean inter-particle spacing (Davis et al. 1985). Galaxies are identified within haloes as self-bound structures using the

SUBFIND algorithm (Springel et al. 2001; Dolag et al. 2009). We consider only galaxies with at least 500 stellar particles, corresponding to a stellar mass $M_* \approx 9 \times 10^8 M_\odot$. Galaxies in the mass range of interest in this study are sufficiently well resolved, as those with $\sigma_e > 80 \text{ km s}^{-1}$ have $M_* > 10^{10} M_\odot$, corresponding to $\gtrsim 5600$ stellar particles. Unless otherwise specified, all global galactic properties shown in this paper (e.g. MLE, age, metallicity, [Mg/Fe]) are computed considering star particles within the 2d projected half-light radius, r_e , of each galaxy, measured with the line-of-sight parallel to the z -axis of the simulation box.

4.3 Is the (M/L) -excess a good tracer of the IMF?

We wish to investigate trends between the IMF and global galaxy properties in a way that is testable with observations. Since dynamical studies use the MLE as a proxy for the IMF, it is important to check that this parameter correlates with the IMF for our galaxy sample. For each galaxy, we compute the MLE relative to the Salpeter IMF as

$$\text{MLE}_r = \log_{10}(M/L_r) - \log_{10}(M/L_r)_{\text{Salp}}, \quad (4.1)$$

where M and L_r are the true stellar mass and SDSS r -band luminosity of each galaxy, respectively, and $(M/L_r)_{\text{Salp}}$ is the stellar mass-to-light ratio that the galaxy would have had if evolved with a Salpeter IMF given the same distribution of ages, initial masses, and metallicities of its stars (note that $(M/L_r)_{\text{Salp}}$ is equivalent to the ratio between the Salpeter-inferred stellar mass [$L_r \times (M/L_r)_{\text{Salp}}$] and the true luminosity). Luminosities and masses of individual star particles are computed using FSPS¹, given each star particle’s age, metallicity, and IMF. We make no dust correction other than ignoring the luminosities of star particles with age $< 10 \text{ Myr}$, as such stars are expected to be obscured by their birth clouds (e.g. Charlot & Fall 2000).

In Fig. 4.1 we show MLE_r as a function of IMF slope for galaxies with $\sigma_e > 80 \text{ km s}^{-1}$ in our variable IMF simulations at $z = 0.1$, coloured by age. For LoM-50, MLE_r is an excellent tracer of the IMF, with very little dependence on age or metallicity. For HiM-50, MLE_r is only a good tracer of the IMF at fixed age (and, ideally, old age since the slope is very shallow for ages $\lesssim 3 \text{ Gyr}$), as can be seen by the strong vertical age gradient (i.e. the colour of the data points) at fixed high-mass slope in the right panel.

To compare our results with observed trends between MLE_r and galaxy properties in the literature, we select galaxies from our simulations using approximately the same selection criteria as the ATLAS^{3D} sample used by Cappellari et al. (2013b, hereafter C13). Their galaxy sample is complete down to $M_K = -21.5 \text{ mag}$, consisting of 260 morphologically-selected elliptical and lenticular galaxies, chosen to have old stellar populations ($H\beta$ equivalent width less than 2.3 \AA). For our “mock C13” sample, we select galaxies with $M_K < -21.5 \text{ mag}$ and intrinsic $u^* - r^* > 2$. The $u^* - r^*$ colour cut roughly separates galaxies in the red sequence from the blue cloud for EAGLE galaxies

¹We use the Basel spectral library (Lejeune et al. 1997, 1998; Westera et al. 2002) with Padova isochrones (Marigo & Girardi 2007; Marigo et al. 2008).

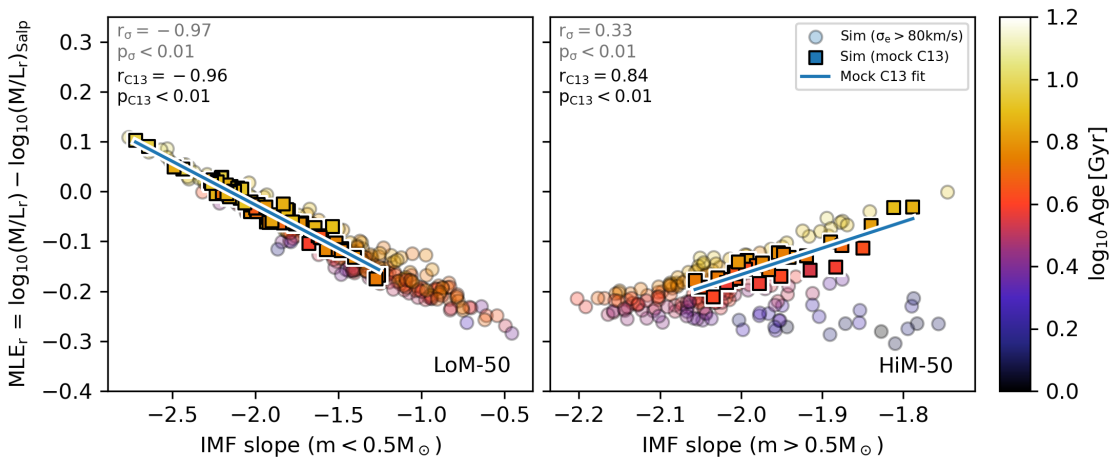


Figure 4.1: Excess r -band mass-to-light ratio relative to that for a Salpeter IMF as a function of IMF slope for galaxies with $\sigma_e > 10^{1.9}$ (≈ 80) km s^{-1} at $z = 0.1$, coloured by stellar age. All quantities are r -band light-weighted means measured within the 2d projected r -band half-light radius. The left and right panels show low-mass ($m < 0.5 M_{\odot}$) and high-mass ($m > 0.5 M_{\odot}$) IMF slopes for LoM-50 and HiM-50, respectively. Galaxies selected in a similar way to C13 (see text) are shown as opaque squares while all others are shown as translucent circles. The Pearson correlation coefficient, r , and its p -value are indicated in each panel for the $\sigma_e > 10^{1.9} \text{ km s}^{-1}$ and mock C13 samples in grey and black, respectively. Blue solid lines show least-squares fits to the mock C13 samples (see Table 4.1). MLE_r is an excellent proxy for the low-mass IMF slope variations, but is only a good proxy for high-mass slope variations for old galaxies, with age-dependent scatter.

(Correa et al. 2017) and ensures that we exclude galaxies with light-weighted ages younger than ≈ 3 Gyr.

The mock C13 galaxies are highlighted as opaque squares in Fig. 4.1. Since these galaxies are selected to be older than ≈ 3 Gyr, their MLE is a reasonable tracer of the IMF in HiM-50, but with more scatter than for LoM-50 due to the residual age dependence.² These dependencies should be kept in mind when interpreting the trends between the MLE_r and the global galaxy properties shown in the next section.

4.4 Trends between the (M/L)-excess and global galactic properties

There is currently much debate regarding possible trends between the IMF and global galaxy properties other than velocity dispersion, such as age, metallicity, and alpha enhancement. In this section we investigate these trends in our (self-consistent, calibrated) variable IMF simulations, where the IMF is governed by the local pressure in the ISM. In the left and right columns of Fig. 4.2 we show MLE_r as a function of these properties in LoM-50 and HiM-50, respectively, and compare with observed trends for ETGs from the ATLAS^{3D} survey (McDermid et al. 2014) and another sample from Conroy & van Dokkum (2012b). Note that while McDermid et al. (2014) measure MLE within a circular aperture of radius r_e , they (as well as Conroy & van Dokkum 2012b)³ measure age, metallicity, and $[Mg/Fe]$ within $r_e/8$. For many of our galaxies, $r_e/8$ would be close to the gravitational softening scale of the simulation. Indeed, performing our analysis within this aperture only serves to add resolution-related noise to the plots. Thus, since McDermid et al. (2014) claim that their results are unchanged for an aperture choice of r_e , we report our results consistently within r_e . For completeness we show all galaxies with $\sigma_e > 10^{1.9}$ (≈ 80) km s^{-1} (the σ_e -complete sample; translucent circles), but focus our comparison with observations on galaxies consistent with the C13 selection criteria (opaque squares). This σ_e limit of 80 km s^{-1} was chosen because it is the lowest σ_e value that our mock C13 samples reach.

4.4.1 MLE vs age

First we investigate the relationship between the MLE and galaxy age. In the top row of Fig. 4.2 we show MLE_r as a function of the L_r -weighted mean stellar age of galaxies in LoM-50 (left panel) and HiM-50 (right panel). For both simulations we see a strong trend of increasing MLE_r with age, where older galaxies tend to have higher (i.e. heavier) MLE_r . This result is in qualitative agreement with McDermid et al. (2014), but with a steeper slope for LoM-50, and smaller scatter for HiM-50. Note as well that the positive trend found by McDermid et al. (2014) is sensitive to the

²Note that the trend flattens at the Kroupa value for high-mass slopes steeper than -2.1 , and the trend would actually reverse if the high-mass slope were to become steeper than Salpeter (< -2.35).

³Also note that Conroy & van Dokkum (2012b) measure dynamical M/L within r_e but spectroscopic M/L within $r_e/8$.

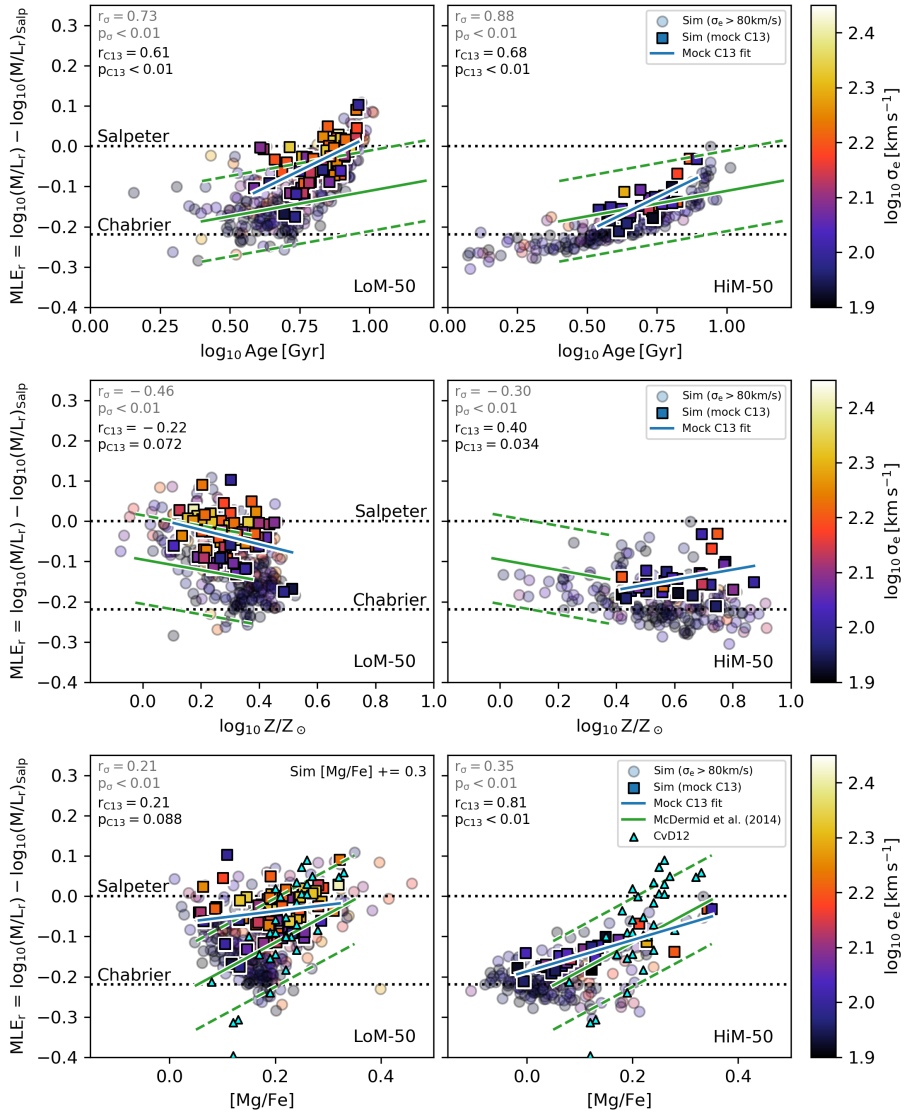


Figure 4.2: Excess r -band M/L -ratio with respect to that for a Salpeter IMF (MLE_r) as a function of r -band light-weighted mean age (top row), stellar metallicity (middle row) and stellar alpha-enhancement (bottom row), for galaxies with $\sigma_e > 10^{1.9}$ (≈ 80) km s^{-1} in the LoM-50 (left column) and HiM-50 (right column) simulations at $z = 0.1$. Points are coloured by σ_e . All quantities are computed within $(2d\text{-projected}) r_e$. Galaxies selected in a similar way to C13 (see text) are shown as opaque squares while all others are shown as translucent circles. Blue solid lines show least-squares fits to the mock C13 samples (see Table 4.1). The simulation values for $[\text{Mg}/\text{Fe}]$ have been increased by 0.3 dex for LoM-50. We assume $Z_{\odot} = 0.127$ and take other solar abundances from Asplund et al. (2009). We show the linear fits with 1σ scatter found in McDermid et al. (2014) as green-solid and -dashed lines, respectively, and the MLE_r - $[\text{Mg}/\text{Fe}]$ relation of Conroy & van Dokkum (2012b) as cyan triangles. Metallicities from McDermid et al. (2014) have been converted to our solar scale. For both variable IMF simulations we see strong positive correlations of MLE_r with age and $[\text{Mg}/\text{Fe}]$. When considering all galaxies with $\sigma_e > 80 \text{ km s}^{-1}$, we find a weak but significant negative correlation with Z for both simulations, but the correlation disappears for mock C13 galaxies.

Table 4.1: Fit parameters to the r -band mass-to-light ratio excess, MLE_r , for mock C13 galaxies in our variable IMF simulations. Columns 2 and 3 show the result of a linear least-squares fit of the relation between each parameter (indicated in Column 1) individually and MLE_r , of the form $\text{MLE}_r = \alpha x + b$. Column 4 shows the coefficient of determination, while columns 5 and 6 show the Spearman- r value and the corresponding p -value.

x	a	b	R^2	Spearman r	p
LoM-50					
$\log_{10} P_{\text{birth}} / (\text{K cm}^{-3})$	0.12 ± 0.00	-0.69 ± 0.02	0.96	0.99	< 0.01
$\log_{10} \sigma_e / (\text{km s}^{-1})$	0.22 ± 0.05	-0.52 ± 0.11	0.22	0.48	< 0.01
$\log_{10} \text{Age}/\text{Gyr}$	0.34 ± 0.06	-0.32 ± 0.05	0.32	0.61	< 0.01
$\log_{10} Z/Z_{\odot}$	-0.18 ± 0.08	0.01 ± 0.02	0.08	-0.22	0.07
[Mg/Fe]	0.16 ± 0.10	-0.02 ± 0.01	0.04	0.21	0.09
$\log_{10} r_e/\text{kpc}$	-0.04 ± 0.04	-0.01 ± 0.02	0.02	-0.06	0.65
$\log_{10} M_{*,\text{Chab}}$	0.08 ± 0.03	-0.92 ± 0.29	0.12	0.38	< 0.01
$M_K - 5 \log_{10} h$	-0.02 ± 0.01	-0.53 ± 0.25	0.06	-0.26	0.03
$\log_{10} M_{\text{BH}}/M_{*}$	0.11 ± 0.02	0.31 ± 0.06	0.34	0.46	< 0.01
$\log_{10} \sigma_e^2/r_e [\text{km}^2 \text{s}^{-2} \text{kpc}^{-1}]$	0.15 ± 0.02	-0.59 ± 0.09	0.37	0.56	< 0.01
HiM-50					
$\log_{10} P_{\text{birth}} / (\text{K cm}^{-3})$	0.07 ± 0.01	-0.51 ± 0.03	0.87	0.91	< 0.01
$\log_{10} \sigma_e / (\text{km s}^{-1})$	0.19 ± 0.08	-0.52 ± 0.15	0.18	0.48	< 0.01
$\log_{10} \text{Age}/\text{Gyr}$	0.34 ± 0.06	-0.38 ± 0.04	0.53	0.68	< 0.01
$\log_{10} Z/Z_{\odot}$	0.13 ± 0.06	-0.22 ± 0.04	0.15	0.39	0.04
[Mg/Fe]	0.39 ± 0.05	-0.19 ± 0.01	0.72	0.81	< 0.01
$\log_{10} r_e/\text{kpc}$	0.12 ± 0.08	-0.24 ± 0.06	0.09	0.24	0.21
$\log_{10} M_{*,\text{Chab}}$	0.09 ± 0.04	-1.10 ± 0.40	0.17	0.36	0.06
$M_K - 5 \log_{10} h$	-0.02 ± 0.02	-0.66 ± 0.34	0.08	-0.21	0.26
$\log_{10} M_{\text{BH}}/M_{*}$	-0.01 ± 0.02	-0.16 ± 0.06	< 0.01	0.24	0.21
$\log_{10} \sigma_e^2/r_e [\text{km}^2 \text{s}^{-2} \text{kpc}^{-1}]$	0.08 ± 0.05	-0.40 ± 0.15	0.10	0.36	0.06

Table 4.2: As in Table 4.1 but for all galaxies with $\sigma_e > 10^{1.9} \text{ km s}^{-1}$.

x	a	b	R^2	Spearman r	p
LoM-50					
$\log_{10} P_{\text{birth}} / (\text{K cm}^{-3})$	0.12 ± 0.00	-0.70 ± 0.01	0.96	0.98	< 0.01
$\log_{10} \sigma_e / (\text{km s}^{-1})$	0.28 ± 0.03	-0.68 ± 0.07	0.18	0.45	< 0.01
$\log_{10} \text{Age}/\text{Gyr}$	0.37 ± 0.02	-0.37 ± 0.02	0.46	0.72	< 0.01
$\log_{10} Z/Z_{\odot}$	-0.32 ± 0.03	0.00 ± 0.01	0.22	-0.47	< 0.01
[Mg/Fe]	0.28 ± 0.06	-0.06 ± 0.01	0.07	0.21	< 0.01
$\log_{10} r_e / \text{kpc}$	-0.14 ± 0.02	-0.01 ± 0.01	0.17	-0.39	< 0.01
$\log_{10} M_{\star, \text{Chab}}$	0.04 ± 0.01	-0.57 ± 0.15	0.03	0.14	0.01
$M_K - 5 \log_{10} h$	0.00 ± 0.01	-0.03 ± 0.12	< 0.01	0.04	0.45
$\log_{10} M_{\text{BH}}/M_{\star}$	0.13 ± 0.01	0.32 ± 0.03	0.41	0.68	< 0.01
$\log_{10} \sigma_e^2 / r_e [\text{km}^2 \text{ s}^{-2} \text{ kpc}^{-1}]$	0.20 ± 0.01	-0.82 ± 0.04	0.50	0.72	< 0.01
HiM-50					
$\log_{10} P_{\text{birth}} / (\text{K cm}^{-3})$	0.05 ± 0.01	-0.38 ± 0.03	0.23	0.39	< 0.01
$\log_{10} \sigma_e / (\text{km s}^{-1})$	0.06 ± 0.04	-0.28 ± 0.09	< 0.01	0.12	0.10
$\log_{10} \text{Age}/\text{Gyr}$	0.22 ± 0.01	-0.30 ± 0.01	0.68	0.87	< 0.01
$\log_{10} Z/Z_{\odot}$	-0.08 ± 0.02	-0.12 ± 0.01	0.07	-0.30	< 0.01
[Mg/Fe]	0.32 ± 0.04	-0.19 ± 0.00	0.27	0.36	< 0.01
$\log_{10} r_e / \text{kpc}$	0.07 ± 0.02	-0.22 ± 0.02	0.03	0.28	< 0.01
$\log_{10} M_{\star, \text{Chab}}$	-0.05 ± 0.01	0.34 ± 0.13	0.07	-0.24	< 0.01
$M_K - 5 \log_{10} h$	0.03 ± 0.00	0.42 ± 0.09	0.18	0.39	< 0.01
$\log_{10} M_{\text{BH}}/M_{\star}$	0.05 ± 0.01	-0.03 ± 0.02	0.21	0.52	< 0.01
$\log_{10} \sigma_e^2 / r_e [\text{km}^2 \text{ s}^{-2} \text{ kpc}^{-1}]$	-0.02 ± 0.02	-0.11 ± 0.06	< 0.01	-0.09	0.19

methodology used, and in fact disappears when $(M/L_r)_{\text{Salp}}$ is derived from individual line strengths rather than full spectral fitting. It is thus quite interesting that we find strong positive correlations with age for both simulations.

For LoM-50, this trend is driven by the higher pressures at which stars form at higher redshift (as was shown for Ref-50 by Crain et al. 2015 and will be investigated further for our simulations in Paper III), yielding more bottom-heavy IMFs for older ages. For HiM-50, the trend with age is tighter due to the fact that, in addition to the trend of higher birth ISM pressure with increasing formation redshift, the MLE_r increases with age for a stellar population with a top-heavy IMF, even if the IMF is fixed. The result is that, even though the IMF itself depends only on birth ISM pressure, in the end the MLE_r correlates more strongly with age than with IMF slope (compare the upper-right panel of Fig. 4.2 with the right panel of Fig. 4.1; also Fig. 2 of Paper I). This is especially true for the σ_e -complete sample due to its large range of ages, while the age dependence is reduced for the mock C13 sample due to the exclusion of young galaxies.

We also note that galaxies with $\sigma_e > 80 \text{ km s}^{-1}$ in HiM-50 extend to quite young ages ($< 1 \text{ Gyr}$), whereas in the LoM-50 case only a handful of galaxies are $< 3 \text{ Gyr}$ old (although the $u^* - r^*$ selection criterion removes all galaxies with light-weighted ages younger than 3 Gyr in our mock C13 samples). This age difference is due to the higher SFRs in the HiM-50 simulation relative to LoM-50, which were discussed in Paper I. We remind the reader that we ignore the luminosities of star particles with ages less than 10 Myr. Without this cut, the age and MLE_r would extend to even lower values due to the ongoing star formation in HiM-50 galaxies.

We conclude that both LoM-50 and HiM-50 agree qualitatively with the positive trend of MLE_r with age inferred from the ATLAS^{3D} survey by McDermid et al. (2014), but with a stronger correlation. We encourage other observational IMF studies to measure the correlation between IMF diagnostics and age as well in order to help test these predictions.

4.4.2 MLE vs metallicity

Observationally, evidence for trends between the IMF and metal abundances have been reported, but with conflicting results. While spectroscopic studies find strong positive trends of bottom-heaviness with local metallicity (Martín-Navarro et al. 2015c; Conroy et al. 2017), dynamical studies find no significant correlation between MLE_r and global metallicity (McDermid et al. 2014; Li et al. 2017). In the middle row of Fig. 4.2 we plot MLE_r vs (dust-free) L_r -weighted metallicity measured within r_e . We assume $Z_{\odot} = 0.0127$ and convert observationally-derived metallicities from the literature to this scale. The offset of HiM-50 galaxies toward higher metallicities is due to the higher nucleosynthetic yields resulting from a top-heavy IMF, as discussed in Paper I.

For both variable IMF simulations, we see a weak but significant trend of decreasing MLE_r with metallicity for the sample with $\sigma > 80 \text{ km s}^{-1}$. For both LoM-50 and HiM-50, the negative correlation of MLE_r with metallicity is a consequence of the positive and negative relationships of the MLE_r and Z , respectively, with age. Interestingly,

in HiM-50 the negative correlation with metallicity is weaker than in LoM-50 despite the stronger dependence of MLE_r on age. This is the result of the strong effect that a top-heavy IMF has on the metal yields. At fixed age, a galaxy with higher MLE has on average an IMF with a shallower high-mass slope, resulting in higher metal yields and thus higher metallicities. The effect is strongest for the oldest galaxies where the scatter in MLE_r is greatest (see upper right panel of Fig. 4.2). Thus, the oldest galaxies with high MLE_r that would have had low metallicity with a Chabrier IMF get shifted toward higher metallicity in the middle-right panel of Fig. 4.2, reducing the strength of the negative $\text{MLE}_r - Z$ correlation.

Restricting our sample to the mock C13 galaxies, the negative trend with Z is weaker and no longer significant for LoM-50, and is weakly positive for HiM-50. The negative trend for HiM-50 disappears for this sample because we remove the low-metallicity, old galaxies with intermediate MLE that help drive the negative trend in the σ_e -complete selection. These galaxies are excluded from the mock C13 selection due to the luminosity cut. The weakness of these trends is in agreement with the weakly negative but non-significant correlation of McDermid et al. (2014), as well as the lack of correlation found by Li et al. (2017). Interestingly, our results are in stark contrast with the positive correlation between the IMF slope and spatially-resolved *local* local metallicity of Martín-Navarro et al. (2015c). We make a fairer comparison to their result in Paper III, where we show that locally we do in fact find a positive correlation between MLE_r and metallicity.

We conclude that, for a σ_e -complete sample of galaxies, the MLE_r is predicted to anticorrelate with total stellar metallicity for low-mass IMF slope variations, while being relatively insensitive to metallicity for high-mass slope variations. In both cases these correlations disappear for samples consistent with the selection criteria of the ATLAS^{3D} survey, in agreement with dynamical studies.

4.4.3 MLE vs [Mg/Fe]

In the bottom row of Fig. 4.2 we plot MLE_r as a function of $[\text{Mg}/\text{Fe}]^4$, both measured within r_e . For LoM-50 we increase the $[\text{Mg}/\text{Fe}]$ values by 0.3 dex to facilitate comparison with the observed trends. This procedure is somewhat arbitrary, but is motivated by the fact that Segers et al. (2016) showed that $[\text{Mg}/\text{Fe}]$ is underestimated by EAGLE and that the nucleosynthetic yields are uncertain by about a factor of 2 (Wiersma et al. 2009b); thus the slopes of these trends are more robust than the absolute values. This procedure is not necessary for HiM-50 due to the increased metal production resulting from a top-heavy IMF (see Fig. 9 of Paper I).

For both simulations, for the $\sigma_e > 80 \text{ km s}^{-1}$ selection we see weak but significant positive correlations between MLE_r and $[\text{Mg}/\text{Fe}]$. When selecting only mock C13 galaxies, the trend for LoM-50 is still positive but no longer significant. These trends are in qualitative agreement with the positive trends found by Conroy & van Dokkum (2012b) and McDermid et al. (2014), and highlight the importance of sample selection in determining the significance of these correlations. For HiM-50, the $\text{MLE}_r - [\text{Mg}/\text{Fe}]$

⁴Solar abundances for Mg and Fe are taken from Asplund et al. (2009).

relation is stronger than in LoM-50, likely due to a combination of the fact that $[\text{Mg}/\text{Fe}]$ correlates strongly with age in high-mass galaxies (Segers et al. 2016) and the fact that the $[\text{Mg}/\text{Fe}]$ ratios are strongly affected by the shallow high-mass IMF slopes resulting from the HiM IMF parametrization (see Paper I). The correlation strengthens for the mock C13 selection due to the exclusion of young, blue galaxies with intermediate $[\text{Mg}/\text{Fe}]$ values, although given the low number of high- $[\text{Mg}/\text{Fe}]$ mock C13 galaxies in HiM-50, the strength of this correlation may be sensitive to our mock C13 selection criteria.

In Section 4.4.6 we show that the trend between MLE_r and $[\text{Mg}/\text{Fe}]$ for LoM-50 galaxies is solely due to the correlation between $[\text{Mg}/\text{Fe}]$ and σ_e , while that for HiM-50 is partially due to the correlation between $[\text{Mg}/\text{Fe}]$ and age. The former is consistent with La Barbera et al. (2015) who found that, while the observations are consistent with a correlation between MLE and $[\text{Mg}/\text{Fe}]$, this correlation disappears at fixed central velocity dispersion.

4.4.4 MLE vs Chabrier-inferred galaxy mass, luminosity, and size

In order to build intuition on how the IMF varies from galaxy to galaxy, it is also useful to predict trends between the MLE and other basic galactic properties that have not yet been investigated observationally. In Fig. 4.3 we show the MLE_r as a function of, from top to bottom, Chabrier-interpreted stellar mass ($M_{*,\text{Chab}}$), K -band luminosity, and 2D projected half-light radius for LoM-50 (left column) and HiM-50 (right column) for all galaxies with $\sigma_e > 10^{1.6} \text{ km s}^{-1}$, coloured by σ_e . Note that we now include galaxies of lower σ_e than in Fig. 4.2 to facilitate comparison with the $\text{MLE}_r - \sigma_e$ relation shown in Fig. 5 of Paper I, and to show the full transition from Chabrier-like to bottom- or top-heavy IMFs over a wide range of masses and luminosities. Those that would be selected by ATLAS^{3D} (i.e. are in our mock C13 samples) are shown as opaque squares, while others are shown as translucent circles. $M_{*,\text{Chab}}$ is computed by multiplying each galaxy's K -band luminosity by the stellar M/L_K that it would have had if its stellar populations had evolved with a Chabrier IMF (given the same ages and metallicities). Note that this is still not exactly the same as would be inferred observationally, as it does not take into account possible biases in the inferred ages or metallicities due to IMF variations.

The top row shows MLE_r as a function of $M_{*,\text{Chab}}$. For LoM-50 we see a strong trend of increasing bottom-heaviness with mass for galaxies with $M_{*,\text{Chab}} > 10^{10} M_\odot$. Galaxies below this limit tend to have Chabrier-like IMFs. The scatter here is stronger than in the $\text{MLE}_r - \sigma_e$ relation, leading to a somewhat weaker correlation of MLE_r with $M_{*,\text{Chab}}$ for LoM-50. In agreement with Clauwens et al. (2015), galaxies in our mock C13 sample are only complete down to $M_{*,\text{Chab}} \approx 10^{10.5} M_\odot$, much higher than the $6 \times 10^9 M_\odot$ quoted by Cappellari et al. (2013a). For HiM-50, it is only for the mock C13 galaxies that we see even a weakly positive relation between MLE_r and $M_{*,\text{Chab}}$ due to a bias toward high-MLE galaxies at high mass due to the cut in $u^* - r^*$: at fixed mass, galaxies with low MLE tend to be younger, and thus bluer, and are more likely to be excluded from our mock C13 sample. However, in contrast to the significant,

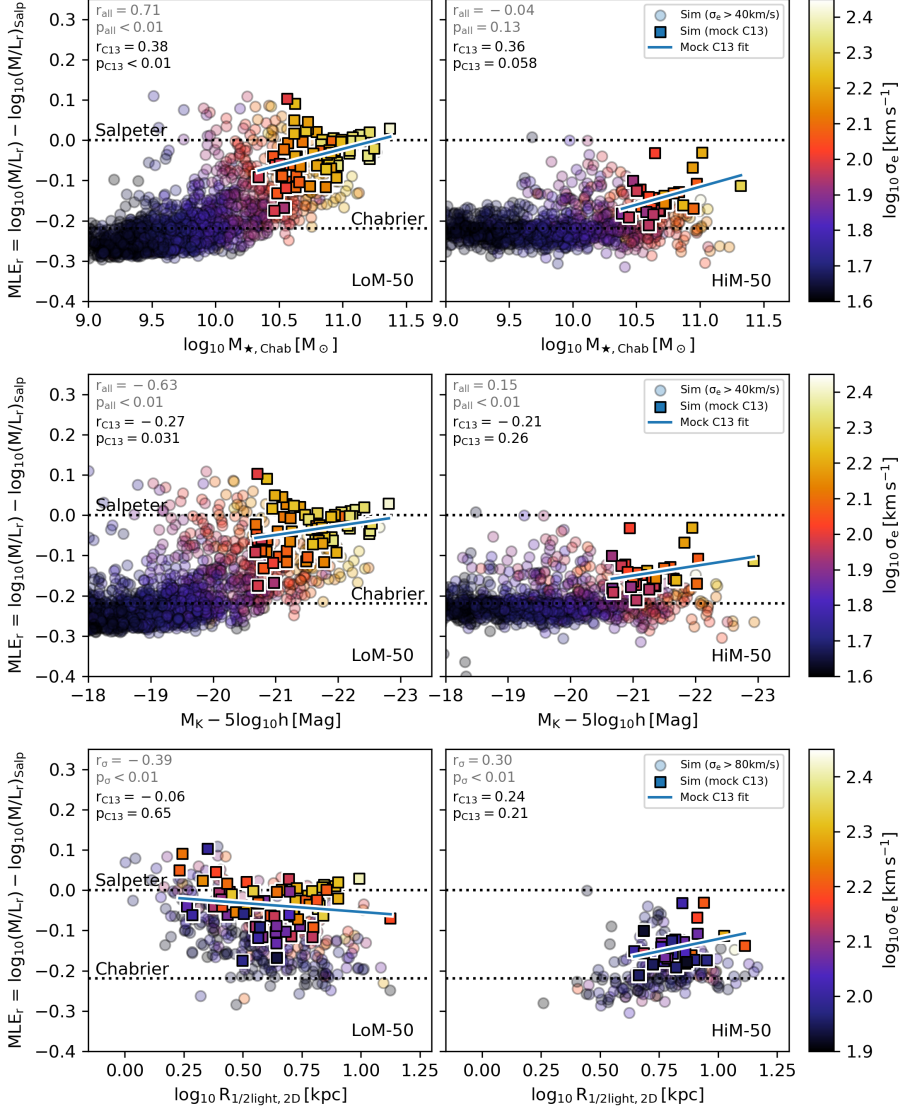


Figure 4.3: As Fig. 4.2 but now showing M/L_r excess as a function of, from top to bottom, stellar mass reinterpreted assuming a Chabrier IMF, K-band absolute magnitude, and projected r -band half-light radius. For completeness we include all galaxies with $\sigma_e > 10^{1.6} (\approx 40) \text{ km s}^{-1}$ in the upper two rows, while the lower row shows galaxies with $\sigma_e > 10^{1.9} (\approx 80) \text{ km s}^{-1}$. We see roughly the same trends of MLE_r with $M_{\star, \text{Chab}}$ and M_K as with σ_e (see Fig. 5 of Paper I), but with greater scatter. In LoM-50, smaller high- σ_e galaxies tend to form the more bottom-heavy populations, while larger counterparts form the more top-heavy populations in HiM-50.

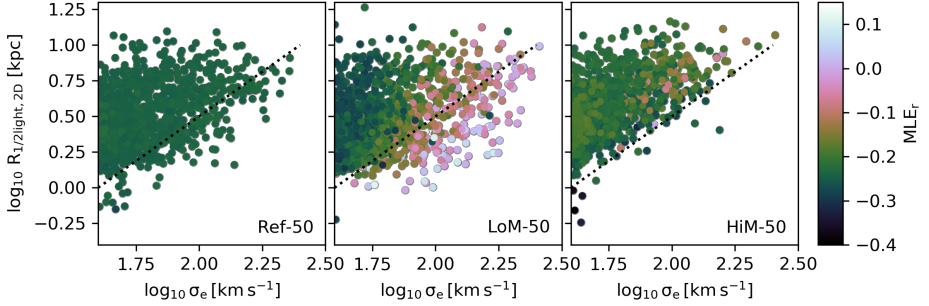


Figure 4.4: Effect of IMF variations on the relation between r -band half-light radius and σ_e . We show all galaxies with $\sigma_e > 10^{1.6} \text{ km s}^{-1}$ at $z = 0.1$ in, from left to right, Ref-50, LoM-50 and HiM-50, respectively. Points are coloured by MLE_r . The same (arbitrary) dotted line is repeated in each panel to guide the eye. Galaxies that are smaller at fixed σ_e have larger MLE_r in LoM-50. In HiM-50, the $r_e - \sigma_e$ relation is tighter, likely due to the stronger feedback in high-pressure (i.e. top-heavy IMF) environments.

positive $\text{MLE}_r - \sigma_e$ correlation for this sample, this positive $\text{MLE}_r - M_{*,\text{Chab}}$ relation for mock C13 HiM-50 galaxies is not significant, and may be sensitive to the way in which mock C13 galaxies are selected. Note that using true M_* on the x -axis rather than $M_{*,\text{Chab}}$ would shift the highest-MLE galaxies to larger mass by $\approx 0.2 - 0.3$ dex, and using Salpeter-inferred M_* would shift all points systematically to higher mass by 0.22 dex, neither of which would make any difference to these results.

The middle row of Fig. 4.3 shows MLE_r as a function of K-band absolute magnitude. For both simulations the trend is very similar to that with $M_{*,\text{Chab}}$, but with a shallower slope (in this case the positive relation between the MLE_r and luminosity yields a negative Spearman r for the correlation with magnitude).

The bottom row shows MLE_r as a function of 2D projected r -band half-light radius, r_e . In this row we show only galaxies with $\sigma_e > 10^{1.9} \text{ km s}^{-1}$ (as in Fig. 4.2) to remove the high number of low-mass galaxies with Chabrier-like IMFs that would reduce the significance of any correlation. Here, the two simulations show markedly different behaviour. While MLE_r decreases with r_e for LoM-50, it increases for HiM-50. To help explain this behaviour, we plot in Fig. 4.4 the $r_e - \sigma_e$ relation for each simulation, coloured by MLE_r (note that this figure contains the same information as the bottom row of Fig. 4.3). For HiM-50 (right panel), we see a positive correlation between r_e and σ_e , with no noticeable gradient in MLE_r at fixed σ_e . Thus, for HiM-50 the $\text{MLE}_r - r_e$ relation matches qualitatively the $\text{MLE}_r - \sigma_e$ relation.

In the middle panel of Fig. 4.4, we see that, as in HiM-50, LoM-50 galaxies increase in size with increasing σ_e , but they also exhibit stronger scatter in the $r_e - \sigma_e$ relation toward smaller galaxies. There is a strong MLE_r gradient at fixed σ_e here, where, at fixed σ_e , smaller galaxies tend to have larger MLE_r , resulting in a negative correlation between MLE_r and r_e at fixed σ_e . This anti-correlation counteracts the (positive) $\text{MLE}_r - \sigma_e$ relation, resulting in a net negative correlation between MLE_r and r_e for the σ_e -complete sample in LoM-50 (lower left panel of Fig. 4.3). Interestingly, the trend disappears for the mock C13 sample as many of the smallest (and thus highest MLE_r)

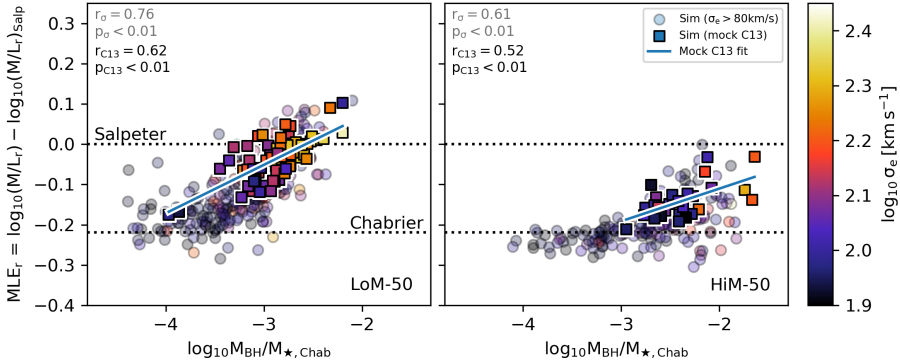


Figure 4.5: As Fig. 4.2 but now showing the stellar MLE_r as a function of the ratio between M_{BH} and the stellar mass inferred assuming a Chabrier IMF, $M_{*,\text{Chab}}$. In both variable IMF simulations we see a clear trend of increasing MLE_r of the stellar population with higher $M_{\text{BH}}/M_{*,\text{Chab}}$. This result shows that an observed correlation between MLE_r and $M_{\text{BH}}/M_{*,\text{Chab}}$ does not necessarily imply that M_{BH} is systematically underestimated for high $M_{\text{BH}}/M_{*,\text{Chab}}$ objects. Instead, the trend may be real and a signpost for a variable IMF. The correlations for LoM-50 and HiM-50 come mostly from the fact that galaxies with enhanced $M_{\text{BH}}/M_{*,\text{Chab}}$ tend to originate in higher-pressure and older environments, respectively (Barber et al. 2016).

high- σ_e galaxies are excluded due to the luminosity cut, causing these two effects (positive $MLE_r - \sigma_e$ relation coupled with negative $MLE_r - r_e$ at fixed σ_e) to roughly cancel out.

This behaviour can be explained by the impact of these variable IMF prescriptions on feedback, and thus r_e , at fixed σ_e . In both cases, galaxies that are smaller at fixed σ_e tend to have formed their stars at higher pressures, giving them larger MLE_r values. In LoM-50, such galaxies experience weaker feedback due to their bottom-heavy IMFs, further decreasing their sizes relative to galaxies of similar σ_e in Ref-50 (compare the middle and left panels of Fig. 4.4). The behaviour is different for HiM-50 due to the fact that galaxies that form at high pressure instead experience stronger feedback due to the top-heavy IMF. This enhanced feedback increases their sizes due to the increased macroscopic efficiency of the ejection of low-angular momentum gas, pushing them upward in the right panel of Fig. 4.4 (or to the right in the lower right panel of Fig. 4.3). Interestingly, this feedback effect tightens the relationship between r_e and σ_e relative to the Ref-50 simulation, resulting in an $MLE_r - r_e$ relation that matches qualitatively the $MLE_r - \sigma_e$ relation.

4.4.5 MLE_r vs M_{BH}/M_*

Some studies (e.g. Pechetti et al. 2017) have speculated that the extra dynamical mass inferred in the centres of massive ETGs may be due to an overmassive BH, rather than a variable IMF. For example, NGC 1277 has been found to have an overmassive BH (van den Bosch et al. 2012; Walsh et al. 2016) as well as a bottom-heavy IMF (Martín-Navarro et al. 2015d). If central BH masses are computed assuming a stellar population with a Chabrier IMF, while dynamical stellar M/L ratios are inferred assuming central

BH masses that lie on the observed $M_{\text{BH}} - \sigma$ relation (e.g. Cappellari et al. 2013a), one would expect a positive correlation between these quantities due to independent studies assigning the excess dynamical mass to either a heavier stellar population or to a massive BH.

It was shown by Barber et al. (2016) that in the reference EAGLE model, which assumes a universal Chabrier IMF, older galaxies tend to have higher BH masses at fixed stellar mass. Since we saw a strong trend between the MLE_r and age in Section 4.4.3, we thus investigate if there is also a trend between the MLE_r and $M_{\text{BH}}/M_{*,\text{Chab}}$, shown in Fig. 4.5 for our galaxy sample. For both variable IMF simulations, we see a significant positive correlation, where galaxies with high $M_{\text{BH}}/M_{*,\text{Chab}}$ also tend to have heavier MLE_r . Interestingly, we find a stronger trend of MLE_r with $M_{\text{BH}}/M_{*,\text{Chab}}$ for LoM-50 than for HiM-50. This indicates that the trend is not driven by age, but rather by the fact that the high-pressure environments that lead to the assignment of a heavy IMF also tend to foster the production of overmassive BHs. We have checked that these trends are qualitatively unchanged if using the true M_* values on the x -axis instead, except with a systematic decrease in M_{BH}/M_* of $\approx 0.1 - 0.2$ dex. We have thus shown that if the IMF is truly becoming more heavy in high-pressure environments (and hence for higher velocity dispersions), and there is no confusion between the BH mass and stellar mass, we still obtain a positive trend between MLE_r and M_{BH}/M_* . Thus, observation of this trend does not necessarily imply that the inferred M/L ratios are increasing due to a systematic underestimate of the BH masses in these high- M_{BH}/M_* galaxies.

The predicted correlation between MLE_r and $M_{\text{BH}}/M_{*,\text{Chab}}$ has important implications for the dynamical measurement of BH masses, especially for recently observed galaxies with puzzlingly overmassive BHs. Both of our IMF prescriptions predict a higher *stellar* M/L ratio in such galaxies, which must be taken into account when inferring BH masses. Indeed, for our LoM IMF prescription, one would underestimate the stellar mass by a factor of two if one assumes a M/L ratio consistent with a Chabrier IMF when converting the K-band luminosity to M_* , which would result in an overestimation of M_{BH} . Both the underestimate of M_* and the overestimate of the M_{BH} serve to artificially increase the ratio $M_{\text{BH}}/M_{*,\text{Chab}}$. Thus, we suggest that authors who find overmassive black holes in high-mass galaxies consider the possibility that *also* the IMF may be either top- or bottom-heavy in these systems.

Indeed, one may turn this argument around and suggest that if one were to seek galaxies with non-Milky Way IMFs, a promising place to look is in galaxies with abnormally high M_{BH}/M_* , such as NGC 1277, NGC 1271 (Walsh et al. 2015), and ultra-compact dwarf (UCD) galaxies for which BH mass measurements are available (e.g. M60-UCD1, Seth et al. 2014, although tidal stripping may be responsible for the high BH masses in UCDs; Barber et al. 2016).

4.4.6 Which observables correlate most strongly with the MLE?

We now determine which of the observable parameters σ_e , age, [Mg/Fe], metallicity, and r_e best predict MLE_r .⁵ To do so, we first standardize the logarithm of each parameter such that the mean and dispersion are 0 and 1, respectively, and perform an ordinary linear regression fit to the (standardized) MLE_r using all of these parameters simultaneously. We then determine the change in the adjusted coefficient of determination, R^2 , when each variable is added to the model last, a quantity we will denote as ΔR^2 . Since R^2 gives us the fraction of the variance in MLE_r that is explained by the variance in the parameters of the model, ΔR^2 gives us insight into the fraction of the variance in MLE_r that can be accounted for by the variance in each parameter individually, taking into account the information available through the other input parameters. Note that the sum of ΔR^2 values will only equal the total R^2 if all of the input variables are completely uncorrelated. For example, two input variables that are strongly correlated will each have $\Delta R^2 \approx 0$, even if individually they can explain much of the scatter in MLE_r . Thus, to gain a sense of the contribution of each variable to the total variance in MLE_r , we rescale the ΔR^2 values such that they sum to R^2 .

We first perform this analysis on the mock C13 samples, as they should be more directly comparable to galaxy samples in observational IMF studies. The total R^2 values (i.e. the fraction of the variance in MLE_r that can be explained by all of these parameters) are 0.53 and 0.89 for LoM-50 and HiM-50, respectively. For LoM-50, we find that σ_e , r_e , and age are the most important variables, with $\Delta R^2 = 0.20, 0.20$, and 0.14 , respectively, with much smaller contributions from metallicity and [Mg/Fe]. For HiM-50, [Mg/Fe] is the most important parameter with $\Delta R^2 = 0.45$, followed by age (0.34) and metallicity (0.12), with negligible contribution from σ_e or r_e . These results are summarized in Table 4.3.

We conclude that, in a scenario in which the IMF varies at the low-mass end and in such a way as to give the observed trend between MLE_r and σ_e (LoM), then when all other variables are kept fixed we obtain the strongest trend of MLE_r with σ_e , r_e , and age, with little to no *residual* dependence on metallicity or [Mg/Fe]. The strong trends with σ_e , r_e , and age in our simulations come from the correlation between these parameters and birth ISM pressure, which governs the IMF variations. Indeed, if we include mean light-weighted birth ISM pressure in the fits, the total R^2 increases to 0.97 , and ΔR^2 drops to < 0.002 for all of the other input variables, while that for birth ISM pressure is 0.44 .⁶

On the other hand, if the IMF varies at the high-mass end (HiM), we find that the MLE_r depends mainly on the age and [Mg/Fe] of the system, with a secondary dependence on metallicity. The strong contribution from [Mg/Fe] comes from the fact that [Mg/Fe] correlates strongly with birth ISM pressure in HiM-50 galaxies, likely

⁵Note that in this analysis we leave out mass and luminosity because these are used to compute MLE in the first place, so correlations between them and the MLE would not be as meaningful.

⁶Note that R^2 is not exactly 1.0 even when correlating MLE with birth ISM pressure directly, due to the fact that the MLE is averaged over many star particles with a potentially wide range of M/L ratios, and that the MLE is not a perfect measure of the IMF even for individual star particles due to some age and metallicity dependence.

due to the enhanced Mg yields resulting from the IMF becoming top-heavier towards higher pressure environments. Indeed, for the HiM-50 simulation, the correlation between $[\text{Mg}/\text{Fe}]$ and birth ISM pressure is stronger than that between σ_e and birth ISM pressure, eliminating a need to include σ_e in the fit to the MLE when $[\text{Mg}/\text{Fe}]$ is also included. Remarkably, we find that even adding birth ISM pressure to the list of parameters in the above procedures does not add much new information. In this case, total R^2 increases from 0.89 to 0.96, with $\Delta R^2 = 0.52$ and 0.45 for age and birth ISM pressure, respectively, with negligible contributions from the other input variables. The strong age contribution is due to the dependence of the MLE_r on age when the high-mass slope is shallower than the Salpeter value. Indeed, this age dependence would exist even for a non-variable top-heavy IMF. Note as well that a fit to MLE_r using only birth ISM pressure as an input variable results in $R^2 = 0.97$ and 0.87 for LoM-50 and HiM-50, respectively (see Table 4.1). This result highlights the importance of age on the MLE_r for high-mass, but not low-mass, IMF slope variations.

For completeness, we repeat this analysis for the full sample of galaxies with $\sigma_e > 10^{1.9} \text{ km s}^{-1}$, rather than only those that would have been selected by C13. The results are presented in Tables 4.2 and 4.4. For LoM-50, we find qualitatively the same conclusions as for the mock C13 sample, except that now r_e provides much more information than it did for the mock C13 sample (compare Tables 4.3 and 4.4), due to the inclusion of compact galaxies with high σ_e that are too dim to be included in the mock C13 sample. For HiM-50, age, rather than $[\text{Mg}/\text{Fe}]$, becomes the dominant contributor to the scatter in MLE_r due to the inclusion of young galaxies in the σ_e -complete sample (see Fig. 4.1). These results highlight the importance of sample selection in determining with which property the IMF correlates most strongly.

Finally, we wish to address the question of whether the MLE correlates more strongly with σ_e or $[\text{Mg}/\text{Fe}]$. Repeating the analysis above for mock C13 galaxies but now only including σ_e and $[\text{Mg}/\text{Fe}]$ in the input parameters, we find that for LoM-50, we obtain $R^2 = 0.19$, with $\Delta R^2 = 0.21$ and -0.02 for σ_e and $[\text{Mg}/\text{Fe}]$, respectively⁷. The opposite is true for HiM-50, where we obtain $R^2 = 0.70$, and $\Delta R^2 = -0.01$ and 0.71 for σ_e and $[\text{Mg}/\text{Fe}]$, respectively. Thus, at fixed σ_e no correlation exists between MLE_r and $[\text{Mg}/\text{Fe}]$ for low-mass slope variations, while for high-mass slope variations, no correlation exists between MLE_r and σ_e at fixed $[\text{Mg}/\text{Fe}]$. These differences are due to the fact that σ_e correlates more strongly than $[\text{Mg}/\text{Fe}]$ with birth ISM pressure in LoM-50, but the opposite is true in HiM-50 due to the enhanced Mg yields resulting from a top-heavy IMF in high-pressure environments.

It will be interesting to see on which variables the MLE depends most strongly for observed galaxies, as our results suggest that such relations may be used to break the degeneracy between parametrizations of the IMF. La Barbera et al. (2015) find that the IMF, when parametrized as a top-light “bimodal” IMF, shows no correlation with $[\text{Mg}/\text{Fe}]$ at fixed σ , which is consistent with our LoM-50 simulation. It would be interesting to know if this is still true when parametrizing the IMF with low-mass slope variations instead (as in LoM). Indeed, Conroy & van Dokkum (2012b) find

⁷Note that since we use the adjusted R^2 , it is possible to have slightly negative ΔR^2 for some variables due to the penalty for adding extra data with no extra information.

Table 4.3: Determination of the importance of different observables for predicting MLE_r for mock C13 galaxies in our variable IMF simulations. Column 2 gives the fraction of the variance in MLE_r that is accounted for by the variance in each variable indicated in Column 1 (see text).

x	ΔR^2
LoM-50	
$\log_{10} \sigma_e / (\text{km s}^{-1})$	0.20
$\log_{10} \text{Age/Gyr}$	0.14
$\log_{10} Z/Z_\odot$	< 0.01
[Mg/Fe]	< 0.01
$\log_{10} R_e/\text{kpc}$	0.20
HiM-50	
$\log_{10} \sigma_e / (\text{km s}^{-1})$	< 0.01
$\log_{10} \text{Age/Gyr}$	0.34
$\log_{10} Z/Z_\odot$	0.12
[Mg/Fe]	0.45
$\log_{10} R_e/\text{kpc}$	< 0.01

that the IMF correlates more strongly with [Mg/Fe] than with σ when varying the low-mass slope of the IMF. However, comparisons between IMF studies are difficult due to differences in apertures, methods, and IMF parametrizations employed. We encourage spectroscopic IMF studies to test different parametrizations of the IMF to assess the robustness of correlations between the IMF and galaxy properties, which can then be compared with the predictions presented here. Note that this does not apply to studies that measure the MLE dynamically, as no assumption of IMF parametrization is needed.

4.5 MLE of satellite galaxies

We also briefly investigate the effect of environment on the IMF, where in Fig. 4.6 we show the $\text{MLE}_r - \sigma_e$ relation at $z = 0.1$ for the two variable IMF simulations split into central and satellite galaxies. Central galaxies are defined for each FoF group as the subhalo to which the most bound gas particle of the group is bound, while all other subhaloes within the group are satellites. For both simulations, on average there is little difference between the two populations, given their significant overlap at fixed σ_e . However, some satellites tend to scatter toward higher MLE_r -values than centrals, especially for $\sigma_e < 100 \text{ km s}^{-1}$. This effect is stronger in LoM-50 (although it is still visible in HiM-50), resulting in a median MLE_r for satellites that is larger by $\approx 0.05 \text{ dex}$ at $\sigma \approx 100 \text{ km s}^{-1}$. These outliers are likely the stellar cores left over from tidal stripping events. This result can be understood in the context of radial IMF variations, where the central, more tightly bound stars, being born at higher pressures than those in the outer regions, have heavier IMFs than the outer regions that have since been stripped. Indeed, we will show in Paper III that such radial IMF gradients

Table 4.4: As in Table 4.3 but for all galaxies with $\sigma_e > 10^{1.9} \text{ km s}^{-1}$. Relative to the mock C13 sample, the importance of r_e and age are enhanced for LoM-50 and HiM-50, respectively, due to inclusion of dim, compact galaxies with high MLE_r in the former, and young, low- MLE_r galaxies in the latter.

x	ΔR^2
LoM-50	
$\log_{10} \sigma_e / (\text{km s}^{-1})$	0.22
$\log_{10} \text{Age/Gyr}$	0.16
$\log_{10} Z/Z_\odot$	< 0.01
[Mg/Fe]	< 0.01
$\log_{10} R_e/\text{kpc}$	0.41
HiM-50	
$\log_{10} \sigma_e / (\text{km s}^{-1})$	< 0.01
$\log_{10} \text{Age/Gyr}$	0.69
$\log_{10} Z/Z_\odot$	0.06
[Mg/Fe]	0.16
$\log_{10} R_e/\text{kpc}$	< 0.01

are stronger in LoM-50 galaxies than in HiM-50.

This result has important consequences for the inference of the stellar mass of satellite galaxies, where, for these variable IMF prescriptions, the underestimate of the inferred stellar masses (assuming a Chabrier IMF) may be as high as a factor of two if they have been significantly stripped. Indeed, recent studies (e.g. Mieske et al. 2013; Seth et al. 2014; Villaume et al. 2017b) find elevated dynamical M/L ratios in UCDs, and have argued for one of two scenarios: either i) these UCDs are the remnant cores of tidally stripped progenitor galaxies and the extra mass comes from a now overmassive central BH, or ii) the IMF in these galaxies is top- or bottom-heavy. Our results show that both cases can be expected to occur simultaneously, as tidal stripping will increase both MLE_r , as the “IMF-lighter” outskirts are stripped, as well as M_{BH}/M_* , as the galaxy loses stellar mass.

These results are possibly at odds with the recent work of Rosani et al. (2018), who found no environmental dependence of the IMF in the σ_e -stacked spectra of ETGs from SDSS. However, such an analysis would miss outliers due to the σ_e -stacking. Better statistics at the high-mass end would be required for a more in-depth comparison with their work.

4.6 Summary and Conclusions

We use cosmological, hydrodynamical simulations with self-consistent variable IMF prescriptions to investigate trends between the mass-to-light excess (MLE) relative to that expected for a Salpeter IMF and global galaxy properties such as age, metallicity, and alpha abundance. These simulations follow the EAGLE reference model (Schaye et al. 2015) except that the IMF becomes either bottom-heavy (the LoM-

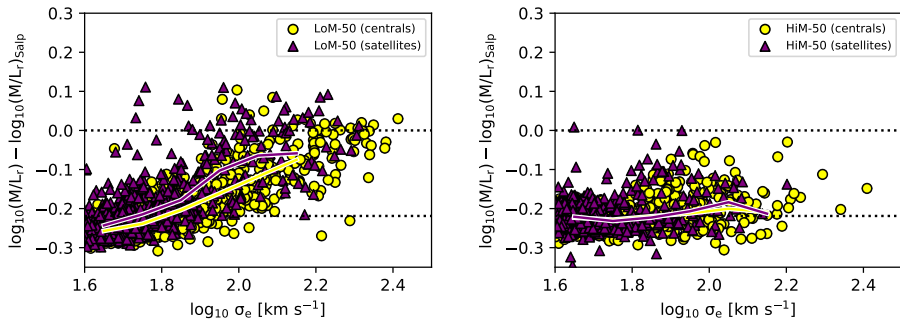


Figure 4.6: Excess M/L_r -ratio relative to a Salpeter IMF as a function of the central stellar velocity dispersion, σ_e , separated into central (yellow circles) and satellite (purple triangles) galaxies at $z = 0.1$. The left and right panels show galaxies from LoM-50 and HiM-50, respectively. All quantities are measured within the 2D projected stellar r -band half-light radius. Solid lines indicate running medians of bin size 0.1 dex in σ_e . Satellites generally follow the same trend as centrals, but lower- σ_e satellites scatter toward higher MLE_r than centrals due to tidal stripping leaving only the IMF-heavy, inner regions bound to the subhalo.

50 simulation) or top-heavy (HiM-50) for individual star particles formed in high-pressure (or, equivalently, high star formation rate surface density) environments. These simulations are unique in that the IMF variations have been calibrated to match the observed trend of increasing MLE with central stellar velocity dispersion, σ_e (Cappellari et al. 2013b, hereafter C13). This calibration is possible due to the fact that stars in the centres of ETGs form at higher pressure with increasing σ_e . The MLE increases with σ_e due to an increased fraction of low-mass stars in LoM-50, and an increasing mass fraction of stellar remnants and decreased luminosity in HiM-50. We verified in Paper I that the variable IMF simulations reproduce the observables used to calibrate the EAGLE subgrid models for feedback: the galaxy luminosity function, half-light radii and BH masses. The goal of this paper is to determine the similarities and differences in the relationships between the MLE and global galaxy properties that are expected to result from a galaxy formation model with self-consistent, *calibrated* IMF variations, in order to help interpret such relationships for observed galaxies and distinguish between different IMF variation scenarios.

Our conclusions are as follows:

- The MLE is only a good indicator of IMF slope, independent of age or metallicity, if the high-mass slope is kept fixed at the “reference” value (in our case Salpeter). If the high-mass slope is varied, as is the case for HiM-50, the MLE becomes as sensitive to age as it is to the IMF (Fig. 4.1).
- Trends of MLE with overall galactic properties were investigated for properties measured within the half-light radius, r_e , for galaxies selected in a way similar to the sample of C13 from ATLAS^{3D} (Fig. 4.2). For LoM-50, MLE correlates positively with age and [Mg/Fe], and negatively with metallicity. However, the significance of the correlations of MLE with metallicity or [Mg/Fe] depends on

galaxy selection effects. The anti-correlation with metallicity is the result of the decreasing Z with σ_e at high σ_e and the tight MLE– σ_e relation in that simulation. For HiM-50, MLE also correlates positively with age and [Mg/Fe] but has no significant correlation with metallicity due to the fact that the C13 selection criteria exclude faint, old, low-metallicity galaxies with high MLE that would otherwise help drive a negative trend in a σ_e -complete sample. Fits are shown in Fig. 4.2 and Table 4.1. We will show in a companion paper that the spatially resolved versions of these relations (i.e trends *within* galaxies) differ qualitatively from the global trends presented here.

- For both LoM-50 and HiM-50, the MLE correlates positively with mass and luminosity, but with more scatter than the MLE– σ_e trend (Fig. 4.3). For LoM-50, MLE anti-correlates with half-light radius, r_e , at fixed σ_e due to the fact that smaller high- σ_e galaxies form stars at higher pressures. This anti-correlation is, however, sensitive to observational selection effects that may prefer larger systems. MLE correlates positively with r_e for HiM-50 due to a lack of small high- σ_e galaxies, which tightens the positive relation between r_e and σ_e in the HiM-50 simulation (Fig. 4.4). These differences can be explained by the weaker (stronger) stellar feedback in high-pressure environments in LoM-50 (HiM-50) which can decrease (increase) galaxy sizes.
- A luminosity-complete sample of old, early-type galaxies, as is used in Cappellari et al. (2013b), exhibits significant biases in the correlations between the MLE and global galaxy properties such as metallicity, stellar mass, luminosity, and size relative to a galaxy sample that is complete in σ_e (Figs. 4.2 and 4.3). Care must thus be taken by observational studies to ensure that selections on properties such as morphology, age, or luminosity do not affect the inferred relations.
- Of the variables σ_e , age, metallicity, [Mg/Fe], and r_e , we determined the importance of each variable in explaining the variance in the MLE. For LoM-50, σ_e , r_e , and age account for the most variance in MLE, while the contributions from metallicity and [Mg/Fe] are much smaller. This result reflects the correlations of birth ISM pressure with σ_e , r_e , and age, and the weak effect that low-mass slope variations have on abundances. For HiM-50, [Mg/Fe] and age are the largest contributors to the variance in the MLE, with a smaller but significant contribution from metallicity, and negligible contributions from σ_e and r_e . This strong age-dependence is due to the sensitivity of the MLE on age for a top-heavy IMF, rather than to any age dependence of the IMF itself. The dependence on abundances likely arises due to the impact of the top-heavy IMF on the stellar yields (see Table 4.3).
- MLE correlates quite strongly with $M_{\text{BH}}/M_{\star, \text{Chab}}$ for both variable IMF simulations (Fig. 4.5). This finding suggests that in the variable IMF scenario, galaxies with black holes that are bona fide overmassive relative to the $M_{\text{BH}} - M_{\star}$ relation should also have “heavy” IMFs. This correlation likely results from the fact that older galaxies tend to form their stars and BHs at higher

pressures, leading to both overmassive BHs (Barber et al. 2016) and heavy IMFs. We conclude that even though a degeneracy in principle exists between the dynamical calculation of M_{BH} and stellar M/L ratio in observed galaxies, a correlation between $M_{\text{BH}}/M_{*,\text{Chab}}$ and MLE does not imply that overmassive BHs are necessarily the result of incorrect IMF assumptions, nor that excess M/L ratios are solely the result of overmassive BHs.

- Satellite galaxies mainly follow the same MLE– σ_e trend as central galaxies, with a few per cent scattering toward high MLE due to tidal stripping removing the outer “light IMF” regions, leaving only the “heavy IMF” core prior to being completely destroyed by tidal forces. This effect is stronger for LoM-50 than for HiM-50 (Fig. 4.6).

Overall, we have found that an IMF that varies with the local physical conditions, in our case birth ISM pressure, yields a galaxy population for which the MLE correlates with many global galaxy properties. Interestingly, if the high-mass end of the IMF varies, then some correlations can be as strong or stronger than the correlation with birth pressure due to the strong dependence of MLE on age. Our two IMF prescriptions yield qualitatively similar correlations between the MLE and global galaxy properties, particularly with age and $[\text{Mg}/\text{Fe}]$. The difference between their predicted correlations with r_e as well as that between the importance of different parameters in predicting the MLE, can be used to differentiate between these two IMF variation scenarios. In Paper III we will investigate further the predicted differences between these simulations by probing the spatially-resolved inner regions of high-mass galaxies to uncover the local behaviour of IMF variations and their impact on, and scaling with, other spatially-resolved properties. Paper III will additionally investigate the effect of these IMF variations on the evolution of galaxies in the simulations.

Acknowledgements

We are grateful to the anonymous referee for helping to improve the quality of the paper. This work used the DiRAC Data Centric system at Durham University, operated by the Institute for Computational Cosmology on behalf of the STFC DiRAC HPC Facility (www.dirac.ac.uk). This equipment was funded by BIS National E-infrastructure capital grant ST/K00042X/1, STFC capital grants ST/H008519/1 and ST/K00087X/1, STFC DiRAC Operations grant ST/K003267/1 and Durham University. DiRAC is part of the National E-Infrastructure. RAC is a Royal Society University Research Fellows. We also gratefully acknowledge PRACE for awarding us access to the resource Curie based in France at Très Grand Centre de Calcul. This work was sponsored by the Dutch National Computing Facilities Foundation (NCF) for the use of supercomputer facilities, with financial support from the Netherlands Organization for Scientific Research (NWO). This research made use of `ASTROPY`, a community-developed core `PYTHON` package for Astronomy (Astropy Collaboration 2013).



Calibrated, cosmological, hydrodynamical simulations with variable IMFs III: Spatially-resolved properties and evolution

Recent spatially-resolved observations of massive early-type galaxies (ETGs) have uncovered evidence for radial gradients of the stellar initial mass function (IMF), ranging from super-Salpeter IMFs in the centre to Milky Way-like beyond the half-light radius, r_e . We compare these findings with our new cosmological, hydrodynamical simulations based on the EAGLE model that self-consistently vary the IMF on a per-particle basis such that it becomes either bottom-heavy (LoM-50) or top-heavy (HiM-50) in high-pressure environments. These simulations were calibrated to reproduce inferred IMF variations such that the IMF becomes “heavier” due to either excess dwarf stars or stellar remnants, respectively, in galaxies with increasing stellar velocity dispersion. In agreement with observations, both simulations produce negative radial IMF gradients, transitioning from high to low excess mass-to-light ratio (MLE) at around r_e . We find negative metallicity radial gradients for both simulations, but positive and flat $[\text{Mg}/\text{Fe}]$ gradients in LoM-50 and HiM-50, respectively. Measured in radial bins, the MLE increases strongly with local metallicity for both simulations, in agreement with observations. However, the local MLE increases and decreases with local $[\text{Mg}/\text{Fe}]$ in LoM-50 and HiM-50, respectively. These qualitative differences can be used to break degeneracies in the manner with which the IMF varies in these high-mass ETGs. At $z = 2$, we find that the MLE has a higher and lower normalization for bottom- and top-heavy IMF variations, respectively. We speculate that a hybrid of our LoM and HiM models may be able to reconcile observed IMF diagnostics in star-forming galaxies and ETGs.

Christopher Barber, Joop Schaye and Robert A. Crain
MNRAS, submitted.

5.1 Introduction

How early-type galaxies (ETGs) form and evolve over cosmic time is an area of active research, where one of the leading theories invokes an “inside-out” formation scenario that occurs in two distinct phases (Bezanson et al. 2009; Oser et al. 2010; Barro et al. 2013; Clauwens et al. 2018). First, the dense stellar core is formed at high redshift, in a rapid, high-pressure burst of star formation. In the second phase, stellar mass is accreted through minor and major mergers with other galaxies, adding material to the outer regions of ETGs. The different physical conditions under which the stars form in each of these phases gives rise to gradients in stellar properties as a function of radius (Mehlert et al. 2003; Kuntschner et al. 2010; Greene et al. 2015).

Equipped with the spatial and spectral resolving power of modern, panoramic integral field units, observational studies have recently inferred that the stellar initial mass function (IMF) varies radially in the centres of some local high-mass ETGs. In general, such studies conclude that the IMF is bottom-heavy in galaxy centres due to an excess of dwarf stars, transitioning to an IMF consistent with a Kroupa (i.e. Milky-Way-like) IMF from ≈ 0.1 to 1 times the half-light radius, r_e (Boroson & Thompson 1991; Martín-Navarro et al. 2015b; La Barbera et al. 2016; van Dokkum et al. 2017; Sarzi et al. 2018; Oldham & Auger 2018a). The presence of such gradients is still energetically debated, however, with some studies finding no gradients or arguing that it is currently too difficult to disentangle the IMF from radial abundance gradients (McConnell et al. 2016; Zieleniewski et al. 2017; Davis & McDermid 2017; Alton et al. 2017, 2018; Vaughan et al. 2018a,b).

Such findings are important, since the IMF is usually assumed to be universal, both in the interpretation of observations and when making predictions with galaxy formation models. For example, radial IMF gradients imply that the stellar mass-to-light ratio in these galaxies varies as a function of radius, which could have a strong impact on dynamical mass models in which it is typically assumed that the M/L ratios measured in the central regions of galaxies apply globally (see Bernardi et al. 2018b; Sonnenfeld et al. 2018; Oldham & Auger 2018b). Indeed, radial IMF variations may affect measurements of the IMF itself when inferring it within some fixed aperture.

Understanding how the IMF varies within a galaxy can give insights into the nature of the variation itself, both in terms of the physical origin of the variations, as well which part of the IMF is varying, and in which direction. For example, Martín-Navarro et al. (2015c) concluded that the spatially-resolved IMF correlates with local metallicity in 24 high-mass ETGs from the CALIFA survey, which could imply that metallicity may play an important role in shaping the IMF. This result is qualitatively consistent with the recent findings of van Dokkum et al. (2017) for 6 high-mass ETGs. Interestingly, these two studies assume very different parametrizations of IMF variations, steepening the low-mass and high-mass IMF slopes, respectively. Since most metals are produced by high-mass stars, the parametrization of the IMF variations is crucial to the predictions of galaxy formation models that attempt to invoke such IMF variations. For instance, if the high-mass slope correlates with metallicity, it is not clear if such correlations are due to a causation in either direction or a coincidence, since

both quantities also scale strongly with radius.

That present-day high-mass ETGs formed the majority of their stars at high redshift leads to questions concerning how the IMF may have evolved over time. Indeed, observations of strongly star-forming galaxies at high redshift conclude that the high-mass slope of the IMF may need to be shallower to account for their H α equivalent widths (Nanayakkara et al. 2017) or abundance ratios (Zhang et al. 2018). On the other hand, observations of present-day high-mass ETGs, which are the descendants of high-redshift starbursts, are typically found to have bottom-heavy stellar populations, with their stellar spectra indicating an excess of dwarf stars relative to a Milky Way-like IMF (e.g. Conroy & van Dokkum 2012b; La Barbera et al. 2013). These apparently contradictory results could be evidence of a time dependence of IMF variations. Indeed, different forms of IMF parametrization can lead to very different predictions of IMF-related observational diagnostics at the present day, even for a fixed mass-to-light ratio (Barber et al. 2018a, hereafter Paper I). These differences may be even stronger at high redshift when the stars are actually forming.

Such issues can be addressed with galaxy formation models that explicitly include IMF variations. The recent cosmological, hydrodynamical simulations of Paper I are currently the most well-suited to answer these questions. The IMF variations in these simulations were assumed to depend on the local pressure of star-forming gas and were calibrated to reproduce the correlation between galaxy-wide mass-to-light excess and central stellar velocity dispersion, σ_e , inferred by Cappellari et al. (2013b). This match was achieved by increasing the contribution of either low-mass dwarf stars or stellar remnants (black holes, neutron stars, and white dwarfs) to the stellar M/L by varying the low-mass or high-mass IMF slope, respectively, to become bottom- or top-heavy in high-pressure environments on a per-particle basis. The IMF variations in these simulations are fully self-consistent in terms of the local star formation law, stellar energetic feedback, and nucleosynthetic yields.

We showed in Paper I that these simulations, which employ the EAGLE model for galaxy formation (Schaye et al. 2015), agree with the observables used to calibrate this model, namely the present day galaxy luminosity function, half-light radii, and supermassive black hole masses. In Barber et al. (2018b, hereafter Paper II) we investigated correlations between the “galaxy-wide” IMF and galaxy properties at $z = 0.1$, including metallicity, [Mg/Fe], age, stellar mass, luminosity, size, and black hole mass. In this paper, the third in this series, we use our variable IMF simulations (summarized in Section 5.2) to investigate if radial IMF gradients, which were not considered in the initial IMF calibrations, are predicted by our models (Section 5.3.2), and see how plausible IMF variations may affect radial gradients in stellar population properties such as the M/L ratio, metallicities, and α -enhancement (Section 5.3.3). We also investigate how the local IMF varies with local properties, and directly compare with recent observations (Section 5.3.4). In Section 5.4 we investigate the evolution of the IMF and its effect on the evolution of galaxies in the simulations. We discuss our models and possible extensions in Section 5.5. Finally, we present our conclusions in Section 5.6. The simulation data is publicly available at <http://icc.dur.ac.uk/Eagle/database.php>.

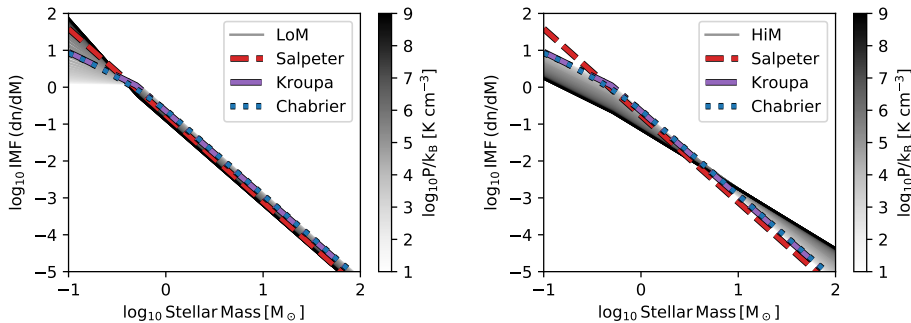


Figure 5.1: IMF variation prescriptions employed by LoM-50 (left panel) and HiM-50 (right panel). Grey lines show the IMF assigned to stellar populations for a range in birth ISM pressures (see greyscale bar). For all IMFs the integrated mass is normalized to $1 M_{\odot}$. In LoM-50, the low-mass ($m < 0.5 M_{\odot}$) IMF slope is varied such that the IMF transitions from bottom-light to bottom-heavy from low- to high-pressure environments. In HiM-50, the high-mass ($m > 0.5 M_{\odot}$) IMF slope is instead varied to become top-heavy in high-pressure environments. Figure reproduced from Fig. 2 of Paper I.

5.2 Simulations

The simulations used in this work are a variation on the EAGLE project, a suite of cosmological, hydrodynamical simulations of galaxy formation and evolution (Schaye et al. 2015; Crain et al. 2015; McAlpine et al. 2016). They were run using the Tree-Particle-mesh smooth particle hydrodynamics code P-Gadget-3 (last described by Springel 2005) in a periodic, comoving volume of $(50 \text{ Mpc})^3$ from $z = 127$ to $z = 0$. They have the same resolution as the fiducial EAGLE model, with particle mass of $m_g = 1.8 \times 10^6 M_{\odot}$ and $m_{\text{DM}} = 9.7 \times 10^6 M_{\odot}$ for gas and dark matter, respectively. The gravitational softening length was set to 2.66 co-moving kpc for $z > 2.8$ and held fixed at 0.70 proper kpc thereafter. A Lambda cold dark matter cosmogony is assumed, with cosmological parameters chosen for consistency with Planck 2013 ($\Omega_b = 0.04825$, $\Omega_m = 0.307$, $\Omega_{\Lambda} = 0.693$, $h = 0.6777$; Planck Collaboration 2014).

In the reference EAGLE model, physical processes that occur below the resolution limit of the simulation are modelled via “sub-grid” prescriptions. Gas particles cool radiatively according to cooling rates determined for the 11 individually-tracked elements that are most important for cooling (Wiersma et al. 2009a), and are photoheated by an evolving, spatially uniform Haardt & Madau (2001) UV/X-ray background and the cosmic microwave background. When gas particles become sufficiently dense and cool (Schaye 2004), they become eligible to stochastically transform into star particles. These star particles evolve and lose mass via supernovae (SNe) type Ia and II, and winds from AGB stars and massive stars (Wiersma et al. 2009b) according to an IMF (which in the reference EAGLE model is assumed to universally follow a Chabrier 2003 form) and metallicity-dependent lifetimes of Portinari et al. (1997). Thermal stellar feedback is implemented stochastically (Dalla Vecchia & Schaye 2012) and was calibrated to match the $z \approx 0$ galaxy stellar mass

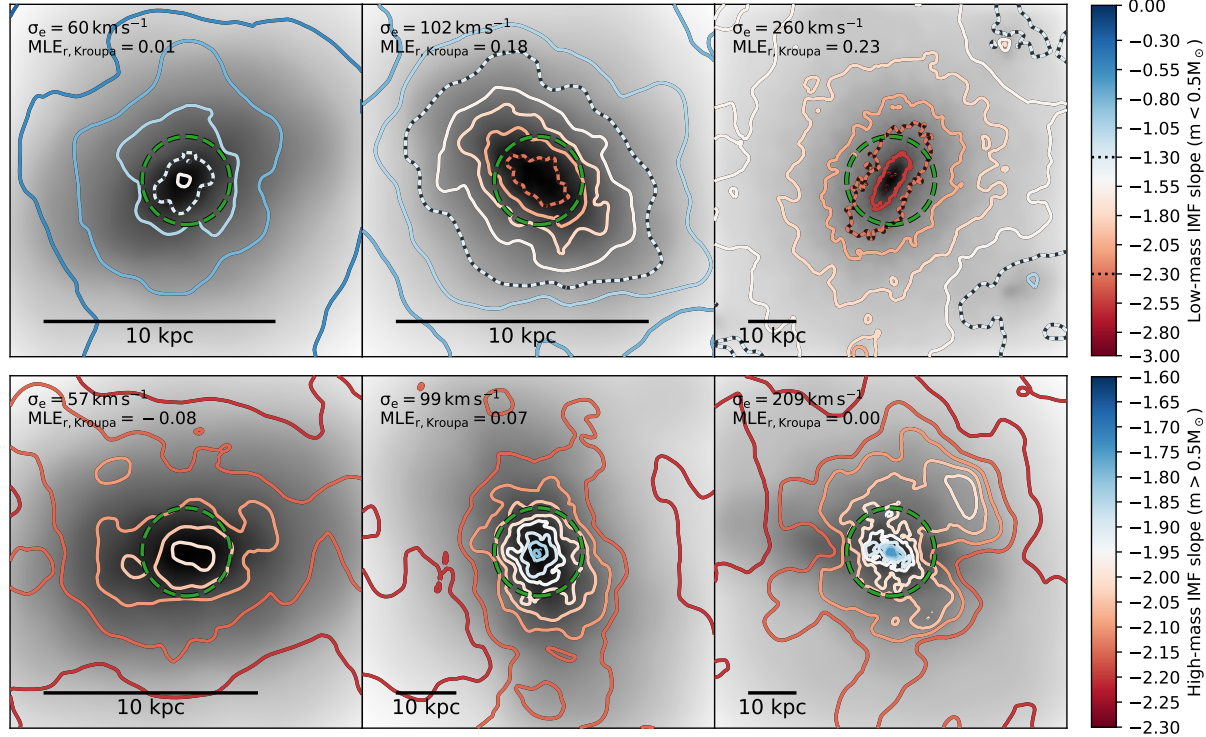


Figure 5.2: IMF maps for three example galaxies of different masses from each of LoM-50 (top row) and HiM-50 (bottom row) at $z = 0.1$. Greyscale maps show logarithmic projected stellar mass surface density. The extent of each image is 8 times the 2D projected SDSS r -band half-light radii, r_e , which is marked by a dashed green circle in each panel. Physical proper kpc are indicated with scale bars. Coloured contours (corresponding to ticks in the colour bars) denote mass-weighted IMF slope for $m < 0.5 M_\odot$ (top row) and $m > 0.5 M_\odot$ (bottom row). Bluer and redder colours correspond to shallower and steeper IMF slopes, respectively. In the upper row we highlight the low-mass IMF slope contours corresponding to Kroupa and Salpeter IMFs as dotted white and red lines, respectively, where applicable. The stellar velocity dispersion, σ_e , and excess mass-to-light ratio relative to a Kroupa IMF ($\text{MLE}_{r, \text{Kroupa}}$, Equation 5.1), both r -band weighted and measured within r_e , are indicated in the upper left corner of each panel. Note that the upper and lower rows do not correspond to the same galaxies. LoM-50 (HiM-50) galaxies with higher σ_e tend to have more bottom-heavy (top-heavy) IMFs in their central regions, with steep gradients of increasing heaviness toward their centres. Lower-mass galaxies have Chabrier-like IMFs and weaker IMF gradients.

function (GSMF) and galaxy sizes. Supermassive black holes are seeded in high-mass haloes and can grow via BH-BH mergers or gas accretion (Springel et al. 2005; Booth & Schaye 2009; Rosas-Guevara et al. 2015), the latter leading to thermal AGN feedback that quenches star formation in high-mass galaxies. We refer the reader to Schaye et al. (2015) for a more detailed description of the EAGLE model and to Crain et al. (2015) for details of its calibration.

The models employed in our two variable IMF simulations (first presented in Paper I) differ from the reference EAGLE model in that, rather than assuming a fixed Chabrier IMF for all stellar populations, they self-consistently vary the IMF for individual star particles as a function of the pressure of the interstellar medium (ISM) in which each star particle forms¹. The IMF is defined over the range $0.1 - 100 M_{\odot}$ with a mass-dependent slope $x(m)$ as $dn/dm \propto m^{x(m)}$. The two IMF variation prescriptions studied are shown in Fig. 5.1. The left panel shows the model termed “LoM”, where the IMF transitions from bottom-light to bottom-heavy from low to high pressures by varying the low-mass ($m < 0.5 M_{\odot}$) slope of the IMF while keeping the high-mass slope fixed at the Kroupa value of $x = -2.3$. For the second prescription, called “HiM” (right panel), we instead vary the high-mass slope ($m > 0.5 M_{\odot}$) to transition from Kroupa-like to top-heavy from low to high pressures while keeping the low-mass slope fixed at the Kroupa value of $x = -1.3$. Due to the finite resolution of EAGLE, this pressure corresponds to the ISM pressure averaged on scales of ≈ 1 kpc. Note that for a self-gravitating disc, variations with pressure are equivalent to variations with star formation rate (SFR) surface density (Schaye & Dalla Vecchia 2008). Crucially, both IMF variation prescriptions were calibrated to broadly reproduce the correlation between the excess mass-to-light ratio relative to that expected given a fixed IMF (MLE), and central stellar velocity dispersion, σ_e , inferred for high-mass ETGs by Cappellari et al. (2013b). Stellar feedback, the star formation law, and metal yields were all modified to self-consistently account for the local IMF variations. We refer the reader to Paper I for further details of these IMF prescriptions and their calibration.

Since the simulations do not explicitly model the emission of optical light, we compute photometric luminosities for all stellar particles (in post-processing) using the flexible stellar population synthesis (FSPS) software package (Conroy et al. 2009; Conroy & Gunn 2010), using the Basel spectral library (Lejeune et al. 1997, 1998; Westera et al. 2002) with Padova isochrones (Marigo & Girardi 2007; Marigo et al. 2008), where the stellar population’s age, metallicity, initial stellar mass, and IMF are all taken into account. For consistency we also recompute stellar masses using FSPS, and note that for the highest-mass ($M_{\star} > 10^{11} M_{\odot}$) galaxies in HiM-50 this leads to larger stellar masses of up to 0.2 dex due to differences in how stellar remnants are computed in FSPS and the Wiersma et al. (2009b) model built into EAGLE. We assume that stellar populations with age < 10 Myr have zero luminosity since such populations are expected to be obscured by their birth clouds (Charlot & Fall 2000), but otherwise

¹We note also that on kpc scales the pressure correlates well with the star formation rate surface density through the Kennicutt-Schmidt law (e.g. Schaye & Dalla Vecchia 2008), so our IMF prescription can also be interpreted as implementing a dependence of the IMF on other variables such as the radiation or cosmic ray density.

account for no further effects of dust.

Galaxies are identified in the simulations using a friends-of-friends halo finder combined with the `SUBFIND` algorithm which identifies self-bound structures (Springel et al. 2001; Dolag et al. 2009). We ensure that all galaxies studied in this work are well-sampled, with each containing at least 500 bound stellar particles. Unless otherwise stated, we compute global galaxy properties such as the stellar velocity dispersion, σ_e , as a Sloan Digital Sky Survey (SDSS) r -band light-weighted average over all bound star particles within the 2D projected r -band half-light radius, r_e , of each galaxy, where the projection is along the “random” z -axis of the simulation.

In the upper row of Fig. 5.2 we show random projections of three example galaxies taken from LoM-50 at $z = 0.1$ with $\sigma_e \approx 60, 100$, and $> 150 \text{ km s}^{-1}$. The greyscale background shows projected stellar mass density maps, while coloured contours show maps of the mass-weighted low-mass ($m < 0.5 M_\odot$) IMF slope. For the high- σ_e galaxies, we see strong radial gradients of the IMF slope, starting as Chabrier-like in the outskirts and becoming more bottom-heavy towards the centre. Some lower- σ_e galaxies also show IMF gradients, but these are much weaker than those with higher σ_e . Analogously, in the lower row of Fig. 5.2 we show the same but for the HiM-50 simulation (with a different set of galaxies). Here we also see strong radial gradients in the highest- σ_e galaxies, but now the IMF becomes more top-heavy toward the centre.

We show these trends statistically in Fig. 5.3, where in the upper and lower panels we plot respectively for LoM-50 and HiM-50 the radial profiles of the median IMF slope over the region of the IMF that is varied for star particles belonging to subhaloes in bins of σ_e . We see here that while high- σ_e galaxies ($\sigma_e > 125 \text{ km s}^{-1}$) have strong radial IMF gradients, low- σ_e galaxies ($30 < \sigma_e / \text{km s}^{-1} < 50$) have relatively flat profiles, remaining Kroupa-like at all radii. In the next section we explore these radial trends in high- σ_e galaxies in detail and compare with observations.

5.3 IMF trends within galaxies

In this section we present the spatially-resolved properties of high- σ_e galaxies in our variable IMF simulations. Section 5.3.1 describes the sample of high-mass ETGs selected for comparison with observations, for which we investigate radial gradients in the IMF and some of its observational diagnostics in Section 5.3.2. Section 5.3.3 shows the effect of IMF variations on gradients in stellar properties, and in Section 5.3.4 we present the resulting correlations between the local IMF and stellar properties within individual galaxies.

5.3.1 Sample selection

In order to compare the internal properties of galaxies in our variable IMF simulations with observations, we select ETGs with $\sigma_e > 150 \text{ km s}^{-1}$, hereafter referred to as the “Sigma150” sample. As in Papers I and II, we define ETGs as those with intrinsic (dust-free) $u^* - r^* > 2$. The σ_e limit of 150 km s^{-1} was chosen as a compromise between having a statistically significant number of galaxies in our sample and fairness

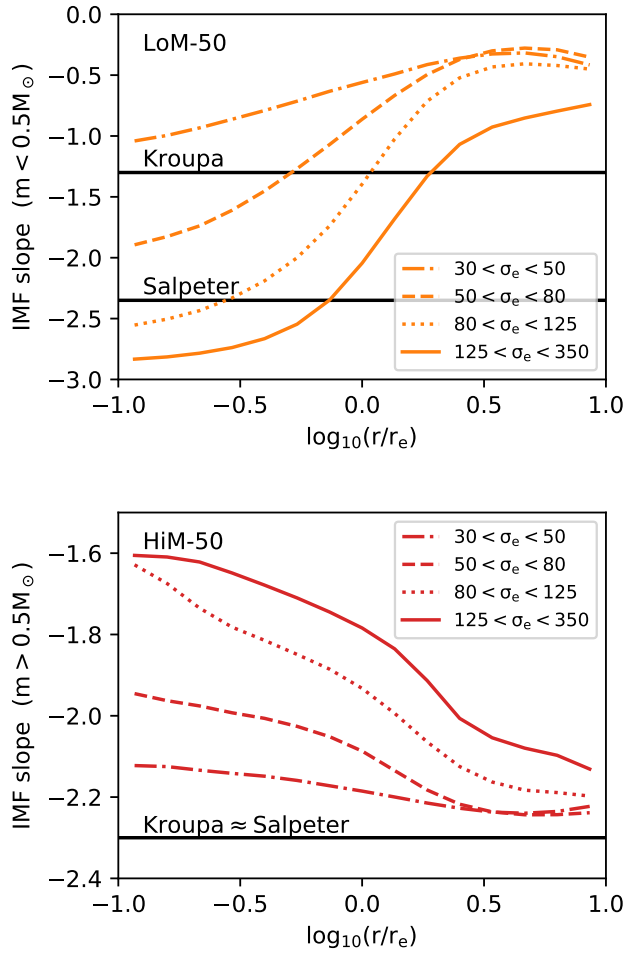


Figure 5.3: IMF slope as a function of 2d projected galactocentric radius at $z = 0.1$, normalized to the half-light radius of each galaxy. Coloured lines show median values for all stars belonging to subhaloes with stellar velocity dispersion, σ_e , in bins defined by the legend (in units of km s^{-1}). The upper panel shows the low-mass ($m < 0.5 M_\odot$) slope for LoM-50 galaxies while the lower panel shows the high-mass ($m > 0.5 M_\odot$) slope for HiM-50 galaxies. IMF slopes for Salpeter and Kroupa IMFs are indicated with horizontal solid lines. In both simulations IMF gradients are stronger in higher- σ_e galaxies.

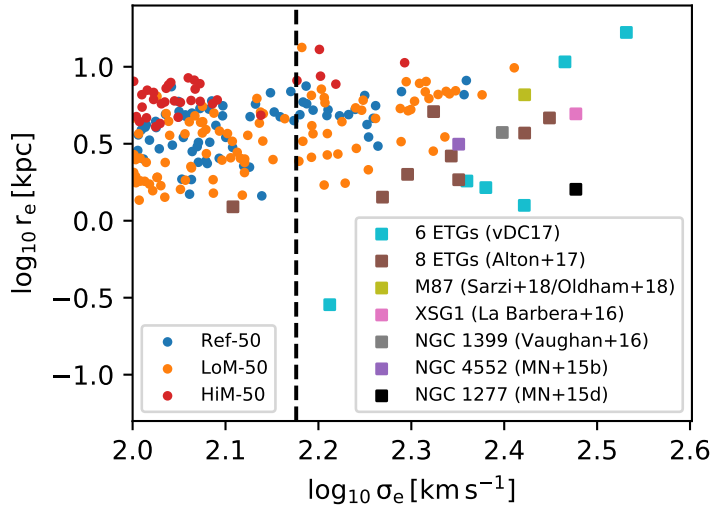


Figure 5.4: Projected proper r -band half-light radius, r_e , as a function of projected r -band light-weighted stellar velocity dispersion measured within r_e , σ_e , for early-type galaxies (ETGs; defined as those with intrinsic $u^* - r^* > 2$) in Ref-50 (dark blue dots), LoM-50 (orange dots) and HiM-50 (red dots) at $z = 0.1$. We compare with observed ETGs with recently measured spatially-resolved IMFs shown as squares: the 6 high- σ_e ETGs studied by van Dokkum et al. (2017) in cyan, eight ETGs studied by Alton et al. (2017) in brown, M87 (studied separately by Sarzi et al. 2018 and Oldham & Auger 2018a), XSG1 in pink (La Barbera et al. 2016), NGC 1399 in grey (Vaughan et al. 2018b), NGC 4552 in purple (Martín-Navarro et al. 2015b), and NGC 1277 in black (Martín-Navarro et al. 2015d, values from van den Bosch et al. 2012). Where possible, distances were taken from Cappellari et al. (2011) and σ_e and r_e from the above-mentioned references or Cappellari et al. (2013a). For each simulation we select ETGs with $\sigma_e > 150 \text{ km s}^{-1}$ (hereafter the “Sigma150” sample) for comparison with observations, indicated by the vertical dashed line. Our Sigma150 galaxies have on average lower σ_e than the observed samples, which should be kept in mind when comparing our results with observations.

of comparison with observational samples of high- σ galaxies. This selection leaves us with 40 and 5 Sigma150 galaxies in LoM-50 and HiM-50, respectively. The difference in sample sizes is due to a combination of lower typical σ_e values and lower passive fractions in HiM-50 galaxies (see Paper I). Note that selecting all galaxies with $\sigma_e > 150 \text{ km s}^{-1}$ rather than only ETGs would increase our sample sizes for LoM-50 and HiM-50 to 67 and 12 respectively, but would make no qualitative difference to any of the results presented in this paper.

Fig. 5.4 shows r_e as a function of σ_e for our simulated ETGs, and compares with various observed high- σ ETGs that have spatially-resolved IMF measurements. These observed samples will be described in Section 5.3.2. Our Sigma150 galaxies are slightly larger and have lower σ_e on average compared to the observational sample. However, note that for three of the observed galaxies from van Dokkum et al. 2017, including the smallest one, r_e is measured along the projected semi-minor axis, which may be smaller than our (circularly-averaged) r_e values. These differences should be kept in mind when comparing IMF diagnostics with observed galaxies in future sections.

5.3.2 Radial IMF gradients

To measure the radial dependence of the IMF within our galaxies, it is important to account for the non-circularity of the galaxy surface brightness profiles (see Fig. 5.2), as is also done in observational studies (e.g. Parikh et al. 2018). To do so, we fit an ellipse, with semi-major axis² equal to the circularly-averaged r_e , to the 2D projected surface brightness profile of each galaxy. We then measure the r -band light-weighted IMF slope for each galaxy within concentric elliptical shells by scaling this ellipse such that its semi-major axis is logarithmically-spaced in bins of width 0.1 dex, ranging from $\log_{10} r/r_e = -1$ to 1. We caution that, given the gravitational softening length of 0.7 kpc and that r_e for most of our galaxies lies in the range 2-10 kpc, any radial gradients at $r \lesssim 0.1 - 0.3 r_e$ are likely affected by numerical resolution or the equation of state imposed on star-forming gas in EAGLE (Benítez-Llambay et al. 2018). Therefore we show radial profiles only for $r > 0.1 r_e$. Additionally, radii larger than $10 r_e$ would be well beyond what can be measured observationally. Indeed, due to the fact that spectroscopic IMF studies require a signal-to-noise ratio of at least 100 to detect variations in the dwarf-to-giant ratio, most such studies measure the IMF within, at most, a couple of r_e (e.g. Vaughan et al. 2018a).

In this section we explore radial gradients for various IMF-dependent diagnostics, including the IMF slope (Section 5.3.2.1), mass-to-light excess (Section 5.3.2.2), and the dwarf-to-giant ratio (Section 5.3.2.3).

²This choice is motivated by some observational IMF studies that measure r_e along the semi-major axis of the galaxy (e.g. Martín-Navarro et al. 2015d; van Dokkum et al. 2017). For ETGs, the difference between the circularly-averaged r_e and the r_e measured along the semi-major axis is usually small, around 0.1 dex (see Table 1 of Cappellari et al. 2013a), so this choice has little impact on our results.

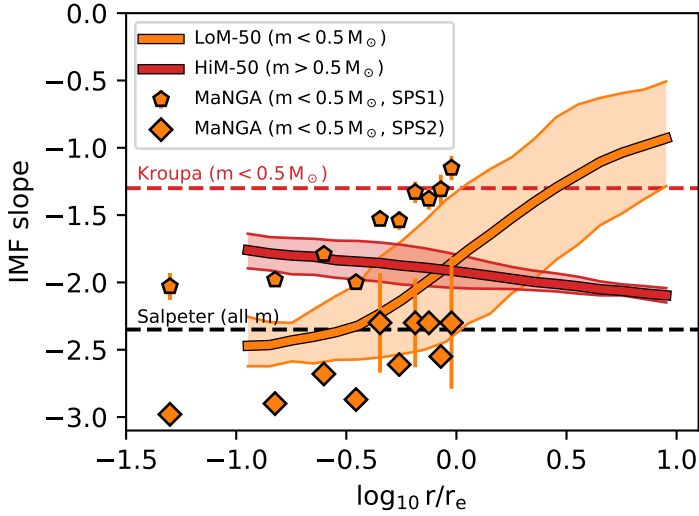


Figure 5.5: Radial variations in the r -band light-weighted IMF slope for ETGs with $\sigma_e > 150 \text{ km s}^{-1}$ in the LoM-50 (orange) and HiM-50 (red) simulations at $z = 0.1$. We show only the slope for the mass range of the IMF that is varying: $m < 0.5 M_\odot$ and $m > 0.5 M_\odot$ for LoM-50 and HiM-50, respectively. Solid thick lines show mean values averaged over all galaxies within logarithmically-binned 2D concentric elliptical shells with semi-major axis r/r_e , while solid filled regions show 10-90th percentiles. The dashed-red line marks the low-mass slope for a Kroupa IMF (which is also the low-mass slope for all galaxies in HiM-50), while the black-dashed line marks the Salpeter slope at all masses. We compare LoM-50 with low-mass slope variations for 122 ETGs in the mass range $\log_{10} M_*/M_\odot \in [10.5, 10.8]$ from SDSS-MaNGA as orange points where pentagons and diamonds correspond to differences in stellar population synthesis (SPS) modelling (Parikh et al. 2018). In both simulations we find strong radial IMF gradients, with the IMF becoming more bottom- and top-heavy toward the centres of galaxies for LoM-50 and HiM-50, respectively. Our low-mass slope variations in LoM-50 agree well with observations within the errors associated with SPS modelling.

5.3.2.1 IMF slope radial gradients

Fig. 5.5 shows the IMF slope as a function of r/r_e for our Sigma150 samples in LoM-50 and HiM-50 at $z = 0.1$, where we show the (varying) low-mass and high-mass slopes for the respective simulations. For both simulations we see strong radial gradients, with the IMF becoming bottom- and top-heavy toward the centre for LoM-50 and HiM-50, respectively.

We compare our LoM-50 simulation with observed gradients in the low-mass IMF slope ($m < 0.5 M_\odot$) inferred by Parikh et al. (2018) from NaI absorption features in the radially binned stacked spectra of 122 morphologically-selected ETGs from the SDSSIV Mapping Nearby Galaxies at APO (MaNGA) survey with $\log_{10} M_*/M_\odot \in [10.5, 10.8]$. To demonstrate the systematic uncertainty in the determination of the IMF slope via spectroscopic modelling, we show their results using two different stellar population synthesis (SPS) models: SPS1 uses the stellar population models of optical Lick absorption indices of Thomas et al. (2011a) in combination with Maraston & Strömbäck (2011) models based on the theoretical MARCS (Gustafsson et al. 2008) library, while SPS2 uses the Villaume et al. (2017a) extended NASA Infrared Telescope Facility (IRTF) stellar library. While both models yield significant radial gradients in the IMF slope, they are significantly offset from one another. Encouragingly, they seem to straddle our LoM-50 results, making the agreement between our simulations and these observations very good within the systematic uncertainties of the SPS modelling.

Note that HiM-50, which by construction has a low-mass slope fixed at the Kroupa value (dashed red line in Fig. 5.5), is not consistent with these observations. Indeed, observational SPS studies that parametrize IMF variations by varying the high-mass IMF slope typically find that it becomes steeper toward the centre (e.g. Martín-Navarro et al. 2015b; La Barbera et al. 2016), which is also in conflict with the HiM-50 simulation. However, such studies are only sensitive to the low-mass end of the IMF since only the long-lived stars (with $m \lesssim 1 M_\odot$) remain present in the old ETGs that are the focus of these IMF studies. Studies that are sensitive to the high-mass end of the IMF (e.g. Gunawardhana et al. 2011) and which inspired our HiM IMF variation prescription, have not yet explored radial gradients of the high-mass slope within galaxies. It will thus be an important test of the HiM-50 model to establish whether observations that are sensitive to the high-mass end of the IMF find its slope becomes shallower toward the centres of high-mass galaxies.

These strong radial IMF gradients are a consequence of similar gradients in birth ISM pressure, which we show explicitly in the upper panel of Fig. 5.6 for our Sigma150 galaxies³. For all of our simulations, including Ref-50, birth ISM pressure increases by over 2 orders of magnitude from the outskirts to the centre. Interestingly, HiM-50 exhibits much more scatter in the central $r < 0.3 r_e$ than in either the Ref-50 or LoM-50 simulations, which translates into the greater scatter in the IMF slope in HiM-50 than in LoM-50 (relative to the range over which it is varied in each case), shown in

³Note that the profiles presented in Fig. 5.6 use the locations of the stars at $z = 0.1$, rather than at their formation, and thus may be subject to radial migration (e.g. Fig. 9 of Furlong et al. 2017). However, since radial migration affects all other $z = 0.1$ radial profiles presented in this work in the same way, showing these pressure and age profiles at $z = 0.1$ allows us to interpret our IMF trends.

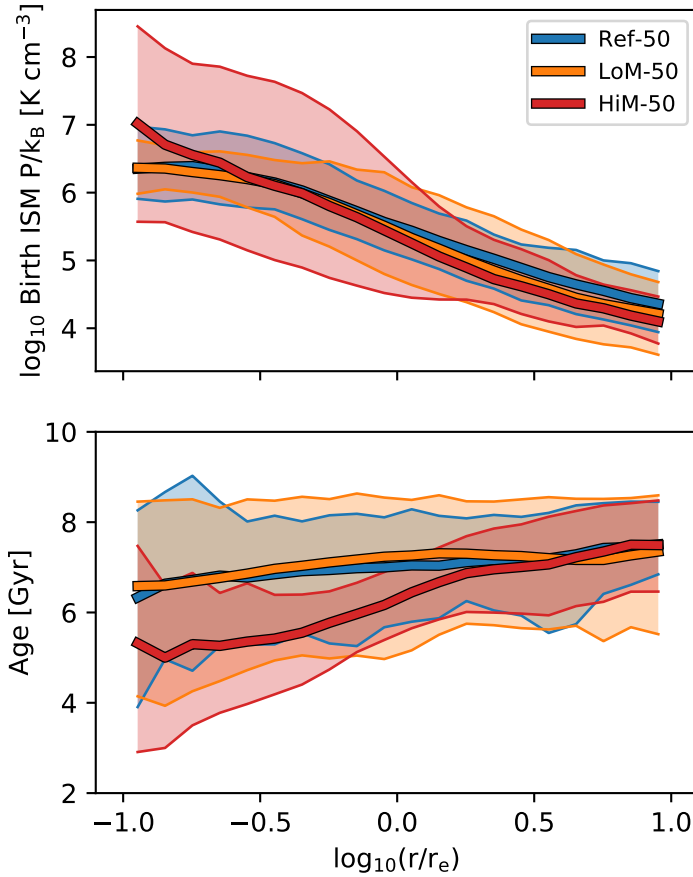


Figure 5.6: Radial variations of spatially-resolved properties of ETGs with $\sigma_e > 150 \text{ km s}^{-1}$ in Ref-50 (blue), LoM-50 (orange), and HiM-50 (red) at $z = 0.1$. We show r -band light-weighted birth ISM pressure and stellar age in the upper and lower panels, respectively, within logarithmically-binned 2D projected concentric elliptical shells with semi-major axis r/r_e (note that we use the locations of the stars at $z = 0.1$, not at their formation time). Thick lines show values averaged over all galaxies, while filled regions show 10-90th percentiles. The average birth pressure profiles are not very different between the three simulations, except with more scatter in HiM-50 than in LoM-50 or Ref-50. The age profiles for Ref-50 and LoM-50 are similar, but stars in HiM-50 galaxies are younger by $\approx 1 - 2$ Gyr for $r < r_e$

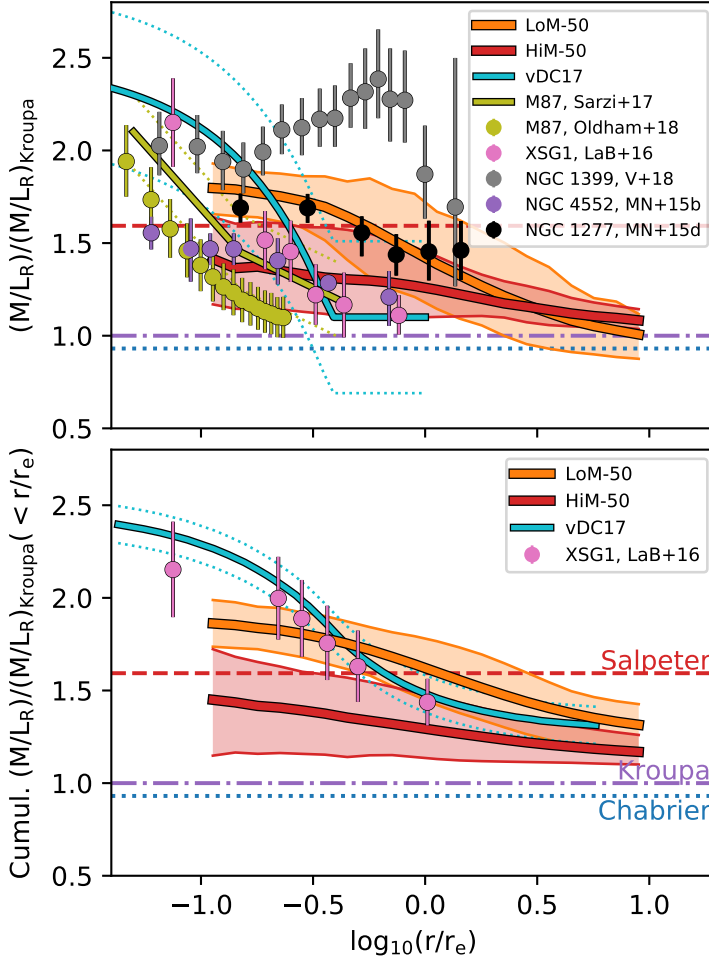


Figure 5.7: Radial variations in the r -band mass-to-light excess relative to a Kroupa IMF, $\text{MLE}_{r,\text{Kroupa}}$, within ETGs with $\sigma_e > 150 \text{ km s}^{-1}$ in the LoM-50 (orange) and HiM-50 (red) simulations at $z = 0.1$. Radii are normalized to their r -band half-light radii, r_e . Solid thick lines show mean values averaged over all galaxies in each r/r_e bin, while solid filled regions show 10-90th percentiles. In the upper panel we show $\text{MLE}_{r,\text{Kroupa}}$ measured within logarithmically-binned 2D projected concentric elliptical shells with semi-major axis r/r_e , while the lower panel shows mean luminosity-weighted $\text{MLE}_{r,\text{Kroupa}}$ within circular 2D projected apertures of radius r/r_e . Radial MLE gradients for various observed ETGs are over-plotted (see legend and text). Horizontal red-dashed, purple-dot-dashed, and blue-dotted lines mark the expected values for universal Salpeter, Kroupa, and Chabrier IMFs, respectively. For both LoM-50 and HiM-50, the IMF is heavy in the centres and transitions to Kroupa-like at a few times r_e , qualitatively consistent with observations (although note that HiM-50 agrees with the spectroscopic observational studies for the wrong reasons; see Fig. 5.8).

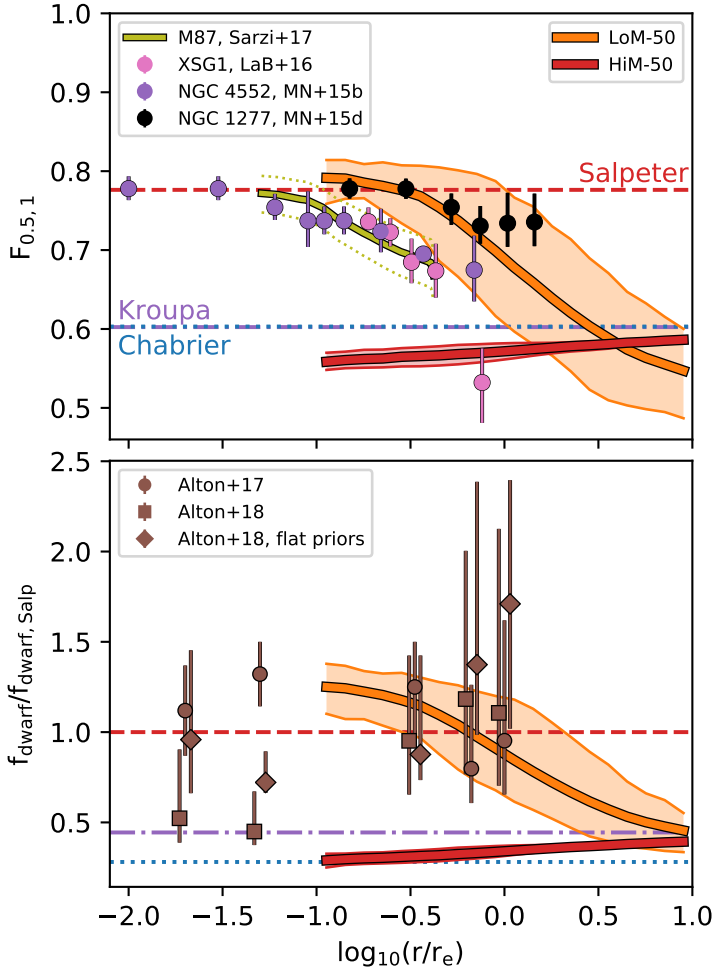


Figure 5.8: As Fig. 5.7 but now showing dwarf-to-giant ratio radial profiles. In the upper panel we define this ratio as the mass fraction of stars with $m < 0.5 M_{\odot}$ relative to those with $m < 1 M_{\odot}$ in the IMF, $F_{0.5,1}$. In the lower panel, this ratio is defined as the fraction of the total r -band luminosity contributed by low-mass ($m < 0.5 M_{\odot}$) stars at $z = 0.1$, f_{dwarf} . Due to the dependence of this quantity on the age of the stellar population, in each bin we divide by the value computed for a fixed Salpeter IMF, given the same ages and metallicities of the stars. Both quantities are measured within logarithmically-binned 2D concentric elliptical shells of semi-major axis r/r_e . In the upper panel we compare with $F_{0.5,1}$ profiles found for M87 (yellow line), XSG1 (pink points), and NGC 4552 (purple points), and NGC 1277 (black points). In the lower panel we show the average f_{dwarf} for stacked spectra of 8 ETGs from Alton et al. (2018) as brown squares with error bars. Brown diamonds show their results assuming a flat prior in f_{dwarf} , while brown circles show their results for the same galaxies using older SPS models and fewer absorption features (Alton et al. 2017). Horizontal red-dashed, purple-dot-dashed, and blue-dotted lines mark the expected values for universal Salpeter, Kroupa, and Chabrier IMFs. While LoM-50 galaxies match the observed dwarf-to-giant ratio radial gradients, the near-constant Kroupa/Chabrier values for HiM-50 galaxies are in tension with the observations.

Fig. 5.5. This greater diversity in birth ISM pressures is likely a consequence of the fact that stellar feedback is burstier in HiM-50 due to the shallower high-mass slope of the IMF in high-pressure environments, potentially leading to a less uniform ISM and thus a broader range of ISM pressures.

5.3.2.2 Mass-to-light excess radial gradients

Many observational IMF studies parametrize the IMF via the excess M/L ratio relative to that expected given a fixed reference IMF. We refer to this quantity as the M/L -excess, or MLE. The MLE is directly related to what dynamical IMF studies actually measure, and is easily computed given a best-fit IMF in spectroscopic studies. We define the MLE in the r -band as

$$\text{MLE}_{r,\text{Kroupa}} = \frac{(M/L_r)}{(M/L_r)_{\text{Kroupa}}}. \quad (5.1)$$

Note that here we use a non-logarithmic definition and compare M/L relative to a Kroupa IMF (in contrast to the logarithmic, Salpeter-relative definition used in Papers I and II) to facilitate comparison with observational studies that tend to use the same definition.

In the upper panel of Fig. 5.7 we plot $\text{MLE}_{r,\text{Kroupa}}$ measured within 2D projected elliptical concentric shells as a function of r/r_e for our Sigma150 galaxies at $z = 0.1$. For both simulations, the MLE is consistent with a Kroupa IMF at large radii (greater than a few r_e), gradually transitioning to larger values toward the centre. For LoM-50, all galaxies show clear negative radial gradients, while HiM-50 galaxies show much greater diversity: some have negative MLE gradients as strong as those in LoM-50, while others show no gradient at all. This diversity occurs despite the strong radial gradients in the IMF high-mass slope for the HiM-50 simulation, and is likely due to the additional dependence of the MLE on age when the high-mass slope is shallower than that for the reference IMF (Papers I and II). The lower panel of Fig. 5.6 shows that the mean r -band light-weighted age exhibits strong variation within r_e of the Sigma150 galaxies in HiM-50, leading to the diversity in MLE. For both simulations, these radial trends in the MLE explain the aperture effects in the $\text{MLE}-\sigma_e$ relation we saw in Paper I.

We compare our radial MLE trends with those for various observed galaxies in the upper panel of Fig. 5.7. As a yellow line we show the radial MLE gradient of M87 derived spectroscopically by Sarzi et al. (2018), where we have performed a by-eye fit through their data points, assigning it 0.2 dex scatter. Oldham & Auger (2018a) also obtain a negative gradient when inferring the spatially-resolved MLE in M87 dynamically (yellow points), which is offset systematically to lower MLE values by about 0.2 dex relative to the Sarzi et al. (2018) result. We also compare with spectroscopic results for XSG1 (pink points; La Barbera et al. 2016), NGC 1399 (grey points; Vaughan et al. 2018b), NGC 4552 (purple points; Martín-Navarro et al. 2015b), and NGC 1277 (black points; Martín-Navarro et al. 2015d). For the latter two studies we convert Γ_b to $\text{MLE}_{r,\text{Kroupa}}$ assuming their published age gradients. Finally, as a cyan line we show the radial MLE trend of van Dokkum et al. (2017), which is a fit to

the spectroscopically-determined MLE as a function of radius for 6 massive ETGs with $\sigma \sim 200 - 340 \text{ km s}^{-1}$.

For most of these observed systems, the MLE varies from super-Salpeter in the centre to Chabrier-like at around $0.4 r_e$, while NGC 1399 and NGC 1277 remain Salpeter-like out to at least $\approx 1 r_e$. Our simulated galaxies make qualitatively the same transition, but at larger radii, near or slightly above $1 r_e$. Given the wide diversity in the observed trends, it is difficult to rule out either IMF parametrization with this test. Indeed, LoM-50 galaxies rise to larger values of MLE than HiM-50, which may be more consistent with most of these observed trends at the smallest radii. On the other hand, HiM-50 is more consistent with the Kroupa-like MLE values in some of the observations at $r/r_e \approx 1/3$ to 1, and with the shallow MLE gradient in NGC 4552 at all radii. The MLE values inferred for NGC 1399 are much larger than those for the other observed and simulated ETGs; the reason for this is unclear, but Vaughan et al. (2018b) speculate that these variances could be due to either differences in SPS modelling or the stochastic nature of galaxy formation. We thus conclude that both LoM-50 and HiM-50 are consistent with the overall observed radial MLE gradients (although in Section 5.3.2.3 we show that HiM-50 agrees with the MLE gradients derived from these spectroscopic studies for the wrong reasons). We reiterate that these radial variations were not considered in the calibration of our IMF variation prescriptions.

Also of interest is the cumulative MLE measured within circular apertures of increasing radius, which we plot in the lower panel of Fig. 5.7. Again we see negative radial gradients, but with shallower slopes since the outer bins now contain the light from the central regions as well. We compare with spectroscopic results for six ETGs by van Dokkum et al. (2017) and for XSG1 from La Barbera et al. (2016). Both simulations agree with these observations at r_e , which is unsurprising given that they were calibrated to match the observed $\text{MLE}_r - \sigma_e$ relation (though only using data from Cappellari et al. 2013b), where MLE_r is measured within r_e . At smaller radii, the simulated gradients are shallower than the observed trends. However, LoM-50 galaxies are in excellent agreement with XSG1, and given the diversity in MLE gradients inferred from observations shown in the upper panel of Fig. 5.7, it is unclear if these discrepancies are robust.

Note as well that some studies find evidence for a lack of radial IMF gradients in high-mass ETGs. For example, Davis & McDermid (2017) use gas kinematics to infer the dynamical MLE radially within 7 ETGs, finding that, although the IMF seems to vary between galaxies, there is no systematic radial gradient. This data would thus support the HiM-50 model, in which it is possible to have flat MLE profiles even with significant gradients in the IMF slope, owing to the age-sensitivity of the relationship between MLE and high-mass IMF slope.

5.3.2.3 Dwarf fraction radial gradients

Another method of diagnosing the IMF is via the fraction of mass contributed by low-mass relative to high-mass stars. This quantity is much closer to what is actually measured when inferring the IMF from gravity-sensitive stellar absorption features, compared with the IMF slope or MLE. Since in the old stellar populations present in

typical ETGs, we expect that stars with $m \gtrsim 1 M_{\odot}$ should have died off, we define this fraction as

$$F_{0.5,1} = \frac{\int_{0.1}^{0.5} M \Phi(M) dM}{\int_{0.1}^1 M \Phi(M) dM}. \quad (5.2)$$

where $\Phi(M)$ is the IMF. We already showed in Paper I that this fraction, measured galaxy-wide, increases with σ_e in LoM-50 galaxies, in agreement with spectroscopic IMF studies (e.g. Conroy & van Dokkum 2012b; La Barbera et al. 2013). In the upper panel of Fig. 5.8 we plot $F_{0.5,1}$ as a function of radius for our Sigma150 galaxies at $z = 0.1$. Consistent with the IMF slope gradients seen in Fig. 5.5, we find a strong negative gradient in $F_{0.5,1}$ for LoM-50, transitioning from Salpeter to Chabrier-like at around r_e . For HiM-50, the trend is much shallower because $F_{0.5,1}$ is not very sensitive to high-mass slope variations. Interestingly, HiM-50 shows a shallow but positive radial $F_{0.5,1}$ gradient due to the shallower high-mass IMF slopes in the galaxy centres (see Fig. 5.5).

We compare these $F_{0.5,1}$ radial profiles with results for M87 (yellow line; Sarzi et al. 2018), XSG1 (pink points; La Barbera et al. 2016), NGC 4552 (purple points; Martín-Navarro et al. 2015b), and NGC 1277 (black points; Martín-Navarro et al. 2015d), where for all of these studies we have converted the radial profiles of the high-mass IMF slope of a “Bimodal” IMF (Γ_b) to profiles in $F_{0.5,1}$. All of these studies find negative gradients in $F_{0.5,1}$, consistent with LoM-50, although our simulated trend is shifted toward larger radii. HiM-50, on the other hand, is inconsistent with these studies, implying that a prescription that varies only the high-mass slope of the IMF towards values shallower than Salpeter is unable to explain these observations.

An alternative definition of the dwarf-to-giant ratio is the fraction of the *luminosity* that is contributed by low-mass ($m < 0.5 M_{\odot}$) dwarf stars, f_{dwarf} . It has been shown by Alton et al. (2017) that this quantity correlates very strongly with the equivalent widths of IMF-sensitive stellar absorption features, and thus may be a better diagnostic of the low-mass regime of the IMF than $F_{0.5,1}$. However, since f_{dwarf} by itself is also dependent on age, we normalize f_{dwarf} for our galaxies by $f_{\text{dwarf,Salp}}$, the value that would have been obtained had the stars evolved instead with a Salpeter IMF, given the same ages and metallicities. Our (*r*-band-weighted) $f_{\text{dwarf}}/f_{\text{dwarf,Salp}}$ radial profiles are presented in the lower panel of Fig. 5.8, where we find qualitatively the same gradients as in the case of $F_{0.5,1}$.

Alton et al. (2018) spectroscopically measure the radially-resolved IMF in stacked spectra of 7 ETGs, where they parametrize the IMF by f_{dwarf} . We show their main results as brown squares in Fig. 5.8. They do not provide $f_{\text{dwarf,Salp}}$ for these stacks, so we have normalized their results by the $f_{\text{dwarf,Salp}}$ at an age of 10 Gyr presented in Table C2 of Alton et al. (2017), multiplied by the ratio $\text{age}/(10 \text{ Gyr})$. This procedure assumes a linear relationship between $f_{\text{dwarf,Salp}}$ and age, which is the case for our variable IMF simulations. The error bars include the uncertainty in the age.

Owing to the large scatter of the Alton et al. (2018) results, they are consistent with both a flat IMF gradient and the steep negative f_{dwarf} gradient in LoM-50 galaxies. This apparent paradox is also due in part to the fact that for LoM-50, f_{dwarf} transitions

to a Kroupa value at around r_e , which is where the observations stop due to limited S/N . Deeper observations toward the outskirts of these galaxies would be required to establish if their IMF gradients are truly flat.

Note as well that Alton et al. (2018) find that f_{dwarf} is sensitive to assumptions made in the modelling of these galaxies. To demonstrate this sensitivity, as grey points we show the results of Alton et al. (2018) where they impose flat priors on f_{dwarf} itself (rather than on the low-mass IMF slopes; brown diamonds). This procedure increases the $f_{\text{dwarf}}/f_{\text{dwarf,Salp}}$ values in the central regions. For completeness, we also include the results of Alton et al. (2017) as brown circles, where the same analysis was performed on the same galaxies, except with fewer absorption features and a less up-to-date SPS model. Here f_{dwarf} becomes super-Salpeter at small radii. Thus, spectroscopic inferences of the IMF are quite sensitive to the methods used (even on the same galaxies), leading to potentially strong systematic errors. A better understanding of the systematics involved in spectroscopic modelling, as well as higher resolution in simulations, will be required to quantitatively compare the IMF in the inner regions of simulated and observed galaxies.

Overall, we find that radial IMF gradients are a natural prediction of models in which the IMF is a function of local physical conditions in the ISM (in our case the pressure at which the stellar populations are born). For low-mass slope variations, our radial gradients in the IMF low-mass slope, MLE, and dwarf-to-giant ratio are all in agreement with observational IMF studies which find such gradients, but this model may not be able to explain studies that do not find such gradients. HiM-50, on the other hand, is perhaps more consistent with the diversity in the MLE radial gradients from observational studies which can range from strongly negative to flat, but is inconsistent with the negative radial dwarf-to-giant ratio gradients inferred from spectroscopic studies. Stronger consensus from observational studies will be pivotal in further constraining proposed IMF variation prescriptions.

5.3.3 Radial gradients in stellar population properties

Since the IMF varies strongly with radius, it is also interesting to investigate how the gradients of other stellar properties are affected by variations in the IMF. Here we investigate gradients in metallicity, $[\text{Mg}/\text{Fe}]$, and r -band M/L ratio for each galaxy binned radially in the same logarithmically-spaced elliptical bins as in the previous section. We plot these results in Fig. 5.9 for our Sigma150 samples in Ref-50, LoM-50, and HiM-50 at $z = 0.1$.

The upper panel of Fig. 5.9 shows the radial metallicity profiles of our simulated galaxies, all of which have strongly negative gradients. Since, as we saw in Paper I, LoM-50 galaxies showed the same stellar mass–metallicity relation as Ref-50, it is unsurprising that they also have similar metallicity gradients. While HiM-50 galaxies exhibit the same gradient, the profiles are normalized to larger metallicity by ≈ 0.2 dex at all radii. This is the result of a higher production of metals due to a top-heavy IMF. Indeed, the offset appears to be strongest at small radii, where the IMF is most top-heavy in HiM-50. For comparison we show the metallicity gradients in high-mass

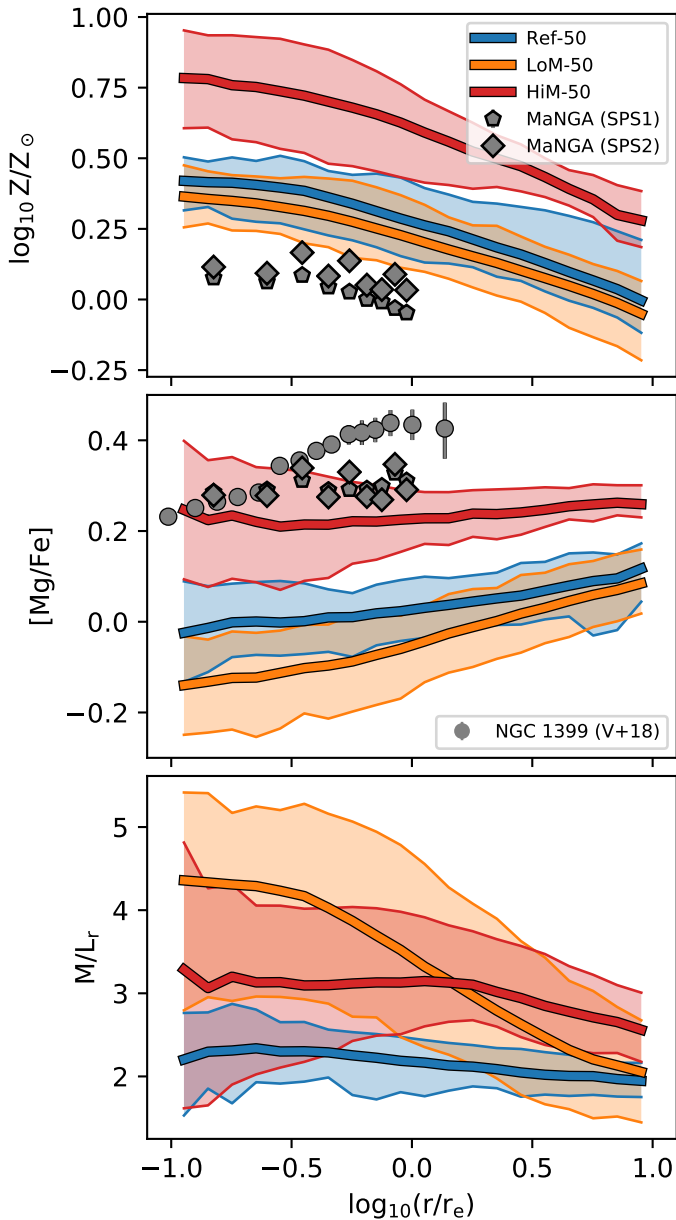


Figure 5.9: As Fig. 5.6 but showing, from top to bottom, radial gradients in the stellar metallicity, stellar α -enhancement $[\text{Mg}/\text{Fe}]$, and r -band stellar M/L ratio for our Sigma150 ETGs. We show metallicity and $[\text{Mg}/\text{Fe}]$ gradients for high-mass galaxies from SDSSIV-MaNGA from Parikh et al. (2018), where pentagons and diamonds correspond to using two different SPS models. The $[\text{Mg}/\text{Fe}]$ radial gradient in NGC 1399 is shown as grey circles (Vaughan et al. 2018b). While negative metallicity gradients are preserved in all of our simulations, the $[\text{Mg}/\text{Fe}]$ gradients are more positive and nearly flat for LoM-50 and HiM-50, respectively. M/L gradients are negative in LoM-50, while in HiM-50 the gradients are much more diverse within r_e .

ETGs found with SDSSIV-MaNGA by Parikh et al. (2018) (symbols as in Fig. 5.5). The shapes of the simulated profiles agree well with the observed results, but with some systematic offsets in normalization. However, these offsets are consistent with the factor two uncertainty in the nucleosynthetic yields in the simulations (Wiersma et al. 2009b) as well as the systematic offsets between different metallicity calibrators which can be as high as 0.7 dex (Kewley & Ellison 2008), and are thus not particularly constraining.

In the middle panel of Fig. 5.9 we show radial $[\text{Mg}/\text{Fe}]$ profiles for our simulated ETGs. The profile of Ref-50 is fairly flat out to $1 r_e$, and slowly rises beyond it. That of HiM-50 is even flatter but, as for the metallicity gradients, it is offset by $\approx 0.2 - 0.3$ dex. LoM-50, however, shows steeper positive radial gradients due to a deficit of α -elements in the inner regions. These results are in broad agreement with $[\text{Mg}/\text{Fe}]$ gradients in observed galaxies which seem to vary on a case-by-case basis from either being flat (Mehlert et al. 2003; Parikh et al. 2018), to weakly positive (Spolaor et al. 2008; Brough et al. 2007), or strongly positive (as is the case for NGC 1399; Vaughan et al. 2018b). The offsets between our simulations relative to Ref-50 are consistent with those for the (galaxy-wide) $[\text{Mg}/\text{Fe}] - \sigma_e$ relation seen in Paper I, and are due to the decreased (increased) number of type II SNe resulting from a steeper (shallower) IMF slope in LoM-50 (HiM-50).

The r -band M/L ratio radial profiles are shown in the lower panel of Fig. 5.9. While in Ref-50 the gradient is generally flat with $M/L_r \approx 2 - 3 M_\odot/L_\odot$ at all radii, in LoM-50 it increases by a factor ≈ 2 toward the centre, as expected given the MLE gradients seen in Fig. 5.7. HiM-50 ETGs have a much greater diversity in M/L , ranging from 1 to 5 below $0.3 r_e$. These non-constant M/L ratios may have important consequences for dynamical mass measurements (see Bernardi et al. 2018b; Sonnenfeld et al. 2018; Oldham & Auger 2018b), particularly when such masses are used to infer the IMF (Cappellari et al. 2013b). Here we have shown that in the case of IMF variations, the assumption of a constant M/L within r_e is not justified.

5.3.4 IMF vs local quantities

We now study the correlation between the IMF (parametrized by the MLE), and local galaxy properties. To this end we investigate the trends between MLE and metallicity, $[\text{Mg}/\text{Fe}]$, and age, measured in the same logarithmically-spaced elliptical annuli as in the previous subsections. Crucially, the question of whether or not such correlations exist can depend on how the data are combined. First we ask, if we consider the data from all of the radial bins in all of the Sigma150 galaxies simultaneously, is there a correlation between MLE and local properties? This procedure is similar to what is done by some observational studies such as Martín-Navarro et al. (2015c) or van Dokkum et al. (2017).

In the top-left panel of Fig. 5.10 we show $\text{MLE}_{r, \text{Kroupa}}$ as a function of stellar metallicity. Here each thin line shows the trend for an individual galaxy in radial bins, while thick solid lines show the best least absolute deviation (LAD) fit result when fitting to all galaxies simultaneously, with corresponding Spearman r -values and

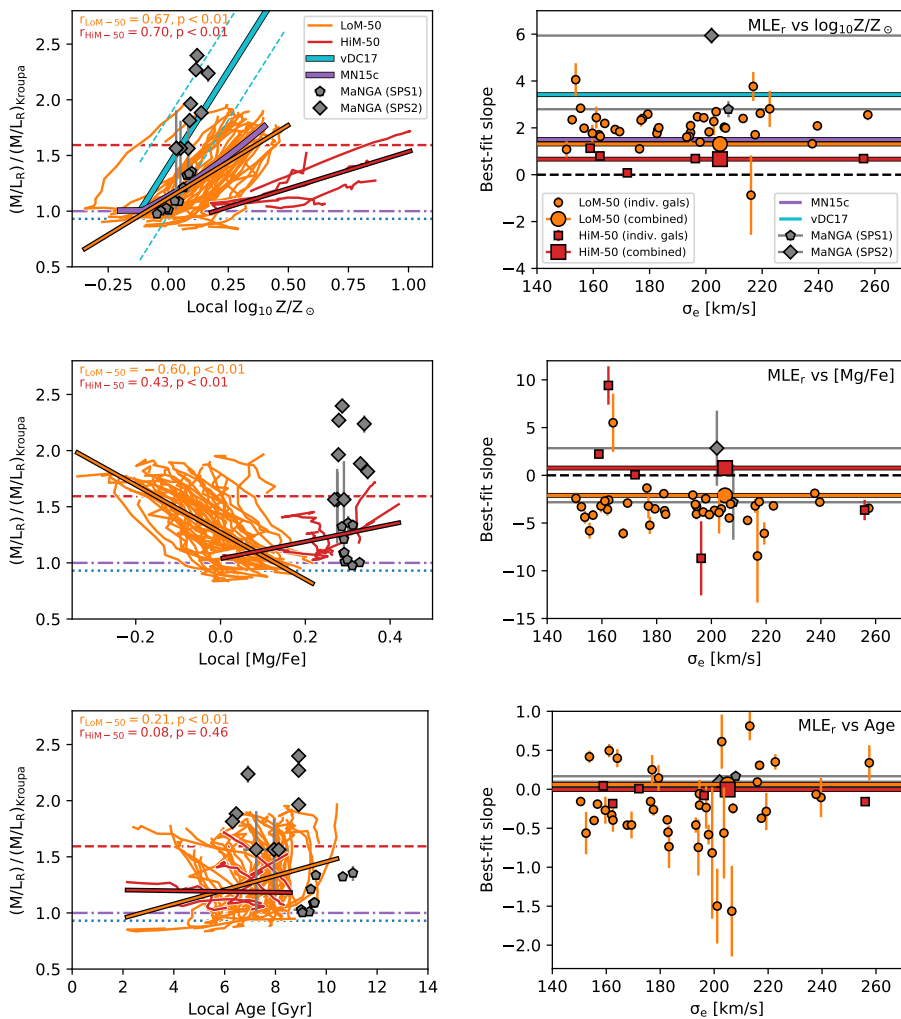


Figure 5.10: Left column: Local excess r -band M/L relative to a Kroupa IMF ($\text{MLE}_{r,\text{Kroupa}}$) as a function of local stellar metallicity (upper row), stellar [Mg/Fe] (middle row), and stellar age (lower row) within ETGs with $\sigma_e > 150 \text{ km s}^{-1}$ from LoM-50 (orange) and HiM-50 (red) at $z = 0.1$. All quantities are r -band light-weighted. Each thin coloured line shows values for an individual galaxy in logarithmically-spaced radial bins from 1 kpc to $10 r_e$. Least absolute deviation (LAD) fits to all galaxies simultaneously are shown thicker, outlined in black, with Spearman r -values and their p -values indicated in each panel. Trends for high-mass ETGs from SDSSIV-MaNGA for two different SPS models from Parikh et al. (2018) are shown as grey pentagons and diamonds, respectively. The observed local MLE-metallicity relation found by Martín-Navarro et al. (2015c) is shown as a purple solid line and that for 6 massive ETGs from van Dokkum et al. (2017) is shown as a solid cyan line with intrinsic scatter shown as cyan dashed lines. Expected MLE values for fixed Salpeter, Kroupa, and Chabrier IMFs are indicated with horizontal red-dashed, purple-dot-dashed, and blue-dotted lines, respectively. **Right column:** Logarithmic slopes of LAD fits to the local $\text{MLE}_{r,\text{Kroupa}}$ as a function of local properties within individual galaxies with $\sigma_e > 150 \text{ km s}^{-1}$ in LoM-50 (orange circles) and HiM-50 (red squares), plotted as a function of σ_e . Each small point in the right column corresponds to a thin line in the left, while larger symbols show the slopes of the LAD fits to all of these galaxies simultaneously. $\text{MLE}_{r,\text{Kroupa}}$ systematically correlates positively with local metallicity in both simulations, in qualitative agreement with the observations. The correlation with local [Mg/Fe] is negative and positive in LoM-50 and HiM-50, respectively, but for HiM-50 it differs substantially between galaxies. When combining results from all galaxies, $\text{MLE}_{r,\text{Kroupa}}$ increases weakly with local age for LoM-50, but on average decreases for individual galaxies. No correlation with local age is found for HiM-50 galaxies.

their p -values indicated in the upper left of each panel for LoM-50 (orange) and HiM-50 (red). For both simulations, we see overall a significant positive relation, likely due to the fact that both the IMF and metallicity vary radially monotonically. For comparison, we show the same trend for the 6 ETGs studied by van Dokkum et al. (2017) as a thick cyan line⁴, as well as the relation by Martín-Navarro et al. (2015c), and that for the highest-mass bin ($10.5 < \log_{10} M_*/M_\odot < 10.8$) of SDSS-MaNGA by Parikh et al. (2018). All of these studies find strong positive correlations of the IMF slope with increasing local metallicity, in good agreement with our findings. However, the shallower slope of this relation for HiM-50 galaxies is in slight tension with the observations. Note that our IMF (and MLE) does not depend physically on metallicity. Thus, a strong, tight correlation with metallicity can be expected even if the IMF varies with another property of the ISM, in our case pressure.

The above analysis may be sensitive to correlations between the MLE and global galaxy properties if the range of global values among galaxies is larger than the range of local values within them. To eliminate such effects, we also measure the slope of this correlation for each individual galaxy. We show these results in the upper right panel of Fig. 5.10. For nearly every Sigma150 ETG in both LoM-50 and HiM-50, we find a significant positive correlation between the local MLE and local metallicity. We compare with the slopes of the observed relations shown in the left panel. For Parikh et al. (2018) we manually perform a least-squares fit to their data only for the highest-mass bin, rather than over all 3 mass bins as in that paper, as the latter analysis would be sensitive to a global correlation between MLE and age (as can be seen by the lack of overlap in radially-resolved age in their highest and lowest mass galaxy bins in their Fig. 17). The slopes of our relations for individual galaxies in LoM-50 are consistent with those observed, while the slopes for HiM-50 galaxies, albeit consistently positive, are shallower than the observed trends. Note as well that, strictly speaking, it is not completely fair to compare HiM-50 with these observational studies since they measure the IMF spectroscopically, constraining the dwarf-to-giant ratio. Indeed, the dwarf-to-giant ratio in HiM-50, being relatively constant with radius (Fig. 5.8) would not correlate with changes in local stellar properties. We also do not see any correlation of these best-fit slopes with σ_e for these high- σ_e galaxies.

We also perform the same investigation into the correlation between local $\text{MLE}_{r,\text{Kroupa}}$ and local $[\text{Mg}/\text{Fe}]$, shown in the middle row of Fig. 5.10. Here we see strikingly different behaviour. When taking all of the galaxies together (solid thick lines in the middle left panel), we find a strong negative correlation of $\text{MLE}_{r,\text{Kroupa}}$ with $[\text{Mg}/\text{Fe}]$ in LoM-50, while that for HiM-50 galaxies is positive. This difference between the simulations opens up a novel method of discriminating between these IMF parametrizations. When looking at galaxies individually, this negative relation persists for the majority of LoM-50 galaxies, but no systematic trend is obvious for our 5 HiM-50 ETGs. Thus, the positive relation seen when combining results from these five HiM-50 galaxies likely reflects the strong global $\text{MLE}-[\text{Mg}/\text{Fe}]$ relation for HiM-50 ETGs (see Fig. 2 of Paper II). Care should thus be taken when inferring local IMF

⁴We have shifted the van Dokkum et al. (2017) values to the right by 0.3 dex to convert from $[\text{Fe}/\text{H}]$ to Z/Z_\odot , given their fairly consistent $[\text{Mg}/\text{Fe}]$ values of 0.3 dex and the relation from Thomas et al. (2003).

relations to first remove global trends between galaxies.

These correlations between the MLE and $[\text{Mg}/\text{Fe}]$ may be in tension with radially-resolved IMF studies, in which typically no significant correlation between the IMF and local $[\text{Mg}/\text{Fe}]$ is found (e.g. Martín-Navarro et al. 2015c; van Dokkum et al. 2017; Parikh et al. 2018, but see Sarzi et al. 2018). However, the best-fit slopes from Parikh et al. (2018), while consistent with zero, are also consistent with our findings, both for LoM-50 and HiM-50 (middle right panel). Thus, the correlations between the local MLE and local $[\text{Mg}/\text{Fe}]$ may be washed out in some current studies by observational uncertainties.

In the lower row of Fig. 5.10 we perform the same analysis but for the correlation between local $\text{MLE}_{r, \text{Kroupa}}$ and local stellar age. For LoM-50, when considering the entire sample together, we find a weak positive correlation with age (shown by the solid orange line and corresponding Spearman r -value in the lower left panel). However, the same is not true for individual galaxies (orange points in the lower right panel), where the best-fit slope tends to scatter around 0 at all σ_e . For HiM-50 we do not find any systematic correlation with local age in either case. Thus, for both simulations we see no significant systematic correlation between MLE and age within individual galaxies. Indeed, the positive trend for LoM-50 seen in the lower left panel merely reflect the strong dependence of the MLE on age when measured “galaxy-wide” (see Fig. 2 of Paper II). These differences are subtle, but are extremely important in trends between the IMF and local properties in observational studies, especially when combining results from galaxies with a wide range of global properties, as is often necessary to obtain sufficiently high S/N ratio out to large radii.

Overall, these results highlight the importance of removing global trends between the MLE and integrated galaxy properties before interpreting trends within galaxies. For both simulations we find strong positive correlations of MLE with local metallicity, and the average negative (for LoM-50) and positive (for HiM-50) correlations with $[\text{Mg}/\text{Fe}]$ will be useful in discriminating between scenarios in which the IMF becomes either bottom-heavy or top-heavy in high-pressure environments.

5.4 Redshift dependence of galaxy properties

In Paper I we investigated the galaxy-wide correlations between IMF-related diagnostics such as the MLE, $F_{0.5,1}$, and ionizing flux with global galaxy properties such as σ_e and star formation rate (SFR), finding good agreement with observations. In this section we switch from the spatially-resolved properties discussed in the previous sections to investigate the evolution of these (global) IMF scaling relations (Section 5.4.1), as well as the effect that our IMF variation models have on the evolution of the cosmic properties in the simulations (Section 5.4.2).

5.4.1 Redshift dependence of the IMF

Some models of IMF variation in the literature invoke time-dependent IMF variations to explain the enhanced dwarf-to-giant ratios as well as high metal enrichment in high-

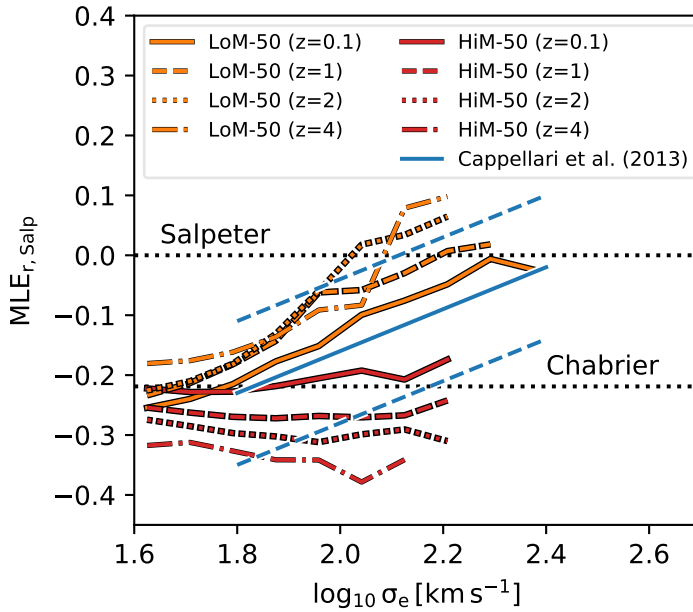


Figure 5.11: Galaxy-wide $\text{MLE}_{r,\text{Salp}}$ as a function of σ_e for LoM-50 (orange) and HiM-50 (red) at $z = 0.1$ (solid lines), $z = 1$ (dashed lines), $z = 2$ (dotted lines), and $z = 4$ (dash-dotted lines) for all galaxies with $\sigma_e > 10^{1.6} \text{ km s}^{-1}$ at each redshift. Thick lines shown medians for bins with more than 5 galaxies. All quantities are r -band light-weighted and measured within the 2D projected r -band half-light radius of each galaxy. A blue solid line indicates the Cappellari et al. (2013b) relation at $z \approx 0$, with dashed blue lines denoting intrinsic scatter. Horizontal black dotted lines mark the Salpeter and Chabrier $\text{MLE}_{r,\text{Salp}}$ values. For the LoM-50 (HiM-50) run, galaxies have a heavier (lighter) $\text{MLE}_{r,\text{Salp}}$ with increasing redshift.

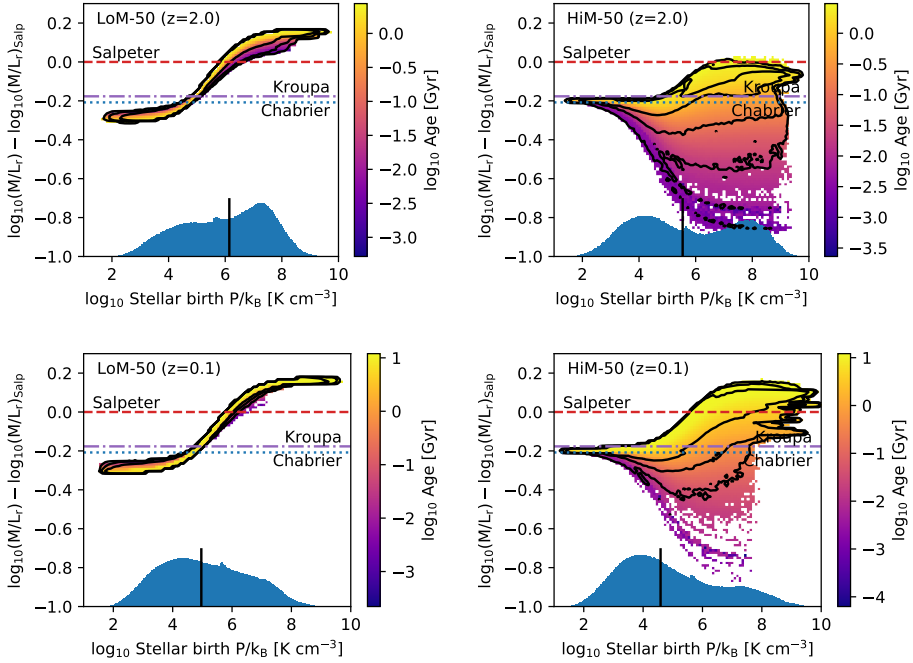


Figure 5.12: Redshift dependence of the $\text{MLE}_{r,\text{Salp}} - \sigma_e$ relation for individual stellar particles in the LoM-50 (left column) and HiM-50 (right column) simulations. 2D histograms in the upper and lower rows show $\text{MLE}_{r,\text{Salp}}$ as a function of birth ISM pressure for stars within the half-light radius of galaxies with $\sigma_e > 100 \text{ km s}^{-1}$ at $z = 2$ and $z = 0.1$, respectively. 2D bins are coloured by the mean age of stars within each bin. Contours show boundaries of (1000, 100, 10) stars per bin. Blue 1D histograms show the normalized distribution of birth ISM pressures on a linear scale; black horizontal lines show the medians of these distributions. In the LoM-50 case, higher birth ISM pressures at high z result in a larger fraction of dwarf stars than at $z = 0.1$. As $\text{MLE}_{r,\text{Salp}}$ is relatively independent of age for this IMF, the effect is immediate. In the HiM case, most stars born at high pressure have not lived long enough for the $\text{MLE}_{r,\text{Salp}}$ to become “heavy” (i.e. for massive stars to die off, reducing the light and increasing the mass due to BHs/NSs), so they still have low M/L ratios relative to Salpeter at this high redshift.

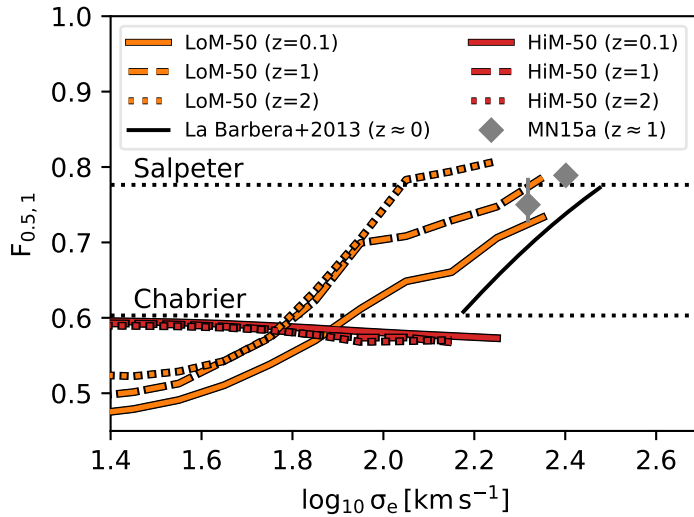


Figure 5.13: Redshift dependence of dwarf fractions in LoM-50 and HiM-50. The mass fraction of stars with $m < 0.5 M_{\odot}$ relative to those with $m < 1 M_{\odot}$ in the IMF, $F_{0.5,1}$, is shown as a function of σ_e . Line styles are as in Fig. 5.11. The result of La Barbera et al. (2013) at $z \approx 0$ (assuming a bimodal IMF) is shown as a solid black line. Values for quiescent galaxies at $z \approx 1$ from Martín-Navarro et al. (2015a) are shown as grey diamonds with 1σ error bars. The $F_{0.5,1} - \sigma_e$ relation evolves significantly for LoM-50, but not for HiM-50.

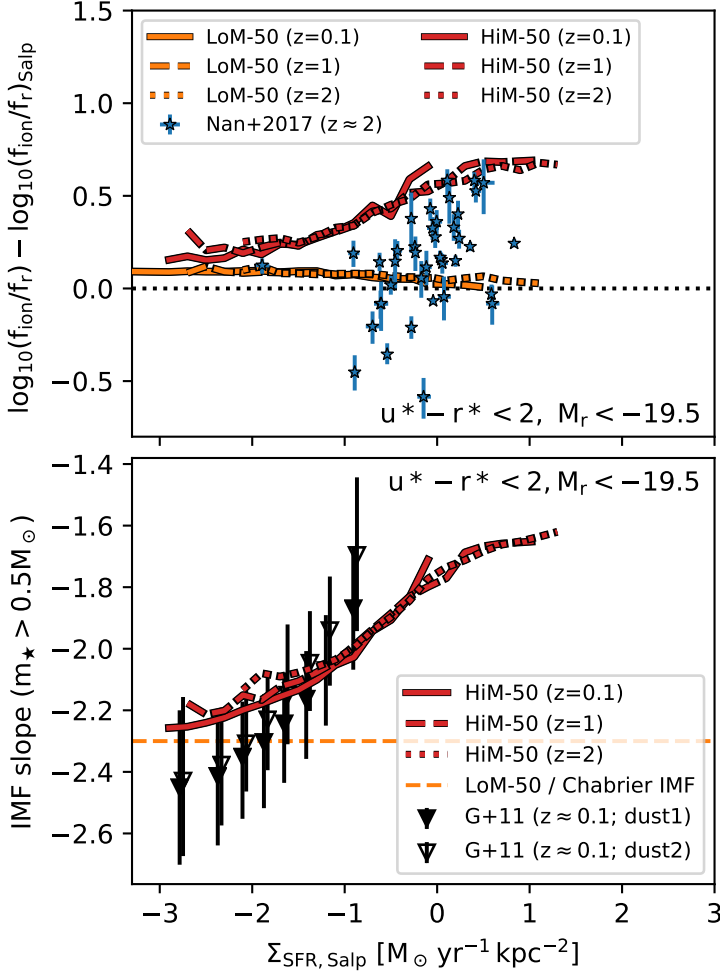


Figure 5.14: Upper panel: Ionizing flux relative to SDSS r -band flux, normalized by the value expected for a Salpeter IMF, as a function of Salpeter-reinterpreted star formation rate (SFR) surface density, $\Sigma_{\text{SFR,Salp}}$, in bright ($M_r < -19.5$), star-forming (intrinsic $u^* - r^* < 2$) galaxies in LoM-50 (orange) and HiM-50 (red) at different redshifts. Line styles are as in Fig. 5.11. For reference we include observations of H α equivalent width relative to that expected for a Salpeter IMF for star-forming galaxies at $z \approx 2$ by Nanayakkara et al. (2017). Lower panel: FUV-weighted high-mass ($m > 0.5 M_\odot$) IMF slope as a function of $\Sigma_{\text{SFR,Salp}}$ for the same galaxy sample as in the upper panel. The high-mass slope for all LoM-50 galaxies (the Chabrier value) is shown as a dashed orange line. For reference we include observations of local star-forming galaxies by Gunawardhana et al. (2011) for two different dust extinction models. The ionizing-to- r band flux ratio and IMF slopes do not evolve appreciably with redshift at fixed $\Sigma_{\text{SFR,Salp}}$ for either simulation, but for HiM-50 the relation extends to larger $\Sigma_{\text{SFR,Salp}}$, and thus larger f_{ion}/f_r and shallower high-mass IMF slopes, at higher redshift. The observed trends of shallower IMF slope or stronger H α EWs with increasing $\Sigma_{\text{SFR,Salp}}$ at all redshifts are qualitatively consistent with our HiM-50 simulation.

mass ETGs (e.g. Arnaud et al. 1992; Weidner et al. 2013; Ferreras et al. 2015; Martín-Navarro 2016, first a top-heavy starburst, then a prolonged bottom-heavy mode). Since our IMF depends on pressure, and typical birth ISM pressures decrease with time, our average IMF is also implicitly time-dependent. Indeed, for our HiM IMF prescription, high-pressure starbursts will naturally be given a top-heavy IMF while lower-pressure, less rapid star formation will proceed with an IMF closer to Kroupa (bottom heavy).

We now investigate the evolution of IMF-related diagnostics in our simulations for unresolved, galaxy-averaged properties. As in Papers I and II, we compute these properties as r -band light-weighted mean quantities measured within a circular projected aperture of radius r_e . Also for consistency with Papers I and II, we redefine the MLE as

$$\text{MLE}_{r,\text{Salp}} = \log_{10}(M/L_r) - \log_{10}(M/L_r)_{\text{Salp}}, \quad (5.3)$$

which is effectively a rescaled version of $\text{MLE}_{r,\text{Kroupa}}$.

In Fig. 5.11, we show the median relation between $\text{MLE}_{r,\text{Salp}}$ and σ_e at $z = 0.1, 1, 2,$ and 4 (different line styles) for LoM-50 (orange) and HiM-50 (red) for all galaxies with $\sigma_e > 10^{1.6} \text{ km s}^{-1}$ at each redshift. Despite being calibrated to roughly the same value at $z = 0.1$, the redshift evolution of the $\text{MLE}_{r,\text{Salp}} - \sigma_e$ relation differs greatly between the two IMF prescriptions. While the MLE of high- σ_e galaxies increases with redshift for LoM-50 galaxies, it decreases for HiM-50 galaxies. At $z = 2$, for example, the typical $\text{MLE}_{r,\text{Salp}}$ in LoM-50 is ≈ 0.1 dex higher than the $z = 0.1$ relation, with most galaxies in this mass range having a super-Salpeter IMF. On the other hand, galaxies in HiM-50 are ≈ 0.1 dex *lower* at $z = 2$ than at $z = 0.1$.

We can understand these differences via Fig. 5.12, where we show $\text{MLE}_{r,\text{Salp}}$ as a function of stellar birth ISM pressure at $z = 2$ and 0.1 , respectively, for stars within the half-light radius of galaxies with $\sigma_e > 100 \text{ km s}^{-1}$. Blue histograms show the distribution of birth ISM pressures for these stars. For the LoM-50 simulation shown in the left column, we see that the $\text{MLE}_{r,\text{Salp}}$ -pressure relation is nearly identical at high and low redshift, due to the age-independence of the MLE for this form of the IMF (see Fig. 5 of Paper I). However, the blue histograms show that birth ISM pressures of stars were typically much higher at $z = 2$ than at $z = 0.1$. This result is due to the fact that densities are in general higher at higher redshift, and thus the pressures at which stars form are also higher.

On the other hand, for the HiM-50 simulation, not only were the stars formed at higher pressure at high redshift, but also the shape of the $\text{MLE}_{r,\text{Salp}}$ -pressure relation changes over time, becoming more “heavy” as time goes on. This effect is due to the age dependence of the MLE for an IMF with a shallow high-mass slope. Stellar particles at high pressure are born “light”, with low MLE due to a prevalence of high-mass stars, but over time become “heavy” due to stellar evolution removing these bright stars and leaving behind stellar-mass BHs and NSs.

Martín-Navarro et al. (2015a) recently inferred from spectroscopic observations that the IMF of ETGs at $z \approx 1$ is consistent with that of ETGs at low redshift. To compare with their results, we plot in Fig. 5.13 the mass ratio between stars with $m < 0.5 M_\odot$ and $m < 1 M_\odot$ in the galaxy-averaged IMF, $F_{0.5,1}$ (Equation 5.2), as a function of σ_e . As with the MLE, $F_{0.5,1}$ becomes “heavier” (i.e. higher $F_{0.5,1}$ values) at

larger redshift for LoM-50. However, since $F_{0.5,1}$ is rather insensitive to the high-mass IMF slope, the correlation remains flat at the Chabrier value for HiM-50 at all redshifts.

The result from Martín-Navarro et al. (2015a) is shown in Fig. 5.13 as grey diamonds, which agrees well with the trend for LoM-50 at $z = 1$. Indeed, the magnitude of the weak evolution seen in Martín-Navarro et al. (2015a) from $z = 0$ to 1 is reproduced well by LoM-50. This good agreement is quite interesting given the fact that Martín-Navarro et al. (2015a) model the increased dwarf fractions by steepening the high-mass slope of the IMF, rather than the low-mass slope as is done in our LoM model. This result highlights the degeneracy between the low- and high-mass slopes in setting the dwarf-to-giant ratio derived in spectroscopic IMF studies of old ETGs.

While of our two variable IMF models, only LoM-50 is able to reproduce observational IMF trends based on the dwarf-to-giant ratio, HiM-50 alone is consistent with those based on the $H\alpha$ flux of local star-forming galaxies (see Paper I). High-redshift observations of star-forming galaxies also find evidence for shallow high-mass IMF slopes in such systems (e.g. Nanayakkara et al. 2017; Zhang et al. 2018). In particular, Nanayakkara et al. (2017) find that the enhanced $H\alpha$ equivalent widths (EW) of $z \approx 2$ galaxies could be explained with an IMF slope shallower than (under our IMF definition) -2.0 . To compare with their data, we compute the ratio of ionizing flux to the SDSS r -band flux, f_{ion}/f_r , for our simulated galaxies, where f_{ion} is the flux of photons with $\lambda < 912 \text{ \AA}$, and is a proxy for the $H\alpha$ flux (Shivaei et al. 2018). Note that f_{ion} includes light from stars of all ages, while f_r is only computed for those with age $> 10 \text{ Myr}$. The ratio f_{ion}/f_r is then a rough proxy for $H\alpha$ EW, which is the $H\alpha$ flux relative to the continuum. To remove systematics in converting from this quantity to $H\alpha$ EW, we normalize by the value expected given a Salpeter IMF, making it the “excess” f_{ion}/f_r . Since in Paper I we found that the high-mass IMF slope correlates strongly with SFR surface density (a result of the pressure dependence of the IMF), in the upper panel of Fig. 5.14 we plot the excess f_{ion}/f_r as a function of Salpeter-reinterpreted SFR surface density $\Sigma_{\text{SFR,Salp}}$, at different redshifts. $\Sigma_{\text{SFR,Salp}}$ is computed as in Paper I, where $\Sigma_{\text{SFR,Salp}} = \text{SFR}_{\text{Salp}}/(2\pi r_{e,\text{FUV}}^2)$, where SFR_{Salp} is the total SFR within a 3D aperture of radius 30 pkpc multiplied by the ratio between the GALEX FUV flux and that expected given a Salpeter IMF, and $r_{e,\text{FUV}}$ is the half-light radius in the FUV band. Here we show only star-forming galaxies (intrinsic $u^* - r^* < 2$) with $M_r < -19.5$, for consistency with the selection of Gunawardhana et al. (2011).

In the upper panel of Fig. 5.14 we see that the excess $f_{\text{ion}}/f_r - \Sigma_{\text{SFR,Salp}}$ relation is positive for star-forming galaxies in HiM-50 but flat for those in LoM-50. It also does not evolve with redshift, but is instead extended to larger $\Sigma_{\text{SFR,Salp}}$, and thus to larger excess f_{ion}/f_r . We compare with results from the ZFIRE survey by Nanayakkara et al. (2017), shown as blue stars. We use their SFRs derived from the $H\alpha$ luminosity, which, due to its sensitivity to SFR on very short time scales, is most consistent with our simulated instantaneous SFRs. For their galaxies we compute $\Sigma_{\text{SFR,Salp}}$ as $\text{SFR}/(2q\pi r_e^2)$, where r_e is obtained by cross-matching the ZFOURGE galaxies with CANDELS and using sizes from Van Der Wel et al. (2012), and $q = b/a$ is the minor-to-major axis ratio. While they find a trend of increasing excess $H\alpha$ EW with increasing $\Sigma_{\text{SFR,Salp}}$ (in

qualitative agreement with HiM-50 albeit with large scatter), their values tend to be lower than those of HiM-50, suggesting that our IMF variations may be too strong in the HiM model.

It is also interesting that the ionizing excess falls below the Salpeter value for some ZFIRE galaxies with $\Sigma_{\text{SFR}} < 1 M_{\odot} \text{ yr}^{-1} \text{ kpc}^{-2}$. It is tempting to infer from this result that IMF high-mass slopes steeper than Salpeter are required at lower pressures. However, such low values may also result in the case that these galaxies are post-starburst systems. In this case, the long-lived stars created in the starburst event serve to enhance the continuum more than the $\text{H}\alpha$ flux, leading to lower $\text{H}\alpha$ EWs than expected for a constant star formation history, even with a fixed IMF (see Fig. 17 of Nanayakkara et al. 2017). Thus, stronger constraints on their star formation histories would be required to make inferences on the IMF slope in this regime.

To aid comparison with observations of high-redshift star-forming galaxies, we show in the lower panel of Fig. 5.14 the high-mass slope of the IMF as a function of $\Sigma_{\text{SFR,Salp}}$ at different redshifts. For reference we also show the IMF slope at $z \approx 0.1$ for star-forming galaxies from the GAMA survey inferred by Gunawardhana et al. (2011) assuming either Calzetti (2001)/Cardelli et al. (1989) or Fischera & Dopita (2005) dust corrections (dust1 and dust2, respectively). As for the ionizing fluxes, this relation does not evolve with redshift for the simulated galaxies, but shifts to higher $\Sigma_{\text{SFR,Salp}}$, making the average high-mass slope shallower in high- z star-forming galaxies. These slopes are shallower than those found for the $z \approx 2$ observations by Nanayakkara et al. (2017), for which high-mass IMF slopes of ≈ -2 may be needed to explain their $\text{H}\alpha$ EWs. Zhang et al. (2018) recently concluded that high-mass IMF slopes as shallow as -2.1 would be required to explain the $^{13}\text{CO}/\text{C}^{18}\text{O}$ ratios observed in $z \approx 2 - 3$ submillimetre galaxies, which is also steeper than predicted by HiM-50. These findings suggest that the high-mass slope may be too shallow in our HiM-50 simulation.

5.4.2 Redshift-dependent cosmic properties

We now briefly investigate the redshift evolution of star formation in the simulations. The upper panel of Fig. 5.15 shows the evolution of the cosmic comoving stellar mass density, ρ_{\star} , in our variable IMF simulations compared with Ref-50. At all redshifts, ρ_{\star} lies systematically above and below Ref-50 in LoM-50 and HiM-50, respectively. The offsets are stronger at high redshift and gradually come into closer agreement with Ref-50 with time, where from $z = 5$ to $z = 0$ the offset for LoM-50 drops from ≈ 0.1 to 0.07 dex, and that for HiM-50 drops from -0.3 to -0.1 dex. The stronger offsets at high redshift are likely due to the fact that the stars that formed at the highest pressures tend to have formed earlier, while those with more Chabrier-like IMFs typically formed later. Note as well that here we plot the stellar masses directly from the EAGLE simulation, with no post-processing with FSPS. Since FSPS assumes higher remnant masses for metal-rich stellar populations than the Wiersma et al. (2009b) models built into EAGLE, ρ_{\star} shown here for HiM-50 may be lower than that that would be derived using FSPS.

These offsets can be explained with the cosmic SFR density, ρ_{SFR} , shown in the

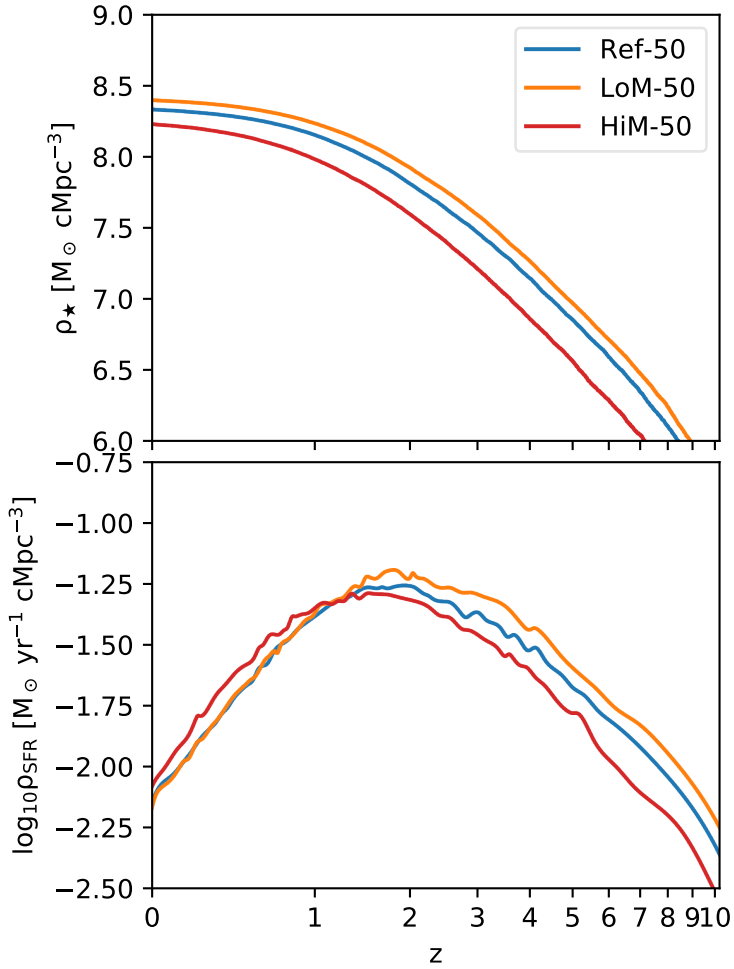


Figure 5.15: Comoving cosmic stellar mass density (top panel) and SFR density (bottom panel) as a function of redshift in the Ref-50 (blue), LoM-50 (orange) and HiM-50 (red) simulations. Star formation is enhanced and suppressed at high z in LoM-50 and HiM-50, respectively.

lower panel of Fig. 5.15. Note that here we show the true values, rather than those that would be inferred assuming a fixed IMF. For LoM-50, ρ_{SFR} is consistent with Ref-50 at low redshift, but at $z > 1.5$ it lies systematically ≈ 0.1 dex above the Ref-50 relation. This offset is likely due to the increased SFR from the star formation law renormalization that is required observationally (see Paper I), since at high redshift, most star formation occurs at high pressure, leading to bottom-heavy IMFs and thus a higher normalization of the star formation law.

For HiM-50, the opposite is true, where at high redshift the SFR is lower than Ref-50 by ≈ 0.1 dex. This could be due to the renormalization of the star formation law as well (which is decreased at high pressure in HiM-50), and/or due to the stronger stellar feedback associated with shallow high-mass IMF slopes. Stronger feedback would be more effective at keeping gas out of galaxies, delaying its reaccretion to later times. This hypothesis is supported by the fact that ρ_{SFR} is larger by ≈ 0.1 dex at $z < 1.5$, and the fact that the cold gas fractions are larger by ≈ 0.5 dex in high-mass galaxies in HiM-50 relative to Ref-50 and HiM-50 (see Fig. 12 of Paper I).

We showed in Paper I that the K -band luminosity functions of Ref-50, LoM-50, and HiM-50 are all consistent with observations at $z \approx 0$. We investigated the evolution of this relation for our simulations, finding no significant difference between them. However, the poor statistics at the bright end of the luminosity functions in our (50 Mpc)³ boxes preclude a detailed comparison, since it is at the bright (high-mass) end where the IMF is expected to have the largest impact. Simulations with larger volumes would thus be required to make a proper comparison.

5.5 Discussion

Throughout this project (Papers I, II, and this work), we have tested a model of galaxy formation and evolution that self-consistently includes local IMF variations that have been calibrated to reproduce the observed MLE– σ_e relation of Cappellari et al. (2013a). In this section we discuss some of the lessons learned and propose some steps for the future.

To make the simulations self-consistent, we made the stellar feedback, star formation law, and the metal yields depend on the IMF. Ensuring that each of these processes was self-consistent was vital in capturing the full effect of the IMF variations. Interestingly, this resulted in galaxy observables such as the luminosity function and BH masses to be mostly unchanged relative to a model with a fixed Chabrier IMF.

As discussed in Papers I and II, this is partially because while the change in IMF modifies the galaxies' masses through its effect on the stellar feedback, for the luminosity function this effect is largely cancelled by the modified M/L ratios resulting from the IMF variations. This story is, however, further complicated by the fact that in the mass regime in which the IMF varies significantly from the Chabrier form ($M_* \gtrsim 10^{10.5} M_\odot$) both stellar and AGN feedback play important roles in regulating the inflow of gas onto the galaxy. In this regime one might expect BH feedback (and thus BH growth and the $z = 0$ BH masses) to adjust to account for the modified stellar feedback resulting from IMF variations. However, we found that our modifications to

make the star formation law self-consistent precluded this (likely by adjusting the gas densities near the BHs), leading to similar BH masses as in the reference model. Thus, when performing variable IMF simulations, it is very important to include both self-consistent prescriptions for stellar feedback and the star formation law to ensure that the full effect of the IMF variations is captured and a realistic population of galaxies is produced.

For other galaxy properties, such as the metallicity and alpha enhancement, we have shown that the choice of IMF parametrization is extremely important when implementing IMF variations into galaxy formation models. Indeed, even though the LoM and HiM models produced similar MLE- σ_e relations, they resulted in very different metallicities and alpha abundances because the high-mass slope is especially important in setting the feedback strength and metal enrichment of galaxies. We thus encourage observational studies that infer the IMF slope to be careful in choosing which part of the IMF they should vary. For example, La Barbera et al. (2013) use the effect on the dwarf-to-giant ratio imprinted onto the spectra of old ETGs to constrain the IMF slope at all masses (0.1 to 100 M_\odot) or only at high masses. However, we have shown that the dwarf-to-giant ratio can be increased simply by varying the IMF only at low masses, leaving any variation of the high-mass IMF unconstrained by spectroscopic measurements of (old) ETGs. Indeed, we argue that varying only the low-mass slope is much preferred over the high-mass slope due to the strong effect the latter has on metal enrichment and stellar feedback in galaxy formation models, making the former the simplest model that explains the observations (see also Martín-Navarro 2016).

Despite the success of our variable IMF simulations in terms of reproducing observationally-inferred global and radial trends, we have shown that they are unable to simultaneously reproduce the inferred dwarf-to-giant ratios in ETGs, which prefer LoM, as well as the ionizing properties of late-type galaxies, which prefer HiM. In order to match all of these observations simultaneously, a more complex model of IMF variations, such as a hybrid of the LoM and HiM models, may be required. Indeed, the shallow high-mass slope in the HiM model was required to obtain sufficiently large MLE values from stellar remnants to reproduce the MLE $_r - \sigma_e$ relation of Cappellari et al. (2013b) when the low-mass slope was kept fixed. If the low-mass slope were allowed to vary in tandem with the high-mass slope, such shallow high-mass slopes would no longer be required to obtain large MLE values, as the MLE would then increase due to a combination of excess dwarf stars *as well as* excess stellar remnants. Such a model would need to become simultaneously bottom-heavy and top-heavy towards higher-pressure environments, possibly by steepening and levelling the low-mass and high-mass IMF slopes, respectively. This “butterfly” IMF model would need to be calibrated to simultaneously reproduce the MLE and dwarf-to-giant ratios of high-mass ETGs, as well as the ionizing fluxes of strongly star-forming galaxies. A similar model has already been implemented into semi-analytic models of galaxy formation with promising potential to reconcile these observations (Fontanot et al. 2018b), and would thus be interesting to implement into our self-consistent hydrodynamical, cosmological simulations.

5.6 Summary and Conclusions

In Paper I we presented two cosmological, hydrodynamical simulations based on the EAGLE model that self-consistently vary the IMF to become either more bottom-heavy (LoM-50) or top-heavy (HiM-50) locally in high-pressure environments. These IMF prescriptions were calibrated to match the observed relation between the “galaxy-wide” excess mass-to-light ratio relative to a fixed IMF (the MLE) as a function of stellar velocity dispersion, by respectively increasing the mass fraction of dwarfs or stellar remnants in high-pressure environments (Fig. 5.1). In Paper II we showed how the MLE varies globally between galaxies as a function of various galaxy properties, including metal enrichment, age, and BH mass. In this paper, we investigate radial trends within the galaxies in these simulations to compare with the EAGLE simulations with a universal, Chabrier IMF (Ref-50) and with observed radial gradients of IMF diagnostics and abundances in high-mass galaxies, in addition to investigating the redshift dependence of the IMF in our simulations.

In order to investigate internal trends that could be compared in a meaningful way with observations, we select all galaxies with intrinsic $u^* - r^* > 2$ and $\sigma_e > 150 \text{ km s}^{-1}$ from each simulation, hereafter referred to as the “Sigma150” sample (Fig. 5.4). Our conclusions regarding trends within these galaxies are as follows:

- High- σ_e galaxies exhibit strong radial IMF gradients, being either bottom- or top-heavy in the centre for LoM-50 and HiM-50 galaxies, respectively, and gradually transitioning to a Chabrier/Kroupa-like IMF beyond the half-light radius (Figs. 5.2, 5.3 and 5.5). These trends result from the inside-out growth of galaxies, where the stars in central regions tend to have formed earlier from interstellar gas with higher pressures than the stars in the outer regions (Fig. 5.6).
- For both simulations the IMF gradients result in an increase in the MLE toward the central regions, in qualitative agreement with recently observed MLE gradients in high-mass ETGs. While all high- σ_e galaxies in LoM-50 display negative MLE gradients, HiM-50 galaxies exhibit more diverse behaviour, with radial MLE gradients ranging from strongly negative to flat (Fig. 5.7). When measuring the IMF via the fraction of mass or light coming from low-mass dwarf stars, LoM-50 is consistent with observations of the centres of high-mass ETGs, while HiM-50 is in tension with the data (Fig. 5.8).
- The difference in the radial MLE behaviour between LoM-50 and HiM-50 is likely a result of the strong dependence of the MLE on age in HiM-50, even at fixed IMF slope, as well as the larger scatter in birth ISM pressure within r_e in HiM-50 galaxies (Fig. 5.6).
- All of our simulations produce negative stellar metallicity gradients, in agreement with observations. LoM-50 and Ref-50 produce weakly positive stellar [Mg/Fe] gradients. However, HiM-50 has enhanced [Mg/Fe] within r_e , causing [Mg/Fe] gradients to be much flatter, which may be more consistent with observed flat [Mg/Fe] profiles in high-mass ETGs (e.g. Mehlert et al. 2003;

Parikh et al. 2018). While M/L gradients are flat in Ref-50, LoM-50 galaxies have strong negative M/L gradients and HiM-50 galaxies show a large diversity in M/L gradients, ranging from strongly positive to strongly negative (Fig. 5.9). Such gradients must be taken into account when making inferences on the IMF via dynamical masses.

- We find strong positive correlations between the local MLE and local stellar metallicity for both LoM-50 and HiM-50 galaxies, qualitatively consistent with observations (Fig. 5.10, top row). This is true when considering all galaxies simultaneously or for individual galaxies. Correlations between MLE and local metallicity can thus occur naturally even when the IMF is not governed by metallicity at all.
- We find strong negative and positive correlations between the local MLE and local stellar $[Mg/Fe]$ for LoM-50 and HiM-50, respectively, when considering all galaxies simultaneously (Fig. 5.10, middle row). This finding may aid in distinguishing between these two IMF variation scenarios with observations.
- When considering all Sigma150 galaxies simultaneously, the local MLE shows a weak positive correlation with the local stellar age for LoM-50 (Fig. 5.10, bottom row). However, the local MLE shows no systematic correlation with local age for individual galaxies in either simulation, implying that the overall local MLE–age correlations seen for the whole Sigma150 population are a global, rather than a local, property, consistent with the strong positive global MLE–age relation reported in Paper II. It is thus important for studies of the spatially-resolved IMF to remove global trends between the MLE and galaxy properties before making inferences on local ones.

We have investigated the redshift dependence of the IMF and global galaxy properties in our variable IMF simulations. Our results are as follows:

- For LoM-50, the MLE– σ_e relation has a higher normalization at $z = 2$ than at $z = 0.1$ due to the typically higher pressures at which stars form at high redshift. In contrast, HiM-50 produces a much lower normalization at $z = 2$ despite the time dependence of stellar birth ISM pressures resulting in more top-heavy IMFs at early times (Fig. 5.11). This lower normalization arises due to the age dependence of the MLE parameter for the HiM prescription (Fig. 5.12).
- The dwarf-to-giant fraction increases weakly toward higher redshifts for high- σ_e galaxies in LoM-50, consistent with the observed evolution for quiescent galaxies (Fig. 5.13). HiM-50 is inconsistent with these observations.
- The ionizing flux of star-forming galaxies in HiM-50 increases with star formation rate surface density due to shallower IMF slopes at high pressures, and shows little evolution. This trend is consistent with observed star-forming galaxies, but our IMF slopes may be too shallow relative to the high-redshift observations (Fig. 5.14).

- We speculate that a model with a hybrid IMF, which incorporates both a shallow high-mass slope and a steep low-mass slope at high pressures, may be able to simultaneously reproduce the observed ionizing flux in star-forming galaxies as well as the MLE and dwarf-to-giant ratio in ETGs.
- At $z > 2$, the cosmic SFR density is higher and lower in LoM-50 and HiM-50, respectively, than in Ref-50. However, below $z \sim 1$, LoM-50 matches Ref-50 while HiM-50 lies above Ref-50. The peak of star formation is shifted toward lower redshift in HiM-50 (Fig. 5.15). This shift is likely caused by a combination of the decreased star formation law and burstier stellar feedback at high z in HiM-50, decreasing the SFR at high z and delaying the infall of cold gas onto galaxies.

The findings presented in this paper highlight the importance of being able to spatially resolve the galaxies in which the IMF is constrained. Indeed, radial IMF gradients can have significant implications for dynamical mass measurements used to constrain the IMF (e.g. Bernardi et al. 2018b), as well as when comparing quantities measured within different apertures (see van Dokkum et al. 2017). We have also shown that correlations between the IMF and local galaxy properties can differ both qualitatively and quantitatively from global relations between the same quantities. Thus, studies that do spatially resolve the IMF should take care to avoid confusing global and local IMF scaling relations when combining results for different galaxies.

Acknowledgements

We are grateful to the anonymous referee for improving the quality of this work. Madusha Gunawardhana for helpful discussions and Themiya Nanayakkara for providing data from ZFIRE. This work used the DiRAC Data Centric system at Durham University, operated by the Institute for Computational Cosmology on behalf of the STFC DiRAC HPC Facility (www.dirac.ac.uk). This equipment was funded by BIS National E-infrastructure capital grant ST/K00042X/1, STFC capital grants ST/H008519/1 and ST/K00087X/1, STFC DiRAC Operations grant ST/K003267/1 and Durham University. DiRAC is part of the National E-Infrastructure. RAC is a Royal Society University Research Fellows. We also gratefully acknowledge PRACE for awarding us access to the resource Curie based in France at Très Grand Centre de Calcul. This work was sponsored by the Dutch National Computing Facilities Foundation (NCF) for the use of supercomputer facilities, with financial support from the Netherlands Organization for Scientific Research (NWO). This research made use of `ASTROPY`, a community-developed core `PYTHON` package for Astronomy (Astropy Collaboration 2013). This work has benefited from the use of `Py-SPHViewer` (Benítez-Llambay 2017).

Bibliography

- Agarwal B., Davis A. J., Khochfar S., Natarajan P., Dunlop J. S., 2013, *MNRAS*, 432, 3438
- Alton P. D., Smith R. J., Lucey J. R., 2017, *MNRAS*, 468, 1594
- Alton P. D., Smith R. J., Lucey J. R., 2018, *MNRAS*
- Arnaud M., Rothenflug R., Boulade O., Vigroux L., Vangioni-Flam E., 1992, *A&A*, 254, 49
- Arrigoni M., Trager S. C., Somerville R. S., Gibson B. K., 2010, *MNRAS*, 402, 173
- Asplund M., Grevesse N., Sauval A. J., Scott P., 2009, *ARA&A*, 47, 481
- Astropy Collaboration 2013, *A&A*, 558, A33
- Auger M. W., Treu T., Gavazzi R., Bolton A. S., Koopmans L. V., Marshall P. J., 2010, *ApJ*, 721, L163
- Bahé Y. M., et al., 2016, *MNRAS*, 456, 1115
- Bahé Y. M., et al., 2017, *MNRAS*, 470, 4186
- Baldry I. K., et al., 2012, *MNRAS*, 421, 621
- Barber C., Schaye J., Bower R. G., Crain R. A., Schaller M., Theuns T., 2016, *MNRAS*, 460, 1147
- Barber C., Crain R. A., Schaye J., 2018a, *MNRAS*, 479, 5448
- Barber C., Schaye J., Crain R. A., 2018b, preprint (arXiv:1806.09406),
- Barnabè M., Spiniello C., Koopmans L. V., Trager S. C., Czoske O., Treu T., 2013, *MNRAS*, 436, 253
- Barnes J. E., Hernquist L., 1992, *ARA&A*, 30, 705
- Barnes D. J., et al., 2017, *MNRAS*, 471, 1088
- Barro G., et al., 2013, *ApJ*, 765
- Barth A. J., Darling J., Baker A. J., Boizelle B. D., Buote D. A., Ho L. C., Walsh J. L., 2016, *ApJ*, 823, 51
- Bastian N., Covey K. R., Meyer M. R., 2010, *ARA&A*, 48, 339
- Bate M. R., 2009, *MNRAS*, 392, 1363
- Bate M. R., Bonnell I. A., 2005, *MNRAS*, 356, 1201
- Baugh C. M., Lacey C. G., Frenk C. S., Granato G. L., Silva L., Bressan A., Benson A. J., Cole S., 2005, *MNRAS*, 356, 1191
- Behroozi P. S., Wechsler R. H., Conroy C., 2013, *ApJ*, 770
- Bekki K., 2013, *MNRAS*, 436, 2254
- Bekki K., Couch W. J., Drinkwater M. J., Shioya Y., 2003, *MNRAS*, 344, 399
- Benítez-Llambay A., 2017, *Astrophysics Source Code Library*, record ascl:1712.003
- Benítez-Llambay A., Navarro J. F., Frenk C. S., Ludlow A. D., 2018, *MNRAS*, 473, 1019
- Benson A. J., Bower R. G., Frenk C. S., Lacey C. G., Baugh C. M., Cole S., 2003, *ApJ*, 599, 38
- Bernardi M., et al., 2018a, *MNRAS*, 475, 757
- Bernardi M., Sheth R. K., Dominguez-Sanchez H., Fischer J. L., Chae K. H., Huertas-Company M., Shankar F., 2018b, *MNRAS*, 477, 2560

- Bezanson R., Van Dokkum P. G., Tal T., Marchesini D., Kriek M., Franx M., Coppi P., 2009, *ApJ*, 697, 1290
- Binney J., Tremaine S., 1987, *Galactic dynamics*. Princeton University Press, Princeton, NJ, <http://adsabs.harvard.edu/abs/1987gady.book.....B>
- Blancato K., Genel S., Bryan G., 2017, *ApJ*, 845, 21
- Blom C., Forbes D. A., Foster C., Romanowsky A. J., Brodie J. P., 2014, *MNRAS*, 439, 2420
- Bogdán Á., et al., 2012, *ApJ*, 753, 140
- Bondi H., Hoyle F., 1944, *MNRAS*, 104, 273
- Booth C. M., Schaye J., 2009, *MNRAS*, 398, 53
- Booth C. M., Schaye J., 2010, *MNRAS*, 405, L1
- Booth C. M., Schaye J., 2011, *MNRAS*, 413, 1158
- Boroson T. A., Thompson I. B., 1991, *AJ*, 101, 111
- Bower R. G., Schaye J., Frenk C. S., Theuns T., Schaller M., Crain R. A., McAlpine S., 2017, *MNRAS*, 465, 32
- Brodie J. P., Romanowsky A. J., Strader J., Forbes D. A., 2011, *AJ*, 142, 199
- Brooks A. M., Governato F., Quinn T., Brook C. B., Wadsley J., 2009, *ApJ*, 694, 396
- Brough S., Proctor R., Forbes D. A., Couch W. J., Collins C. A., Burke D. J., Mann R. G., 2007, *MNRAS*, 378, 1507
- Bruzual G., Charlot S., 2003, *MNRAS*, 344, 1000
- Calzetti D., 2001, *PASP*, 113, 1449
- Camps P., Baes M., 2015, *Astron. Comput.*, 9, 20
- Caplar N., Lilly S. J., Trakhtenbrot B., 2015, *ApJ*, 811, 148
- Cappellari M., et al., 2011, *MNRAS*, 413, 813
- Cappellari M., et al., 2013a, *MNRAS*, 432, 1709
- Cappellari M., et al., 2013b, *MNRAS*, 432, 1862
- Cardelli J., Clayton G., Mathis J., 1989, in Allamandola L., Tielens A., eds, *IAU Symposium Vol. 135, Interstellar Dust*. p. 5, <http://adsabs.harvard.edu/abs/1989IAUS...135P...5C>
- Catinella B., et al., 2018, *MNRAS*, 476, 875
- Cenarro A. J., Gorgas J., Vazdekis A., Cardiel N., Peletier R. F., 2003, *MNRAS*, 339, L12
- Chabrier G., 2003, *ApJ*, 586, 1
- Chang Y. Y., Wel A. V. D., Cunha E. D., Rix H. W., 2015, *ApJS*, 219
- Charlot S., Fall S. M., 2000, *ApJ*, 539, 718
- Chilingarian I. V., Mieske S., Hilker M., Infante L., 2011, *MNRAS*, 412, 1627
- Clauwens B., Schaye J., Franx M., 2015, *MNRAS*, 449, 4091
- Clauwens B., Schaye J., Franx M., 2016, *MNRAS*, 462, 2832
- Clauwens B., Schaye J., Franx M., Bower R. G., 2018, *MNRAS*, 478, 3994
- Collier W. P., Smith R. J., Lucey J. R., 2018, *MNRAS*
- Conroy C., Gunn J. E., 2010, *ApJ*, 712, 833
- Conroy C., van Dokkum P., 2012a, *ApJ*, 747, 22
- Conroy C., van Dokkum P. G., 2012b, *ApJ*, 760, 71
- Conroy C., Gunn J. E., White M., 2009, *ApJ*, 699, 486
- Conroy C., Graves G. J., van Dokkum P. G., 2014, *ApJ*, 780, 33
- Conroy C., van Dokkum P., Villaume A., 2017, *ApJ*, 837, 8
- Correa C. A., Schaye J., Clauwens B., Bower R. G., Crain R. A., Schaller M., Theuns T., Thob

- A. C., 2017, MNRAS, 472, L45
- Crain R. A., et al., 2015, MNRAS, 450, 1937
- Crain R. A., et al., 2017, MNRAS, 464, 4204
- Da Rocha C., Mieske S., Georgiev I. Y., Hilker M., Ziegler B. L., Mendes de Oliveira C., 2011, A&A, 525, A86
- Dahlen T., al. E., 2008, ApJ, 681, 462
- Dalla Vecchia C., Schaye J., 2012, MNRAS, 426, 140
- Davies L. J., et al., 2016, MNRAS, 461, 458
- Davis T. A., McDermid R. M., 2017, MNRAS, 464, 453
- Davis M., Efstathiou G., Frenk C. S., White S. D. M., 1985, ApJ, 292, 371
- De Lucia G., Fontanot F., Hirschmann M., 2017, MNRAS, 466, L88
- De Rossi M. E., Bower R. G., Font A. S., Schaye J., Theuns T., 2017, MNRAS, 472, 3354
- Dekel A., et al., 2009, Nature, 457, 451
- Dilday B., et al., 2010, ApJ, 713, 1026
- Dolag K., Borgani S., Murante G., Springel V., 2009, MNRAS, 399, 497
- Driver S. P., et al., 2012, MNRAS, 427, 3244
- Dutton A. A., Mendel J. T., Simard L., 2012, MNRAS, 422, L33
- Emsellem E., 2013, MNRAS, 433, 1862
- Fabian A. C., 1999, MNRAS, 308, L39
- Fabian A. C., Sanders J. S., Haehnelt M., Rees M. J., Miller J. M., 2013, MNRAS, 431, L38
- Fall S. M., Efstathiou G., 1980, MNRAS, 193, 189
- Ferrarese L., Merritt D., 2000, ApJ, 539, L9
- Ferré-Mateu A., Mezcua M., Trujillo I., Balcells M., van den Bosch R. C. E., 2015, ApJ, 808, 79
- Ferreras I., La Barbera F., de la Rosa I. G., Alexandre V., de Carvalho R. R., Falcón-Barroso J., Ricciardelli E., 2013, MNRAS, 429, L15
- Ferreras I., Weidner C., Vazdekis A., La Barbera F., 2015, MNRAS, 448, L82
- Fischera J., Dopita M., 2005, ApJ, 619, 340
- Fontanot F., 2014, MNRAS, 442, 3138
- Fontanot F., De Lucia G., Hirschmann M., Bruzual G., Charlot S., Zibetti S., 2017, MNRAS, 464, 3812
- Fontanot F., La Barbera F., De Lucia G., Pasquali A., Vazdekis A., 2018a, MNRAS
- Fontanot F., De Lucia G., Xie L., Hirschmann M., Bruzual G., Charlot S., 2018b, MNRAS, 475, 2467
- Furlong M., et al., 2015, MNRAS, 450, 4486
- Furlong M., et al., 2017, MNRAS, 465, 722
- Gallazzi A., Charlot S., Brinchmann J., White S. D., Tremonti C. A., 2005, MNRAS, 362, 41
- Gargiulo I. D., et al., 2015, MNRAS, 446, 3820
- Gebhardt K., et al., 2000, ApJ, 539, L13
- Graham A. W., Durré M., Savorgnan G. A. D., Medling A. M., Batcheldor D., Scott N., Watson B., Marconi A., 2016, ApJ, 819, 43
- Graur O., Maoz D., 2013, MNRAS, 430, 1746
- Graur O., et al., 2014, ApJ, 783, 28
- Greene J. E., Peng C. Y., Ludwig R. R., 2010, ApJ, 709, 937
- Greene J. E., Janish R., Ma C. P., McConnell N. J., Blakeslee J. P., Thomas J., Murphy J. D., 2015, ApJ, 807

- Gültekin K., et al., 2009, *ApJ*, 698, 198
- Gunawardhana M. L. P., et al., 2011, *MNRAS*, 415, 1647
- Gustafsson B., Edvardsson B., Eriksson K., Jorgensen U. G., Nordlund A., Plez B., 2008, *A&A*, 486, 951
- Guszejnov D., Hopkins P. F., Ma X., 2017, *MNRAS*, 472, 2107
- Gutcke T. A., Springel V., 2017, preprint (arXiv:1710.04222)
- Haardt F., Madau P., 2001, in Neumann D. M., Tran J. T. V., eds, *Clusters of Galaxies and the High Redshift Universe Observed in X-rays*. Savoie, France, p. 64, <http://adsabs.harvard.edu/abs/2001cghr.confE..64H>
- Haas M. R., Schaye J., Booth C. M., Vecchia C. D., Springel V., Theuns T., Wiersma R. P. C., 2013, *MNRAS*, 435, 2931
- Habergham S. M., Anderson J. P., James P. A., 2010, *ApJ*, 717, 342
- Hennebelle P., Chabrier G., 2013, *ApJ*, 770, 150
- Hilz M., Naab T., Ostriker J. P., Thomas J., Burkert A., Jesseit R., 2012, *MNRAS*, 425, 3119
- Hopkins P. F., 2012, *MNRAS*, 423, 2037
- Hopkins P. F., 2013, *MNRAS*, 428, 2840
- Humphrey P. J., Buote D. A., Brighenti F., Gebhardt K., Mathews W. G., 2009, *ApJ*, 703, 1257
- Jahnke K., Macciò A. V., 2011, *ApJ*, 734, 92
- Jahnke K., et al., 2009, *ApJ*, 706, L215
- Jappsen A.-K., Klessen R. S., Larson R. B., Li Y., Mac Low M.-M., 2005, *A&A*, 435, 611
- Javier Cenarro A., Trujillo I., 2009, *ApJ*, 696, L43
- Jiang L., Helly J. C., Cole S., Frenk C. S., 2014, *MNRAS*, 440, 2115
- Katz N., 1992, *ApJ*, 391, 502
- Kelvin L. S., et al., 2012, *MNRAS*, 421, 1007
- Kennicutt, Jr. R. C., 1998, *ApJ*, 498, 541
- Kereš D., Katz N., Weinberg D. H., Davé R., 2005, *MNRAS*, 363, 2
- Kewley L. J., Ellison S. L., 2008, *ApJ*, 681, 1183
- King A., 2003, *ApJ*, 596, L27
- Kormendy J., Ho L. C., 2013, *ARA&A*, 51, 511
- Kormendy J., Richstone D., 1995, *ARA&A*, 33, 581
- Kroupa P., 2001, *MNRAS*, 322, 231
- Kroupa P., Weidner C., 2003, *ApJ*, 598, 1076
- Krumholz M. R., 2011, *ApJ*, 743, 110
- Kuntschner H., et al., 2010, *MNRAS*, 408, 97
- La Barbera F., Ferreras I., Vazdekis A., de la Rosa I. G., de Carvalho R. R., Trevisan M., Falcón-Barroso J., Ricciardelli E., 2013, *MNRAS*, 433, 3017
- La Barbera F., Ferreras I., Vazdekis A., 2015, *MNRAS*, 449, L137
- La Barbera F., Vazdekis A., Ferreras I., Pasquali A., Cappellari M., Martín-Navarro I., Schönebeck F., Falcón-Barroso J., 2016, *MNRAS*, 457, 1468
- Lagos C. d. P., et al., 2015, *MNRAS*, 452, 3815
- Lagos C. d. P., et al., 2018, *MNRAS*, 473, 4956
- Lange R., et al., 2015, *MNRAS*, 447, 2603
- Lasker R., van den Bosch R. C. E., van de Ven G., Ferreras I., La Barbera F., Vazdekis A., Falcón-Barroso J., 2013, *MNRAS*, 434, L31
- Lejeune T., Cuisinier F., Buser R., 1997, *A&AS*, 125, 229

- Lejeune T., Cuisinier F., Buser R., 1998, *A&AS*, 130, 65
- Lemaître G., 1927, *Annales de la Société Scientifique de Bruxelles*, 47, 49
- Li H., et al., 2017, *ApJ*, 838, 77
- Lupton R. H., Blanton M. R., Fekete G., Hogg D. W., O'Mullane W., Szalay A. S., Wherry N., 2004, *PASP*, 116, 133
- Lyubenova M., et al., 2016, *MNRAS*, 463, 3220
- Magorrian J., et al., 1998, *AJ*, 115, 2285
- Maraston C., Strömbäck G., 2011, *MNRAS*, 418, 2785
- Marigo P., Girardi L., 2007, *A&A*, 469, 239
- Marigo P., Girardi L., Bressan A., Groenewegen M. A. T., Silva L., Granato G. L., 2008, *A&A*, 482, 883
- Martín-Navarro I., 2016, *MNRAS*, 456, L104
- Martín-Navarro I., et al., 2015a, *ApJ*, 798, L4
- Martín-Navarro I., La Barbera F., Vazdekis A., Falcón-Barroso J., Ferreras I., 2015b, *MNRAS*, 447, 1033
- Martín-Navarro I., et al., 2015c, *ApJ*, 806, L31
- Martín-Navarro I., La Barbera F., Vazdekis A., Ferré-Mateu A., Trujillo I., Beasley M. A., 2015d, *MNRAS*, 451, 1081
- McAlpine S., et al., 2016, *Astron. Comput.*, 15, 72
- McAlpine S., Bower R. G., Rosario D. J., Crain R. A., Schaller M., Schaye J., Theuns T., 2018, preprint (arXiv:1805.08293)
- McConnell N. J., Ma C.-P., 2013, *ApJ*, 764, 184
- McConnell N. J., Lu J. R., Mann A. W., 2016, *ApJ*, 821, 39
- McDermid R. M., et al., 2014, *ApJ*, 792, 5
- McDermid R. M., et al., 2015, *MNRAS*, 448, 3484
- Mehlert D., Thomas D., Saglia R. P., Bender R., Wegner G., 2003, *A&A*, 407, 423
- Meurer G. R., et al., 2009, *ApJ*, 695, 765
- Mieske S., Frank M. J., Baumgardt H., Lützgendorf N., Neumayer N., Hilker M., 2013, *A&A*, 558, A14
- Mo H. J., Mao S., White S. D., 1998, *MNRAS*, 295, 319
- Moster B. P., Naab T., White S. D., 2013, *MNRAS*, 428, 3121
- Moustakas J., et al., 2013, *ApJ*, 767
- Naab T., Jesseit R., Burkert A., 2006, *MNRAS*, 372, 839
- Nanayakkara T., et al., 2017, *MNRAS*, 468, 3071
- Narayanan D., Davé R., 2012, *MNRAS*, 423, 3601
- Narayanan D., Davé R., 2013, *MNRAS*, 436, 2892
- Navarro J. F., Frenk C. S., White S. D. M., 1995, *MNRAS*, 275, 56
- Newman A. B., Smith R. J., Conroy C., Villaume A., van Dokkum P., 2017, *ApJ*, 845, 18
- Norris M. A., et al., 2014, *MNRAS*, 443, 1151
- Norris M. A., Escudero C. G., Faifer F. R., Kannappan S. J., Forte J. C., van den Bosch R. C. E., 2015, *MNRAS*, 451, 3615
- Oldham L., Auger M., 2018a, *MNRAS*, 474, 4169
- Oldham L. J., Auger M. W., 2018b, *MNRAS*, 476, 133
- Oser L., Ostriker J. P., Naab T., Johansson P. H., Burkert A., 2010, *ApJ*, 725, 2312
- Oser L., Naab T., Ostriker J. P., Johansson P. H., 2012, *ApJ*, 744, 63

- Paalvast M., Brinchmann J., 2017, MNRAS, 470, 1612
- Parikh T., et al., 2018, MNRAS, 477, 3954
- Pechetti R., Seth A., Cappellari M., McDermid R., den Brok M., Mieske S., Strader J., 2017, ApJ, 850, 15
- Peng C. Y., 2007, ApJ, 671, 1098
- Perrett K., et al., 2012, AJ, 144, 59
- Pfeffer J., Griffen B. F., Baumgardt H., Hilker M., 2014, MNRAS, 444, 3670
- Pfeffer J., Hilker M., Baumgardt H., Griffen B. F., 2016, MNRAS, 458, 2492
- Planck Collaboration 2014, A&A, 571, A1
- Portinari L., Chiosi C., Bressan A., 1997, A&A, 334, 38
- Posacki S., Cappellari M., Treu T., Pellegrini S., Ciotti L., 2015, MNRAS, 446, 493
- Qu Y., et al., 2016, Submitted to MNRAS
- Quilis V., 2004, MNRAS, 352, 1426
- Rahmati A., Pawlik A. H., Raičević M., Schaye J., 2013, MNRAS, 430, 2427
- Rahmati A., Schaye J., Bower R. G., Crain R. A., Furlong M., Schaller M., Theuns T., 2015, MNRAS, 452, 2034
- Rahmati A., Schaye J., Crain R. A., Oppenheimer B. D., Schaller M., Theuns T., 2016, MNRAS
- Robertson B., Bullock J. S., Cox T. J., Di Matteo T., Hernquist L., Springel V., Yoshida N., 2006, ApJ, 645, 986
- Rosani G., Pasquali A., La Barbera F., Ferreras I., Vazdekis A., 2018, MNRAS, 476, 5233
- Rosas-Guevara Y. M., et al., 2015, MNRAS, 454, 1038
- Rosas-Guevara Y., et al., 2016, eprint arXiv:1604.00020, p. 17
- Rusli S. P., Thomas J., Erwin P., Saglia R. P., Nowak N., Bender R., 2011, MNRAS, 410, 1223
- Saglia R. P., et al., 2016, ApJ, 818, 47
- Sales L. V., Navarro J. F., Schaye J., Vecchia C. D., Springel V., Booth C. M., 2010, MNRAS, 409, 1541
- Salpeter E. E., 1955, ApJ, 121, 161
- Sarzi M., Spiniello C., La Barbera F., Krajnović D., van den Bosch R., 2018, MNRAS
- Saulder C., van den Bosch R. C. E., Mieske S., 2015, A&A, 578, A134
- Schaller M., et al., 2015a, MNRAS, 451, 1247
- Schaller M., Dalla Vecchia C., Schaye J., Bower R. G., Theuns T., Crain R. A., Furlong M., McCarthy I. G., 2015b, MNRAS, 454, 2277
- Scharwächter J., Combes F., Salomé P., Sun M., Krips M., 2016, MNRAS, 457, 4272
- Schaye J., 2004, ApJ, 609, 667
- Schaye J., Dalla Vecchia C., 2008, MNRAS, 383, 1210
- Schaye J., et al., 2010, MNRAS, 402, 1536
- Schaye J., et al., 2015, MNRAS, 446, 521
- Segers M. C., Schaye J., Bower R. G., Crain R. A., Schaller M., Theuns T., 2016, MNRAS, 461, L102
- Seth A. C., et al., 2014, Nature, 513, 398
- Shen S., Mo H. J., White S. D. M., Blanton M. R., Kauffmann G., Voges W., Brinkmann J., Csabai I., 2003, MNRAS, 343, 978
- Shivaei I., et al., 2018, ApJ, 855, 13
- Silk J., Rees M. J., 1998, A&A, 331, L1
- Smith R. J., 2014, MNRAS, 443, L69

- Smith R. J., Lucey J. R., Carter D., 2012, MNRAS, 426, 2994
- Smith R. J., Alton P., Lucey J. R., Conroy C., Carter D., 2015, MNRAS, 454, L71
- Sonnenfeld A., Treu T., Marshall P. J., Suyu S. H., Gavazzi R., Auger M. W., Nipoti C., 2015, ApJ, 800
- Sonnenfeld A., Nipoti C., Treu T., 2017, MNRAS, 465, 2397
- Sonnenfeld A., Leauthaud A., Auger M. W., Gavazzi R., Treu T., More S., Komiyama Y., 2018, preprint (arXiv:1801.01883)
- Spiniello C., Koopmans L. V., Trager S. C., Czoske O., Treu T., 2011, MNRAS, 417, 3000
- Spiniello C., Trager S. C., Koopmans L. V., Chen Y. P., 2012, ApJ, 753, 32
- Spiniello C., Trager S., Koopmans L. V., Conroy C., 2014, MNRAS, 438, 1483
- Spolaor M., Forbes D. A., Proctor R. N., Hau G. K., Brough S., 2008, MNRAS, 385, 675
- Springel V., 2005, MNRAS, 364, 1105
- Springel V., 2010, MNRAS, 401, 791
- Springel V., White S. D. M., Tormen G., Kauffmann G., 2001, MNRAS, 328, 726
- Springel V., Di Matteo T., Hernquist L., 2005, MNRAS, 361, 776
- Teyssier R., 2002, A&A, 385, 337
- Thomas D., Maraston C., Bender R., 2003, Monthly Notice of the Royal Astronomical Society, 339, 897
- Thomas D., Maraston C., Schawinski K., Sarzi M., Silk J., 2010, MNRAS, 404, 1775
- Thomas D., Maraston C., Johansson J., 2011a, MNRAS, 412, 2183
- Thomas J., et al., 2011b, MNRAS, 415, 545
- Toomre A., Toomre J., 1972, ApJ, 178, 623
- Tortora C., Romanowsky A. J., Napolitano N. R., 2013, ApJ, 765
- Trakhtenbrot B., et al., 2015, Science, 349, 168
- Trayford J. W., et al., 2015, MNRAS, 452, 2879
- Tremonti C. A., et al., 2004, ApJ, 613, 898
- Treu T., Auger M. W., Koopmans L. V. E., Gavazzi R., Marshall P. J., Bolton A. S., 2010, ApJ, 709, 1195
- Van Der Wel A., et al., 2012, ApJS, 203, 12
- Van Dokkum P. G., Conroy C., 2010, Nature, 468, 940
- Vaughan S. P., Davies R. L., Zieleniewski S., Houghton R. C., 2018a, MNRAS, 475, 1073
- Vaughan S. P., Davies R. L., Zieleniewski S., Houghton R. C. W., 2018b, MNRAS, sty1434
- Vazdekis A., Casuso E., Peletier R. F., Beckman J. E., 1996, ApJS, 106, 307
- Vazdekis A., Sánchez-Blázquez P., Falcón-Barroso J., Cenarro A. J., Beasley M. A., Cardiel N., Gorgas J., Peletier R. F., 2010, MNRAS, 404, 1639
- Vazdekis A., Ricciardelli E., Cenarro A. J., Rivero-González J. G., Díaz-García L. A., Falcón-Barroso J., 2012, MNRAS, 424, 157
- Villaume A., Conroy C., Johnson B., Rayner J., Mann A. W., van Dokkum P., 2017a, ApJS, 230, 38
- Villaume A., Brodie J., Conroy C., Romanowsky A. J., van Dokkum P., 2017b, ApJ, 850, L14
- Volonteri M., Haardt F., Gültekin K., 2008, MNRAS, 384, 1387
- Volonteri M., Dubois Y., Pichon C., Devriendt J., 2016, MNRAS, 460, 2979
- Walsh J. L., et al., 2015, ApJ, 808, 16
- Walsh J. L., van den Bosch R. C. E., Gebhardt K., Yildirim A., Richstone D. O., Gültekin K., Husemann B., 2016, ApJ, 817, 2

- Weidner C., Ferreras I., Vazdekis A., Barbera F. L., 2013, MNRAS, 435, 2274
- Westera P., Lejeune T., Buser R., Cuisinier F., A. G. B., 2002, A&A, 381, 524
- White S. D. M., Rees M. J., 1978, MNRAS, 183, 341
- Wiersma R. P. C., Schaye J., Smith B. D., 2009a, MNRAS, 393, 99
- Wiersma R. P. C. R., Schaye J., Theuns T., Dalla Vecchia C., Tornatore L., 2009b, MNRAS, 399, 574
- Yildirim A., van den Bosch R. C. E., van de Ven G., Husemann B., Lyubenova M., Walsh J. L., Gebhardt K., Gültekin K., 2015, MNRAS, 452, 1792
- Zahid H. J., Dima G. I., Kudritzki R.-P., Kewley L. J., Geller M. J., Hwang H. S., Silverman J. D., Kashino D., 2014, ApJ, 791, 130
- Zhang Z.-Y., Romano D., Ivison R. J., Papadopoulos P. P., Matteucci F., 2018, Nature, 558, 260
- Zieleniewski S., Houghton R. C., Thatte N., Davies R. L., Vaughan S. P., 2017, MNRAS, 465, 192
- van Dokkum P., Conroy C., Villaume A., Brodie J., Romanowsky A., 2017, ApJ, 841, 23
- van Loon J. T., Sansom A. E., 2015, MNRAS, 453, 2342
- van den Bosch R. C. E., Gebhardt K., Gültekin K., van de Ven G., van der Wel A., Walsh J. L., 2012, Nature, 491, 729

Nederlandse Samenvatting

Sterrenstelsels zijn als exotische eilanden in de uitgestrekte en lege oceaan van de kosmos, die langzaam gas omzetten in sterren, planeten, en mensen. Ze omringen ons aan alle kanten, in verschillende vormen, maten, en kleuren. Ons eigen sterrenstelsel, de Melkweg, biedt plaats aan miljarden sterren, met daaronder ook onze Zon en de Aarde vanwaar we op het universum uitkijken. Om te leren wat onze plek is in de Melkweg, en ook wat de plek van de Melkweg is in het universum, moeten we bestuderen hoe sterrenstelsel vormen en evolueren.

Een van de beste manieren om theorieën over de formatie en evolutie van sterrenstelsels te testen is het draaien van numerieke simulaties van een representatief deel van het Universum waarin sterrenstelsels vormen en evolueren in een kosmologische context. De sterrenstelsels die in zo'n simulatie vormen kunnen dan worden vergeleken met de sterrenstelsels die we om eens heen zien. Hoewel het bemoedigend is als ze overeenkomen (want dan doen we iets goed), is het het meest interessant als ze niet overeenkomen, want dan klopt onze theorie niet en moeten we deze aanpassen, wat ons in staat stelt om onze theorie te verbeteren en daardoor een beetje meer te weten te komen over hoe het Universum werkt. In dit proefschrift bestudeer ik grote statistische ensembles van sterrenstelsels die gegenereerd zijn in zulke simulaties om de extra "monsterlijke" hoeveelheden materie te begrijpen die recentelijk zijn ontdekt diep in de centrale regionen van echte sterrenstelsels.

Hoofdstuk 2: Monsterlijke zwarte gaten

Zwarte gaten zijn ballen materie met een hoge dichtheid die zo klein en zo massief zijn dat zelfs licht er niet aan kan ontsnappen. Ze vormen normaal gesproken uit de overgebleven kern van een hoge-massa ster (meer dan 8 keer de massa van de zon) wanneer die aan het eind van zijn leven explodeert als een supernova. Er wordt aangenomen dat alle sterrenstelsels in hun centrum een zogeheten "superzwaar" zwart gat bevatten, met massa's die wel een miljoen tot een miljard keer groter zijn dan de massa van de zon. Hoe een zwart gat zo superzwaar wordt is nog niet bekend, maar we weten al wel dat de massa van een zwart gat groter is als het het sterrenstelsel een grotere massa heeft: zwaardere sterrenstelsels bevatten zwaardere zwarte gaten. De achterliggende fysica voor dit verband is echter nog onduidelijk.

Recentelijk hebben astronomen enkele sterrenstelsels ontdekt waar de zwarte gaten een veel hogere massa hebben dan werd verwacht op basis van de massa van het sterrenstelsel. Als we deze uitschieters kunnen begrijpen kan dat hints geven over

de oorsprong van het verband tussen de massa's van zwarte gaten en de sterrenmassa van sterrenstelsels. In **Hoofdstuk 2** onderzocht ik of sterrenstelsels met “monsterlijke” zwarte gaten verwacht worden in mijn ensemble van gesimuleerde sterrenstelsels zoals voorspeld door de huidige formatie en evolutie theorieën van sterrenstelsels. Stelsels met zulke superzware zwarte gaten worden inderdaad verwacht, en ze vormen via twee kanalen.

Het eerst kanaal heet “getijde-verscheuring”. Wanneer een sterrenstelsel een satelliet wordt van een zwaarder sterrenstelsel ervaart het getijde-krachten, dezelfde krachten die op Aarde verantwoordelijk zijn voor de getijden van de zee: de maan trekt sterker aan het water dan de Aarde, en probeert het water letterlijk van de aarde weg te scheuren. Gelukkig voor ons zijn de getijde krachten van de Maan niet sterk genoeg om dit te doen. Satelliet stelsels zijn niet zo gelukkig, en kunnen worden verscheurd door de getijde krachten van het zwaardere stelsel. Omdat de buitenste delen van het satelliet stelsel eerst worden weggescheurd gaat de sterrenmassa van het satelliet stelsel omlaag, waardoor de sterrenmassa relatief klein is vergeleken met de massa van superzware zwarte gat in het centrum, dat onverstoord in het centrum van het satelliet stelsel staat.

Het tweede kanaal heeft te maken met de formatietijd van het sterrenstelsel. Zwarte gaten groeien door het omringende gas op te zuigen. Als het centrum van een sterrenstelsel veel gas bevat, zal het zwarte gat dat opzuigen en naar een hoge massa groeien. Echter, om het gas naar het zwarte gat te krijgen moet het erin vallen, tijdens die val zal het gas een schijf vormen, zoals water in een badkuip een draaikolk vormt terwijl het wegloopt. De wrijving in deze stofschijschijf verhoogt de temperatuur zo erg dat de energie het gas uit het sterrenstelsel kan blazen, waardoor het zwarte gat niet verder kan groeien. De maximale massa van een zwart gat wordt dus bepaald door zijn vermogen om te voorkomen dat het gas er te snel in valt. In het begin had het universum, en dus ook de sterrenstelsels, een hoge dichtheid. Voor stelsels van dezelfde massa was het toen dus moeilijker het gas weg te houden, vergeleken met de lagere dichtheid van nu. Stelsels met dezelfde massa moesten vroeger dus een veel zwaarder zwart gat vormen om te voorkomen dat gas naar binnen viel dan nu. Dat betekent dus dat sterrenstelsels die vroeg vormen en daarna niet meer veranderen een “monsterlijk” superzwaar zwart gat moeten bevatten.

Hoofdstukken 3, 4, en 5: Sterpopulatie monsters

De sterrenkunde is een van de weinige wetenschappen waar we de objecten die we bestuderen niet kunnen aanraken. Bijna alles wat we over sterrenstelsels weten, komt van het ontleden van het licht dat we van de stelsels ontvangen. Zelfs zoiets fundamenteels als de massa van een stelsel kan lastig te meten zijn, omdat dit afhangt van hoe je de lichtkracht van een sterrenstelsel omzet naar massa. Deze omzetting wordt gewoonweg gedaan door de helderheid van het stelsels te vermenigvuldigen met verhouding tussen massa en licht die verwacht wordt voor het stelsel. Dit is echter niet zo eenvoudig omdat de verhouding tussen massa en licht voor individuele sterren afhangt van de massa van de ster (en ook van de leeftijd). Sterren met een lage massa (ongeveer 10 procent van de massa van de Zon), zijn vrij zwak en hebben een hoge

massa-licht verhouding, terwijl sterren met een hoge massa heel helder zijn (en een lagere massa-licht verhouding hebben). De verdeling van sterren van verschillende massa die gevormd worden in een sterrenstelsel (de “initiële massa functie”, of IMF) bepaalt dus de conversie van helderheid naar massa voor dat stelsel, en is de meest onzekere factor voor de massa bepaling.

Voor de Melkweg is het relatief eenvoudig om de IMF te meten door simpelweg sterren van verschillende massa’s te tellen. Voor sterrenstelsels die verder weg staan is het echter niet zo makkelijk omdat de sterren overlappen, wat het onmogelijk maakt om ze individueel te tellen. Daarom nemen de meeste astronomen aan dat de IMF in andere sterrenstelsels hetzelfde is als in de Melkweg. Recentelijk hebben enkele astronomen echter ontdekt dat massa licht-verhouding die gebruikt wordt voor het centrum van de zwaarste stelsels meer dan twee keer zo hoog is als in de Melkweg. Dit zou kunnen betekenen dat er meer dwergsterren met lage massa’s bestaan dan werd gedacht, en die te zwak zijn om te detecteren, of dat er veel meer zwarte gaten met een massa vergelijkbaar met die van sterren bestaan, de overblijfselen van de supernova explosies van hoge massa sterren.

Het huidige model voor de formatie en ontwikkeling van sterrenstelsel dat ik in hoofdstuk 2 gebruikte neemt aan dat alle sterrenstelsels een universele, Melkweg-achtige, IMF hebben. Met de recente ontdekking dat de aanname van zo’n universele IMF misschien niet correct is, heb ik de simulatie-code aangepast zodat de IMF van de gesimuleerde stelsels afhangt van de omgeving waarin de sterren vormen. Omdat zwaardere sterrenstelsels sterren vormen onder hogere druk, hebben we de IMF afhankelijk gemaakt van de druk op zo’n manier dat het waargenomen overschot in de massa-licht verhouding, ten opzichte van de Melkweg-achtige IMF (het MLO, die vaak wordt gebruikt als meting van de IMF), en de massa’s van de sterrenstelsels werden gereproduceerd. We deden een simulatie waar we de massa-licht verhouding verhoogden door het aantal lage-massa dwergsterren dat door de simulatie geproduceerd wordt te verhogen, terwijl we in een andere simulatie het aantal hoge-massa sterren verhoogden, zodat er meer zwarte gaten ontstaan en de massa-licht verhouding hoger wordt. We draaiden deze simulaties om te zien wat voor effect deze veranderingen hadden op de sterrenstelsels die in de simulaties vormden, en wat het effect is op de omzetting van waarnemingen (e.g. lichtkracht) naar fysieke grootheden (zoals massa) en om te bepalen wat voor voorspellingen we konden doen om een onderscheid te maken tussen deze twee scenario’s.

Hoofdstuk 3 beschrijft de twee simulaties in detail. Ondanks de variaties in de IMF blijken de sterrenstelsels die zich in de simulaties vormen dezelfde fundamentele eigenschappen te hebben, zoals lichtkracht, afmeting, en de massa van het centrale zwarte gat. Echter, de simulatie met meer hoge-massa sterren bevatte een veel groter aandeel van metalen, en ook veel meer energetische supernova explosies, waardoor de sterrenstelsels groter waren en snellere stervorming dan wat in het echt wordt waargenomen.

Hoofdstuk 4 laat zien dat het massa-licht overschot afhangt van een aantal fysieke eigenschappen van de sterrenstelsels. Deze verbanden kunnen afwijken van de verwachting, en deze afwijking is sterk afhankelijk van hoe de stelsels geselecteerd

worden. We demonstreren ook dat het MLO sterker afhangt van de leeftijd van de sterpopulatie dan de IMF in sommige gevallen. Stelsels met te zware zwarte gaten hebben vaak ook een hoger MLO, wat betekent dat sterpopulatie monsters waarschijnlijk ook monsterlijke zwarte gaten bevatten.

In **Hoofdstuk 5** onderzoeken we hoe de IMF varieert als functie van de straal binnen de stelsels, en ook hoe de IMF varieert als functie van tijd. Het blijkt dat, omdat de druk waarbij sterren worden gevormd hoger is naarmate we dichterbij het centrum van het sterrenstelsel komen, de IMF zwaarder wordt in het centrum van het stelsel, wat resulteert in een overgang van een hoge massa-licht verhouding in het centrum naar een lagere massa-licht verhouding aan de rand van het stelsel. Dit resultaat kan grote gevolgen hebben voor de omzetting van lichtkracht naar massa, gezien normaal wordt aangenomen dat de massa-licht verhouding in het hele stelsel hetzelfde is. We laten ook zien dat het verband tussen de MLO en de hoeveelheid metalen verschilt tussen de twee simulaties, wat een mogelijke manier biedt om deze twee IMF mogelijkheden van elkaar te onderscheiden.

In het algemeen zijn geen van de twee simulaties voldoende om alle waarnemingen gerelateerd aan de IMF te verklaren. Mogelijk is de combinatie van de twee scenario's, waarin we dus het aandeel van zowel lage- als hoge-massa sterren verhogen in aanwezigheid van hoge druk, een veelbelovende manier om variaties in de IMF verder te onderzoeken.

Publications

Refereed Publications

Barber C., Schaye J., Crain R. A., *Calibrated, cosmological hydrodynamical simulations with variable IMFs II: Correlations between the IMF and global galaxy properties*, accepted for publication in MNRAS.

Barber C., Crain R. A., Schaye J., 2018, *Calibrated, cosmological hydrodynamical simulations with variable IMFs I: method and effect on global galaxy scaling relations*, MNRAS, 479, 5448.

Ploekinger S., Sharma K., Schaye J., Crain R. A., Schaller M., **Barber C.**, 2017, *Tidal dwarf galaxies in cosmological simulations*, MNRAS, 474, 580.

Barber C., Schaye J., Bower R. G., Crain R. A., Schaller M., Theuns T., 2016, *The origin of compact galaxies with anomalously high black hole masses*, MNRAS, 460, 1147.

Barber C., Starkeburg E., Navarro J. F., McConnachie A. W., 2015, *Galactic tides and the shape and orientation of dwarf galaxy satellites*, MNRAS, 447, 1112.

Barber C., Courteau S., Roediger J., Schiavon R., 2014, *Validation of optimized population synthesis through mock spectra and Galactic globular clusters*, MNRAS, 440, 2953.

Barber C., Starkeburg E., Navarro J., McConnachie A. W., Fattahi A., 2014, *The orbital ellipticity of satellite galaxies and the mass of the Milky Way*, MNRAS, 437, 959.

Fattahi A., Navarro J. F., Starkeburg E., **Barber C.**, McConnachie A. W., 2013, *Galaxy Pairs in the Local Group*, MNRAS, 431, 73.

Publications submitted

Barber C., Schaye J., Crain R. A., *Calibrated, cosmological hydrodynamical simulations with variable IMFs III: Spatially-resolved properties and evolution*, submitted to MNRAS.

van Son L. A. C., **Barber C.**, Bahé Y. M., Schaye J., Barnes D. J., Crain R. A., Kay S. T., Theuns T., Dalla Vecchia C. *Galaxies with monstrous black holes in galaxy cluster environments*, submitted to MNRAS.

Curriculum Vitae

I was born on 21 March, 1989 in Ottawa, Ontario, Canada. I was fortunate to grow up in the small village of Merrickville where the stars are seen much more easily than in a city, giving me a close connection with the night sky at an early age. Even when we moved to the city of Ottawa, I still recall the dozens of camping trips to the uninhabited parts of Canada where light pollution is minimal, lying in a field under the stars and realizing that what is out there is so much bigger than anything going on on our little spinning ball of dust. Since then I have always been fascinated with the night sky.

I have always been interested in Science, and was one of those kids who would get a microscope for Christmas and spend hours looking at dead fruit flies on the slide. I had a knack for Science in middle school, but it wasn't until I attended South Carleton High School in 2004 that my interest in physics was really sparked by the enthusiasm of my excellent Science teachers.

In 2007, I decided to combine my interest in astronomy and physics and pursued an undergraduate degree in Astrophysics at Queen's University in Kingston, Ontario, Canada. There I learned the power of the scientific method, and through it the amazing things we can learn about the Universe. I completed my 4th year thesis project with Prof. Stephane Courteau and Dr. Joel Roediger on the validation of using numerical full spectrum synthesis on the integrated spectra of Galactic globular clusters to derive the distribution of stellar properties within them.

From there I decided to continue along the academic career path, in 2011 doing a Master's in Astrophysics at the University of Victoria in British Columbia, Canada. There I worked with Prof. Julio Navarro and Dr. Else Starkenburg studying the formation and evolution of dwarf galaxies using semi-analytic models combined with dark matter-only simulations.

Seeking adventure in a foreign country, I attended Leiden University in 2014 to pursue a PhD studying galaxy formation and evolution using the EAGLE simulations with Prof. Joop Schaye. The research presented in this thesis is the result of those PhD studies. I have been fortunate enough to have presented my research at various international conferences in the Netherlands, England, Italy, Germany, and Belgium.

I have recently become fascinated by advances in machine learning techniques and their usefulness in helping to solve real-world problems. This is why I have decided to pursue a new career in data science, for which my academic career has prepared me well. My love for astronomy will never die, and I look forward to involving myself in outreach programs to help inspire future generations of scientists in the years to come.

Acknowledgements

There are so many amazing people who have helped me get to where I am today that need to be thanked, as I am certain it wouldn't have happened without their inspiration, support, and leadership throughout the years.

First and foremost, I thank my high school physics teacher Ian Collins for being a great inspiration by making physics fun, you were truly the reason why I decided to go into science in University. I thank my Queen's physics buddies Bheeshmon, Carolyn, Greg, Joel, Meghan, Mitch, Naoya, and Popo for helping each other get through undergrad. Our reunions and camping/hiking trips since then have been amazing, and I'm looking forward to more in the future! Thanks as well to my Uvic friends Azi, Jason, Steph, Masen, Hannah, Charli, and Adrien (and many others) for the laughs, beers, hiking trips, and wings nights. Else, you helped me immensely in finishing my Master's, and as the first Dutch person I ever met you definitely played a big part in my decision to move to the Netherlands. Azi, thank you so much for the emergency evening ice cream and chocolate, Iranian dancing, and eating my leftover bananas at the end of the week, you definitely made the Master's much more fun!

And of course there are many wonderful people at the Sterrewacht to thank. First, thanks to the computer and secretarial staff for keeping everything running smoothly throughout the years despite the huge number of researchers in the department. Marijke, thanks for being an awesome officemate (and sorry about the bananas). Monica, Marco, Alex, Joki, Tiago, Lorrie, Sylvia, Camila, Sowgat, Matthieu, James, Yannick, Stijn, Nastasha, thanks for the weekly bouldering sessions and the sense of community and support you all brought to the group, and for making preprint meetings so much more fun. Thanks Lieke for being such a smart, motivated student and making my life as your supervisor super easy, I'm sure you'll go far in whichever direction in life you choose.

Andrew, Geert Jan, Mike, Ann-Sofie, and Eva, thanks for all the bizarre conversations at lunch, coffee, and borrel, as well as all the movies, board games, and D&D nights. Andrew and Geert Jan, thanks for coming back to North America with me, I'm looking forward to bothering you with visits over the next few years (and GJ thanks for translating my summary). Mike and Charlotte, thanks for teaching me what "cream tea" is and helping me with my British accent, I think I've nailed it now, maybe you'll be able to teach me the Edinburgh one soon. Ann-Sofie, thanks for sharing my weird sense of humour, you should come visit us in Canada, I promise there will be snow! Eva, thanks for being an awesome co-paranymph with me. Mike and Ann-Sofie, thanks for being my paranymphs! And especially Charlotte, thanks for all the cake.

Aayush, Jorryt, Christian, Nico, Gaby, Ricardo, David, Valeria, Luke, Niels, thanks for the fun conversations and parties over the years. Allison, keep that Canadian spirit alive. Thomas, keep on being a smooth operator, I hope to see you floating around in space someday!

Thanks to the social committee, especially Henriette, Margot, Ann-Sofie, Steven and Maike, the unsung heroes of the Sterrewacht BBQ, Sinterklaas, and the Christmas lunch. Also thanks to the Borrel committees for keeping me hydrated throughout the years: David, Mason, Allison, Christian, Ann-Sofie, myself, Nico, Pedro, Santiago, Eleonora, Kim, Maria Christina, Francisca, Kirsty, Hiddo, Fraser, and Stijn.

To my family, thanks for all of the support and for always believing in me, never having a doubt that I could get anywhere I wanted to in life. Especially thanks to Kyle for designing the cover of this thesis. Most of all, thank you Zoë for following me to every end of the Earth over the years, as well as for your constant, loving support and silly sense of humour which kept me (mostly) sane. I'm looking forward to the next step in our journey together back in Canada where, yes, we can finally get a dog.